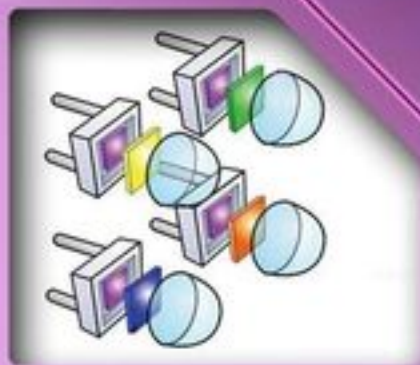


Edited by
Adrian Kitai

Luminescent Materials

and Applications



 **WILEY**

Wiley Series
in Materials for
Electronic
& Optoelectronic
Applications

Luminescent Materials and Applications

Wiley Series in Materials for Electronic and Optoelectronic Applications

Series Editors

Dr Peter Capper, *SELEX Sensors and Airborne Systems Infrared Ltd., Southampton, UK*

Professor Safa Kasap, *University of Saskatchewan, Canada*

Professor Arthur Willoughby, *University of Southampton, Southampton, UK*

Published Titles

Bulk Crystal Growth of Electronic, Optical and Optoelectronic Materials,
Edited by P. Capper

Properties of Group-IV, III–V and II–VI Semiconductors, S. Adachi

Charge Transport in Disordered Solids with Applications in Electronics, Edited by
S. Baranovski

Optical Properties of Condensed Matter and Applications, Edited by J. Singh

Thin Film Solar Cells: Fabrication, Characterization and Applications, Edited by
J. Poortmans and V. Arkhipov

Dielectric Films for Advanced Microelectronics, Edited by M.R. Baklanov, M. Green and
K. Maex

Liquid Phase Epitaxy of Electronic, Optical and Optoelectronic Materials, Edited by
P. Capper and M. Mauk

Molecular Electronics: From Principles to Practice, M. Petty

Forthcoming Titles

Photovoltaic Materials: From Crystalline Silicon to Third-Generation Approaches,
Edited by G.J. Conibeer

CVD Diamond for Electronic Devices and Sensors, Edited by R.S. Sussman

Zinc Oxide Materials for Electronic and Optoelectronic Device Applications,
Edited by C. Litton, D.C. Reynolds and T.C. Collins

Silicon Photonics: Fundamentals and Devices, M.J. Deen and P.K. Basu

Luminescent Materials and Applications

Adrian Kitai

*Departments of Materials Science and Engineering
and Engineering Physics, McMaster University,
Ontario, Canada*



John Wiley & Sons, Ltd

Copyright © 2008 John Wiley & Sons Ltd, The Atrium, Southern Gate, Chichester,
West Sussex PO19 8SQ, England
Telephone (+44) 1243 779777

Email (for orders and customer service enquiries): cs-books@wiley.co.uk
Visit our Home Page on www.wileyeurope.com or www.wiley.com

All Rights Reserved. No part of this publication may be reproduced, stored in a retrieval system or transmitted in any form or by any means, electronic, mechanical, photocopying, recording, scanning or otherwise, except under the terms of the Copyright, Designs and Patents Act 1988 or under the terms of a licence issued by the Copyright Licensing Agency Ltd, 90 Tottenham Court Road, London W1T 4LP, UK, without the permission in writing of the Publisher. Requests to the Publisher should be addressed to the Permissions Department, John Wiley & Sons Ltd, The Atrium, Southern Gate, Chichester, West Sussex PO19 8SQ, England, or emailed to permreq@wiley.co.uk, or faxed to (+44) 1243 770620.

Designations used by companies to distinguish their products are often claimed as trademarks. All brand names and product names used in this book are trade names, service marks, trademarks or registered trademarks of their respective owners. The Publisher is not associated with any product or vendor mentioned in this book.

This publication is designed to provide accurate and authoritative information in regard to the subject matter covered. It is sold on the understanding that the Publisher is not engaged in rendering professional services. If professional advice or other expert assistance is required, the services of a competent professional should be sought.

The Publisher and the Author make no representations or warranties with respect to the accuracy or completeness of the contents of this work and specifically disclaim all warranties, including without limitation any implied warranties of fitness for a particular purpose. The advice and strategies contained herein may not be suitable for every situation. In view of ongoing research, equipment modifications, changes in governmental regulations, and the constant flow of information relating to the use of experimental reagents, equipment, and devices, the reader is urged to review and evaluate the information provided in the package insert or instructions for each chemical, piece of equipment, reagent, or device for, among other things, any changes in the instructions or indication of usage and for added warnings and precautions. The fact that an organization or Website is referred to in this work as a citation and/or a potential source of further information does not mean that the author or the publisher endorses the information the organization or Website may provide or recommendations it may make. Further, readers should be aware that Internet Websites listed in this work may have changed or disappeared between when this work was written and when it is read. No warranty may be created or extended by any promotional statements for this work. Neither the Publisher nor the Author shall be liable for any damages arising herefrom.

Other Wiley Editorial Offices

John Wiley & Sons Inc., 111 River Street, Hoboken, NJ 07030, USA

Jossey-Bass, 989 Market Street, San Francisco, CA 94103-1741, USA

Wiley-VCH Verlag GmbH, Boschstr. 12, D-69469 Weinheim, Germany

John Wiley & Sons Australia Ltd, 42 McDougall Street, Milton, Queensland 4064, Australia

John Wiley & Sons (Asia) Pte Ltd, 2 Clementi Loop #02-01, Jin Xing Distripark, Singapore 129809

John Wiley & Sons Ltd, 6045 Freemont Blvd, Mississauga, Ontario L5R 4J3, Canada

Wiley also publishes its books in a variety of electronic formats. Some content that appears in print may not be available in electronic books.

Library of Congress Cataloging-in-Publication Data

Kitai, Adrian, 1957-

Luminescent materials and applications / Adrian Kitai.

p. cm.

Includes bibliographical references and index.

ISBN 978-0-470-05818-3 (cloth)

1. Electroluminescent devices—Materials.
 2. Electroluminescence.
 3. Luminescence. I. Title.
- TK7871K58 2008
621.36—dc22

2007037113 oc.

British Library Cataloguing in Publication Data

A catalogue record for this book is available from the British Library

ISBN 978-0-470-05818-3

Typeset in SNP Best-set Typesetter Ltd., Hong Kong

Printed and bound by Markono Print Media Pte Ltd, Singapore

Contents

Series Preface	xi
Preface	xiii
1 Principles of Luminescence	1
<i>Adrian H. Kitai</i>	
1.1 Introduction	1
1.2 Radiation Theory	1
1.3 Simple Harmonic Radiator	4
1.4 Quantum Description	5
1.5 Selection Rules	7
1.6 Einstein Coefficients	8
1.7 Harmonic Perturbation	9
1.8 Blackbody Radiation	12
1.9 Dipole–Dipole Energy Transfer	15
1.10 Energy Levels in Atoms	16
1.11 Crystal Field Splitting	17
Acknowledgement	18
References	18
2 Phosphor Quantum Dots	19
<i>Debasis Bera, Lei Qian and Paul H. Holloway</i>	
2.1 Introduction	19
2.2 Nanostructured Materials	22
2.3 Quantum Dots	23
2.3.1 History of quantum dots	24
2.3.2 Structure and properties relationship	25
2.3.3 Quantum confinement effects on band gap	26
2.4 Relaxation Processes of Excitons	30
2.4.1 Radiative relaxation	31
2.4.2 Non-radiative relaxation process	34
2.5 Blinking Effect	35
2.6 Surface Passivation	35
2.6.1 Organically capped Qdots	36
2.6.2 Inorganically passivated Qdots	37

2.7	Synthesis Processes	38
2.7.1	Top-down synthesis	38
2.7.2	Bottom-up approach	39
2.8	Optical Properties and Applications	42
2.8.1	II-VI Qdots	42
2.8.2	III-V Qdots	62
2.8.3	IV-VI Qdots	63
2.9	Perspective	64
	Acknowledgement	65
	References	65
3	Color Conversion Phosphors for LEDs	75
	<i>Jack Silver and Robert Withnall</i>	
3.1	Introduction	75
3.2	Disadvantages of using LEDs without Color Conversion Phosphors	76
3.3	Phosphors for Converting the Color of Light Emitted by LEDs	79
3.3.1	General considerations	79
3.3.2	Requirements of color conversion phosphors	79
3.3.3	Commonly used activators in color conversion phosphors	81
3.3.4	Strategies for generating white light from LEDs	81
3.3.5	Outstanding problems with color conversion phosphors for LEDs	82
3.4	Survey of the Synthesis and Properties of some Currently Available Color Conversion Phosphors	83
3.4.1	Phosphor synthesis	83
3.4.2	Metal oxide-based phosphors	83
3.4.3	Metal sulfide-based phosphors	95
3.4.4	Metal nitrides	100
3.4.5	Alkaline earth metal oxo-nitrides	102
3.5	Multi-Phosphor pcLEDs	102
3.6	Quantum Dots	103
3.7	Conclusions	104
	Acknowledgements	104
	References	104
4	Development of White OLED Technology for Application in Full-Color Displays and Solid-State Lighting	111
	<i>T. K. Hatwar and Jeff Spindler</i>	
4.1	Introduction	111
4.2	Generation of White Light	112
4.2.1	High-performance 2-layer white OLED architecture	113
4.2.2	Optimization of white color-two emitting layer (yellow/blue) configuration	114
4.2.3	White OLED device performance	117
4.2.4	White stability comparison with other colors and the mechanism of operational stability	120
4.2.5	Method of emitter selection to obtain suitable white color	121
4.3	White OLEDs for Display Applications	122
4.3.1	Methods of color patterning	122
4.3.2	OLED full color displays	124

4.3.3	Development of RGBW 4-pixel pattern	126
4.3.4	Full-color displays based on the RGBW format	127
4.3.5	White OLED structures for improved color gamut	128
4.3.6	Low-voltage white OLEDs	128
4.4	White OLED Tandem Architecture	130
4.4.1	Tandem architecture	131
4.4.2	Optimization of tandem stacks	131
4.4.3	Performance of tandem structure	133
4.4.4	Tandem structures for improved color gamut	135
4.4.5	Full-color displays using white OLED tandems	136
4.4.6	White tandem and improved color filters for wide color gamut	137
4.5	White OLEDs Based on Triplets	140
4.5.1	White based on fluorescent and phosphorescent emitters	141
4.5.2	Hybrid tandem-white OLEDs	141
4.6	White OLEDs Based on Conjugated Polymers	142
4.7	White OLEDs for Solid-State Lighting	143
4.7.1	Performance and cost goals for OLED lighting	143
4.7.2	Color rendition improvement using tandem white	144
4.7.3	Light extraction and enhancement using scattering layer	145
4.7.4	Top-emitting white with scattering layer	146
4.7.5	Prototypes of SSL panels	147
4.8	Advanced Manufacturing of Large-Area Coatings	149
4.8.1	Vacuum-thermal evaporation using linear sources	150
4.8.2	Flash evaporation sources	152
4.8.3	Thin-film encapsulation	153
4.9	Future Outlook	155
	Acknowledgements	156
	References	156
5	Polymer Light-Emitting Electrochemical Cells	161
	<i>Jun Gao</i>	
5.1	Introduction	161
5.1.1	EL from organic small molecules	162
5.1.2	Electroluminescence from conjugated polymers	163
5.1.3	Polymer light-emitting electrochemical cells	167
5.2	LEC Operating Mechanism and Device Characteristics	168
5.2.1	LEC Operating mechanism	168
5.2.2	LEC device characteristics	171
5.3	LEC Materials	176
5.3.1	Luminescent polymers	176
5.3.2	Electrolyte materials	180
5.4	Frozen-Junction LECs	183
5.5	Planar LECs	188
5.5.1	Planar LECs with millimeter interelectrode spacing	190
5.5.2	LECs with a relaxed p-n junction	195
5.5.3	Polymer bulk homojunction LECs	196
5.6	Conclusions and Outlook	201
	References	202

6 LED Materials and Devices	207
<i>Tsunemasa Taguchi</i>	
6.1 Introduction	207
6.2 LED Structures and Efficiencies	208
6.3 Typical LEDs and Features	211
6.4 Generation of White Light	212
6.4.1 Two methods	212
6.4.2 Characteristics of n-UV white LEDs	214
6.4.3 Design and system	217
6.5 Devices and Applications	218
6.6 Future Prospects	220
6.7 Conclusions	222
References	222
7 Thin Film Electroluminescence	223
<i>Adrian H. Kitai</i>	
7.1 Introduction	223
7.2 Background of EL	223
7.2.1 Thick film dielectric EL structure	224
7.2.2 Ceramic sheet dielectric EL	225
7.2.3 Thick top dielectric EL	226
7.2.4 Sphere-supported thin film EL	226
7.3 Theory of Operation	226
7.4 Electroluminescent Phosphors	233
7.5 Device Structures	235
7.5.1 Glass substrate thin film dielectric EL	235
7.5.2 Thick film dielectric EL	237
7.5.3 Ceramic sheet dielectric EL	240
7.5.4 Thick rear dielectric EL devices	240
7.5.5 Sphere-supported thin film EL (SSTFEL)	241
7.6 EL Phosphor Thin Film Growth	242
7.6.1 Vacuum evaporation	242
7.6.2 Atomic layer deposition	243
7.6.3 Sputter deposition	244
7.7 Full-Color Electroluminescence	245
7.7.1 Color by white	245
7.7.2 Patterned phosphors	246
7.7.3 Color by blue	246
7.8 Conclusions	247
References	248
8 AC Powder Electroluminescence	249
<i>Feng Chen and Yingwei Xiang</i>	
8.1 Background	249
8.1.1 Direct current powder electroluminescence (DCPEL)	249
8.1.2 AC powder electroluminescence (ACPEL)	252
8.2 Structure and Materials of AC Powder EL Devices	254

8.3 The Mechanism of Light Emission for AC ZnS-Powder-EL Device	257
8.4 EL Characteristics of AC Powder EL Materials	261
8.5 Preparation of Powder EL materials	262
8.5.1 Preparation of pure II-VI compounds (starting materials)	263
8.5.2 Activators (dopants)	264
8.5.3 EL emission spectra	264
8.6 Limitations of AC Powder EL Devices	265
8.6.1 Lifetime and luminance degradation	265
8.6.2 Luminance and relative high operating voltage	266
8.6.3 Moisture and operating environment	266
8.7 Applications of ACPEL	267
References	267
Index	269

Series Preface

WILEY SERIES IN MATERIALS FOR ELECTRONIC AND OPTOELECTRONIC APPLICATIONS

This book series is devoted to the rapidly developing class of materials used for electronic and optoelectronic applications. It is designed to provide much-needed information on the fundamental scientific principles of these materials, together with how these are employed in technological applications. The books are aimed at (postgraduate) students, researchers and technologists, engaged in research, development and the study of materials in electronics and photonics, and industrial scientists developing new materials, devices and circuits for the electronic, optoelectronic and communications industries.

The development of new electronic and optoelectronic materials depends not only on materials engineering at a practical level, but also on a clear understanding of the properties of materials, and the fundamental science behind these properties. It is the properties of a material that eventually determine its usefulness in an application. The series therefore also includes such titles as electrical conduction in solids, optical properties, thermal properties, etc., all with applications and examples of materials in electronics and optoelectronics. The characterization of materials is also covered within the series in as much as it is impossible to develop new materials without the proper characterization of their structure and properties. Structure-property relationships have always been fundamentally and intrinsically important to materials science and engineering.

Materials science is well known for being one of the most interdisciplinary sciences. It is the interdisciplinary aspect of materials science that has led to many exciting discoveries, new materials and new applications. It is not unusual to find scientists with chemical engineering background working on materials projects with applications in electronics. In selecting titles for the series, we have tried to maintain the interdisciplinary aspect of the field, and hence its excitement to researchers in this field.

PETER CAPPER
SAFA KASAP
ARTHUR WILLOUGHBY

Preface

Luminescence is a subject that continues to play a major technological role for humankind. We greatly value the ability to create well-illuminated indoor and outdoor spaces. We have whole-heartedly embraced light emitting flat panel displays. We continue to dream about new light sources such as flexible sheets of light that may one day replace glass tubes or glass-based displays.

This book reviews key types of solid-state luminescence that are of current interest, including organic light emitting materials and devices, inorganic light emitting diode materials and devices, down-conversion materials, nanomaterials that exhibit interesting quantum confinement effects, and powder and thin film electroluminescent phosphor materials and devices.

This book employs a science-based approach, and the chapter authors all have a strong interest in the fundamental physics that forms a basis for the phenomenon of luminescence. As such, this book may be used as a starting point to gain an understanding of various types and mechanisms of luminescence for students and professionals.

It may also be used to gain an understanding of the implementation of various types and mechanisms of luminescence into practical devices. The book presents both the physics as well as the materials aspects of the field of solid-state luminescence. Without the achievement of materials having purity and suitable morphology as well as manufacturability, solid-state luminescence would become a curiosity only.

Solid-state luminescence is now set to significantly displace gas discharge luminescence in many areas in much the same way that gas discharges have displaced tungsten filament incandescence already. One can say this with confidence owing to the high conversion efficiencies now demonstrated for inorganic and organic light emitting diodes. Efficiency values well over 100 lumens per watt are now achievable in fully solid state light emitters. It is our hope that this book not only educates, but that it also stimulates further progress in this rapidly evolving field.

I would like to thank the chapter authors for their outstanding cooperation with the rather arduous book-creating process, and would also like to thank the excellent staff at Wiley for their professionalism and dedication in bringing this book to life.

Adrian Kitai
McMaster University, Canada

1 Principles of Luminescence

Adrian H. Kitai

McMASTER UNIVERSITY, Hamilton, Ontario, ON 68S-4L7, Canada

1.1	Introduction	1
1.2	Radiation theory	1
1.3	Simple harmonic radiator	4
1.4	Quantum description	5
1.5	Selection rules	7
1.6	Einstein coefficients	8
1.7	Harmonic perturbation	9
1.8	Blackbody radiation	12
1.9	Dipole–dipole energy transfer	15
1.10	Energy levels in atoms	16
1.11	Crystal field splitting	17
	Acknowledgement	18
	References	18

1.1 INTRODUCTION

Technologically important forms of luminescence may be split up into several categories (Table 1.1). Although the means by which the luminescence is excited varies, all luminescence is generated by means of accelerating charges. The portion of the electromagnetic spectrum visible to the human eye is in wavelengths from 400 to 700 nm. The evolution of the relatively narrow sensitivity range of the human eye is complex, but is intimately related to the solar spectrum, the absorbing behavior of the terrestrial atmosphere, and the reflecting properties of organic materials. Green is the dominant color in nature and, not surprisingly, the wavelength at which the human eye is most sensitive. In this chapter, we cover the physical basis for radiation and radiation sources in solids that produce visible light.

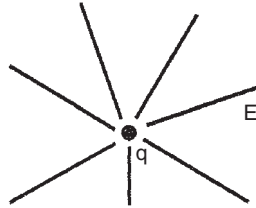
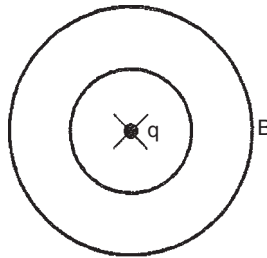
1.2 RADIATION THEORY

A stationary point charge has an associated electric field E (Figure 1.1). A charge moving with uniform velocity relative to the observer gives rise to a magnetic field (Figure 1.2). Electric and magnetic fields both store energy, and the total energy density is given by

$$\mathcal{E} = \frac{1}{2} \epsilon_0 E^2 + \frac{1}{2\mu_0} B^2$$

Table 1.1 Luminescence types, applications and typical efficiencies (visible output power/electrical input power)

Luminescence type	Typical application	Luminous efficiency
Blackbody radiation	Tungsten filament lamp	~5%
Photoluminescence	Fluorescent lamp	~20%
Cathodoluminescence	Television screen	~10%
Electroluminescence	Light-emitting diode, flat panel display	0.1–50%

**Figure 1.1** The lines of electric field E due to a point charge q . Solid State Luminescence, Adrian Kitai, Copyright 1993 with kind permission from Springer Science and Business Media**Figure 1.2** The lines of magnetic field B due to a point charge q moving into the page with uniform velocity. Solid State Luminescence, Adrian Kitai, Copyright 1993 with kind permission from Springer Science and Business Media

It is important to note that the energy density moves with the charge so long as the charge is either stationary or undergoing uniform motion; this is evident since a new reference frame may be constructed in which the observer is stationary with respect to the charge.

However, for an accelerated charge, energy continuously leaves the charge to compensate exactly for the work done in causing the charge to accelerate. Consider the charge q in Figure 1.3. Initially at rest in position **A**, it then accelerates to position **B** and stops there. The electric field lines now emanate from position **B**, but would, if further out, have emanated from position **A**, since the field lines cannot convey information about the location of the charge at speeds greater than the velocity of light c . This results in kinks in the lines of electric field which propagate away from q with velocity c . Each time q accelerates, a new series of propagating kinks is generated. Each kink is made up of a component of E that is transverse to the direction of expansion, which we call E_{\perp} . If the velocity of the charge during its acceleration does not exceed a small fraction of c , then for r :

$$E_{\perp} = \frac{qa}{4\pi\epsilon_0 c^2 r} \sin\theta$$

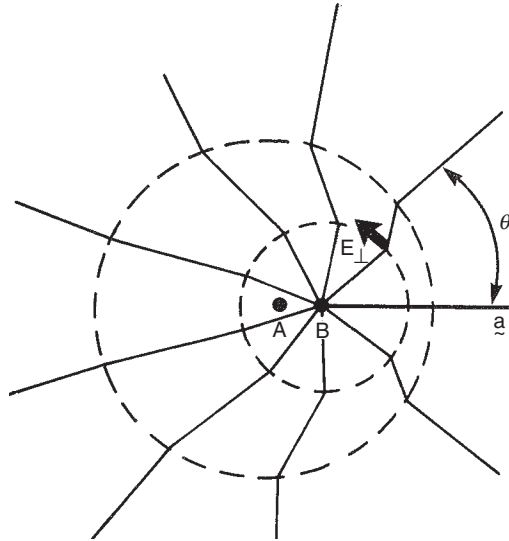


Figure 1.3 Lines of electric field emanating from an accelerating charge (after Eisberg and Resnick [1]). Solid State Luminescence, Adrian Kitai, Copyright 1993 with kind permission from Springer Science and Business Media

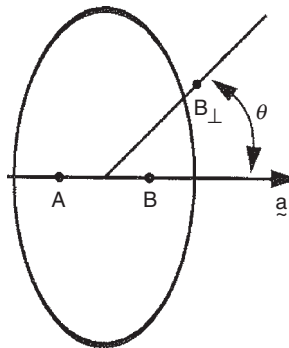


Figure 1.4 Lines of magnetic field B emanating from an accelerating charge. B is perpendicular to the page. Solid State Luminescence, Adrian Kitai, Copyright 1993 with kind permission from Springer Science and Business Media

Here, a is acceleration, and r is the distance between the charge and the position where the electric field is evaluated. The strongest transverse field occurs in directions normal to the direction of acceleration (Figure 1.3).

Likewise, a transverse magnetic field B_{\perp} is generated during the acceleration of the charge (Figure 1.4), given by

$$B_{\perp} = \frac{\mu_0 q a}{4\pi c r} \sin \theta$$

The two transverse fields propagate outwards with velocity c each time q undergoes acceleration, giving rise to the electromagnetic radiation, the frequency of which matches

the frequency with which q accelerates. Note that E_{\perp} and B_{\perp} are perpendicular to each other. The energy density of the radiation is

$$\mathcal{E} = \frac{1}{2} \epsilon_0 E_{\perp}^2 + \frac{1}{2\mu_0} B_{\perp}^2$$

The Poynting vector or energy flow per unit area (radiation intensity) is

$$\begin{aligned} S &= \frac{1}{\mu_0} \mathbf{E}_{\perp} \times \mathbf{B}_{\perp} \\ &= \frac{q^2 a^2}{16\pi\epsilon_0 c^3 r^2} \sin^2 \theta \hat{r} \end{aligned}$$

where \hat{r} is a unit radial vector.

Maximum energy is emitted in a ring perpendicular to the direction of acceleration, but no energy is emitted along the line of motion. To obtain the *total* radiated energy per unit time or power P leaving q due to its acceleration, we integrate S over a sphere surrounding q to obtain

$$P = \int S(\theta) dA = \int_0^{\pi} S(\theta) 2\pi r^2 \sin \theta d\theta$$

since dA is a ring of area $2\pi r^2 \sin^{\theta} \theta d\theta$.

Substituting for $S(\theta)$, we obtain

$$P = \frac{1}{4\pi\epsilon_0} \frac{2}{3} \frac{q^2 a^2}{c^3}$$

1.3 SIMPLE HARMONIC RADIATOR

If a charge q moves about the origin of the x -axis with position $x = A \sin \omega t$, then we can easily calculate the average power radiated away from the oscillating charge. Note that

$$a = \frac{d^2 x}{dt^2} = -A\omega^2 \sin \omega t$$

and

$$P = \frac{2q^2 A^2 \omega^4 \sin^2 \omega t}{4\pi\epsilon_0 3c^3}$$

Now, average power \bar{P} is the root-mean-square power, which gives

$$\bar{P} = \frac{q^2 A^2 \omega^4}{4\pi\epsilon_0 3c^3} \quad (1.1)$$

If we now consider that an equal and opposite stationary charge $-q$ is located at $x = 0$, then we have a dipole radiator with electric dipole moment of amplitude $p = qA$. Now we may write

$$\bar{P} = \frac{p^2 \omega^4}{12\pi\epsilon_0 c^3}$$

Non-oscillatory radiation also exists; the synchrotron radiation source is an example of a radiator that relies on the constant centripetal acceleration of an orbiting charge. Quadrupole and higher-order poles may exist, even in the absence of a dipole moment, but they have lower rates of energy release.

1.4 QUANTUM DESCRIPTION

A charge q (possibly an electron) does not exhibit energy loss or radiation when in a stationary state or eigenstate of a potential energy field. This requires that no net acceleration of the charge occurs, in spite of its uncertainty in position and momentum dictated by the Heisenberg uncertainty principle. However, experience tells us that radiation may be produced when a charge moves from one stationary state to another. It will be the purpose of this section to show that radiation may only be produced if an oscillating dipole results from a charge moving from one stationary state to another.

Consider a charge q initially in stationary state φ_n and eventually in state $\varphi_{n'}$. During the transition, a superposition state is created which we call φ_s :

$$\psi_2 = a\psi_n + b\psi_{n'}, \quad |a|^2 + |b|^2 = 1$$

where a and b are time-dependent coefficients. Initially, $a = 1$, $b = 0$ and finally, $a = 0$, $b = 1$.

Quantum mechanics allows us to calculate the expected value of the position $\langle r \rangle$ of a particle in a quantum state. For example, for stationary state φ_s ,

$$\langle r \rangle_n = \langle \psi_n | r | \psi_n \rangle = \int_V |\psi_n|^2 r \, dV$$

provided φ_n is not normalized, and V represents all space. Since, by definition, $|\varphi_n|^2$ is not a function of time because φ_n is a stationary state, the answer to this integral is always time independent and may be written as r_0 . Note that the time dependence of a stationary state is given by $|e^{(iE/\hbar)t}|^2 = e^{(iE/\hbar)t} e^{(-iE/\hbar)t} = 1$. If we now calculate the expectation value of the position of q for the superposition state φ_s , we obtain

$$\begin{aligned} \langle r \rangle_s &= \langle a\psi_n + b\psi_{n'} | r | a\psi_n + b\psi_{n'} \rangle \\ &= |a|^2 \langle \psi_n | r | \psi_n \rangle + b^2 \langle \psi_{n'} | r | \psi_{n'} \rangle + a^* b \langle \psi_n | r | \psi_{n'} \rangle + b^* a \langle \psi_{n'} | r | \psi_n \rangle \end{aligned}$$

We let

$$\psi_n = \phi_n \exp\left(-i \frac{E_n}{\hbar} t\right)$$

where ϕ_n is the spatially dependent part of φ_n . Hence

$$\begin{aligned} \langle r(t) \rangle_s &= a * b \langle \phi_n | r | \phi_{n'} \rangle \exp\left[\frac{i(E_n - E_{n'})}{\hbar} t\right] + b * a \langle \phi_{n'} | r | \phi_n \rangle \exp\left[\frac{i(E_n - E_{n'})}{\hbar} t\right] \\ &= 2 \operatorname{Re} \left\{ a * b \langle \phi_n | r | \phi_{n'} \rangle \exp\left[\frac{i(E_n - E_{n'})}{\hbar} t\right] \right\} \end{aligned}$$

since the position must be a real number. This may be written as

$$\begin{aligned} \langle r(t) \rangle_s &= 2 |a * b \langle \phi_n | r | \phi_{n'} \rangle| \cos(\omega_{nn'} t + \delta) \\ &= 2 |r_{nn'}| \cos(\omega_{nn'} t + \delta) \end{aligned} \quad (1.2)$$

Note that we have introduced the relationship $E = \hbar\omega$ that defines the energy of one photon generated by the charge q as it moves from φ_n to $\varphi_{n'}$. Note also that $\langle r(t) \rangle$ is oscillating with frequency $\omega_{nn'} = (E_n - E_{n'})/\hbar$ such that the required number of oscillations at the required frequency releases one photon having energy $E = \hbar\omega_{nn'}$ from the oscillating charge. The term $r_{nn'}$ also varies with time, but does so slowly compared with the cosine term. Consider that an electron oscillates about $x = 0$ with amplitude $A = 1 \text{ \AA}$ to produce a photon with $\lambda = 550 \text{ nm}$. From Equation (1.1)

$$\bar{P} = \frac{(1.6 \times 10^{-19})^2 \times (10^{-10})^2 (2\pi)^4 \times (3 \times 10^8)}{12\pi (8.85 \times 10^{-12}) (5.5 \times 10^{-7})^4} = 4 \times 10^{-12} \text{ W}$$

since

$$\omega = \frac{2\pi c}{\lambda}$$

One photon of this wavelength has energy $E = hc/\lambda = 3 \times 10^{-19} \text{ J}$. Hence, the approximate length of time taken to release the photon is $(3 \times 10^{-19} \text{ J}) / (4 \times 10^{-12} \text{ J s}^{-1}) = 7.7 \times 10^{-8} \text{ s}$. Since the period of electromagnetic oscillation is $T = \lambda/c = 1.8 \times 10^{-15} \text{ s}$, approximately 10^7 oscillations take place. We have assumed $|r_{nn'}|$ to be a constant, which will be shown not to be the case in a later section.

We may define a photon emission rate $R_{nn'}$ of a continuously oscillating charge. We use Equations (1.1) and (1.2) and $E = \hbar\omega$ to obtain

$$R_{nn'} = \frac{\bar{P}}{\hbar\omega} = \frac{q^2 \omega^3}{3\pi\epsilon_0 c^3 \hbar} |r_{nn'}|^2 \text{ photons s}^{-1}$$

1.5 SELECTION RULES

A particle cannot change quantum states without conserving energy. When energy is released as electromagnetic radiation, we can determine whether or not a particular transition is allowed by calculating the term $|r_{mm'}|$, and seeing whether it is zero or non-zero. The results over a variety of possible transitions give selection rules that name allowed and forbidden transitions.

The transitions involved in the hydrogen atom are of particular importance. We will now derive the well-known selection rules for the electron in hydrogen states, or more generally in one-electron atomic states. We use polar coordinates and begin by calculating $r_{mm'}$:

$$\begin{aligned} r_{mm'} &= \langle n|r|n' \rangle = \int_{\text{all space}} \psi_n^* r \psi_{n'} dV \\ &= \int_0^\infty \int_0^\pi \int_0^{2\pi} \psi_n^*(r, \theta, \phi) r \psi_{n'}(r, \theta, \phi) r^2 \sin\theta d\phi d\theta dr \end{aligned}$$

Note that since we are working in three dimensions, we must consider r in vector form, and let $\varphi(r, \theta, \phi) = R_n(r)\Theta_{lm}(\theta)\Phi_m(\phi)$. Now

$$r_{mm'} = \int_0^\infty R_{n'}(r) r^3 R_n(r) dr \left[\int_0^\pi \int_0^{2\pi} \Theta_{l'm'}(\theta)\Theta_{lm}(\theta)\sin\theta r \Phi_m^*(\phi)\Phi_{m'}(\phi) d\theta d\phi \right]$$

The term in brackets may be broken up into orthogonal components of unit vector $r = \sin\theta\cos\phi\mathbf{x} + \sin\theta\sin\phi\mathbf{y} + \cos\theta\mathbf{z}$, to obtain three terms:

$$\begin{aligned} &\int_0^\pi \sin^2\theta \Theta_{l'm'}(\theta)\Theta_{lm}(\theta) d\theta \int_0^{2\pi} \Phi_m^*(\phi)\Phi_{m'}(\phi) \cos\phi d\phi \mathbf{x} \\ &+ \int_0^\pi \sin^2\theta \Theta_{l'm'}(\theta)\Theta_{lm}(\theta) d\theta \int_0^{2\pi} \Phi_m^*(\phi)\Phi_{m'}(\phi) \sin\phi d\phi \mathbf{y} \\ &+ \int_0^\pi \sin^2\theta \cos\theta \Theta_{l'm'}(\theta)\Theta_{lm}(\theta) d\theta \int_0^{2\pi} \Phi_m^*(\phi)\Phi_{m'}(\phi) d\phi \mathbf{z} \end{aligned} \quad (1.3)$$

Since $\Phi_m(\phi) = e^{im\phi}$, the three integrals in ϕ may be written as

$$\begin{aligned} I_1 &= \int_0^{2\pi} \cos\phi e^{i(m-m')\phi} d\phi \\ I_2 &= \int_0^{2\pi} \sin\phi e^{i(m-m')\phi} d\phi \\ I_3 &= \int_0^{2\pi} e^{i(m-m')\phi} d\phi \end{aligned}$$

I_3 is zero unless $m' = m$.

I_1 may be written as

$$I_1 = \frac{1}{2} \int_0^{2\pi} [e^{i(m-m'+1)\phi} + e^{i(m-m'-1)\phi}] d\phi$$

which is zero unless $m' = m \pm 1$. I_2 gives the same result.

Now consider the integrals in θ , which multiply I_1 , I_2 and I_3 . We shall name them J_1 , J_2 , and J_3 . If I_3 is non-zero, then $m' = m$. Hence we obtain

$$J_3 = \int_0^\pi \sin \theta \cos \theta \Theta_{l'm}^*(\theta) \Theta_{lm}(\theta) d\theta$$

The integral:

$$\int_0^\pi \Theta_{l'm}^*(\theta) \Theta_{lm}(\theta) d\theta$$

is zero unless $l' = l$, a property of the associated Legendre polynomials which, being eigenfunctions, are orthogonal to each other [2]. Since $\cos \theta$ is an odd function over the range $0 \leq \theta \leq \pi$, the parity is reversed in J_3 and hence $J_3 = 0$ unless $l' = l \pm 1$.

If J_1 is non-zero, then $m' = m \pm 1$. Hence, we obtain

$$J_1 = \int_0^\pi \sin^2 \theta \Theta_{l',m\pm 1}^*(\theta) \Theta_{lm}(\theta) d\theta$$

Using the properties of associated Legendre polynomials once again, we note that it is always possible to write $\Theta_{lm}(\theta) = a\Theta_{l-1,m+1}(\theta) + b\Theta_{l+1,m+1}(\theta)$, where a and b are constants. Choosing $m' = m + 1$, we obtain

$$J_1 = \int_0^\pi \sin^2 \theta \Theta_{l',m\pm 1}^*(\theta) [a\Theta_{l-1,m+1}(\theta) + b\Theta_{l+1,m+1}(\theta)] d\theta$$

For a non-zero result, $l' = l \pm 1$ using the orthogonality property. The same conclusion is obtained from the case $m' = m - 1$ and from the J_2 integral. Therefore, we have shown that the selection rules for a one-electron atom are

$$\Delta m = 0, \pm 1 \quad \text{and} \quad \Delta l = \pm 1$$

Note that we have neglected spin-orbit coupling here. Its inclusion would give

$$\Delta l = \pm 1 \quad \text{and} \quad \Delta j = 0, \pm 1$$

Selection rules do not absolutely prohibit transitions that violate them, but they are far less likely to occur. Transitions may take place from oscillating magnetic dipole moments, or higher-order electric pole moments.

These alternatives are easily distinguished from allowed transitions since they occur much more slowly, resulting in photon release times of milliseconds to seconds rather than nanoseconds as calculated earlier. It is important to realize that practical phosphors having atomic luminescent centers often release photons via 'forbidden' transitions. The surrounding atoms in a crystal may lift the restrictions of ideal selections rules because they lower the symmetry of atomic states.

1.6 EINSTEIN COEFFICIENTS

Consider that an ensemble of atoms has electrons in quantum states k of energy E_k , which may make transitions to states l of energy E_l with the release of photons (Figure 1.5).

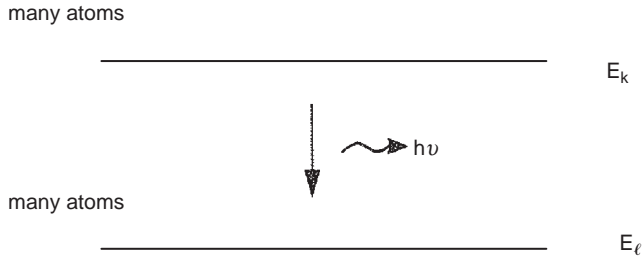


Figure 1.5 The decay of an electron from state k to state l results in the release of a photon. Solid State Luminescence, Adrian Kitai, Copyright 1993 with kind permission from Springer Science and Business Media

In order to begin making such transitions, something is needed to perturb the electrons in states k , otherwise they would not initiate the transitions, and would not populate superposition states ϕ . The study of quantum electrodynamics shows that there is always some electromagnetic field present in the vicinity of an atom, at whatever frequency is required to induce the charge oscillations and to initiate the radiation process. This is because electromagnetic fields are quantized and hence a zero-point energy exists in the field. We call this process **spontaneous emission**.

Alternatively, the transition may be initiated by applied photons (an applied electromagnetic field), which give rise to **stimulated emission**. It is also possible to excite electrons in state l to state k by using photons of suitable energy.

These ideas may be summarized as follows. The rate, at which atoms in the E_k state decay, is W_{kl} . This is proportional to the number of photons of frequency ω supplied by the radiation field, which is proportional to photon energy density $u(\nu)$ and to the number of atoms in the E_k state. The spontaneous process occurs without supplying radiation, and hence its rate is determined simply by the number of atoms in the E_k state, N_k . We may write

$$W_{kl} = [A_{kl} + B_{kl}u(\nu)]N_k = \omega_{kl}N_k \tag{1.4.a}$$

The proportionality constants A and B are called the Einstein A and B coefficients, and ω_{kl} is the rate on a per atom basis.

Atoms in the E_l state may not spontaneously become excited to the E_k state, whereas photons of energy $E_k - E_l$ may be absorbed. Hence:

$$W_{kl} = B_{lk}u(\nu)N_l = \omega_{lk}N_l \tag{1.4.b}$$

At this point, the idea of stimulated emission needs to be developed in order to explain why transition rates are proportional to $u(\nu)$. However, it is clear that A_{kl} is simply another name for $R_{m'}$, the photon emission rate, in the case of dipole radiation.

1.7 HARMONIC PERTURBATION

Consider an atom possessing electron levels k and l that experiences a weak electromagnetic field. By ‘weak’ we require that the potential energy experienced by the electrons due to this field is small compared with the Coulomb potential from the nucleus and other

electrons. The total Hamiltonian is given by the sum of the atomic term $H_0(r)$ and the perturbation term $H'(r, t)$:

$$H(r, t) = H_0(r) + H'(r, t) \quad \text{with} \quad H'(r, t) = H'(r)f(t)$$

If the field is turned on at $t = 0$ with frequency ω , then

$$H'(r, t) = \begin{cases} 0 & t < 0 \\ 2H'(r)\cos\omega t & t \geq 0 \end{cases}$$

Time-dependent perturbation theory [2] may be used to determine the wavefunction that results from the perturbation which is harmonic in this case. Assume the electron is initially in eigenstate $\phi_l(r, t)$. In general, if $\phi_k(r, t)$ are all eigenstates of $H_0(r)$ then the wavefunctions after the perturbation term $H'(r, t)$ is added will be of the form:

$$\psi(r, t) = \sum_k C_k(t)\psi_k(r, t)$$

where

$$C_k = \frac{(\phi_k | H'(r) | \phi_l)}{i\hbar} \int_0^t e^{i\omega_{kl}t'} f(t') dt'$$

and

$$\psi(r, t) = \phi_k(r) e^{i\omega_k t}$$

The probability of a transition from the initial eigenstate $\phi_l(r, t)$ to a new eigenstate $\phi_k(r, t)$ is given simply by $|C_k(t)|^2$. We write

$$P_{l \rightarrow k}(t) = |C_k(t)|^2 = \left(\frac{H'_{kl}}{i\hbar} \right)^2 \left| \int_0^t e^{i\omega_{kl}t'} f(t') dt' \right|^2$$

Because of the weak electromagnetic field, $f(t) = 2\cos\omega t$, and therefore

$$\begin{aligned} C_k(t) &= \frac{H'_{kl}}{i\hbar} \int_0^t e^{i\omega_{kl}t'} (e^{-i\omega t'} + e^{i\omega t'}) dt' \\ &= -\frac{H'_{kl}}{\hbar} \left[\frac{e^{i(\omega_{kl}-\omega)t'} - 1}{\omega_{kl} - \omega} + \frac{e^{i(\omega_{kl}+\omega)t'} - 1}{\omega_{kl} + \omega} \right] \\ &= \frac{2iH'_{kl}}{\hbar} \left\{ \frac{e^{i(\omega_{kl}-\omega)t/2} \sin[(\omega_{kl} - \omega)t/2]}{\omega_{kl} - \omega} + \frac{e^{i(\omega_{kl}+\omega)t/2} \sin[(\omega_{kl} + \omega)t/2]}{\omega_{kl} + \omega} \right\} \end{aligned}$$

Resonance occurs when $\omega_{kl} = \pm \omega$. The two signs signify either a stimulated absorption process ($\omega_{kl} = \omega$) or a stimulated emission process ($\omega_{kl} = -\omega$) since energy is then released (E_{kl} negative). If $\omega_{kl} = \omega$:

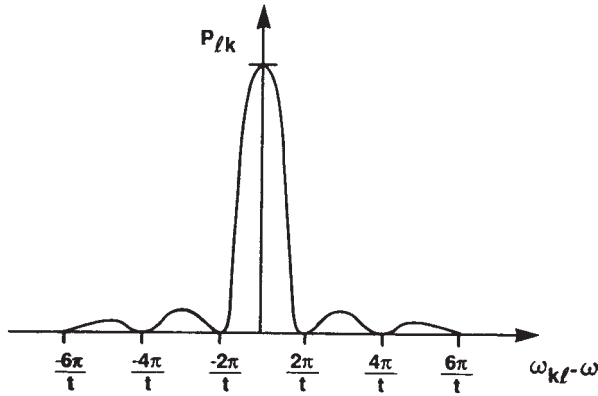


Figure 1.6 Dependence of transition probability on $\omega_{kl} - \omega$ as a result of harmonic perturbation. Solid State Luminescence, Adrian Kitai, Copyright 1993 with kind permission from Springer Science and Business Media

$$P_{lk} = |C_k|^2 = \frac{4|H'_{kl}|^2}{\hbar^2 (\omega_{kl} - \omega)^2} \sin^2 \left[\frac{1}{2} (\omega_{kl} - \omega)t \right] \tag{1.5}$$

The probability of the transition (stimulated emission or absorption) is always proportional to $|H'_{kl}|^2$. P_{lk} is shown in Figure 1.6, which should be thought of as a graph that grows rapidly in height with time t . Note, however, that being taller to begin with, the central peak grows faster than the others with time, and the function resembles a delta function for long time evolution. This is consistent with the uncertainty relationship $\Delta E \Delta t \geq \hbar/2$ since, as time increases, the uncertainty in energy approaches zero.

The term $|H'_{kl}|^2$ may be expressed in terms of the electric field E of the electromagnetic perturbation. If p is the dipole moment of the electron as it undergoes the lk transition, then

$$H' = |-p \cdot E| \propto |E|.$$

Since energy density $u(\nu)$ is proportional to $|E|^2$, it is clear that $|H'_{kl}|^2 \propto u(\nu)$, and so we have shown that the Einstein B coefficients must be multiplied by $u(\nu)$, as in Equations 1.4a and 1.4b.

When we wish to describe the time evolution of the rate of emission for an ensemble of N atoms undergoing stimulated emission, we may use

$$W_{lk} \text{ (transitions s}^{-1}\text{)} = \frac{N_t P_{lk} \text{ (transitions)}}{t \text{ (s)}}$$

Thus it is evident that when $P_{lk} \propto t^2$, then the transition rate increases linearly with time. This situation obtains for small t , since from Equation (1.5) we see that

$$P_{lk} \propto \lim_{n \rightarrow \infty} \frac{\sin^2 [\frac{1}{2}(\omega_{kl} - \omega)t] |H'_{kl}|^2}{(\omega_{kl} - \omega)^2} = \frac{1}{4} t^2$$

Of course, for long times, W_{lk} becomes constant as equilibrium is reached. Note that

$$B_{lk} = B_{kl} \text{ since } P_{lk} = P_{kl}.$$

1.8 BLACKBODY RADIATION

If an ensemble of electron states are in equilibrium, $W_{lk} = W_{kl}$. However, the spontaneous emission process may only take place in one direction, and we can write

$$[A_{kl} + B_{kl}u(\nu)]N_k = W_{kl} = W_{lk} = B_{lk}u(\nu)N_l = B_{kl}u(\nu)N_l$$

Therefore

$$\frac{N_l}{N_k} = \frac{A_{kl} + B_{kl}u(\nu)}{B_{kl}u(\nu)}$$

and

$$u(\nu) = \frac{A_{kl}N_k}{B_{kl}N_l - B_{kl}N_k}$$

Since the populations of atoms having excited states of certain energies will obey Boltzmann statistics:

$$\frac{N_l}{N_k} = e^{(E_k - E_l)/kT} = e^{\hbar\omega/kT}$$

it follows that

$$u(\nu) = \frac{A/B}{e^{\hbar\omega/kT} - 1} \quad (1.6)$$

where subscripts have been dropped.

Consider a cavity with metallic walls uniformly heated to temperature T . If we could observe the cavity through a small hole the wall, we would detect electromagnetic radiation due to the thermally agitated electrons in the cavity walls.

For analysis, suppose the cavity is cubic with edge length a , and principal axes x , y and z (Figure 1.7). Since the cavity walls are electrically conductive, the electric field in the

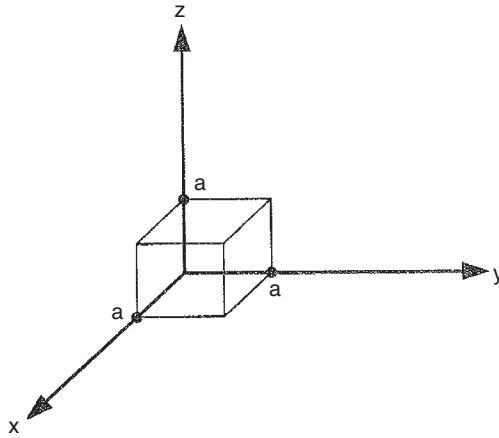


Figure 1.7 Cavity of cubic shape with edge length a (after Solymar and Walsh, [3]). Solid State Luminescence, Adrian Kitai, Copyright 1993 with kind permission from Springer Science and Business Media

radiation field must be zero at the cavity walls, and because of electromagnetic reflections at metallic surfaces, standing waves will only exist in equilibrium. Hence, the E field for waves traveling in the x -direction will be given by

$$E(x, t) = E_0 \sin\left(\frac{2\pi x}{\lambda}\right) \sin(2\pi vt) \quad \text{where } v = \frac{c}{\lambda}$$

To satisfy boundary conditions, $E(a, t) = 0$, and therefore

$$\frac{2\pi a}{\lambda} = n_x \pi, \quad \lambda_x = \frac{2a}{n} \quad \text{and} \quad v_n = \frac{cn_x}{2a}$$

Note that the frequencies are quantized and may be counted using integers n_x . Similar expressions may be written for E_y and E_z . Consider an artificial space having axes (n_x, n_y, n_z) . Such a space consists of a lattice of points, each of which uniquely describes a particular three-dimensional radiation pattern or mode. It is easy to show that all points (n_x, n_y, n_z) , at a given distance $r = 2av/c$ from the origin, represent standing waves of the same frequency ν , but along different directions within the cavity [1]. We can then count the number of cavity modes between spheres of radii $2av/c$ and $2a(v + dv)/c$ (Figure 1.8). Since each point occupies a unit ‘volume’, the number of points in the spherical shell is shell volume $4\pi r^2 dr = 4\pi(2a/c)^3 v^2 dv$. Since we wish only to consider positive values of n , we divide by 8 to count only one octant of the shell, and multiply by 2 because each standing wave has two possible polarizations. Hence, the number of modes over frequency range dv is

$$N(\nu) = \frac{8\pi a^3}{c^3} v^2 dv = \frac{8\pi V}{c^3} v^2 dv$$

Because each mode has a degree of freedom, namely the choice of electric field amplitude, on average each mode will have the same energy E which, from classical kinetic

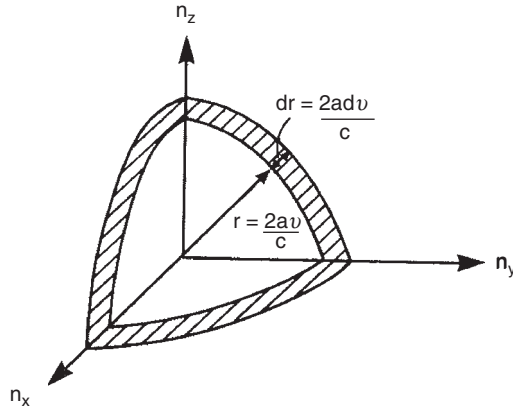


Figure 1.8 Spherical shell enclosing points in (n_x, n_y, n_z) space lattice that represent standing waves that range in frequency from ν to $\nu + d\nu$ (after Solymar and Walsh [3]). *Solid State Luminescence*, Adrian Kitai, Copyright 1993 with kind permission from Springer Science and Business Media

theory, is $E = kT$. Should one mode gain in E , it would lose it owing to collisions of electrons in the cavity walls, which would transfer it to other modes. Therefore the energy per unit cavity volume over the frequency interval $d\nu$ may be expressed in terms of the energy density $u(\nu)$ as

$$u(\nu)d\nu = \frac{8\pi\nu^2}{c^3}kT d\nu \quad (1.7)$$

This expression clearly differs from Equation (1.6). This is because our classical wave theory assumes that the energy of each cavity mode is continuously variable as just stated, even though the allowed cavity modes have discrete frequencies ν . However, in our treatment leading to Equation (1.6), we treated the energy levels giving rise to modes at frequency ν as discrete, such that $h\nu = \Delta E$. Starting with lowest frequency mode, for example along the x -direction, $n_x = 1$ and $\nu_1 = c/2a$. If $n_x = 2$, then $\nu_2 = c/a$. This implies a pair of discrete energy levels, $E_1 = h\nu_1$ and $E_2 = h\nu_2$ with difference $\Delta E = hc/2a$. So long as $\Delta E = kT$, there is no real problem with the classical treatment. However, for higher-order modes, or for lower temperatures, the energy spacing between modes may by far exceed kT and it becomes essential to take the energy of each mode as discrete. Since Equation (1.7) gives the correct result for

$$\lim_{\nu \rightarrow \infty} u(\nu) = \lim_{\nu \rightarrow \infty} \frac{8\pi\nu^2 kT}{c^3} \quad (1.8)$$

we can now evaluate A/B in Equation (1.6) by requiring that

$$\lim_{\nu \rightarrow \infty} \frac{A/B}{e^{h\nu/kT} - 1} = \frac{A/B}{h\nu/kT} = \frac{8\pi\nu^2 kT}{c^3}$$

Therefore

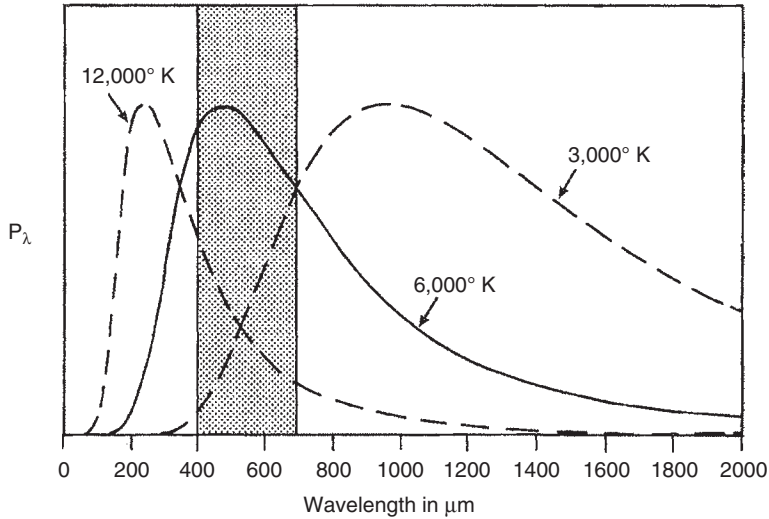


Figure 1.9 Blackbody radiation spectrum showing spectral power density for sources at temperatures of 3000 K, 6000 K and 12000 K. Note that the 6000 K curve matches the visible range best, and is similar to the solar spectrum. The three curves are artificially normalized to appear identical in height. Solid State Luminescence, Adrian Kitai, Copyright 1993 with kind permission from Springer Science and Business Media

$$A/B = \frac{8\pi\nu^3}{c^3}$$

and the final result, valid over all ν and T , is Planck's famous blackbody radiation energy density function:

$$u(\nu) = \frac{8\pi\nu^3}{c^3} \frac{1}{e^{h\nu/kT} - 1}$$

This is shown in Figure 1.9, for three different temperatures.

For visible light sources, tungsten filament lamps, which are blackbody radiators, are limited in filament temperature to somewhat below the melting point of tungsten, or ~ 3000 K. Only a small fraction of the area under the curve in Figure 1.9 corresponds to this temperature in the visible range: the physical basis for the low efficiency of such lamps. A considerable attenuation of short-wavelength (blue-violet) compared with long-wavelength (red) visible is also evident. A lamp operating at 6000 K would approximately match the Sun's surface temperature (5700 K) and be far more efficient. The tungsten halogen lamp allows for a modest gain in performance over a regular tungsten lamp by chemically stabilizing the tungsten filament, allowing for higher filament temperature.

1.9 DIPOLE-DIPOLE ENERGY TRANSFER

We now explain how energy may be transferred from one atom to another without the actual release of a photon.

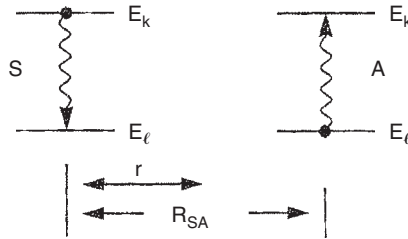


Figure 1.10 Excited atom S a distance R_{SA} from atom A. Solid State Luminescence, Adrian Kitai, Copyright 1993 with kind permission from Springer Science and Business Media

Consider an excited atom, S, and a nearby unexcited, but otherwise identical atom, A (Figure 1.10). As S radiates, it generates an oscillating electric field E due to its oscillating dipole. This field falls off as $1/r^3$ [4] and, provided that its energy does not have time to escape as a photon, it will directly stimulate a transition in A by means of the same process described by Equation (1.4). Since E falls off as $1/r^3$, then the energy density in the electric field

$$u(\nu) = \frac{1}{2} \epsilon_0 E^2$$

falls off as $1/r^6$. Therefore, from Equation (1.4), the rate (or the probability) of energy transfer from S to A depends on R_{SA}^{-6} .

1.10 ENERGY LEVELS IN ATOMS

It is always possible to formulate Schrodinger's equation to give the energy levels of electron states for an atom. Consider an optically active atom in a crystal surrounded by a space lattice of atoms. The total Hamiltonian is

$$H_{\text{tot}} = H_{\text{isolated}} + H_{\text{electrostatic lattice}} + H_{\text{dynamic lattice}}$$

H_{isolated} involves a Coulomb potential due to the atom nucleus and appropriate screening effects of inner shell electrons (H_0). The optically active electrons are now affected by spin-orbit coupling (H_{s0}), and LS coupling or exchange energy (H_c):

$$H_{\text{isolated}} = H_0 + H_{s0} + H_c$$

H_0 is spherically symmetric and yields the one-electron atom states having quantum numbers n, l, m, s . Spectroscopists use notation to describe the shell according to n levels s, p, d, f, g that correspond to $l = 0, 1, 2, 3, 4$, respectively, which represent subshells. For example, a subshell containing five electrons with $n = 3$ and $l = 2$ would be written as $3d^5$. Such a subshell exists in manganese.

Spin-orbit coupling requires the introduction of a new quantum number j , and is caused by the magnetic moments due to electron orbit and electron spin. In fact, $j = l \pm 1/2$, which gives rise to a splitting of each energy level into two levels, unless $l = 0$ (no orbital magnetic moment).

In LS coupling, the effects of more than one electron within unfilled subshells are considered. A Coulombic electron – electron interaction energy term exists. The spin angular momenta of individual electrons add together, as do orbital angular momenta, giving rise to a total spin s' and a total orbital angular momentum l' . For example, consider an atom with configuration $3d^14p^1$. There are, because of both H_{s0} and H_c , 12 levels in this case [1], which are labelled 3D_3 , 1F_3 , 1P_1 , etc. The superscript is $2s' + 1$; the letter designates l' (the same scheme as for l , but now using capital letters to acknowledge addition of orbital angular momenta) and the subscript is j' formed by adding s' and l' as vectors. Energy splittings occur since the average separation and therefore Coulombic energy between electrons depends upon the way in which angular momenta are added.

Additional complications arise if H_{s0} and H_c are similar in strength. The level splittings become more complex, and the LS coupling exclusion principle forbids the existence of certain states.

1.11 CRYSTAL FIELD SPLITTING

When an atom S is placed in a crystal, it experiences the **crystal field**, or the electric field due to surrounding atoms. We will assume that the electrons involved in the energy levels of interest for luminescence are not involved in bonding. This is generally true in practice. Because of crystal symmetry, atoms surrounding S will give rise to an electric field with some symmetry. For example, a tetrahedral crystal site will have tetrahedral symmetry, and an octahedral site will have octahedral symmetry. The electric potential of an electron in atom S due to the crystalline environment may always be expressed in the form:

$$V_s(\theta, \phi) = \sum_{l,m} a_{lm} y_l^m(\theta, \phi)$$

where y_l^m are the **spherical harmonics**. This is analogous to a Fourier series expansion, but is specifically applicable to an atom or sphere surrounded by a field that has angular dependence. The crystal field may now be taken into account, using time-independent perturbation theory if V_s is small. If we know the eigenstates of H_o and add perturbation H' , then to first order:

$$\phi_n = \phi_n^{(0)} + \sum_{i \neq n} \frac{\langle \phi_i^{(0)} | H' | \phi_n^{(0)} \rangle}{E_n^{(0)} - E_i^{(0)}} \phi_i^{(0)}$$

and

$$E_n = E_n^{(0)} + \langle \phi_n^{(0)} | H' | \phi_n^{(0)} \rangle$$

Note that the new eigenstates, ϕ_n and eigenenergies, E_n are based on the eigenstates, $\phi_n^{(0)}$ and eigenenergies $E_n^{(0)}$ of the unperturbed system. To account for the crystal field, we simply substitute $H'(\theta, \phi) = V_s(\theta, \phi)$ and determine the new states due to the crystal field.

If the symmetry of the crystal field is different from the eigenstates involved, which is usually the case, then degenerate states will probably split because of the crystal field. This

is known as crystal field splitting. In this case, $E_n^{(0)} - E_i^{(0)} = 0$ for some $n, i, n \neq i$. In order to determine the ϕ_n and E_n , we must first make the matrix element $\langle \phi_i^{(0)} | H | \phi_n^{(0)} \rangle$ zero whenever $E_i^{(0)} = E_n^{(0)}$, such that these singular terms vanish. This may be accomplished by diagonalizing the submatrix of H'_{in} , which contains the degenerate states. The energy splittings are then obtained directly.

For transition metal ions placed in a crystal field, the three-dimensional states may be more influenced by the crystal field than by H_c . This is known as the strong field scheme [5]. For such an ion in an octahedral crystal field, for example, the five-fold degenerate three-dimensional orbitals split into a two-fold degenerate e_g state and a three-fold degenerate t_{2g} state. The energy separation between the two states is called $10Dq$, where Dq is a parameter determined by the crystal field strength. Now, H_c may be accounted for in a manner analogous to free-ion LS coupling.

In Cr^{3+} , for example, there is a $3d^3$ configuration. If placed in an octahedral crystal field, the splitting depends on the term Dq/B , which is a measure of the crystal field influence. A theoretical treatment [6] gives the splittings.

Transitions that were forbidden in the free ion may become dipole transitions with a crystal field. The lower symmetry allows a dipole moment to exist and these new transitions can take place, although with small rates. Radiative lifetimes of 10^{-3} s are not unusual for transition metal ions such as Mn^{2+} in a tetrahedral crystal field.

ACKNOWLEDGEMENT

This chapter is reproduced from *Solid State Luminescence: Theory, Materials and Devices* (ed. A. H. Kitai, 1993) by permission of the publishers, Chapman and Hall, London.

REFERENCES

- Eisberg, R. and Resnick, R. (1985) *Quantum Physics of Atoms, Molecules, Solids, Nuclei and Particles*, 2nd edn, New York: Wiley.
- Liboff, R.L. (1980) *Introductory Quantum Mechanics*, Oakland, CA: Holden-Day
- Solymar, L. and D. Walsh, D. (1985) *Lectures on the Electrical Properties of Materials*, 3rd edn, Oxford: Oxford University Press.
- Kip, A.F. (1969) *Fundamentals of Electricity and Magnetism*, 2nd edn, New York: McGraw-Hill.
- Yen, W.M. and Selzer, P.M. (1986) *Laser Spectroscopy of Solids*, Vol. 49, 2nd edn, Berlin: Springer.
- Tanabe, Y. and Sugano, S. (1954) *J. Phys. Soc. Jpn.* **9**: 766.

2 Phosphor Quantum Dots

Debasis Bera, Lei Qian and Paul H. Holloway

UNIVERSITY OF FLORIDA, 202 Rhines Hall, PO Box 116400, Gainesville,
FL-32611-6400 USA

2.1 Introduction	19
2.2 Nanostructured materials	22
2.3 Quantum dots	23
2.4 Relaxation processes of excitons	30
2.5 Blinking effect	35
2.6 Surface passivation	35
2.7 Synthesis processes	38
2.8 Optical properties and applications	42
2.9 Perspective	64
Acknowledgement	65
References	65

2.1 INTRODUCTION

The word ‘phosphor’ comes from the Greek language and means ‘light bearer’, to describe light-emitting or luminescent materials; barium sulfide is one of the earlier known naturally occurring phosphors [1]. A phosphor is luminescent, that is, it emits energy from an excited electron as light. The excitation of the electron is caused by absorption of energy from an external source such as another electron, a photon or an electric field. An excited electron occupies a quantum state whose energy is above the minimum energy ground state. In semiconductors and insulators, the electronic ground state is commonly referred to electrons in the valence band, which is completely filled with these electrons. The excited quantum state often lies in the conduction band, which is empty and is separated from the valence band by an energy gap called the band gap, ΔE_g (Figure 2.1). Therefore, unlike metallic materials, small continuous changes in electron energy within the band are not possible. Instead a minimum energy equal to the band gap is necessary to excite an electron in a semiconductor or insulator, and the energy released by de-excitation is often nearly equal to the band gap. The band gap of a semiconductor material is such that at room temperature very few electrons are promoted from the valence band to the conduction band leaving holes in the valence band.

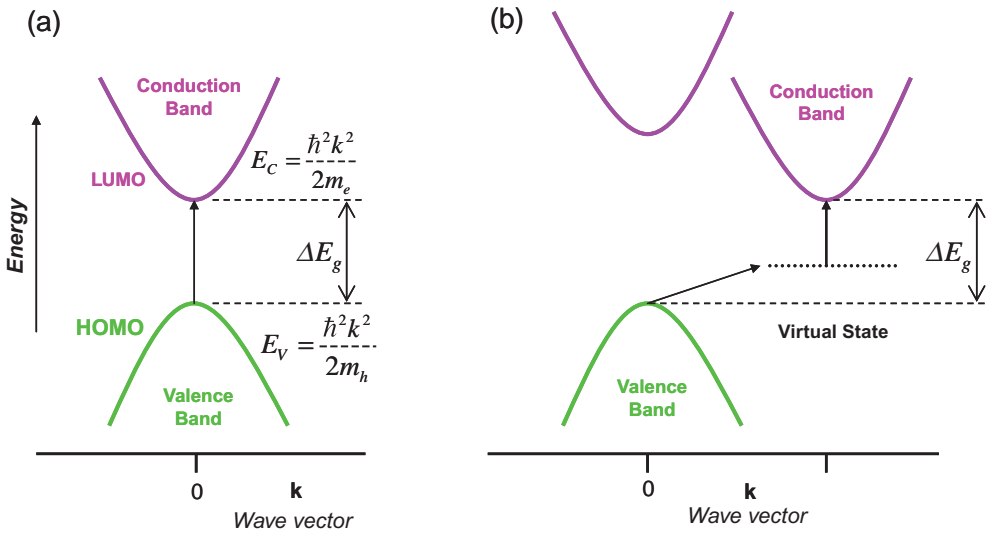


Figure 2.1 Schematic band-energy diagrams for: (a) direct band gap; and (b) indirect band gap semiconductors

Figure 2.1 (a) shows an energy band diagram (plot of allowed quantum state energy vs. wave vector magnitude k) for a direct band gap semiconductor. In the direct band gap semiconductors, the positions of the highest energy state of the valence band (HOMO-highest occupied molecular orbital) and the lowest energy state of the largely unoccupied conduction band (LUMO-lowest unoccupied molecular orbital) are at the same k resulting in a high probability of emitting light. The case of an indirect band gap semiconductor is shown in Figure 2.1 (b), and has the valence band maximum and conduction band minimum at different values of k . Therefore, electrons need to undergo a change of k -value followed by a change in energy. Therefore, the transition requires a change in both energy and momentum. In other words, an indirect transition requires energy excitation of an electron simultaneous with an electron-phonon interaction to give the required momentum change. Therefore, the absorption and recombination efficiency of direct band gap materials is about four orders of magnitude larger than that of indirect material. Zinc sulfoselenide ($\text{ZnS}_{1-x}\text{Se}_x$) and gallium phosphide (GaP) are examples of direct and indirect band gap compound semiconductors, respectively.

As discussed above, luminescence from phosphors can be observed by exciting the electrons to higher energy states, for example, into the conduction band. There are several approaches that provide this excitation [1], such as:

- photoluminescence (PL)
- electroluminescence (EL)
- cathodoluminescence (CL)
- mechanoluminescence
- chemiluminescence
- thermoluminescence.

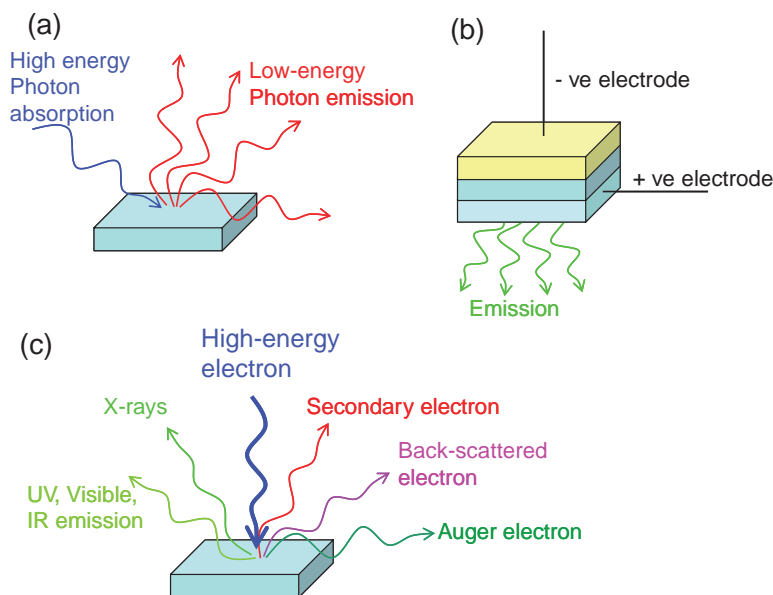


Figure 2.2 Schematic illustrations of: (a) photoluminescence; (b) electroluminescence; and (c) cathodoluminescence

In this chapter, only PL, EL and CL (Figure 2.2) will be discussed, with most emphasis on PL and EL.

When an insulator or semiconductor absorbs electromagnetic radiation (i.e. a photon) an electron may be excited to a higher energy quantum state. If the excited electron returns (relaxes) to a lower energy quantum state by radiating a photon, the process is called photoluminescence (PL). Some of the quantum state relaxation transitions are not allowed, based on the spin and *Laporte* selection rules [2]. The PL intensity depends on the measurement temperature and the energy of the exciting light (known as photoluminescence excitation or PLE spectrum). In general, peaks in the PLE spectrum are higher in energy than those in the PL spectrum. Figure 2.2 (a) schematically illustrates the excitation and emission processes of PL.

When a material emits electromagnetic radiation as a result of the application of an electric field, the process is called electroluminescence (EL). The photon emitted results from radiative recombination of electrons and holes created in the phosphor by the voltage between the two electrodes (Figure 2.2 (b)). One of the electrodes is transparent to the wavelength of the light emitted by the device. The first report of an EL device was in 1907 [3], when Henry Joseph Round observed that light was emitted from silicon carbide under application of a high voltage. As discussed below, there is significant interest in inorganic nanophosphors combined with conducting organic materials to produce EL devices, because of their potentially high efficiencies. Other advantages for EL devices in comparison to conventional lighting systems also include small to large size, flexible substrates and shapes, high brightness, long device lifetimes, lower operating temperatures, non-directionality and antiglare lighting. Depending on the applied bias, thin-film electroluminescence (TFEL) device can be categorized as either DC or AC (ACTFEL) devices.

Cathodoluminescence (CL) is emission of light from a material that is excited by energetic electrons. The exciting primary electrons can be focused into a beam and scanned across the surface (as in a scanning electron microscope), resulting in high spatial resolution CL. The CL process is shown schematically in Figure 2.2 (c), along with other phenomena that result from primary electron–material interactions, for example, X-ray and various electron emissions.

2.2 NANOSTRUCTURED MATERIALS

Nanostructured materials, by definition, can exist as individual particles or clusters of nanoparticles of various shapes and sizes [4, 5]. Research has shown that nanostructured materials generally exhibit geometries that reflect the atomistic bonding analogous to the bulk structure. The nanomaterials are of interest because they can bridge the gap between the bulk and molecular levels and lead to entirely new avenues for application. Nanostructured materials have a high surface-to-volume ratio compared to their bulk counterparts. Therefore, a large fraction of atoms is present on the surface, which makes them possess different thermodynamic properties. During the last two decades, a great deal of attention has been focused on the optoelectronic properties of nanostructured semiconductors with an emphasis on fabrication of the smallest possible particles. The research has revealed that many fundamental properties are size-dependent in the nanometer range. For example, the density of states (DOS), that is the number of quantum states vs. energy for periodic materials with three, two or one dimension, is shown in Figure 2.3 [6]. If the extent of the material is on the order of one to ten nanometers in all three directions, the material is said to be a quantum dots (Qdots). A Qdot is zero-dimensional relative to the bulk, and the DOS depends upon whether or not the Qdots have aggregated (Figure 2.3). The DOS for a molecule and an atom are also shown in Figure 2.3.

The density of electrons in a three-dimensional bulk crystal is so large that the energy of the quantum states becomes nearly continuous (Figure 2.3). However, the limited number of electrons results in discrete quantized energies in the DOS for two, one and zero-dimensional structures (Figure 2.3). The presence of one electronic charge in the Qdots repels the addition of another charge and leads to a staircase-like I-V curve and DOS. The step size of the staircase is proportional to the reciprocal of the radius of the Qdots. The boundaries as to when a material has the properties of bulk, Qdot or atoms, are dependent upon the composition and crystal structure of the compound or elemental solid. When a solid exhibits a distinct variation of optical and electronic properties with a variation of size, it can be called a nanostructure, and is categorized as:

- two-dimensional, e.g. thin films or quantum wells;
- one-dimensional, e.g. quantum wires; or
- zero-dimensional, e.g. Qdots.

Although each of these categories shows interesting optical properties, our discussion will be focused on quantum dots, or Qdots. An enormous range of fundamental properties can be realized by changing the size at a constant composition. In the following sections, we

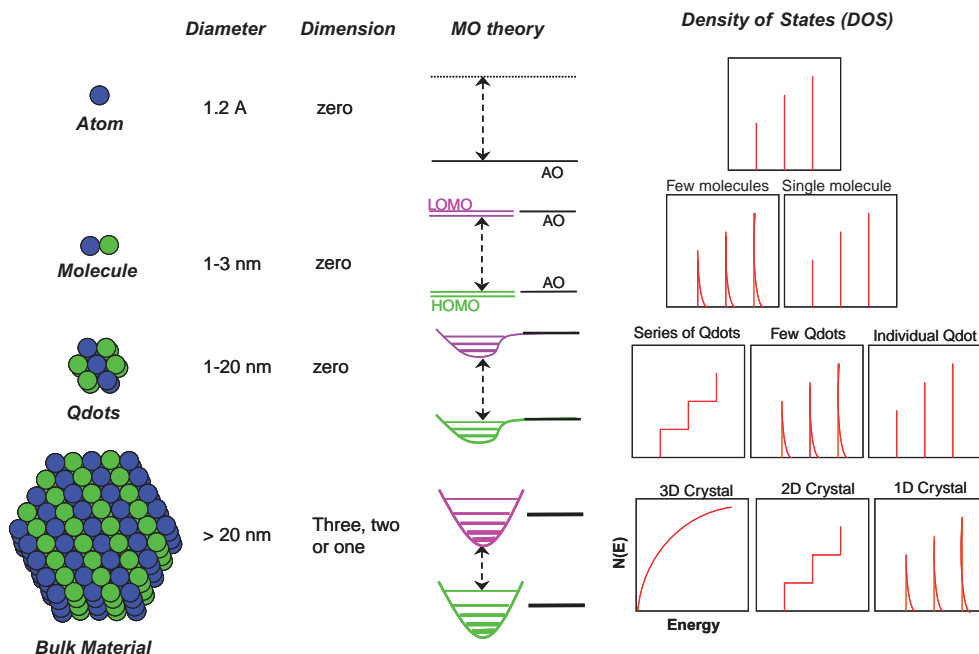


Figure 2.3 Schematic illustration of the changes of the density of quantum states (DOS) with changes in the number of atoms in materials (see text for detailed explanation). AO: atomic orbital, MO: molecular orbital

will discuss the history, structure and properties relationships, and the optical properties of Qdots.

2.3 QUANTUM DOTS

Nanostructured semiconductors or insulators have dimensions and numbers of atoms between the atomic-molecular level and bulk material with a band gap that depends in a complicated fashion upon a number of factors, including the bond type and strength with the nearest neighbors. For isolated atoms, there is no nearest-neighbor interaction. Therefore, sharp and narrow luminescent emission peaks are observed. A molecule consists of only a few atoms and therefore exhibits emission similar to that of an atom. However, a nanoparticle is composed of approximately 100–10000 atoms, and has optical properties distinct from its bulk counterpart. Nanoparticles with dimensions in the range of 1–30 nm are called quantum dots (Qdots). Zero-dimensional Qdots are often described as artificial atoms due to their δ -function-like density of states, which can lead to narrow optical line spectra.

A significant amount of current research is aimed at using the unique optical properties of Qdots in devices, such as light-emitting diodes (LEDs), solar cells and biological markers. Qdots are of interest in biology for several reasons:

- higher extinction coefficients;
- higher quantum yields;
- less photobleaching;
- absorbance and emissions can be tuned with size;
- generally broad excitation window but narrow emission peaks;
- multiple Qdots can be used in the same assay with minimal interference with each other;
- toxicity may be less than conventional organic dyes; and
- the Qdots may be functionalized with different bio-active agents [7–9].

The inorganic Qdots are more photostable under ultraviolet excitation than organic molecules, and their fluorescence is more saturated. The ability to synthesize Qdots with narrow size distributions with high quantum yields [10, 11] has made them an attractive alternative to organic molecules in hybrid light-emitting devices and solar cells.

Qdots can be broadly categorized into either elemental or compound systems. In this chapter, we emphasize compound semiconductor-based nanostructured materials. Compound materials can be categorized according to the columns in the periodic table, e.g.:

- IB-VIIB (CuCl, CuBr, CuI, AgBr, etc.);
- IIB-IVB (ZnO, ZnS, ZnSe, ZnTe, CdO, CdS, CdSe, CdTe, etc.);
- IIIB-VB (GaN, GaP, GaAs, InN, InP, InSb, etc.); and
- IVB-VIB (PbS, PbSe, PbTe, etc.).

Our discussion will be confined mainly to IIB-VIB, IIIB-VB and IVB-VIB Qdot-based phosphors, where frequently the B designations are dropped, that is, the compounds are designated as II-VI or III-V.

2.3.1 History of quantum dots

A process for synthesizing PbS Qdots was developed more than 2000 years ago using low-cost natural materials such as PbO, Ca(OH)₂ and water [12]. The Romans and Greeks used these materials as cosmetics to dye their hair. In more recent history, control of the size of Qdots in silicate glasses is one of the oldest and most frequently used techniques to control the color of glass. In the early twentieth century, CdS and CdSe were incorporated into silicate glasses to obtain red-yellow colors. In 1932, Rocksby [13] used X-ray diffraction to determine the precipitates of CdS and CdSe in producing colors. Semiconductor doped glasses were used in optics as filters. A blue shift of the optical spectrum for nanometer sized CuCl in silicate glass was reported in 1981 by Ekinov and Onushchenko [14]. In 1982, Efros and Efros [15] advanced that quantum size effects (the change of optical and optoelectronic properties with size) could be used to control the color of glass by either changing the size or stoichiometry of CdS_xSe_{1-x}. In 1991, the change in color of

colloidal solutions of semiconductor was discussed by Rosetti *et al.* [16]. Over the last two decades, experimental and theoretical research on nanoparticles has increased significantly [17, 18].

2.3.2 Structure and properties relationship

The most fascinating change of properties in Qdots with particle size less than ~ 30 nm is the drastic differences in the optical absorption, exciton energies and electron-hole pair recombination. Use of these Qdot properties requires strict control on their synthesis and structures because their intrinsic properties are determined by factors such as size, shape, defects, impurities and crystallinity. The dependence on size arises from:

- changes of the surface-to-volume ratio with size;
- quantum confinement effects.

Due to the high surface-to-volume ratio of Qdots, electronic quantum states associated with the surface (called surface states) have significant effects on the optical properties of Qdots. For example, roughly 15% of the atoms in a 5 nm CdS Qdot are at the surface [19]. Such a high surface-to-volume ratio may allow an enhanced or reduced transfer rate of photogenerated charge carriers, due to the high density of surface sites. The surface states of the Qdots may influence the optical absorption, quantum efficiency, luminescent intensity, and spectrum and aging effects [20]. In general, surface states arise from unsatisfied bonds at the reconstructed surface, but may also be affected by nonstoichiometry and voids. The energy of these surface states generally lay in the band gap of the Qdots. Therefore, they can trap charge carriers and lead to radiative and/or nonradiative recombination of electron-hole pairs. As a result, surface states have significant effects on the optical properties of the Qdots.

The most unique property of Qdots is quantum confinement, which modifies the density of states (DOS) near the band edges. Schematic diagrams of the DOS as a function of energy in Figure 2.3, show that Qdots lie between the discrete atomic and continuous bulk materials. Quantum confinement effects are observed when the size is sufficiently small that the energy level spacing of a nanocrystal exceeds kT (where k is Boltzmann's constant and T is temperature). Energy differences $>kT$ restrict the electron and holes mobility in the crystal. Among the many properties that exhibit a dependence upon size in Qdots, two are of particular importance for nanophosphors.

The first is a blue shift (increase) of band gap energy when the nanoparticle diameters are below a particular value that depends on the type of semiconductor. This is called a quantum confinement effect [21, 22] and is discussed below in detail. This effect allows tuning of the energy gap with changes in Qdot size. The band gap energy also depends on the composition of the semiconductor as well as the size. The second important property is the observation of discrete, well separated energy states due to the small number of atoms in Qdots compared to the bulk (Figure 2.3). This leads to the electronic states of each energy level exhibiting wave functions that are more atomic-like. Since solutions of the Schrödinger wave equation for Qdots are very similar to those for electrons bound to a nucleus, the Qdots are called artificial atoms, and atomic-like sharp emission peaks are possible. Typical intraband energy level spacings for Qdots are in the range of 10–100 meV.

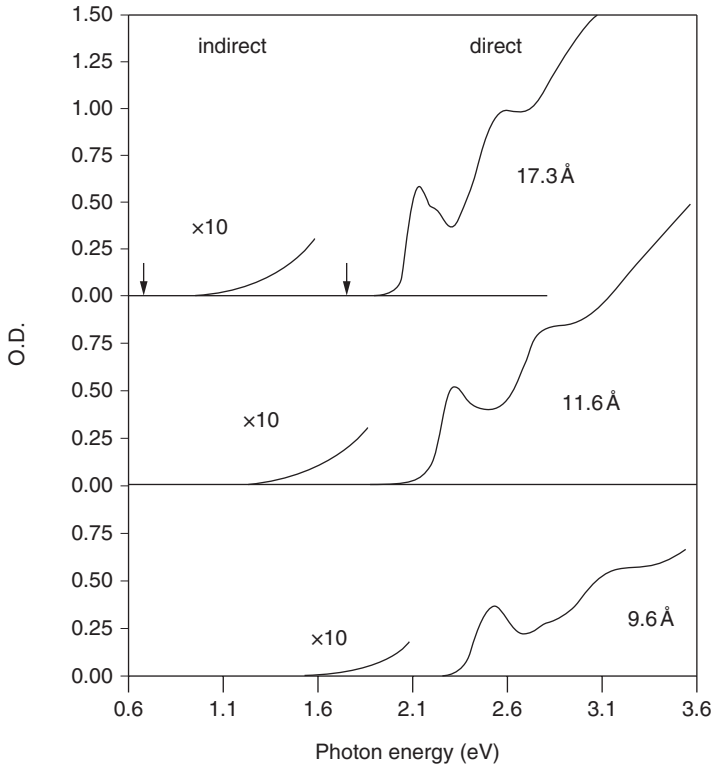


Figure 2.4 CdSe Qdots exhibited direct and indirect band gaps at atmospheric and ~ 9.3 GPa pressures. Arrow marks shows the band gaps of the bulk CdSe at atmospheric pressure and 9 GPa, respectively (reprinted with permission from [23]. Copyright (1994) American Physical Society)

Qdots exhibit solid-solid phase transition like bulk semiconductors, and these transitions have a substantial influence on the optical properties of Qdots. Phase transitions in bulk materials can be induced by varying pressure, temperature and composition [23, 24]. Bulk CdSe may exhibit either a hexagonal wurtzite or a zinc blende rock salt cubic structure with a direct or indirect band gap, respectively. At a pressure of ~ 3 GPa, the CdSe bulk semiconductor can be converted reversibly from low pressure wurtzite to the high pressure rock salt structures [25]. The low intensity optical emission from the rock salt form of CdSe is in the near IR spectral region at 0.67 eV ($1.8\mu\text{m}$). Using high pressure X-ray diffraction and optical absorption, Tolbert and Alivisatos showed that the wurtzite to rock salt structural transformation also occurred in CdSe Qdots [23, 24] (Figure 2.4). The ratio of oscillator strength between direct and indirect structures was unchanged with Qdot size.

2.3.3 Quantum confinement effects on band gap

Quantum confinement generally results in a widening of the band gap with a decrease in size of the Qdots. The band gap in a material is the energy required to create an electron

and a hole at rest (i.e. with zero kinetic energy) at a distance far enough apart that their *Coulombic attraction* is negligible. If one carrier approaches the other, they may form a bound electron-hole pair, an exciton, whose energy is a few meV lower than the band gap. This exciton behaves like a hydrogen atom, except that a hole, not a proton, forms the nucleus. Obviously, the mass of a hole is much smaller than that of a proton, which affects the solutions to the Schrödinger wave equation. The distance between the electron and hole is called the exciton Bohr radius (r_B). If m_e and m_h are the effective masses of electrons and holes, respectively, the exciton Bohr radius can be expressed by

$$r_B = \frac{\hbar^2 \epsilon}{e^2} \left(\frac{1}{m_e} + \frac{1}{m_h} \right) \tag{2.1}$$

where ϵ , \hbar and e are the dielectric constant, reduced *Planck constant* and the charge of an electron, respectively.

If the radius (R) of a Qdot approaches r_B , i.e. $R \approx r_B$, or $R < r_B$, the motion of the electrons and holes are confined spatially to dimensions of the Qdot, which causes an increase of the excitonic transition energy and the observed blue shift in the Qdot band gap and luminescence. The exciton Bohr radius is a threshold value, and the confinement effect becomes important when the Qdot radius is smaller. For small Qdots, the exciton binding energy and bi-exciton binding energy (exciton-exciton interaction energy) is much larger than for bulk materials [26]. Note that for a material with a relatively higher k and smaller m_e and m_h , the r_B is larger. Data for some semiconductors are summarized in Table 2.1.

Two detailed theoretical approaches are used to better predict the exciton properties, specifically the effective mass approximation (EMA) model and linear combination of atomic orbital (LCAO) theory.

2.3.3.1 Effective mass approximation model

This approach, based on the ‘Particle-in-a-Box Model’, is the most widely used model to predict quantum confinement. It was first proposed by Efros and Efros [15] in 1982 and later modified by Brus [27]. It assumes a spherical particle in a potential well with an infinite potential barrier at the particle boundary. For a free particle to assume any position in the box, the relationship between its energy (E) and wave vector (k) is given by

$$E = \frac{\hbar^2 k^2}{2m^*} \tag{2.2}$$

In the EMA model, this relationship (Equation 2.2) is assumed to hold for an electron or hole in the semiconductor, therefore the energy band is parabolic near the band edge. The shift of band gap energy (ΔE_g), due to confinement of the exciton in a Qdot with a diameter R , can be expressed as

$$\Delta E_g = \frac{\hbar^2 \pi^2}{2\mu R^2} - \frac{1.8e^2}{\epsilon R} = \frac{\hbar^2 \pi^2}{2R^2} \left(\frac{1}{m_e} + \frac{1}{m_h} \right) - \frac{1.78e^2}{\epsilon R} - 0.248 E_{Ry}^* \tag{2.3}$$

Table 2.1 Band gap and Bohr radii data for selected semiconductors

Group	Name	Band Gap/eV		Exciton Binding Energy (meV)	Relative Dielectric Constant	Crystal Structure	Lattice Constant (Å)
		4K	300K				
IIB-VIB	ZnO	3.44	3.37	59	8.1	Wurzite	a: 3.250 b: 5.207
	ZnS	3.91	3.8	40	8.3	Wurzite	a: 3.811 c: 6.234
		3.84	3.68	36	8.9	Zinc Blende	5.406
	ZnSe	2.82	2.67	17	8.8	Zinc Blende	5.667
	ZnTe	2.38	2.25	11	8.7	Zinc Blende	6.104
	CdS	2.58	2.42	27	8.6	Zinc Blende	5.832
		2.58	2.53	28		Wurzite	a: 4.135 c: 6.749
	CdSe	1.84	1.714	15	9.4	Wurzite	a: 4.299 c: 7.010
	CdTe	1.60	1.45	10	10.3	Zinc Blende	6.4818
	IIIB-VB	GaN	3.28	3.2	25.2	9.3	Zinc Blende
GaP		2.35	2.25	20.5	11	Zinc Blende	5.4505
GaAs		1.52	1.43	4.2	13.2	Zinc Blende	5.653
InN		2.11	1.97	15.2	9.3	Wurtzite	a: 3.533 c: 5.693
					15.3		
InP		1.42	1.35	6.0	12.6	Zinc Blende	5.867
InAs			0.354		15.2	Zinc Blende	6.0583
InSb		0.24	0.17	0.6	16.8	Zinc Blende	6.479
		(0K)					
IVB-VIB	PbS	0.41	0.29		17.3		
IVB	Si	1.12	1.12	14.4	11.4	Diamond	5.431
	Ge	0.75	0.67	4.15	15.5	Diamond	5.658

where μ is the reduced mass of an electron-hole pair and E_{Ry}^* is Rydberg energy. The first term of the Equation 2.3 represents a relationship between particle-in-a-box quantum localization energy or confinement energy and the radius of the Qdot (R), whereas the second term shows the *Columbic interaction* energy with an R^{-1} dependence. The Rydberg energy term is size independent and is usually negligible, except for semiconductors with small dielectric constants [19]. Based on Equation 2.3, the first excitonic transition (i.e. the band gap) increases as the Qdot radius decreases. However, the EMA model breaks down in the small Qdot regime [19, 28] because the E - k relationship can no longer be approximated as parabolic. Figure 2.5 shows such a deviation of theoretically predicted band gaps for CdS Qdots from the experimental values.

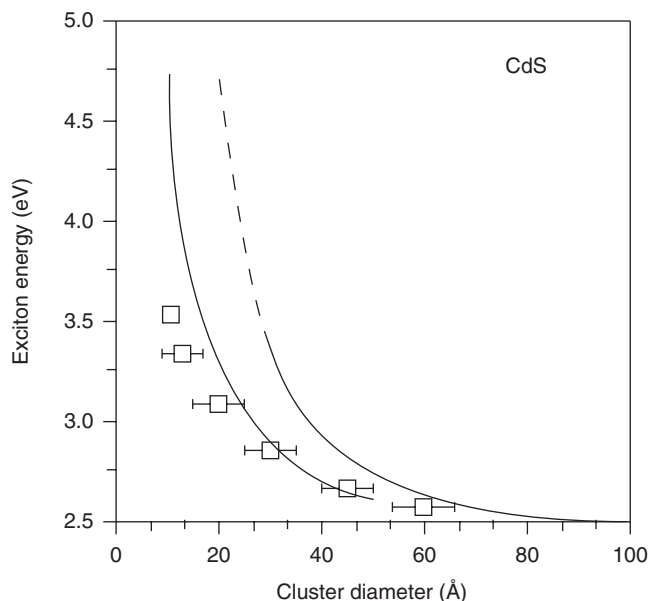


Figure 2.5 Experimentally and theoretically determined band gap as a function size of CdS Qdots. Broken line: calculated parameters based on effective mass approximation, solid-line: tight-bonding calculation; squares: experimental data (reprinted with permission from [19]. Copyright (1991) American Chemical Society)

2.3.3.2 Linear combination of atomic orbital theory-molecular orbital theory

A model based on a linear combination of atomic orbitals – molecular orbitals (LCAO-MO) provides a more detailed basis for predicting the evolution of the electronic structure of clusters from atoms and/or molecules to Qdots to bulk materials, and predicts the dependence of band gap on size of the crystals. Figure 2.3 shows the results of this approach pictorially. In a diatomic molecule, the atomic orbitals (AO) of two individual atoms are combined, producing bonding and anti-bonding molecular orbitals. In this approach, nanosized Qdots are considered as large molecules. As the number of atoms increase, the discrete energy band structure changes from large energy steps to small energy steps, that is to a more continuous energy band. The occupied (bonding) molecular orbital quantum states (equivalent to the valence band) are called the highest occupied molecular orbital (HOMO) levels. The unoccupied antibonding orbitals (equivalent to the conduction band) are called the lowest unoccupied molecular orbital (LUMO) levels. The energy difference between the top of the HOMO and bottom of the LUMO (equal to the band gap, ΔE_g in Figure 2.1) increases and the bands split into discrete energy levels of reduced mixing of AOs for a small number of atoms. Therefore, the small size of the Qdots results in quantized electronic band structures intermediate between the atomic/molecular and bulk crystalline MOs.

Compared to the effective mass approximation, the LCAO-MO model provides a methodology to calculate the electronic structure of much smaller Qdots. In contrast, this method cannot be used to calculate the energy levels of large Qdots due to mathematical complexity and limitations of the computing systems. Nevertheless, the degree of quantum confinement

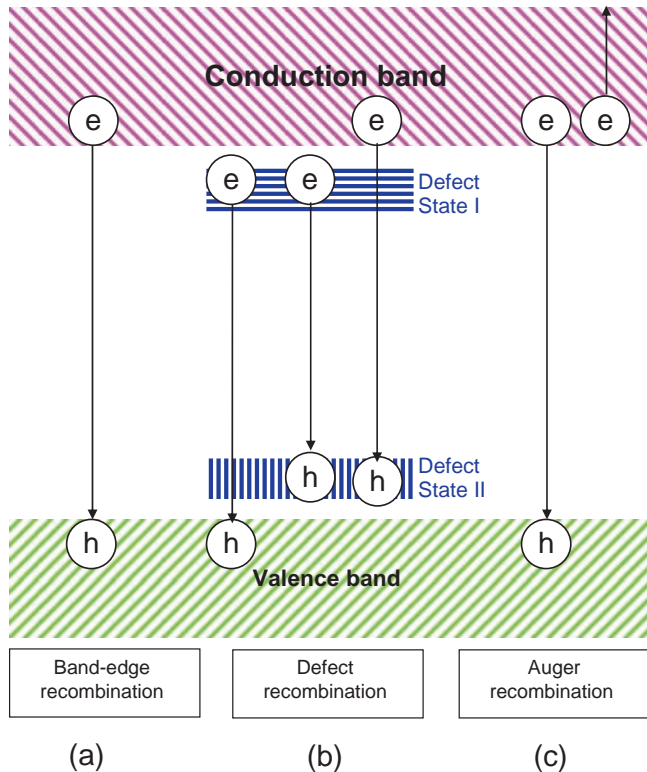


Figure 2.6 A few radiative and nonradiative processes that can occur during luminescence (e: electron, h: hole)

is determined by the ratio of the radius of a Qdot (R) to bulk excitonic Bohr radius (r_B). At crystal sizes greater than the excitonic Bohr diameter ($2r_B$), semiconductor crystals exhibit translational motion confinement of the fully coupled exciton due to a strong Coulombic interaction between the electron and holes, that is, they exhibit single-particle confinement behavior (sometimes called the strong confinement regime). In the intermediate size range ($R \leq r_B$), the transition energies of photoexcited carriers in the crystal are determined by the relative strengths of the kinetic energy of confinement and the electron-hole interaction.

2.4 RELAXATION PROCESS OF EXCITONS

After excitation by an external energy (photon, electric field, primary electron, etc.), electron and hole possess high energies due to transitions from their ground state to an excited state. The energies associated with such optical absorptions are directly determined by the electronic structure of the material. The excited electron and hole may form an exciton, as discussed above. The electron may recombine with the hole and relax to a lower energy state, ultimately reaching the ground state. The excess energy resulting from recombination and relaxation may be either radiative (emits photon) or nonradiative (emitting phonons or *Auger* electrons). In photoluminescence, electrons in a material move to allowed excited quantum states upon absorption of a higher energy photon. Recombination of the electron

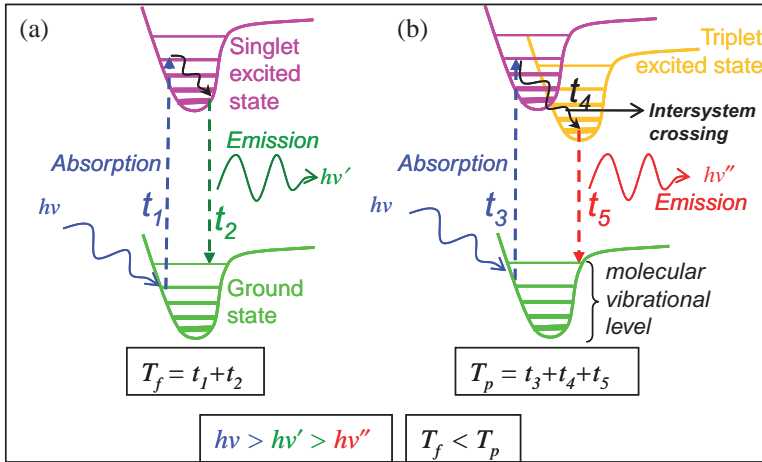


Figure 2.7 Schematic diagram of (a) fluorescence (f) and (b) phosphorescence (p); $h\nu$ is energy, T and t : time [29]

and hole results in emission of a photon (i.e. radiative recombination leads to PL). Some radiative events from band edge, defects and nonradiative processes are depicted in Figure 2.6. These processes are discussed in detail below.

2.4.1 Radiative relaxation

Radiative relaxation results in spontaneous luminescence from Qdots. Such luminescence may result from band edge or near band edge transitions, or from defect and/or activator quantum states.

2.4.1.1 Band edge emission

The most common radiative relaxation processes in intrinsic semiconductors and insulators are band edge and near band edge (exciton) emission. The recombination of an excited electron in the conduction band with a hole in the valence band is called band edge emission (Figure 2.6 (a)). As noted above, an electron and hole may be bound by a few meV to form an exciton. Therefore, radiative recombination of an exciton leads to near band edge emission at energies slightly lower than the band gap. Radiative emission may also be characterized as either fluorescence or phosphorescence, depending upon the path required to relax. Fluorescence exhibits short radiative relaxation lifetimes (10^{-9} – 10^{-5} s), but are still long compared to excitation times (10^{-15} – 10^{-13} s) [29]. Radiative relaxation processes with lifetimes $>10^{-5}$ s are called phosphorescence.

In a typical PL process (Figure 2.7), an electron in a phosphor is excited by absorption of an electromagnetic wave, $h\nu$, from its ground state to an excited state. Through a fast vibrational (nonradiative) process, the excited electron relaxes to its lowest energy excited vibrational state. For electronic relaxation in molecules, nanoparticles or bulk solids, the emitted photon is red shifted relative to the excitation photon energy/wavelength (i.e. *Stokes*

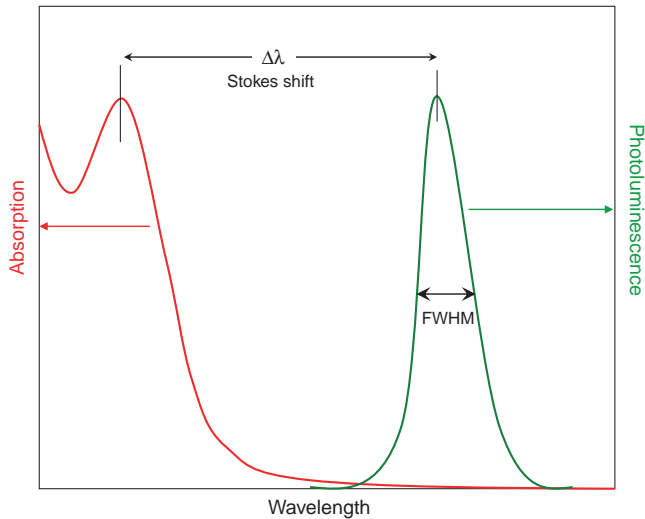


Figure 2.8 Spectral absorption and photoluminescence profile depicting the Stokes shift

shift as discussed below) because of the presence of vibrational levels in the excited state as well as the lower energy (e.g. ground) states (Figure 2.7 (a)). Both organic and inorganic luminescent materials exhibit Stokes shifts. In organic materials, this relaxation process may be complicated by crossing from singlet to triplet excited states (Figure 2.7 (b)) [29]. When intersystem crossing occurs, the lifetime is long (10^{-5} – 10 s) and the emission is classified as phosphorescence. Radiative transitions in inorganic solids that are forbidden by the optical selection rules [2] may also exhibit phosphorescence.

The full width at half maximum (FWHM) of a room-temperature band edge emission peak from Qdots is typically in the range of 15–20 nm. Since the peak originates from a transition between the conduction and valence bands, the energy of the photons is equal to the band gap of the Qdot. The optical absorption spectrum reflects the band structure of the materials because of the large DOS. On the other hand, PL spectra are dominated by the sparse lower energy defect and activator states, because photoexcited carriers rapidly thermalize and are captured by states within $\sim kT$ of the lowest energy levels [30]. Therefore, an increase in wavelength (decrease in energy) is observed between absorbed and emitted photons due to vibrations in molecular or atomic solids. As pointed out above, this red shift is called the Stokes shift (Figure 2.8). In a limited number of cases, the emission energy is shifted to a shorter wavelength (higher energy), and is called an anti-Stokes shift or ‘upconversion’. There is great interest in converting low-energy photons to higher-energy photons via processes such as second-harmonic generation and stimulated Raman [31].

2.4.1.2 Defect emission

Radiative emission from nanophosphors also comes from localized impurity and/or activator quantum states in the band gap (Figure 2.6 (b)). Defect states are called dark states when they lie inside the bands themselves [32]. Depending on the type of defect or impurity, the state can act as a donor (has excess electrons) or an acceptor (has a deficit of electrons). Electrons or holes are attracted to these sites of deficient or excess local charge due to

Coulombic attraction. Similar to the case of excitons, trapped charge on defect/impurity sites can be modeled as a hydrogenic system where binding energy is reduced by the dielectric constant of the material [30]. These defect states can be categorized into either shallow or deep levels, where shallow level defect states have energies near the conduction band or valence band edge. In most cases, a shallow defect exhibits radiative relaxation at temperatures sufficiently low so that thermal energies (kT) do not excite the carriers out of the defects or trap states. Deep levels, on the other hand, are so long-lived that they typically experience nonradiative recombination.

Luminescence from these defect levels can be used to identify their energy, and their concentration is proportional to the intensity. Both PL spectral distribution and intensity change with fluctuations in excitation energy due to contributions from different defect energy levels and the band structure of the host. The excitation energy also determines the initial photoexcited states in the sample, but this state is short-lived because of thermalization of the photoexcited carriers via phonon emission, as discussed above. Relaxation to within kT of the lowest vibrational level of the excited states is usually orders of magnitude faster than the recombination event [30].

Defect states are expected at the surface of a Qdot despite the use of various passivation methods, because of the large surface-to-volume ratio discussed above. The concentration of surface states on the Qdots is a function of the synthesis and passivation processes. These surface states act as traps for charge carriers and excitons, which generally degrade the optical and electrical properties by increasing the rate of nonradiative recombination. However, in some cases, the surface states can also lead to radiative transitions, such as in the case of ZnO. Powders of ZnO have a green emission from defects along with a band edge near ultraviolet emission (the band gap of ZnO is 3.37 eV or 386 nm). It is also reported that the green emission will suppress the band-edge emission.

Theoretical and experimental studies [33, 34] showed that the defect states in a ZnO Qdot can be of several types, including:

- neutral, singly or doubly charged Zn vacancies (V_{Zn});
- neutral or singly charged oxygen vacancies (V_O);
- singly charged or neutral interstitial Zn (Zn_i);
- interstitial O (O_i);
- a complex of V_O and Zn_i (V_OZn_i);
- a complex of V_{Zn} and Zn_i ($V_{Zn}Zn_i$); and
- substitution O at Zn position (O_{Zn}).

According to Aleksandra *et al.* [34], the singly charged oxygen vacancy (V_{O+}) is located at 2.28 eV below the conduction band in the ZnO band gap and results in an emission at ~ 540 nm. The most widely, but not universally, accepted mechanism for green luminescence from ZnO is the electron-hole recombination on singly ionized oxygen vacancies. In solution-based synthesis, the oxygen vacancies appear to be intrinsic and may result from heterogeneous nucleation and growth, enhanced by the large surface area. If the radiative center is associated in part with the surface, their concentration would be expected to decrease with aggregation of Qdots as observed [35].

2.4.1.3 Activator emission

Luminescence from intentionally incorporated impurities is called extrinsic luminescence. These impurities are called activators and they perturb the band structure by creating local quantum states that lies within the band gap. The predominant radiative mechanism in extrinsic luminescence is electron-hole recombination, which can occur via transitions from conduction band to acceptor state, donor state to valance band or donor state to acceptor state. In some cases, this mechanism is localized on the activator atom center. However, these localized transitions are only allowed when two selection rules are met [2]:

1. spin selection rule, i.e. $\Delta s = \pm 1$, where s is the spin quantum number, and
2. Laporte selection rule $\Delta l = 0$, where l is the orbital angular momentum quantum number.

In many cases, the Laporte selection rule is relaxed due to mixing of orbitals, such as d - p mixing in a crystal or ligand field where the orbitals are split into hyperfine structures. Therefore, d - d transition is allowed in some cases for transition elements, such as Mn^{2+} , Fe^{2+} and Cr^{3+} . For Mn^{2+} , the lifetime of the luminescence [36] is in the order of milliseconds due to the forbidden d - d transition.

Similarly, f - f transition are often observed for rare earth elements (e.g. Tm^{3+} , Er^{3+} , Tb^{3+} and Eu^{3+}), although the f levels are largely unaffected by the crystal field of the host, due to shielding by the outer s - and p -orbitals [2]. Because of this shielding effect, f - f transitions typically have atomic-like sharp peaks in the emission spectrum.

2.4.2 Non-radiative relaxation process

As reported above, absorption of energy by a luminescent material may not result in emission of light. Electrons and holes in excited states may return to lower energy and ground states by radiative and/or nonradiative relaxations. Deep level traps have a tendency to undergo nonradiative recombination by emitting phonons. Experimental data show that the time required for nonradiative recombination is short (e.g. tens of picoseconds [37]). Non-radiative relaxation may be categorized as internal conversion, external conversion or Auger recombination [38].

Nonradiative recombination through crystalline and/or molecular vibrations is a common phenomenon in internal conversion. The difference between the energy absorbed by Qdots, $h\nu$, and the band gap, E_g , is generally converted into heat by electron-phonon scattering processes and results in the Stokes shift. Even for a radiative process in an indirect semiconductor, a phonon is generated due to the change of k -value (Figure 2.1 (b)). Furthermore, strain in a lattice can create a local potential well that can also trap electrons and holes and result in a nonradiative transition.

Nonradiative recombination at surface states dominate the external conversion category. As reported above, 15–30% of atoms in a Qdot are at the surface and represent defects due to unsaturated dangling bonds. These defects are dominant channels for nonradiative decay of carriers. The electronic surface states are filled below the *Fermi level* with electrons from the core of the Qdots. Accumulation of charge at the surface creates an electric field or a depletion region that leads to bending of the valence and conduction band edges. Electron and hole carriers generated in this region are swept in opposite directions by the electric

field, prohibiting radiative recombination. This leads to the concept of a ‘dead layer’ [30]. Capping of these defects with organic ligands or inorganic shells leads to an improvement in luminescent efficiency, as discussed below.

Strong carrier-to-carrier interaction can lead to an Auger nonradiative process. Rather than releasing the energy of recombination as a photon or phonon, the excess energy is transferred to another electron that is called an Auger electron (Figure 2.6 (c)). The Auger electron loses its surplus energy by creation of phonons. The Auger recombination process (Figure 2.6 (c)) involves two electrons and a hole in the conduction and valence bands, respectively. Auger recombination can also create a hole deep in the valence band or can be observed for electrons and holes on localized activator levels [38]. In an Auger transition, the momentum and energy must be conserved, therefore indirect semiconductors show much higher Auger recombination rates as compared to direct band gap materials. This is due to the fact that a momentum change is necessary for Auger recombination, and is also required for the transition in indirect band gap semiconductors.

2.5 BLINKING EFFECT

As mentioned above, Qdots have a number of advantages over organic dyes in bio-applications, for example, better photostability, wide absorption edges and narrow, tunable emission. However, they may exhibit a random, intermittent luminescence, which is called ‘blinking’. In blinking, a Qdot emits lights for a time followed by a dark period (Figure 2.9). In 1996, Nirmal *et al.* [39] observed this switching between an emitting and a non-emitting state from a single CdSe Qdot at room temperature. The postulated mechanism of blinking is a photoinduced ionization process [37], which leads to a charged Qdot that results in a separation between electrons and holes. Based on this model, the Qdots would be dark for the lifetime of the ionized state. A nonradiative Auger recombination process would be expected to dominate the quenching of ionized Qdots [37]. However, the experimental results do not completely support this model. For example, a photo-induced Auger process should exhibit a quadratic dependence of the average blinking time on excitation intensity, whereas the experimental result would show a linear behavior. In addition, the bright and dark periods follow an inverse power law [40] given by

$$P(t) = A \cdot t^{-m} \quad (2.4)$$

where $P(t)$ is probability of the blinking period, m is an exponent between 1 and 2 and A is a constant. Several additional mechanisms have been proposed to explain the blinking [32, 41–43], including thermally activated ionization, electron tunneling through fluctuating barriers or into a uniform distribution of traps, or resonant electron tunneling between the excited states of Qdots and dark-trap states that wander randomly in energy. Despite tremendous efforts, the blinking effect is still not properly explained.

2.6 SURFACE PASSIVATION

To use Qdots, stable emission with a high quantum efficiency must be achieved. As discussed above, surface defects in Qdots act as temporary ‘traps’ for the electron, hole or excitons, quenching radiative recombination and reducing the quantum yields. Therefore,

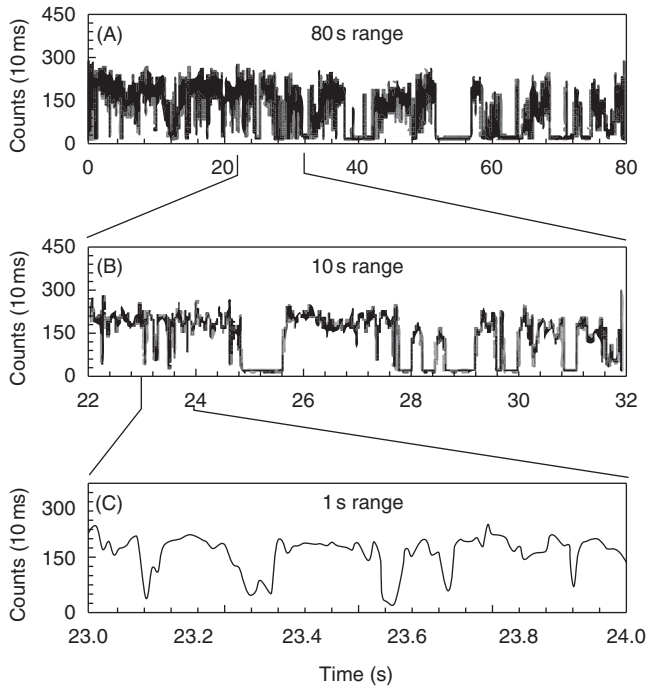


Figure 2.9 Blinking effect from a single 2.9 nm CdSe Qdot [43]. Emission is shown in three expanded timescales (reused with permission from [43] Copyright 2000, American Institute of Physics)

capping or passivation of the surface is crucial for development of photostable Qdots. In principle, a perfectly passivated surface of a Qdot has all dangling bonds saturated and therefore exhibits no surface states, and all near band edge states are quantum-confined internally. For a compound semiconductor, if the anion dangling bonds at the surface are not passivated, a band of surface states is expected in the gap just above the valence band edge. However, passivation of anions with surface cations would also leave dangling bonds that would lead to a broad band of surface states just below the conduction band edge. Therefore, surface modification of Qdots is very demanding and is generally carried out by depositing an organic or inorganic capping layer on the Qdots.

2.6.1 Organically capped Qdots

Generally, monodispersed Qdots are developed by introducing organic molecules that absorb on the Qdot surface and act as capping agents [6]. A schematic illustration of an organically passivated surface is presented in Figure 2.10 (a). Some advantages of organic capping layers include simultaneous achievement of colloidal suspension capping, and the ability to bio-conjugate the Qdots.

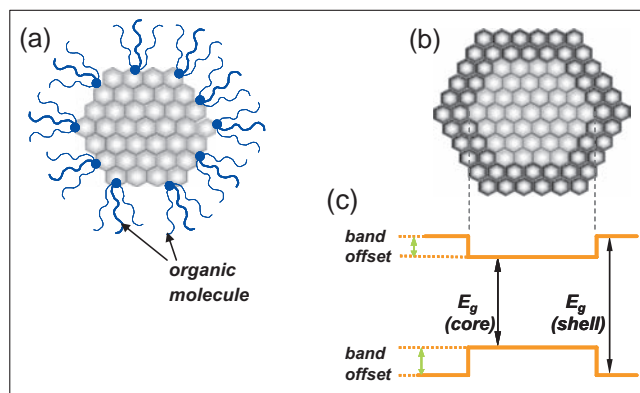


Figure 2.10 Schematic illustration of (a) an organically capped Qdot and (b) an inorganically passivated Qdot (core/shell structure of Qdot). (c) An energy diagram shows the band-gap difference of core and shell of inorganically passivated Qdots

However, the selection of organic ligands that will bond with surface atoms of the Qdots is a delicate issue. In general, phosphenes, (e.g. tri-*n*-octyl phosphine oxide (TOPO)) or mercaptans are the most widely used ligands. Most of the organic capping molecules are distorted in shape and larger than a surface site. As a result, coverage of surface atoms with the organic capping molecules may be sterically hindered. Another crucial issue is the simultaneous passivations of both anionic and cationic surface sites using such capping agents, which is extremely difficult. Therefore, some dangling bonds on the surface are always present when the surface is passivated by organic agents. Finally, the organic capped Qdots are photounstable. The bonding at the interface between the capping molecules and surface atoms is generally weak, leading to the failure of passivation and creation of new surface states under UV irradiation. The surface states of nanocrystals are known by sites of preferential photodegradation and luminescence quenching.

2.6.2 Inorganically passivated Qdots

A second approach to passivation of the Qdots surface is the use of inorganic layers, particularly a material with a larger band gap. The passivating shell is grown either epitaxially (Figure 2.10 (b)) or as a non-epitaxial crystalline or amorphous layer on the core. The quantum efficiency of Qdots is increased by a defect-free, uniform shell coating. When the shell material adapts the lattice parameters of the core during epitaxial growth, coherency strains result and can play an important role in the properties of these core/shell systems. For example, strain may cause the absorption and emission spectra of core/shell Qdots to be red-shifted [44]. The maximum PL efficiency of core/shell Qdots is also dependent upon the thickness of the shell layer, which is less than two monolayers for optimum properties of CdSe/CdS

core/shell nanoparticles. Thicker capping layers lead to formation of misfit dislocations, which are also nonradiative recombination sites that decrease the PL quantum yield.

Generally, a wider band gap shell material is desired to create a potential barrier around the Qdot core to confine the exciton (Figure 2.10 (c)). Confinement of the charge carriers into the core region by the band offset potentials result in efficient and photostable luminescence from Qdots. Additional factors to consider when selecting the Qdot inorganic shell material include whether it is hydrophobic or hydrophilic. Most inorganic core/shell Qdots are not compatible with dispersion in water due to the hydrophobic surface property of the shell. For biological application of Qdots, an appropriate water-compatible coating, such as an amorphous silica layers, is necessary [7]. For best passivation, the shell material should have a lattice parameter within 12% of the core to encourage epitaxy and minimize strain, and a thickness below the critical value that results in misfit dislocations [45].

Inverted core/shell Qdots, for example, ZnSe/CdSe with a larger band gap for the core, show interesting optoelectronic properties. They exhibit either type I or type II interfacial band offsets, depending on the core radius and the shell thickness [46]. Type I offset is shown in Figure 10(c), that is, there is an opposite offset for both the valence and conduction bands. This is the case for bulk ZnSe/CdSe interfaces, where the ZnSe valence band edge is lower than that in CdSe (energy offset ~ 0.14 eV), while the conduction band edge is higher (energy offset ~ 0.86 eV). Such an energy alignment results in confinement of both electrons and holes inside the CdSe shell. However, the situation can change in the case of nanostructures in which the alignment of quantized energy states is determined not only by bulk energy offsets, but also by the confinement energies determined by the heterostructure dimensions.

Core/shell Qdots with type II offsets (valence and conduction band offsets in the same direction) can also provide ‘spatially indirect’ states, in which electrons are spatially confined to the core (or shell) and holes are confined to the shell (or core). The emission energy from type II core/shell nanostructures is smaller than the band gap of either the core or the shell material, due to the interfacial energy offsets. Because of the reduced electron-hole wave function overlap, these structures show extended exciton lifetimes and are useful in photovoltaic and photocatalysis applications [47]. With a large red-shift in emission from type-II core/shell Qdots, near-infrared emission may be possible for *in vivo* bio-analytical and biomedical applications.

2.7 SYNTHESIS PROCESSES

Several routes have been used to synthesize phosphor Qdots. Generally, the techniques for synthesis of Qdots are categorized either as a top-down or bottom-up approach.

2.7.1 Top-down synthesis

In the top-down approaches, a bulk semiconductor is thinned to form the Qdots. Electron beam lithography, reactive-ion etching and/or wet chemical etching are commonly used to achieve Qdots of diameter ~ 30 nm. Controlled shapes and sizes with the desired packing geometries are achievable for systematic experiments on quantum confinements effects. Alternatively, focused ion or laser beams have also been used to fabricate arrays of zero-

dimension dots. Major drawbacks with these processes include incorporation of impurities into the Qdots and structural imperfections by patterning.

Etching, known for more than 20 years, plays an important role in these nanofabrication processes. In dry etching, a reactive gas species is inserted into an etching chamber and a radio frequency voltage is applied to create a plasma, which breaks down the gas molecules into more reactive fragments. These high kinetic energy species strike the surface and form a volatile reaction product to etch a patterned sample. When the energetic species are ions, this etching process is called reactive ion etching (RIE). With a masking pattern, selective etching of the substrate is achieved. Fabrication of GaAs/AlGaAs quantum structures as small as 40 nm has been reported using RIE with a mixture of boron trichloride and argon [48]. This RIE process has been used to produce close-packed arrays for testing of lasing in Qdot semiconductors. Close packed arrays of ZnTe with interdot distance of 180 nm to 360 nm were produced by RIE using CH₄ and H₂ [49].

Focused ion beam (FIB) techniques also offer the possibility of etching Qdots with extremely high lateral precision. Highly focused beams from a molten metal source (e.g. Ga, Au/Si, Au/Si/Be or Pd/As/B) may be used directly to sputter the surface of the semiconductor substrate. The shape, size and inter-particle distance of the Qdots depend on the size of the ion beam but a minimum beam diameter of 8–20 nm has been reported for both lab and commercial systems, allowing etching of Qdots to dimensions of <100 nm [50].

The FIB technique can also be used to selectively deposit material from a precursor gas with a resolution of ~100 nm. Scanning ion beam images (analogous to scanning electron microscope images) can be developed by ion beam nanofabrication at the desired, predetermined locations with high resolution [50]. However, this is a slow, low throughput process employing expensive equipment that leaves residual surface damage.

Another method to achieve patterns with Qdot dimensions is the use of electron beam lithography followed by etching or lift-off processes. This approach offers a high degree of flexibility in the design of nanostructured systems. Any shape of Qdots, wires or rings with precise separation and periodicity may be realized with this technique. This method was successfully employed for the synthesis of III-V and II-VI Qdots with particle sizes as small as 30 nm.

2.7.2 Bottom-up approach

A number of different self-assembly techniques have been used to synthesize the phosphor Qdots, and they may be broadly subdivided into chemical and physical methods. Micro-emulsion, sol-gel, competitive reaction chemistry, hot solution decomposition and electro-chemistry are generally placed in the category of chemical methods. Self-assembly of nanostructures in material grown by molecular beam epitaxy (MBE), sputtering, liquid metal ion sources or aggregation of gaseous monomers are generally categorized under physical methods.

2.7.2.1 Chemical methods

Chemical methods mainly follow the conventional precipitation methods with careful control of parameters for a single solution or mixture of solutions. The precipitation process

invariably involves both nucleation and limited growth of nanoparticles. Nucleation may be categorized as homogeneous, heterogeneous or secondary nucleation [51]. Homogeneous nucleation occurs when solute atoms or molecules combine and reach a critical size without the assistance of a pre-existing solid interface. By varying factors such as temperature, electrostatic double layer thickness, stabilizers or micelle formation, concentrations of precursors, ratios of anionic to cationic species and solvent, Qdots of the desired size, shape and composition can be achieved. Some of the common synthesis processes are briefly discussed below.

Sol-gel Process: Sol-gel techniques have been used for many years to synthesize nanoparticles, including Qdots [20, 52]. In a typical technique, a sol (nanoparticles dispersed in a solvent by Brownian motion) is prepared using a metal precursor (generally alkoxides, acetates or nitrates) in an acidic or basic medium. The three main steps in this process are hydrolysis, condensation (sol-formation) and growth (gel formation). In brief, the metal precursor hydrolyzes in the medium and condenses to form a sol, followed by polymerization to form a network (gel). This method has been used to synthesize II-VI Qdots, such as CdS and ZnO [20, 52]. As an example, ZnO Qdots have been prepared by mixing solutions of Zn-acetate in alcohol and sodium hydroxide, followed by control aging in air [20]. The process is simple, cost-effective and suitable for scale-up. The main disadvantages of the sol-gel process include a broad size distribution and a high concentration of defects. Therefore, this synthesis technique is used sparingly.

Microemulsion: Microemulsion processes are popular methods for synthesizing Qdots at room temperature. The processes can be categorized as either normal microemulsions, such as oil-in-water, or as reverse microemulsions, such as water-in-oil. In some cases, other polar solvents, for example, alcohol, may be used instead of water. The reverse micelle process is popular for synthesizing Qdots where two immiscible liquids (polar water and nonpolar long-chain alkane) are mixed and stirred to form emulsion. Nanometer water droplets dispersed in *n*-alkane solutions can be achieved using surfactants, such as aerosol OT (AOT), cetyl trimethyl-ammonium bromide (CTAB), sodium dodecyl sulphate (SDS) or triton-X. Since the surfactants are terminated by hydrophilic and hydrophobic groups on opposite ends, numerous tiny droplets called micelles are formed in the continuous oil medium. These micelles are thermodynamically stable and can act as ‘nanoreactors’. Mixing of vigorously stirred micellar solutions leads to a continuous exchange of reactants due to dynamic collisions. Growth of the resultant Qdots is limited by the size of the micelle, which is controlled by the molar ratio of water and surfactant (W). The relation between W and the radius (r) of the micelle has been reported as [53]:

$$\left(\frac{r+15}{r}\right)^3 - 1 = \frac{27.5}{W} \quad (2.5)$$

The reverse micelle technique has been used to prepare II-VI core and core/shell Qdots, such as CdSe/ZnS, CdSe/ZnSe and CdS:Mn/ZnS [36, 54, 55]. Some advantages of this process are: easy control of the Qdot size by changing the molar ratio of water to surfactant, a narrow distribution of size as compared to the sol gel process, and ease of dispersion of the Qdots. Some disadvantages include low yield and incorporation of impurities and defects.

Hot-solution decomposition process: High temperature ($\sim 300^\circ\text{C}$) pyrolysis of organometallic compound is a well-established route for the production of Qdots, first discussed in 1993 by Bawendi and co-workers [28]. Precursor such as methyl, acetate, carbonate and oxides of Group II elements are mixed with Group VI phosphene or bis(trimethyl-silyl) (TMS) precursors. A typical procedure involves first degassing and drying of trioctyl-phosphine oxide (TOPO, a coordinating solvent) at 200°C under vacuum (1 torr) in a three-neck round flask inside a dry box. A mixture of methyl-Cd and tri-*n*-octyl-phosphine (TOP) selenide is prepared in a dry box and injected with vigorous stirring into the flask at a temperature of $\sim 300^\circ\text{C}$. The simultaneous injection of precursors into the flask, along with TOPO, results in homogeneous nucleation to form Qdots, with the subsequent growth of Qdots through *Ostwald ripening* being relatively slow. In Ostwald ripening, the higher free energy of smaller Qdots makes them lose mass to large-sized Qdots, eventually disappearing. The net result is a slow increase in the size of Qdots at the reaction temperature of $\sim 230\text{--}250^\circ\text{C}$. The coordinating TOPO solvent stabilizes the Qdot dispersion, improves the passivation of the surface and provides a steric barrier to slow the growth of the Qdots. The final size of the Qdots is mainly controlled by the reaction time and temperature. Aliquots may be removed from the flask at regular intervals during the first few hours and the optical absorption edge used to achieve a desired particle size. This method has been extensively used to synthesize II-VI [56–61] and III-V Qdots [62].

Advantages of this synthesis route are that it provides sufficient thermal energy to anneal defects and results in monodispersed Qdots (typically standard deviation about the average size of 5%). Since growth of the particles in this process is relatively slow and can be controlled by modulating the temperature, a series of Qdot sizes can be prepared from the same precursor bath. Some of the disadvantages of this method include higher costs due to the use of high temperature, toxicity of the organometallic precursors and generally poor dispersions in water.

Other synthesis processes: Sonic waves or microwaves [63, 64] have been passed through a mixture of precursors in water to grow Qdots. These waves provide energy to dissociate the precursor and water molecules, which results in the growth of Qdots. Ultrasound waves have been reportedly used to synthesize Qdots in the size range of 1–5 nm by formation, growth and implosive collapse of bubbles in a liquid [63]. Such acoustic cavitation generates a localized hotspot through adiabatic compression within the gas inside the collapsing bubble, enabling the reactions that form Qdots. In one approach, acetate precursors of metal ions were dispersed in a solution and selenourea was added and sonicated for 1 h under an argon atmosphere [63]. The temperature of the solution rose to 80°C during the time required to produce Qdots.

Hydrothermal synthesis has been used to produce Qdots [65]. Crystallization of inorganic salts from aqueous solution is controlled by pressure and temperature. The solubility of inorganic compounds typically decreases as the temperature and/or pressure is lowered, leading to crystalline precipitates. By changing pressure, temperature, reaction and aging time and reactants, different shapes and sizes of the Qdots can be achieved.

2.7.2.2 Physical methods

Physical methods for synthesizing Qdots begin with processes in which layers are grown in an atom-by-atom process. In general, the layered materials grow as a uniform, often epi-

taxial layer (*Frank-van der Merwe mode* – FvdM) [66], initially as a smooth layer followed by nucleation and growth of small islands often with the size of Qdots (*Volmer–Weber mode* – VW) [67] or as small (Qdots) islands on a substrate (*Stranski-Krastonow mode* – SK) [68]. Depending on the interfacial/surface energies and lattice mismatch (i.e. lattice strain), one of these growth modes are observed. For example, Qdots may be formed by SK growth with an overlayer material that has a good lattice match with the substrate, but the substrate surface energy (σ_1) is less than the sum of the interfacial energy between the substrate and overlayer (γ_{12}) and the overlayer surface energy (σ_2), i.e. when $\sigma_2 + \gamma_{12} > \sigma_1$ [69]. In other cases, formation of Qdots was due to relaxation of strain required to maintain epitaxy. In the case of substrates with an overlayer with a large lattice mismatch and appropriately small surface and interface energies, initial growth of the overlayer occurs through a layer by layer FvdM growth. However, when the film is sufficiently thick (a few monolayers) to induce a large strain energy, the system lowers its total free energy by breaking the film into isolated islands or Qdots (i.e. the VW mode).

Molecular beam epitaxy (MBE) has been used to deposit the overlayers and grow elemental, compound or alloy semiconductor nanostructured materials on a heated substrate under ultra-high vacuum ($\sim 10^{-10}$ Torr) conditions [70, 71]. The basic principle of the MBE process is evaporation from an apertured source (*Knudsen* effusion source) to form a beam of atoms or molecules. The beams in the MBE process can be formed from solids (e.g. elemental gallium and arsenic are used to produce GaAs Qdots) or a combination of solid plus gases (e.g. AsH₃, PH₃ or metal-organics such as tri-methyl gallium or tri-ethyl gallium). The metal-organic sources may leave high concentrations of carbon in the Qdots. MBE has been mainly used to self-assemble Qdots from III-V semiconductors using the large lattice mismatch, for example, InAs on GaAs has a 7% mismatch and leads to SK growth, as discussed above.

Layer growth by physical vapor deposition (PVD) results from condensation of solid from vapors produced by thermal evaporation or sputtering [51]. Different techniques have been used to cause evaporation, such as electron beam heating, resistive or Joule heating, arc-discharge and pulsed laser ablation. In any case, the factors discussed above (strain and surface energies) control the formation of Qdots from the deposited thin films.

Chemical vapor deposition is another method to form thin films from which Qdots can be self assembled. In chemical vapor deposition, precursors are introduced in a chamber at a particular pressure and temperature and they diffuse to the heated substrate, react to form a film, followed by gas-phase by-products desorbing from the substrate and being removed from the chamber. InGaAs and AlInAs Qdots have been synthesized using either surface energy or strained-induced SK growth processes [72].

2.8 OPTICAL PROPERTIES AND APPLICATIONS

2.8.1 II-VI Qdots

II-VI compound semiconductors include the cations of zinc, cadmium and/or mercury combined with anionic oxygen, sulfur, selenium and/or tellurium. These semiconductors generally crystallize in both a face-centered cubic (zinc blende) and a hexagonal (wurtzite) crystal structure (Figure 2.11). For example, the equilibrium crystal structure of both ZnO and ZnS is hexagonal, although ZnS often also exhibits a metastable cubic or a mixed hex-

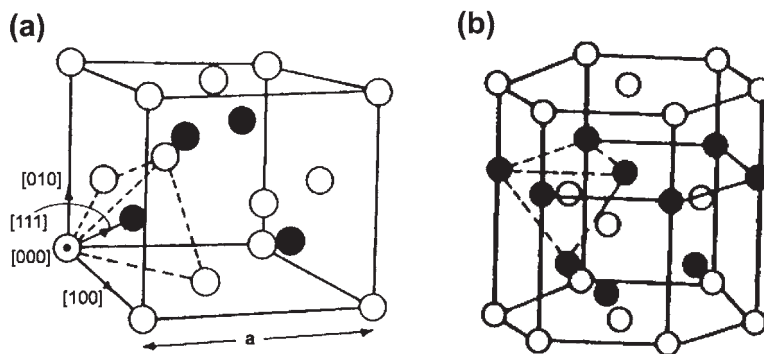


Figure 2.11 Crystal structures of II-IV Qdots: (a) Zinc blende; (b) Wurtzite (with permission from [38]. Copyright (1977) Pergomon Press)

agonal/cubic structure. The II-VI compound semiconductors may exhibit good luminescence because they have a direct band gap. In addition, many of the II-VI semiconductors are often used as a host for luminescent activators, for example, ZnS doped with Mn^{2+} , which emits yellow light. Near band edge emission from excitons can be observed from II-VI semiconductors, especially at low temperatures, from those materials with a low exciton binding energy.

2.8.1.1 ZnO Qdots

Zinc oxide is a material with a large direct band gap of 3.37 eV and a relatively large exciton binding energy of 60 meV. These properties lead to good UV light emission and low-threshold optically pumped lasing at room temperature [73]. Low-dimensional ZnO nanostructured Qdots, wires, rods, tetrapods and ribbons have been widely investigated [74].

Photoluminescence properties: Most of the PL spectra reported from ZnO Qdots were measured at room temperature [75–79] and consists of an UV and a broad visible (green or yellow) peak (Figure 2.12). The UV emission peak at $\sim 380\text{ nm}$ is from near band edge exciton emission, whereas the broad visible at 500–600 nm is due to defects and/or impurities. Although the exact mechanism of the visible emission is still being debated as discussed above, most researchers believe that the green emission results from the recombination of a photogenerated hole with a singly ionized oxygen vacancy in ZnO [75]. In the case of ZnO Qdots, visible emission has been suppressed and the UV peak enhanced by passivation of the surface with surfactants (e.g. tetraoctylammomium bromide or polyvinylpyrrolidone), which suggests that the defect leading to green emission is concentrated at the surface. It was reported that the ratio of the intensity of UV to defect emission is dependent on the excitation density, presumably because of different relaxation rates from the exciton and defect excited states.

In addition to green emission, yellow defect emission has also been commonly reported from ZnO Qdots and has been attributed to oxygen interstitial defects. The data suggest that the defect responsible for yellow emission was not concentrated at the surface. In addition

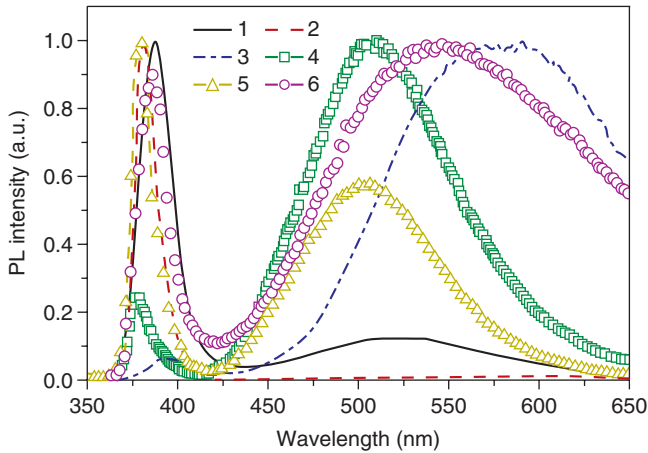


Figure 2.12 Room temperature PL spectra of various ZnO nanostructures: (1) tetrapods, (2) needles, (3) nanorods, (4) shells, (5) highly faceted rods, and (6) ribbons/combs (reprinted with permission from [75]. Copyright (2006) Wiley Interscience)

to green and yellow emission, orange-red emission from oxygen interstitials and near-infrared emission from excess oxygen have also been reported [80]. The relative intensity from defect emission can be controlled by the fabrication or post-fabrication conditions. For example, a hydrogen plasma treatment was shown to enhance UV relative to defect emission, and yellow emission can be reduced by annealing ZnO in a reducing ambient. Suppression of the green emission from ZnO was reported by embedding Qdots in a synthetic opal whose photonic band gap overlapped the emission wavelength [81].

Dijken *et al.* studied the quantum efficiency of ZnO Qdots [82]. Quantum yields of the visible emission from ZnO nanoparticles prepared by colloidal solution were found to decrease from 20% to 12% as the particle radius increased from 0.7 to 1 nm (Figure 2.13) [82]. Bera *et al.* recently reported quantum efficiencies of ~5 % for 3–4 nm ZnO Qdots, and the quantum efficiency decreased with aging time in air due to a reduced concentration of radiative traps [52].

Doped ZnO Qdots: The optical properties of doped ZnO have also been widely investigated.[83–85]. Doping with Er or Mn has been reported to result in preferential orientation of nanorods perpendicular to the substrate [86]. ZnO have also been doped with rare-earth elements, such as Tb [87], Ce [88], Eu [89] and Dy [90]. In the case of Tb-doped ZnO Qdots, emission from both Tb and defect states was observed. The emission from Tb was found to increase with increasing Tb concentration, while that from defect states decreased. Eu-related emission was observed from ZnO:Eu nanorods for a suitable excitation wavelength. However, Dy-doped ZnO nanowires exhibited a relatively strong UV emission with a very weak emission from Dy.

The effects of doping Mn in ZnO nanoparticles depend strongly on the synthesis conditions [91]. The Mn was found to quench green emission [91], while others reported either a reduction in both UV and defect emissions [92] or a blue shift and increase in UV peak intensity [93]. Very similar spectra from ZnO and Mn-doped ZnO were observed after annealing at 800°C [94]. Other dopants, such as sulfur and copper, have been studied in

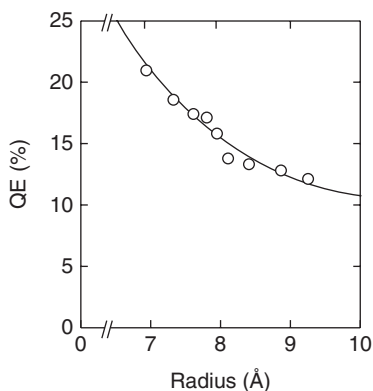


Figure 2.13 Room temperature quantum efficiencies vs. size of ZnO Qdots (reprinted with permission from [82]. Copyright (2001) Elsevier)

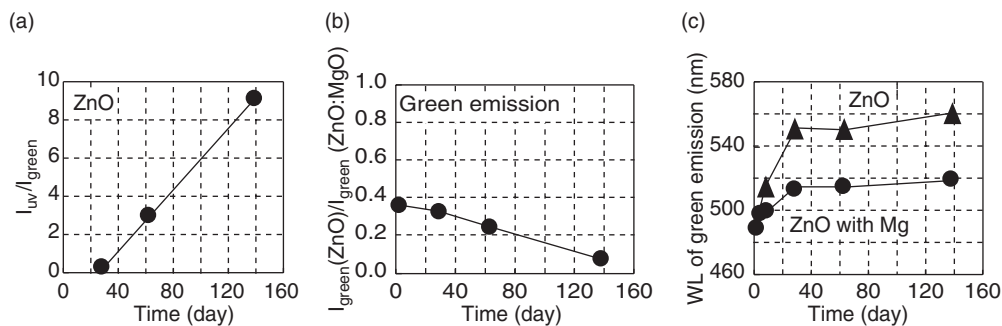


Figure 2.14 (a) Intensity ratio of UV to green emission (I_{UV}/I_{green}) from suspended ZnO Qdots vs. ageing time; (b) Intensity ratio of green emission peak from ZnO Qdots to that from ZnO/ZnMgO Qdots vs. ageing time; (c) Peak wavelength of green emission from suspended ZnO and ZnO/ZnMgO Qdots vs. ageing time (reprinted with permission from [2]. Copyright (2006) Institute of Physics)

ZnO Qdots. Increased intensity and changes in spectral distribution of the broad green defect emission with S doping has been reported [95, 96].

Surface passivation of ZnO Qdots: As reported above, the surfaces of ZnO Qdots can be passivated with organic surfactants. In an innovative approach involving inorganic passivation, Bang *et al.* [20] showed that a wider band gap ZnMgO shell on a ZnO Qdot core enhanced the green emission by factors of 2.5–12.5, with the enhancement factor being dependent upon the ageing time (Figures 2.14 (a) and (b)). While the dominant emission wavelength for both ZnO and ZnO/ZnMgO core/shell nanoparticles aged for 168 days were red shifted, this shift was smaller for ZnO/ZnMgO core/shell Qdots (Figure 2.14(c)). The presence of MgO on the surface of ZnO nanoparticles also prevented their aggregation in the suspension. The red shift during ageing did not result from nanocrystalline growth vs. storage time, but instead was attributed to the filling of radiative recombination centers in the band gap.

Application in solar cell: Various hybrid polymer solar cells have been reported using:

- CdSe [97], TiO₂ [98];
- ZnO [99], PbS [100];
- PbSe [101], CuInS₂ [102]; and
- CuInSe₂ [103].

In general, *n*-type ZnO nanoparticles have high carrier concentrations and electron mobilities, which are important to good performance of hybrid solar cells [104]. Hybrid solar cells based on ZnO nanoparticles exhibited an AM1.5 energy conversion efficiency of 0.9% for poly(3-hexylthiophene) (P3HT), 1.6% for poly[2-methoxy-5-(3',7'-dimethyloctyloxy)-1,4-phenylene vinylene] (MDMO-PPV), and external quantum efficiencies of 27% at 480 nm for P3HT and 40% for MDMO-PPV. The device structure was ITO/poly(3,4-ethylenedioxythiophene):poly(styrene sulfonic acid) (PEDOT:PSS)/ZnO:polymer (26% vol, thickness ~200 nm)/Al. Thermal annealing of the spin cast ZnO nanoparticles/polymer blends improved charge transport and was crucial to achieving the efficiencies reported above.

2.3.1.2 ZnS Qdots

ZnS Qdots are considered to be one of the most important Qdots because of their unique chemical, physical and optoelectronic properties, which make them useful for displays, lighting, sensors and lasers. In addition, transition metal and/or rare earth metal ion doped ZnS is one of the most popular semiconductor phosphors. ZnS is a wide band-gap compound semiconductor ($E_g \sim 3.6$ eV or ~ 340 nm). The luminescence characteristic of impurity-activated ZnS Qdots differ markedly from those of the bulk ZnS. Yang *et al.* [105] hypothesized that these differences result from the size dependence of the properties and their high dispersion.

Doped ZnS Qdots: Doped ZnS Qdots [105, 106] are important semiconductor nanomaterials, with Mn²⁺-doped ZnS Qdots being one of those most studied as a phosphor [107]. In 1994, Bhagrava *et al.* [108] reported high PL quantum yields (~18%) from ZnS:Mn Qdots. Coincident with the intensity enhancement, they reported shorter luminescent lifetimes for the Mn²⁺ emission (decrease from hundreds of microseconds for the bulk to nanoseconds in nanocrystals) [109, 110]. The increased intensity was attributed to an efficient energy transfer from the ZnS host to Mn²⁺ ions facilitated by mixed electronic states. Hybridization of atomic orbitals of ZnS and *d*-orbitals of Mn²⁺ in the nanoparticles was suggested to also be responsible for the relaxation of selection rules for the spin-forbidden ⁴T₁ → ⁶A₁ transition of Mn²⁺, leading to the short emission lifetimes.

Subsequent research demonstrated that while the quantum yield of passivated ZnS:Mn Qdots could be high, the luminescent lifetimes were not significantly smaller from those of the bulk material. However, the luminescence properties were found to be dependent upon the S²⁻ and Mn²⁺ concentrations as well as the structural properties of the Qdots. The ⁴T₁ → ⁶A₁ Mn²⁺ emission intensity generally increases with increasing doping Mn²⁺ concentra-

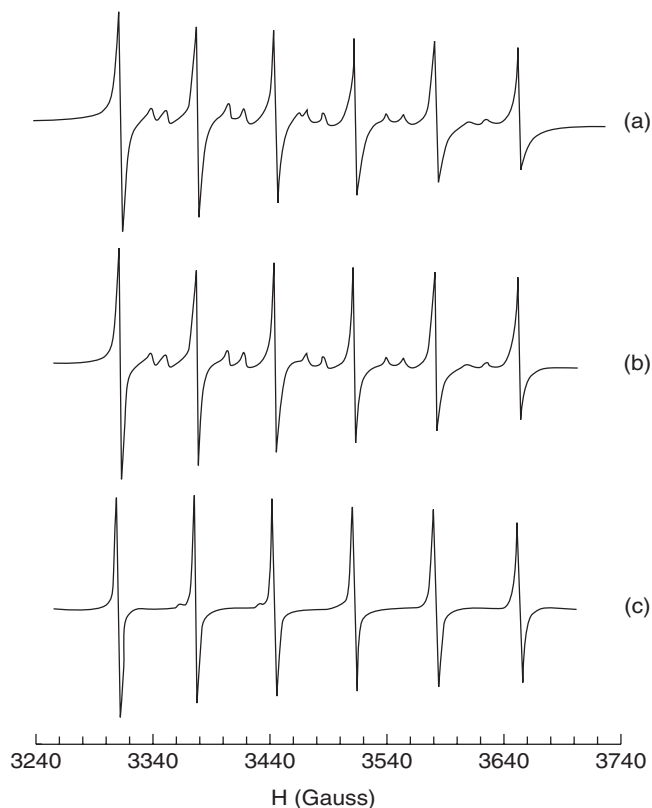


Figure 2.15 EPR spectra for Mn^{2+} in ZnS:Mn sample measured at room temperature: (a) 0.003% Mn^{2+} (experimental results); (b) 0.008% Mn^{2+} (experimental results); and (c) 0.008% Mn^{2+} (simulation) with parameters $g_{xx} = 2.0064$, $g_{yy} = 2.0064$, $g_{zz} = 2.0066$, $D = 37.4 \times 10^{-4} \text{cm}^{-1}$, $E = 12.5 \times 10^{-4} \text{cm}^{-1}$, $A_{xx} = 63.9 \times 10^{-4} \text{cm}^{-1}$, $A_{yy} = 64.0 \times 10^{-4} \text{cm}^{-1}$, and $A_{zz} = 64.4 \times 10^{-4} \text{cm}^{-1}$ (reprinted with permission from [112]. Copyright (2004) American Chemical Society)

tion [111], with quenching of Mn^{2+} emission observed at high Mn^{2+} concentrations (>0.12 at %). The local environment around the Mn^{2+} in the Qdots has been studied using X-ray absorption fine structure (XAFS) and electron spin resonance (ESR). XAFS data show that the Mn^{2+} substitutes on the tetrahedral Zn^{2+} site in the lattice. ESR data are consistent with this conclusion, showing a spectrum for Mn^{2+} spins typical of a tetrahedral crystal field (Figure 2.15) [112]. In some cases, for ZnS:Mn Qdots, the ESR spectrum show a Mn^{2+} signal with octahedral symmetry, but the location of this defect site is not fully understood. Some researchers have suggested that this signal results from Mn^{2+} on the surface of the Qdots vs. the interior, but this assignment has been disputed and attributed to Mn-Mn clustering at high concentrations.

Surface passivation of ZnS Qdots: As discussed in Section 2.6, surface passivation is critical to achieve high quantum efficiencies in Qdots. Bol and Meijerink [113] compared the quantum efficiency for Qdots coated with poly(vinylbutyral)(PVB), poly(vinylalcohol)(PVA), methacrylic acid (MA), and sodium polyphosphate (PP), and the quantum efficiencies of

0.3% to 1% for unpassivated Qdots was increased to ~4% for ZnS:Mn capped with PP. The Mn^{2+} emission at 580 nm from ZnS:Mn/ZnS core/shell Qdots was found to be seven times more intense than from unpassivated ZnS:Mn. The enhanced intensity is believed to result from suppression of nonradiative transitions by the undoped ZnS-shell. Qdots of ZnS:Mn coated by a SiO_2 shell showed an enhanced PL intensity as compared to bare Qdots [114].

UV Irradiation effect on ZnS Qdots: A significant increase in the luminescence quantum efficiency of ZnS Qdots was observed due to UV irradiation. Becker and Bard attributed this phenomenon to irradiation-induced oxygen absorption that blocked nonradiative recombination at surface states [115]. Henglein *et al.* proposed [116] that photoanodic dissolution of the ZnS Qdots was induced by irradiation in the presence of oxygen, which led to the improved efficiencies. Dunstan *et al.* explained the increased efficiencies in terms of a photocorrosion process that created new recombination centers [117]. Yang *et al.* [10] used X-ray photoelectron spectroscopy (XPS) data to show that 400 nm irradiation in air converted ZnS shells to ZnSO_4 , which increased the internal quantum efficiency (IQE) of CdS: Mn/ZnS core/shell structures. UV irradiation in argon did not result in the formation of ZnSO_4 nor did it change the IQE.

UV irradiation of organically passivated ZnS Qdots can either increase or decrease the IQE. Bhargava *et al.* [118] observed an increase upon UV irradiation and speculated that increased cross-linking and polymerization of the passivating organic molecules was the mechanism. Recently, Bol and Meijrink [119] postulated enhanced emission from organically passivated surfaces resulted from either UV curing of samples coated with PVB, PVA or MA, or from a photochemical reaction at Qdot surfaces coated with PP or on unpassivated samples. After UV curing, quantum efficiencies of ~10 % were obtained. However, prolonged UV irradiation (hours to days) in the presence of water and oxygen led to a decreased quantum efficiency. As in the case of Yang *et al.* [10], photochemical reactions could produce ZnSO_4 or $\text{Zn}(\text{OH})_2$, which presumably served as a passivating layer around Qdots, but too thick a layer can lead to lower IQEs.

In the case of ZnS:Mn/ZnS core/shell structures, luminescence intensity was not changed significantly as a result of UV irradiation [120]. For ZnS:Mn/ SiO_2 core/shell nanoparticles, UV irradiation increased the PL intensity [114]. The luminescent intensity from ZnS:Mn²⁺ colloid solutions decreased after the colloids were kept in air at room temperature [121]. This was presumably due to the deterioration of surface structure, which led to an increase of nonradiative relaxation paths.

2.8.1.3 ZnSe Qdots

Zinc selenide (ZnSe) having a wide, direct, bulk band gap of ~2.58 eV (480 nm) has been studied since the 1970s, for applications such as light-emitting devices, solar cells, sensors and optical recording materials. ZnSe offers the possibilities to tune the emission wavelength from blue to ultraviolet via quantum confinement effects. The UV range is difficult to achieve with cadmium-based materials discussed below.

Photoluminescence Properties of ZnS Qdots: The photoluminescence of ZnSe Qdots has been tuned by size over the spectral range 390–440 nm with the PL line widths (FWHM)

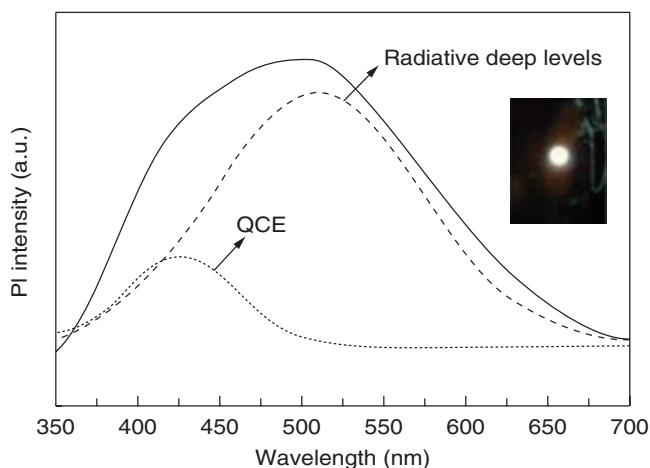


Figure 2.16 Room temperature PL spectrum of organic-capped ZnSe Qdots. Deconvoluted spectrum indicated that the broad emission band consisted of a blue emission band (425 nm) and a green-red emission band (510 nm). The inset showed the organic-capped ZnSe Qdots that produced white light when irradiated with a 325-nm-He-Cd laser (reprinted with permission from [126]. Copyright (2005), American Institute of Physics)

as narrow as 12.7–16.9 nm [122, 123]. Eychmüller *et al.* reported a PL peak at ~390 nm from thiol passivated, water soluble, sulfur-alloyed ZnSeS colloidal Qdots (~2–3 nm in size) [124]. UV irradiation after synthesis improved their IQE to 25–30% for the band gap UV emission. Irradiation resulted in incorporation of sulfur into the ZnSeS Qdots.

Mountziaris *et al.* found that ZnSe Qdots prepared by a microemulsion technique exhibited photoluminescence spectra that were size-dependent and remained unchanged over an ageing period of several months in solution [123]. Strong green emission from ZnSe nanowires was found at all temperatures from room temperature down to 10 K, and was attributed to a recombination of electrons from the conduction band with holes in a medium deep acceptor state [125]. Recently, organics-capped ZnSe Qdots synthesized by a colloidal chemical approach using ZnO and Se powder showed strong white emission (FWHM ~200 nm) under ambient conditions (Figure 2.16) [126]. White emission was speculated to result from a mixture of blue light from ZnSe nanocrystals exhibiting quantum confinement effects and green-red light from radiative deep levels associated with the strained ZnSe lattice. The organic-capped ZnSe Qdots that produced the data in Figure 2.16 were excited with a near-UV InGaN LED to produce white light with CIE (x, y) chromaticity coordinates of (0.38, 0.41).

Two-photon up-conversion from borosilicate glass doped with ZnSe Qdots was observed [127]. Excitation was supplied by a near-infrared tunable femtosecond pulsed laser. Visible light was emitted at an energy approximately equal to twice the energy of the exciting photons. The data support that the emission largely consisted of second harmonic generation (SHG) by two-photon upconversion, with a much weaker luminescence from red-shifted, low-lying trap states.

Enhancement of luminescence in ZnSe Qdots: The PL quantum yields of ZnSe Qdots can be increased by coating with a wider band gap semiconductor, such as ZnS, which has ~5%

lattice mismatch with ZnSe [128]. After passivation with a 1.8 monolayer of ZnS shell, the quantum yields of ZnSe/ZnS core/shell Qdots increased 450% to a quantum yield of ~32%. Kim *et al.* [129] synthesized ZnSe/ZnS Qdots with the SK growth mode using a metal-organic chemical vapor deposition (MOCVD) technique in an atomic layer epitaxy (ALE) mode. The mean dot height was 1–1.9 nm. An apparent temperature dependent, anomalous behavior of confined carriers in the ZnSe Qdots was observed and attributed to thermalized carrier hopping between Qdots. The carrier hopping resulted in a substantial decrease of the PL peak energy and linewidth when the sample was cooled from room temperature to 140 K.

As discussed above, ZnS:Mn²⁺ Qdots with quantum efficiencies of >10% have been synthesized [119]. Undoped ZnSe nanoparticles synthesized with a hot (300°C) solution in hexadecylamine exhibit near band edge emission with quantum efficiencies of up to 15%. Qdots of Mn²⁺-doped ZnSe exhibited a relative weak band edge emission from ZnSe, but very strong emission from the Mn²⁺ ⁴T₁ → ⁶A₁ transition [130–133]. The emission decreased with increasing ageing time. XAFS and ESR data were taken to characterize the local structural and chemical environment of the Mn²⁺ ions. XAFS data demonstrated that there was a reduction in the Zn and Mn first neighboring coordination number in Qdots vs. the bulk, but the Se first neighbor coordination number was constant. This implies that the core of the nanoparticles resembles bulk ZnSe, while the surface of the particle has a higher concentration of metal atoms. It was suggested that Mn²⁺ on the surface possessed an octahedral bonding geometry due to significant OH⁻/O²⁻ coordination, while the interior Mn²⁺ was in the Zn²⁺ tetrahedral site. The overall low Mn²⁺ quantum yield (~0.1%) was attributed to a high concentration of Mn²⁺ on the particle surface. The decrease in Mn²⁺ emission with increasing ageing time was attributed to quenching of luminescence by OH⁻/O²⁻ coordinated to the surface metal ions. In the case of higher overall Mn²⁺ concentration, the resulting higher surface Mn²⁺ concentration increased the disorder of the nanoparticle surface, resulting in an increase in trap state emission.

Nanocrystalline ZnSe particles have been encapsulated by graphite [134], and enhanced blue emission was observed as compared to unencapsulated ZnSe nanoparticles. Mid-gap defect orange emission was quenched by carbon passivation.

2.8.1.4 CdS Qdots

Among the II-VI semiconductors, CdS is one of the most important wide gap semiconductors with a $\Delta E_g \sim 2.5$ eV (~500 nm) for the bulk hexagonal wurtzite phase and $\Delta E_g \sim 3.53$ eV (~350 nm) for the bulk cubic zinc blende phase. Tuning of the emission wavelength by the size and shape of the CdS Qdots has been extensively studied [135–139]. Qdots have been synthesized by a variety of methods including the sol-gel, solvothermal, ion beam and ultrasonic techniques described in Section 2.7. The size, shape and crystalline structure of the CdS Qdots are important factors that control their optical properties.

Optical properties of CdS Qdots: Violet band edge and green-light emission due to trap states are observed from CdS Qdots under UV excitation [137]. The PL intensity depended on the Cd²⁺/S²⁻ ratio, and samples with an excess of S²⁻ ions (Cd²⁺/S²⁻ ratio less than 1:2) were unstable as compared to those with an excess of Cd²⁺ ions. The PL intensity increased very strongly for Cd²⁺/S²⁻ ratios from 1 to 1.5, but saturated at higher ratios. The most efficient blue PL was found for Cd²⁺/S²⁻ >1.5.

Since PL from defects was dominant in as-grown samples, band edge emission can be improved by modifying the surface of CdS Qdots. The luminescent lifetime of the band-edge emission prior to the surface passivation exhibited a fast decay due to a high nonradiative recombination rate. The lifetime was much longer after surface passivation, presumably because the nonradiative relaxation paths were suppressed. Organic surfactant have been used to cap the CdS Qdots and improve the luminescence efficiency [140]. For example, dendrimers were used to stabilize nanoparticles during the synthesis process, as well as to bind them to a flat substrate for printing applications [141]. The optical properties of CdS Qdots cores were also improved by a thin shell of a higher band gap material, for example, ZnS [142]. Up to six monolayers of ZnS have been used to eliminate the influence of surface states.

CdS Qdots have also been coated with metal shells resulting in large and fast third-order optical nonlinearity, due to surface plasmon resonance (SPR). The collective charge oscillation causes a large resonant enhancement of the local field inside and near the particle, which may be used in surface-enhanced Raman scattering and in nonlinear optical devices. Qdots coated with a noble metal have been shown to exhibit coupling between the plasmon resonance from the metal and the quantum size effect of the Qdots that give rise to new properties. Jeang *et al.* reported a red-shift of the exciton absorption peak for the Ag/CdS nanocomposite [143]. Je *et al.* investigated the local field-induced optical properties of CdS/Ag core/shell nanocomposites [144]. They confirmed by theoretical calculations that the strong local field created confined Wannier–Stark states (i.e. the energy spectrum of a crystalline solid in an electric field) that explain the red shift of the exciton peak in the nanocomposite.

Doped CdS Qdots: Lanthanide and transition metal doped II–VI Qdots generally have narrow emission peaks and longer luminescence lifetimes, which make them attractive for biological markers, and Mn-doped CdS Qdots has been studied for these purposes [36, 145–148]. Recently, Yang *et al.* synthesized ZnS passivated CdS:Mn core/shell Qdots using the reverse micelle process (Section 2.7.2). The CdS:Mn/ZnS core/shell Qdots exhibited better quantum yield and photostability vs. organically (*n*-dodecanethiol) capped CdS:Mn Qdots (Figure 2.17) [149–151]. Nonradiative recombination from surface states has been suppressed

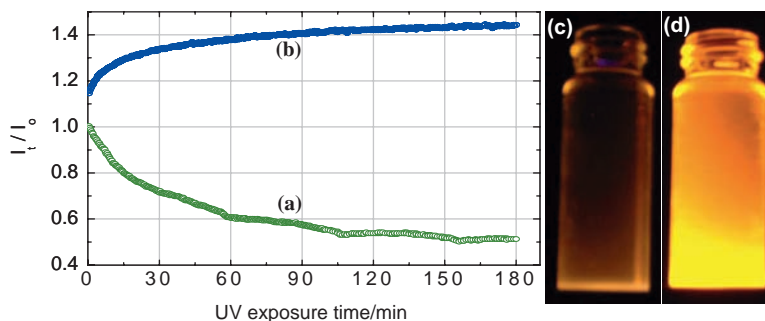


Figure 2.17 Variation of PL intensity in room temperature air from (a) *n*-dodecanethiol and (b) ZnS-passivated CdS:Mn Qdots vs. time of exposure to 400 nm UV light. The monitored wavelengths are 580 nm and 585 nm for *n*-dodecanthiol and ZnS passivated CdS:Mn Qdots, respectively. Comparison of relative brightness from (c) *n*-dodecanthiol passivation and (d) ZnS-passivated CdS:Mn Qdots under 366 nm UV-illumination (reprinted with permission from [10, 15]. Copyright (2004) Wiley Interscience)

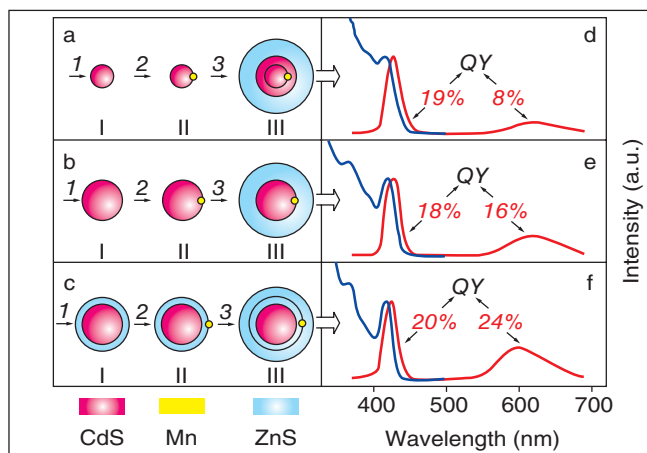


Figure 2.18 Schematic illustration of Mn-doped CdS/ZnS core/shell Qdots with different Mn positions: (a) inside the CdS core; (b) at the core/shell interface; and (c) in the ZnS shell. The final core/shell particles (i.e., IIIa, IIIb and IIIc) have CdS core diameter of 3.8 nm (with a standard deviation of 8%) and ZnS shell thickness of 1.5 nm (deviation 8%). PL spectra (in red) and PLE spectra (in blue) are shown; (d) IIIa; (e) IIIb; and (f) IIIc (reprinted with permission from [152]. Copyright (2006) American Chemical Society)

by ZnS shell passivation, resulting in an IQE of 18% compared to 3.7% for organically passivated CdS:Mn Qdots [10, 151]. The CdS:Mn/ZnS core/shell also shows a 40% increase in photoluminescence intensity with UV irradiation in air due to the photo-oxidation of the ZnS shell to form ZnSO_4 . [96]. This photooxidation product is presumably responsible for the enhanced PL emission, serving as an even better passivating shell than ZnS. Furthermore, Santra, *et al.* [95, 98] demonstrated that the CdS:Mn/ZnS Qdots are good for multi-functional imaging. For example, Gd^{III} -functionalized, silica-coated CdS:Mn/ZnS water soluble Qdots were shown to be fluorescent, radio-opaque, paramagnetic, suitable for attaching biomolecules such as proteins, peptides and antibodies, and were stable in an *in vivo* environment. The magnetic resonance imaging (MRI) properties of these Gd-functionalized Qdots have been demonstrated [7] and good MRI contrast in both the longitudinal (T_1) and transverse (T_2) proton relaxation time-weighted images was demonstrated.

The optical properties of Mn-doped CdS/ZnS Qdots are found by Yang *et al.* [152] to strongly depend on the radial positions of the Mn inside the Qdots (Figure 2.18). The Mn emission IQE was 8% when the dopant was inside the CdS core, 16% when at the core/shell interface and 24% when in the ZnS shell (Figures 2.18 (a), (b) and (c), respectively). Yang *et al.* proposed that the dependence of the Mn IQE on dopant position resulted from Mn-Mn interactions and the effects of strain on the local crystal field. Narrow EPR peaks were attributed to weaker Mn-Mn interactions and less local strain when the Mn dopant was in the ZnS shell.

Electroluminescence device using CdS Qdots: CdS/ZnS core/shell Qdots with core diameters of 4.7–5.2 nm had emission peaks from 460–480 nm and IQEs of ~20–30% [153]. A monolayer of these Qdots exhibited blue electroluminescence in a device with the following structure:

- ITO/CBP/(CdS/ZnS) Qdot monolayer/TAZ/Alq₃/Mg:Ag/Ag (ITO: indium tin oxide;
- CBP: 4,4'-N,N''-dicarbazolyl-biphenyl;
- TAZ:3-(4-biphenyl)-4-phenyl-5-*tert*-butylphenyl-1,2,4-triazole;
- Alq₃: tris-(8-hydroxyquinoline)aluminum).

This electroluminescent (EL) device exhibited a quantum efficiency of only 0.1%. At low currents, emission was dominated by the CdS/ZnS Qdots with a FWHM of 30nm and a peak at 468nm. At higher currents, EL emission from the organic layers dominated.

Yang *et al.* investigated the influence of energy levels on device performance of polymer-Qdot hybrid light-emitting diodes [151, 154]. Direct current (DC) EL devices were tested having a hybrid organic/inorganic multilayer structure of: ITO//PEDOT:PSS (poly(3,4-ethylene-dioxythiophene:poly(styrenesulfonate)//conjugated polymers //CdS:Mn/ZnS//Al, where two different conjugated polymers (poly(*N*-vinylcarbazole) (PVK) and poly(*p*-phenylenevinylene) (PPV)) were used. Compared to a PPV EL device without a CdS:Mn/ZnS layer, the hybrid PPV-based nanocrystalline EL device showed larger currents and considerably enhanced EL emission [154]. These data suggest that the CdS:Mn/ZnS nanocrystal layer serves as an electron transport layer (ETL) in the devices. Orange and green EL emissions were observed from devices with PVK and PPV devices, respectively. These data imply that the electron-hole recombination is confined to the CdS:Mn/ZnS nanocrystalline layer in the PVK-based device, but occur in the polymer layer in the PPV-based device. These observations were shown to be consistent with the energy level diagrams of the EL device interfaces (Figure 2.19).

CdS Qdots as multimodal bio-imaging probe: Santra *et al.* [9, 155, 156] demonstrated *in vivo* bio-imaging capability using amine modified CdS:Mn/ZnS Qdots conjugated to a TAT peptide and administered through the right common carotid artery that supplies blood only to the right side of a rat's brain. Qdots-loaded brain was sliced for histological analysis. Transmission and fluorescence micrographs (Figures 2.20 (a) and (b)) of a cross-section of fixed brain tissue clearly showed the blood capillaries and surrounding brain cells, as shown by broken white circle in Figure 2.20 (a). It was also shown that the TAT conjugated Qdots reached the nucleus of the brain cells, as shown by the green-circled brown spots in Figure 2.20 (a). It is well known that the TAT peptide can rapidly translocate through the plasma membrane and accumulate in the cell nucleus [9] and the histological analysis of the brain tissue supports the fact that TAT-conjugated Qdots crossed the blood-brain barrier, further migrated to brain parenchyma and reached the cell nuclei. Endothelial cells in blood capillaries were found to be highly loaded with CdS:Mn/ZnS Qdots and appear as bright yellow lines in Figure 2.20 (a).

CdS:Mn/ZnS Qdots were characterized for radio-opacity and magnetic hysteresis [149, 155, 156] for possible use as contrast agent in computer tomography (CT) and magnetic resonance imaging (MRI) due to electron dense Cd and paramagnetic Mn, respectively [149]. For radio-opacity, the Qdots sample was compared with a conventional radio-opaque dye, *Omnipaque*, used for CT scans and angiography. From Figure 2.20 (c), it was estimated that the X-ray absorption of Qdots is less than that of *Omnipaque*. Although the Qdot provides sufficient contrast for current radiographic practice, we are attempting to improve this property. A superconductor quantum interface device (SQUID) magnetometer was used to

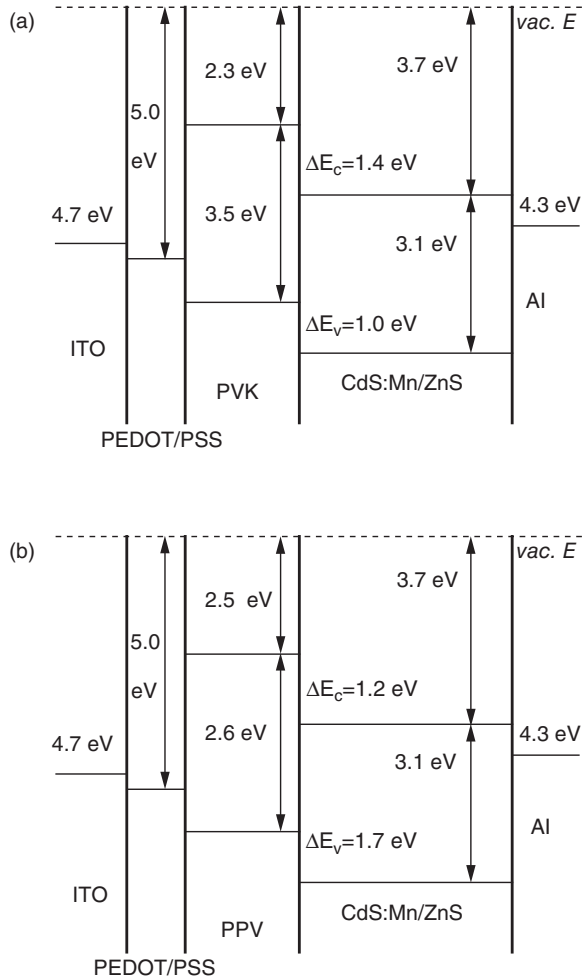


Figure 2.19 Energy level diagrams for the layers in the EL devices (a) PVK-based devices (b) PPV-based devices (reprinted with permission from [154]. Copyright (2003) American Chemical Society)

measure the magnetization of CdS:Mn/ZnS Qdots. A typical room temperature hysteresis curve for paramagnetic CdS:Mn is shown in Figure 2.20 (d). However, this magnetic response is too small for MRI imaging.

To improve the MRI image contrast, water-soluble silica-coated CdS:Mn/ZnS Qdots were functionalized [7] with Gd^{3+} ions. T_1 and T_2 weighted images were acquired with a single slice, spin-echo image sequence [7]. Longitudinal (T_1) and transverse proton relaxation time (T_2) were determined as a function of Gd-functionalized Qdots concentration at 4.7 Tesla. Increased MR signal intensity (Figure 2.21 (a)) is observed with increasing Gd concentrations due to the shorter water relaxation time T_1 . In T_2 weighted images, the MR signal intensity is substantially decreased by the effect of increased Gd on the T_2 of water (Figure 2.21 (b)) For control experiments, T_1 and T_2 weighted images of serial dilutions of

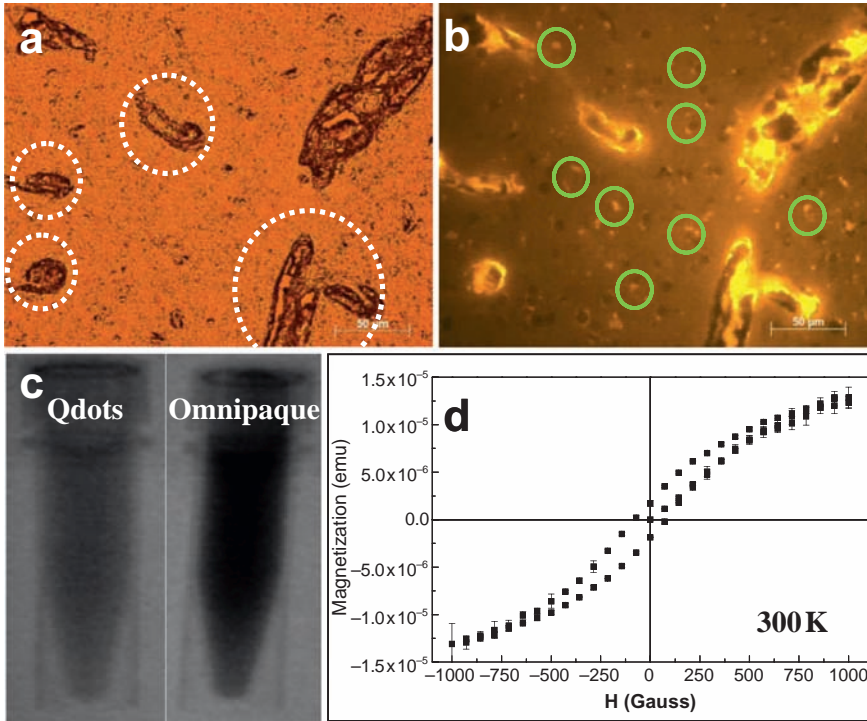


Figure 2.20 (a) Transmission; (b) fluorescence microscopy images (40 \times) of a cross-section of a fixed brain tissue; (c) fluoroscopy images of Qdot (left) and Omnipaque (right) of equal concentration under same magnification; (d) magnetization curve for CdS:Mn/ZnS core/shell Qdots [155, 156]

Qdots without Gd^{III} ions were recorded and could not be distinguished from those of deionized (DI) water.

Normalized T_1 and T_2 weighted intensities vs. repetition time (TR) and echo time (TE), respectively, for DI water and a series of diluted Gd-Qdots (from 0.36 to 0.0012 mM of Gd) show faster recovery of longitudinal magnetization and faster decay of transverse magnetization for higher Gd concentrations [7, 155, 156] (Figures 2.21 (c) and (d)). The efficacy of a contrast agent is generally expressed by its relaxivity (R_i , $i = 1, 2$), which is defined as [157], that is $1/T_i = 1/T^0 + R_i$ [Gd], where T_i is the relaxation time for a contrast agent solution concentration [Gd], and T^0 is the relaxation time in the absence of a contrast agent. From the data in Figures 2.21 (c) and (d), the relaxivities R_1 and R_2 are determined as 20.5 and 151 $\text{mM}^{-1} \text{s}^{-1}$, respectively. When compared with commercially available contrast agents, Gd-Qdots exhibit much higher R_1 and R_2 values under the same magnetic strength of 4.7 T [158]. High relaxivities were achieved by slowing the tumbling rate of the Gd³⁺-based contrast agents (i.e. Gd-DTPA) by grafting the contrast agent to rigid macromolecules and avoiding free rotation of the chelate [159, 160]. Although the Gd-Qdots can serve as either T_1 or T_2 contrast agents, the R_2/R_1 ratio of ~ 7.4 indicates that they may be more effective as a T_2 contrast agent.

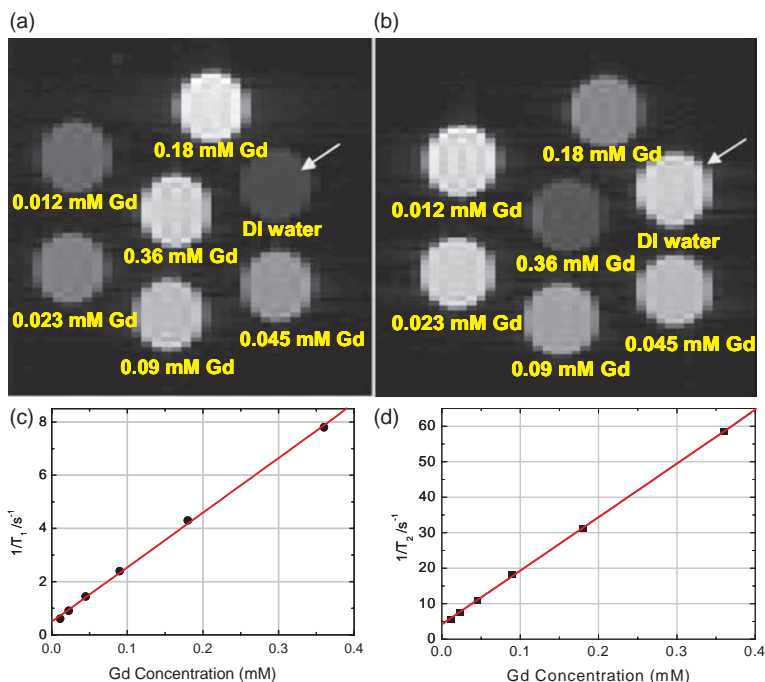


Figure 2.21 Magnetic resonance data from Gd-Qdots: (a) T_1 -weighted (repetition time (TR) = 11 000 ms, echo time (TE) = 4.2 ms); (b) T_2 -weighted (TR = 11 000 ms, TE = 24 ms) images of DI water and serial dilutions of Gd-Qdots (0.36, 0.18, 0.09, 0.045, 0.023, 0.012 mM of Gd). Linear plots of Gd concentration vs. $1/T_1$ (c) and $1/T_2$ (d) to obtain ionic relaxivities of R_1 and R_2 of Gd-Qdots [155, 156]

2.8.1.5 CdSe Qdots

The band gap of bulk CdSe (~ 1.7 eV or 730 nm) makes it attractive for infrared (IR) display and biological applications. CdSe Qdots have a broad absorption spectrum, which allows excitation with a single wavelength of Qdots whose emission has been tuned by their size over the visible to near IR region. Quantum yields of CdSe Qdots approaching 100% have been reported after surface passivation [161]. Under some circumstances, discussed below, CdSe Qdots exhibit fast nonradiative decay due to Auger recombination (Section 2.4.2) leading to lower IQEs.

Optical properties of CdSe Qdots: Emission from CdSe Qdots can be tuned by size to span the entire visible region (420 nm–670 nm) with a narrow FWHM of 20–40 nm (Figure 2.22) [162]. This size-tuned emission color offers the potential to develop a multicolor optical coding techniques, for example, by functionalizing different sized CdSe Qdots with different molecules. Researchers have used Qdots for *in vivo* and *in vitro* imaging and diagnostics of live cell as a complement to or replacement of conventional organic dyes [163, 164]. The luminescent lifetime of CdSe Qdots (several tens of nanoseconds) is longer than that of cell autofluorescence, which permits measurement of marker spectra and loca-



Figure 2.22 Ten distinguishable emission colors of CdSe/ZnS Qdots excited using a near-UV lamp. From left to right (blue to red), the emission maxima are centered at 443, 473, 481, 500, 518, 543, 565, 587, 610 and 655 nm (reprinted by permission from [162]. Copyright (2001) Macmillan Publishers Ltd)

tion without high backgrounds through the use of time-gated fluorescent spectroscopy and/or microscopy. In addition, the photostability of CdSe is excellent and much better than that of conventional organic dyes [165], allowing data acquisition over long times with continuous excitation.

CdSe Qdots of ~ 1.5 nm can emit white light [166, 167] due to emission over a broad band (420–710 nm) from recombination at surface mid-gap states. These Qdots are so small that the electron wave functions significantly overlap with those of surface sites associated with selenium. Photogenerated hole that are trapped on the surface are likely to encounter an electron before nonradiatively relaxing towards the ground state. These Qdots do not suffer from self absorption—a loss in total efficiency due to the shorter wavelength photons emitted by small Qdots being absorbed by larger Qdots. Self absorption is a problem in devices where Qdots, whose sizes have been tuned to emit red, green and blue colors, are simply mixed to achieve white light.

Efficient upconversion has been observed in CdSe Qdots ranging in size from 2.5 to 6 nm, with an approximately quadratic dependence on laser power. The upconversion decay lifetimes are slightly longer than the photoluminescence decay lifetimes, and the long decay lifetime has been associated with surface trap states. The trap states act as an emitter and as an intermediate state for upconversion luminescence [168].

Oxidation of the surface has been observed to decrease the quantum yield of CdSe Qdots due to breaking of Cd–Se bonds and release of Se as SeO_2 . Such oxidation caused an attenuation and blue-shift of the PL, as well as an increased cytotoxicity of CdSe Qdots for biological applications [169].

Surface passivation of CdSe Qdots: As with most II–VI Qdots, surface passivation of CdSe with a wide band-gap shell material is one way to increase the IQE [170–172]. A shell of ZnS has often been used because of its wide band gap and good photostability [173–176]. For CdSe/ZnS core/shell Qdots, the ZnS shell appears to be epitaxial and the interface coherent at low thicknesses. At higher thicknesses, the interface loses coherency due to the formation of misfit dislocations to accommodate the mismatch in lattice constants. The absorption and emission spectra of CdSe Qdots are shifted as a function of ZnS coverage.

The quantum yield of CdSe/ZnS core/shell Qdots is reported to reach a maximum value at ~1.3 monolayers of ZnS, falling to lower yields for thicker and thinner shells. The decrease in quantum yield at higher thicknesses is thought to be due to the formation of defects in the ZnS shell.

The lattice mismatch between CdSe and ZnS (10.6%) is larger than that between CdSe and ZnSe (6.3%) and CdSe and CdS (3.9%), but the band gap is also larger leading to better exciton confinement. ZnSe is also a good shell material for CdSe, because it has a wider band gap (2.72 eV) than that of CdSe (1.76 eV). ZnSe also has the same anion (Se), which leads to a larger offset in the conduction bands and therefore to better confinement of the electrons. Luminescence quantum yields for CdSe/ZnSe core/shell Qdots have been reported in the range of 60–85% [161]. Finally, the smaller lattice mismatch between a CdSe core and a CdS shell facilitates epitaxial growth of a CdS shell. CdSe/CdS core/shell Qdots typically display higher PL quantum yields with longer PL lifetimes.

Double shell Qdots are being studied for improved optical properties. As discussed above, the lattice mismatch and differences in band gap are important to the properties of core/shell Qdots. The band gaps and band offsets of the core and shell materials are also critical to suppression of tunneling of charge carriers from the core to the surface states of the shell. In the case of CdSe/CdS, the lattice mismatch is small but so are the band offsets. For CdSe/ZnS Qdots, the reverse is true with the lattice mismatch being large along with the band offsets. The advantages of both shell materials are combined in core/shell/shell CdSe/CdS/ZnS Qdots [177, 178]. In these double shell nanostructures, the lattice strain at the interface is reduced while large band offsets are maintained. These so-called quantum well-quantum dot (QW-QD) structures also reduce Auger recombination by minimizing wave function overlap of the charge carriers, resulting in longer lifetimes and saturation of emission at low pump intensities [179].

In yet another variation, colloidal QW Qdots have been synthesized with a low band-gap CdSe layer sandwiched between a higher band-gap core of CdS and an outer shell of CdS. The spherical QW Qdots combine the promising characteristics of two-dimensional planar QWs and zero-dimensional colloidal Qdots, which can be used as a strong gain medium for observing lasing [179]. The threshold pump intensity required to achieve lasing is much lower for QW Qdots than in other configurations.

Electroluminescence device using CdSe Qdots: CdSe/ZnS core/shell Qdots have also been used to make high efficiency EL devices, in which the size tuned emission color and nanoparticles were chemically and optically stable [180]. The Qdots film was made by spin coating a solution of aromatic organic materials and aliphatically capped Qdots (~5 nm). The solvent was evaporated and the Qdots assembled into a hexagonal close-packed layer. The Qdot LED had an external quantum efficiency of ~2% with red emission at 615 nm and a FWHM of 27 nm. A white Qdot LED was developed by mixing smaller and larger diameter CdSe/ZnS core/shell Qdots that emitted in the blue, green and red. The efficiency was reduced by the self absorption discussed above, and the stability of the color was strongly affected by the different ageing rates of the different size Qdots. In addition, the device lifetimes were short due to heating at high luminance values. Control of Förster energy vs. charge-trapping processes between the different active layers in a Qdot hybrid device has resulted in efficient white emission from the inorganic Qdots. The maximum brightness of this device was found to be 1500 cd/m² at 62 mA/cm², which corresponds to a current efficiency of 2.2 cd/A [181].

Doped CdSe Qdots: Doping of CdSe Qdots with a number of ions has proved to be difficult. Even for the case of Mn in CdSe, where the bulk solubility is near 50%, the doping levels in Qdots may be low. The initial step for incorporating a dopant into a Qdots is adsorption onto the surface during growth. The adsorption step is affected by surface morphology, crystal facets expressed by the Qdots and the surfactants in the growth solution. Certain crystalline planes (facets) of the Qdots favor Mn adsorption due to higher concentration ratios of Se to Cd [182]. In addition, some surfactants preferentially bind to Mn, competing with surface adsorption and reducing the doping concentrations. Therefore, Mn-doped CdSe Qdots are possible only if these factors are properly controlled [182].

Biological applications of CdSe Qdots: Multicolor optical coding for biological assays has been achieved by using different sizes of CdSe quantum dots with precisely controlled ratios. The use of 10 intensity levels and 6 colors could theoretically encode 1 million nucleic acid or protein sequences. Nie *et al.* embedded different-sized Qdots into highly uniform and reproducible polymeric microbeads, which yielded bead identification accuracies as high as 99.99% [162]. The broad absorption spectra of the Qdots allowed single wavelength excitation of emission from different-sized Qdots. This spectral encoding technology is expected to open up new opportunities in gene expression studies, high-throughput screening, and medical diagnostics.

As discussed above, since the autofluorescence of a live cell excited by UV is in the visible region and overlaps the emission of most labeling materials, it is difficult to get background-free PL spectra. Compared with conventional organic dyes, Qdots have longer lifetimes (several tens of nanoseconds), therefore background-free PL images can be obtained by using time-gated fluorescent microscopy (Figure 2.23) [183]. The photostability of Qdots is better than that of organic dyes, allowing the use of Qdots to monitor biological events over long times.

Another biological application of CdSe Qdots is to build on-off switches by utilizing Förster resonance energy transfer between the Qdot donor and an organic acceptor. The emission from CdSe Qdots can be quenched if they are connected to an organic acceptor because the energy absorbed by the Qdots is transferred to the acceptor via Förster resonant energy transfer (FRET) (Figure 2.24) [184]. If the distance between the Qdots donor and organic acceptor is increased by the addition of foreign organic materials, emission from the Qdots can be turned on again. This so-called on-off switch has the potential to be used as a sensor in many important applications, including healthcare, environmental monitoring and biodefense systems.

2.8.1.6 CdTe Qdots

Unlike other II-VI semiconductors, CdTe Qdots are much less studied, in part due to their low band gap (~ 1.5 eV or 825 nm). In the future, more work is expected on near IR-emitting CdTe Qdots due to their potential for labeling of cells, protein tracking and DNA detection.

Surface passivation of CdTe Qdots: Chemically-reduced bovine serum albumin (BSA) has been used to passivate and functionalize the surface of CdTe Qdots to make them water soluble [185]. It was demonstrated that denatured BSA (dBSA) conjugated to the CdTe

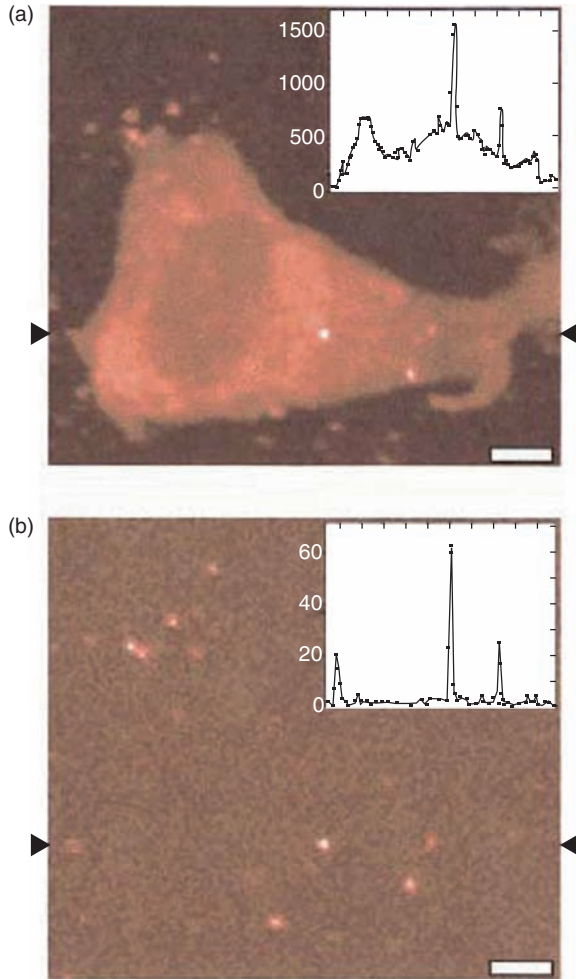


Figure 2.23 Time-resolved confocal images of a fixed 3T3 cell: (a) a micrograph acquired from all the detected photons; (b) gated micrograph constructed from only photons that arrived 35–65 ns after the laser pulse (laser intensity: 0.1 kWcm^{-2} ; integration time per pixel: 25 ms; scale bar: $5 \mu\text{m}$). The insets show cross-sections along the same horizontal line (indicated by the black arrows) for (a) and (b) (reprinted with permission from [183]. Copyright (2001) Optical Society of America)

Qdots surface improved the chemical stability and the photoluminescence quantum yield [185]. This study showed that over a pH range of 6 to 9, the solution of dBSA-coated CdTe Qdots were stable and bright, but higher and lower pH values led to dramatic decreases in PL intensity and chemical stability. Similarly, concentrations of dBSA that were too high or too low in the Qdots solution resulted in a decreased PL quantum yield.

Type-II core/shell CdTe Qdot: Similar to other semiconductor Qdots, the quantum yields of CdTe core Qdots can be enhanced by a wide band-gap shell, such as CdS and ZnTe

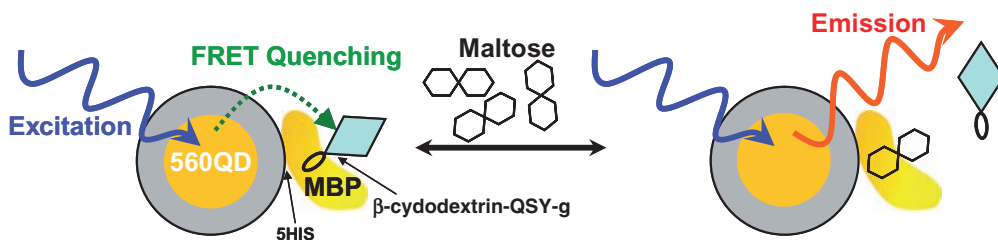


Figure 2.24 A schematic of the function of a 560-QD-MBP nanosensor. Each 560-nm-emitting Qdot is surrounded by an average of ~ 10 MBP moieties (a single MBP is shown for simplicity). Formation of QD-MBP- β -CD-QSY9 (maximum absorption ~ 565 nm) results in quenching of Qdot emission. Added maltose displaces β -CD-QSY9 from the sensor assembly, resulting in an increase in direct Qdot emission [184]

[186–188]. Both of these core/shell nanostructures form type I offsets, that is the valence and conduction band of the shell layer are lower and higher than that of the core, respectively, as discussed earlier. Type-II Qdots interfaces can be formed with CdTe cores [47, 189] that confines one carrier to the core and the other to the shell. As discussed above, Type II Qdots have properties and applications that are different from the type I Qdots, because of the spatial separations of carriers. In CdTe/CdSe type II Qdots, the hole is distributed near the CdTe center of the dot, while the electron is distributed towards the CdSe shell. This degree of control can be especially important in applications where rapid carrier separation followed by charge transfer into a matrix or electrode is important, for example, in photovoltaic or photoconducting devices.

The type II CdTe/CdSe Qdots have PL quantum yields of $<4\%$. Higher quantum yields for type II Qdots can be achieved with a thinner shell to provide more carrier wave function overlap. The spatial separation of carriers and the long radiative lifetimes for CdTe/CdSe Qdots result in fast nonradiative decay channels and low quantum yields. However, CdTe/CdSe/ZnTe core/shell/shell Qdots have exhibited IQEs of up to 20%. The band offsets between CdSe and ZnTe help confine the electron within the dot without affecting the hole wave function, which is still constrained to the core.

The use of near infrared (NIR) or infrared (IR) photons is promising for biomedical imaging in living tissue, due to longer attenuation distances and lack of autofluorescence in the IR region. This technology often requires exogenous contrast agents with combinations of hydrodynamic diameter, absorption, quantum yield and stability that are not possible with conventional organic dyes [190]. The emission of type-II CdTe/CdSe Qdots can be tuned into the NIR while preserving the absorption cross-section. A polydentate phosphine coating has been shown to make the Qdots water soluble, allowing them to be dispersed in serum. Injection of only 400 pmol of NIR-emitting Qdots permitted sentinel lymph nodes that were 1 cm below the surface to be imaged in real time using an excitation power density of only 5 mW/cm^2 [190].

Biological applications of CdTe Qdots: For biological and medical applications, it is of particular importance to study the photophysical properties of Qdots in living cells [191]. The photoinduced optical properties of the intracellular Qdots are of interest. After injecting thiol-capped CdTe Qdots into living cells, the PL intensity increased with time and the

emission peak blue-shifted [191]. Deoxygenation prevented the PL blue shift, suggesting that photoactivated oxygen was responsible. The activated oxygen is presumably formed from the oxygen that intercalates the thiol layer at the Qdot core surface. When Qdots are used as fluorescence probes for cellular imaging, the effects of the PL blue shift and photobleaching must be considered.

Because Qdots are often synthesized in nonpolar, nonaqueous solvents, they must be made water soluble for biology application, for example, by depositing a silica shell or organic layer, as discussed above. Aqueous-based synthesis method have been used to produce silica-capped, highly fluorescent CdTe Qdots [192]. The emission from CdTe Qdots can be tuned to the near-infrared where tissue absorption is at a minimum, and the silica shell can prevent the leakage of toxic Cd^{2+} . Cytotoxicity and the potential interference of Qdots with cellular processes are the subject of intensive studies [192, 193]. In addition to making Qdots water soluble, a silica shell allows easy functionalization with biomolecules such as proteins [8] and results in greater photostability.

Application of CdTe Qdots in photonic devices: Qdot photonic devices, including optical amplifiers and lasers operating at room temperature, have been studied. A major difficulty in achieving lasing is the efficient nonradiative Auger recombination processes. Several strategies have been proposed to improve the lasing, including increased Qdot concentrations in the active layer, use of improved optical feedback structures, and optimized optical waveguides. Two-dimensional waveguides loaded with luminescent colloidal CdTe Qdots grown with a layer-by-layer deposition technique have been investigated [194]. The waveguides exhibit propagation loss coefficients of $<1 \text{ cm}^{-1}$. The losses depend weakly on the width of the waveguides but depend strongly on the surface roughness. High optical gain of $\sim 230 \text{ cm}^{-1}$ can be demonstrated using femtosecond pulses, showing that this kind of Qdot waveguides are suitable for lasers and optical amplifiers.

In the case of photovoltaics, single and multiwall carbon nanotubes (SWNT and MWNT) were linked to CdTe Qdots capped with thioglycolic acid (TGA) to produce solar cells [195]. The nanotubes provided a good hole transport route to the electrode, with CdTe acting as an excited-state electron donor. The highest monochromatic photon quantum efficiency was 2.3% from a hybrid cell consisting of single SWNT/pyrene+/red-emitting CdTe Qdots.

2.8.2 III-V Qdots

III-V semiconductors, such as InGaAlN, GaP, GaAs, InP and InAs, are important for optoelectronic devices. It is possible to engineer III-V Qdots simply by tuning the dot size and composition to emit anywhere from the infrared to the ultraviolet [196, 197]. Nitride-based Qdots have attracted enormous research interest because of their large built-in electric fields [196]. These large fields originate from both spontaneous polarization in the wurtzite crystal structure, as well as the lattice-mismatch strain acting through their large piezoelectric constants.

Emission from InAs/InP Qdots can be controlled by size as well as the As and P concentrations, and are important for fiber optic telecommunication systems [198]. InP-based material can emit over the range of wavelengths necessary for photonic devices, especially near $1.55 \mu\text{m}$. InAsP Qdots are suitable for monolithically integrated photonic devices on a single chip, including lasers, phase modulators, detectors and passive waveguides.

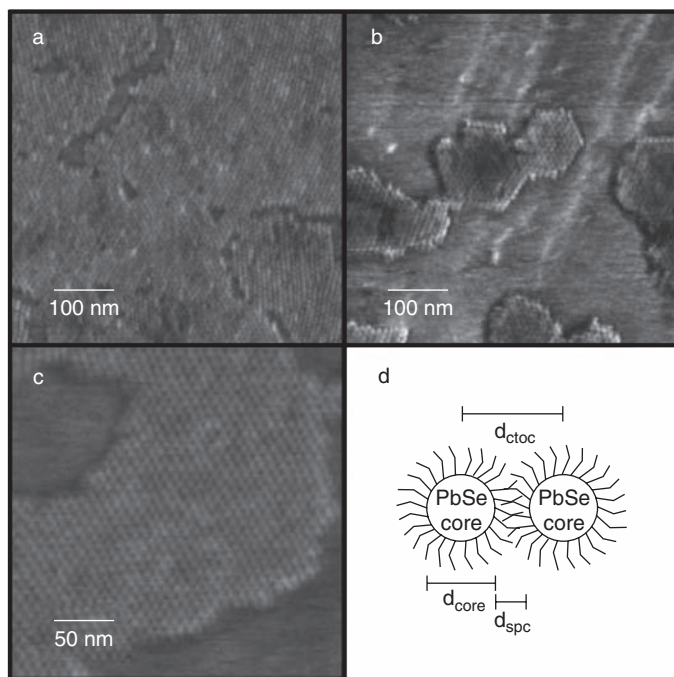


Figure 2.25 AFM images of 5.0 nm PbSe Qdots ordered on the surface of TPD: (a) approximately full monolayer coverage of Qdots were shown by varying the spin solution concentrations; (b) ordered Qdots formed regular hexagonal structures; (c) a highly ordered large domain of PbSe Qdots; (d) a schematic depicts two close packed Qdots surrounded by oleic acid capping molecules (d_{ctoc} : center-to-center spacing; d_{core} : core diameter; d_{spc} : spacing distance between Qdots) (reprinted with permission from [199]. Copyright (2003) Wiley Interscience)

2.8.3 IV-VI Qdots

IV-VI semiconductors have been investigated for infrared electroluminescence, for example, from PbSe Qdots in organic host materials. By tuning the Qdot size, the emission wavelength was changed from 1.33 to 1.56 μm with a FWHM of $<160\text{ nm}$ ($<0.11\text{ eV}$) (Figure 2.25) [199]. Phase segregation during spin-coating was used to fabricate Qdots/organic double heterojunction devices. The Qdots close packed into a hexagonal structure during the spin-coating step (Figure 2.26). The organic films served as a hole transport layer in the Qdot hybrid LED and produced the spectra shown in Figure 2.26.

PbSe Qdots in a polymeric host show large photorefraction (PR), photoconductivity and optical gain when excited with a low-power, continuous-wave laser at 1550 nm [200]. Dynamic-photorefractive holographic gratings were written in the composite. The net optical gain and significant diffraction efficiency achieved with the low-power laser makes this nanocomposite a potential choice for infrared imaging and optical communication applications.

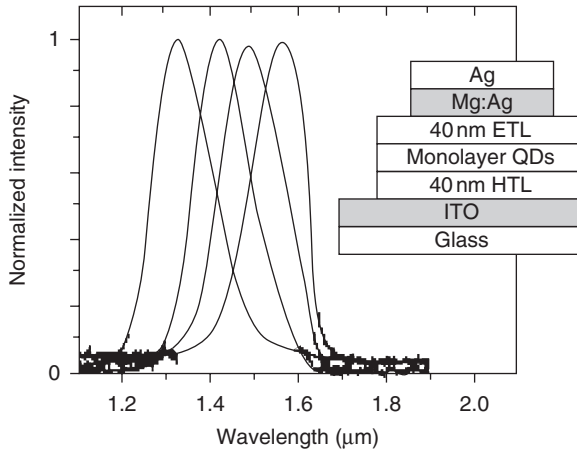


Figure 2.26 PbSe Qdots based Qdot-LED device structure and EL spectra for various size Qdots (reprinted with permission from [199]. Copyright (2003) Wiley Interscience)

2.9 PERSPECTIVE

The properties of phosphor Qdots and some of current applications have been discussed and detailed above. Among the various branches in nanotechnology, zero-dimension nanostructures (Qdots) have paved the way for numerous advances in both fundamental and applied sciences. This is due to the fact that the Qdots exhibit significantly different optical, electronic and physical properties as compared to bulk materials.

With respect to synthesis of Qdots, significant progress has been made in studies of the growth kinetics through both theoretical models and experimental data. Procedures, ranging from simple wet chemical methods to sophisticated and equipment-intensive atomic layer deposition techniques, are being used to synthesize Qdots. The ‘bottom-up’ approaches are being explored with a wider variety of materials to generate Qdots.

Despite the large amount of research, there is still a lot to understand about the use of Qdots in large-scale biological and solid-state optical applications. Although preliminary experiments at the laboratory level have been successful, scaling up the production and retaining the properties of Qdots is not trivial. Continued research and development on Qdots will provide further improvements in quantum efficiency, better device fabrication and new materials, which extend the emission into the near IR region.

Nanobiotechnology is predicted to be a major R&D area for this next century. However, several stumbling blocks need to be overcome to ensure a close marriage of biology and nanotechnology. Bio-functionalizing the Qdots and interface engineering to control when electronic can pass are major challenges. The requirements of applications such as displays, lighting, selective sensors, bio-imaging, magnetic resonance imaging (MRI) contrast agents and bio-labels will require the scientific and engineering community to answer questions about Qdot synthesis, properties, ageing and toxicity.

ACKNOWLEDGEMENT

This work was partially supported by ARL grant W911 NF-04-200023 and ARO grant W991 NF-07-0050. Discussions with Drs. Heesun Yang, Hyeokjin Lee, Jungsik Bang and Sooyeon Seo are gratefully acknowledged .

REFERENCES

1. Shionoya, S. and Yen, W.M. (1998) *Phosphor Handbook*. New York: CRC Press. p. 608.
2. Lee, J.D. (2005) *Concise Inorganic Chemistry*. Noida, India: Blackwell Science. p. 1032.
3. Round, H.J. (1907) 'A note on carborundum', *Elect. World* **49(9)**: 309.
4. Kuchibhatla, S.V.N.T., *et al.* (2007) 'One dimensional nanostructured materials', *Prog. Mat. Sci.* (in press).
5. Bera, D., Kuiry, S.C. and Seal, S. (2004) 'Synthesis of nanostructured materials using template-assisted electrodeposition', *Jom*. **56(1)**: 49–53.
6. Alivisatos, A.P. (1996) 'Perspectives on the physical chemistry of semiconductor nanocrystals'. *J. Phys. Chem.* **100(31)**: 3226–39.
7. Yang, H.S., *et al.* (2006) 'Gd-III-functionalized fluorescent quantum dots as multimodal imaging probes', *Adv. Mat.* **18(21)**: 2890.
8. Santra, S., *et al.* (2005) 'Synthesis and characterization of fluorescent, radio-opaque, and paramagnetic silica nanoparticles for multimodal bioimaging applications', *Adv. Mat.* **17(18)**: 2165–9.
9. Santra, S., *et al.* (2005) 'Rapid and effective labeling of brain tissue using TAT-conjugated CdS: Mn/ZnS quantum dots', *Chem. Comm.* **25**: 3144–6.
10. Yang, H. and Holloway, P.H. (2004) 'Efficient and Photostable ZnS-Passivated CdS:Mn Luminescent Nanocrystals', *Adv. Funct. Mat.* **14(2)**: 152–6.
11. Hines, M.A. and Guyot-Sionnest, P. (1996) 'Synthesis and characterization of strongly luminescing ZnS-Capped CdSe nanocrystals', *J. Phys. Chem.* **100(2)**: 468–71.
12. Walter, P., *et al.* (2006) 'Early use of PbS Nanotechnology for an Ancient Hair Dyeing Formula', *Nano Lett.* **6(10)**: 2215–9.
13. Rocksby, H.P. (1932) *J. Soc. Glass Techn.* **16**: 171.
14. Ekimov, A.I. and Onushchenko, A.A. (1981) 'Quantum Size Effect in 3-Dimensional Microscopic Semiconductor Crystals'. *Jetp Lett.* **34(6)**: p. 345–9.
15. Efros, A.L. and Efros, A.L. (1982) 'Interband Absorption of Light in a Semiconductor Sphere', *Sov. Phys. Semicond.-Ussr* **16(7)**: 772–5.
16. Rossetti, R., *et al.* (1984) 'Size effects in the excited electronic states of small colloidal CdS crystallites', *J. Chem. Phys.* **80(9)**: 4464–9.
17. Sundaram, M., *et al.* (1991) 'New Quantum Structures', *Science* **254(5036)**: 1326–35.
18. Cingolani, R. and Ploog, K. (1991) 'Frequency and Density Dependent Radiative Recombination Processes in Iii-V Semiconductor Quantum-Wells and Superlattices', *Adv. Phys.* **40(5)**: 535–623.
19. Wang, Y. and Herron, N. (1991) 'Nanometer-Sized Semiconductor Clusters - Materials Synthesis, Quantum Size Effects, and Photophysical Properties', *J. Phys. Chem.* **95(2)**: 525–32.
20. Bang, J., Yang, H. and Holloway, P.H. (2006) 'Enhanced and stable green emission of ZnO nanoparticles by surface segregation of Mg', *Nanotech.* **17(4)**: 973–8.
21. Yoffe, A.D. (1993) 'Low-Dimensional Systems – Quantum-size Effects and Electronic-Properties of Semiconductor Microcrystallites (Zero-Dimensional Systems) and Some Quasi-2-Dimensional Systems', *Adv. Phys.* **42(2)**: 173–266.

22. Yoffe, A.D. (2001) 'Semiconductor quantum dots and related systems: electronic, optical, luminescence and related properties of low dimensional systems', *Adv. Phys.* **50(1)**: 1–208.
23. Tolbert, S.H., *et al.* (1994) 'Comparison of Quantum Confinement Effects on the Electronic Absorption-Spectra of Direct and Indirect Gap Semiconductor Nanocrystals', *Phys. Rev. Lett.* **73(24)**: 3266–9.
24. Tolbert, S.H. and Alivisatos, A.P. (1995) 'The Wurtzite to Rock-Salt Structural Transformation in Cdse Nanocrystals under High-Pressure', *J. Chem. Phys.* **102(11)**: 4642–56.
25. Woggon, U. (1997) 'Optical properties of semiconductor quantum dots'. In: *Springer tracts in modern physics* (Kuhn, J., *et al.* eds) Vol. 136. Berlin: Springer-Verlag.
26. Klimov, V.I. (2006) 'Mechanisms for photogeneration and recombination of multiexcitons in semiconductor nanocrystals: Implications for lasing and solar energy conversion', *J. Phys. Chem. B* **110(34)**: 16827–45.
27. Brus, L.E. (1983) 'A Simple-Model for the Ionization-Potential, Electron-Affinity, and Aqueous Redox Potentials of Small Semiconductor Crystallites', *J. Chem. Phys.* **79(11)**: 5566–71.
28. Murray, C.B., Norris, D.J. and Bawendi, M.G. (1993) 'Synthesis and Characterization of Nearly Monodisperse Cde (E = S, Se, Te) Semiconductor Nanocrystallites', *J. Am. Chem. Soc.* **115(19)**: 8706–15.
29. Alexander Ross, J.B., *et al.* (1991) 'Tyrosine Fluorescence and Phosphorescence from Proteins and Polypeptides'. In: *Topics in Fluorescence Spectroscopy*, (Lakowicz, J.R. ed.) Vol. 3. New York and London: Springer. p. 397.
30. Gfroerer, T.H. (2000) 'Photoluminescence in analysis of surface and interfaces'. In: *Encyclopedia of analytical Chemistry* (Meyers, R.A. ed.) Chichester: John Wiley & Sons Ltd. pp. 9209–31.
31. Auzel, F. (2004) 'Upconversion and anti-Stokes processes with f and d ions in solids', *Chem. Rev.* **104(1)**: 139–73.
32. Issac, A., von Borczyskowski, C. and Cichos, F. (2005) 'Correlation between photoluminescence intermittency of CdSe quantum dots and self-trapped states in dielectric media', *Phys. Rev. B* **71(16)**.
33. Xu, P.S., *et al.* (2003) 'The electronic structure and spectral properties of ZnO and its defects, Nuclear Instruments and Methods' In: *Physics Research Section B: Beam Interactions with Materials and Atoms*, **199**: 286–90.
34. Aleksandra, B.D. and Leung, Y.H. (2006) 'Optical Properties of ZnO Nanostructures', *Small* **2(8–9)**: 944–61.
35. Spanhel, L. and Anderson, M.A. (1991) 'Semiconductor Clusters in the Sol-Gel Process – Quantized Aggregation, Gelation, and Crystal-Growth in Concentrated Zno Colloids', *J. Am. Chem. Soc.* **113(8)**: 2826–33.
36. Yang, H., *et al.* (2004) 'CdS:Mn nanocrystals passivated by ZnS: Synthesis and luminescent properties', *J. Chem. Phys.* **121(20)**: 10233–40.
37. Efros, A.L. and Rosen, M. (1997) 'Random telegraph signal in the photoluminescence intensity of a single quantum dot', *Phys. Rev. Lett.* **78(6)**: 1110–13.
38. Williams, E.W. and Hall, R. (1977) 'Luminescence and the light emitting diode'. In: *Science of the Solid State* (Pamplin, B.R. ed.) New York: Pergomon Press. p. 237.
39. Nirmal, M., *et al.* (1996) 'Fluorescence intermittency in single cadmium selenide nanocrystals', *Nature* **383(6603)**: 802–4.
40. Stefani, F.D., *et al.* (2005) 'Quantification of photo-induced and spontaneous quantum-dot luminescence blinking', *Phys. Rev. B* **72(12)**.
41. Stefani, F.D., *et al.* (2005) 'Memory in quantum-dot photoluminescence blinking', *New J. Phys.* **7**.
42. van Sark, W., *et al.* (2002) 'Time-resolved fluorescence spectroscopy study on the photophysical behavior of quantum dots', *J. Fluores.* **12(1)**: p. 69–76.

43. Kuno, M., *et al.* (2000) 'Nonexponential "blinking" kinetics of single CdSe quantum dots: A universal power law behavior', *J. Chem. Phys.* **112**(7): 3117–20.
44. Chen, X.B., *et al.* (2003) 'Coherency strain effects on the optical response of core/shell hetero-nanostructures', *Nano Lett.* **3**(6): 799–803.
45. Peng, X.G., *et al.* (1997) 'Epitaxial growth of highly luminescent CdSe/CdS core/shell nanocrystals with photostability and electronic accessibility', *J. Am. Chem. Soc.* **119**(30): 7019–29.
46. Balet, L.P., *et al.* (2004) 'Inverted core/shell nanocrystals continuously tunable between type-I and type-II localization regimes', *Nano Lett.* **4**(8): 1485–8.
47. Kim, S., *et al.* (2003) 'Type-II quantum dots: CdTe/CdSe(core/shell) and CdSe/ZnTe(core/shell) heterostructures', *J. Am. Chem. Soc.* **125**(38): 11466–7.
48. Scherer, A., Craighead, H.G. and Beebe, E.D. (1987) 'Gallium-Arsenide and Aluminum Gallium-Arsenide Reactive Ion Etching in Boron-Trichloride Argon Mixtures', *J. Vac. Sci. & Tech. B* **5**(6): 1599–605.
49. Tsutsui, K., Hu, E.L. and Wilkinson, C.D.W. (1993) 'Reactive Ion Etched Ii-Vi Quantum Dots – Dependence of Etched Profile on Pattern Geometry', *Jpn. J. App. Phys. Part I-Regular Papers Short Notes & Review Papers* **32**(12B): 6233–6.
50. Chason, E., *et al.* (1997) 'Ion beams in silicon processing and characterization', *J. App. Phys.* **81**(10): 6513–61.
51. Burda, C., *et al.* (2005) 'Chemistry and properties of nanocrystals of different shapes', *Chem. Rev.* **105**(4): 1025–102.
52. Bera, D., *et al.* (2007) 'Optical Properties of ZnO quantum dots produced by a solution-based synthesis process'. *Opt. Mater.* In press, doi:10.1016/j.opmat.2007.06.001.
53. Hoener, C.F., *et al.* (1992) 'Demonstration of a Shell Core Structure in Layered Cdse-Znse Small Particles by X-Ray Photoelectron and Auger Spectroscopies', *J. Phys. Chem.* **96**(9): p. 3812–17.
54. Kortan, A.R., *et al.* (1990) 'Nucleation and Growth of Cdse on Zns Quantum Crystallite Seeds, and Vice Versa, in Inverse Micelle Media', *J. Am. Chem. Soc.* **112**(4): 1327–32.
55. Yang, H.S., Santra, S. and Holloway, P.H. (2005) 'Syntheses and applications of Mn-doped II-VI semiconductor nanocrystals', *J. Nanosci. Nanotech.* **5**(9): 1364–75.
56. Yu, W.W., Wang, Y.A. and Peng, X.G. (2003) 'Formation and stability of size-, shape-, and structure-controlled CdTe nanocrystals: Ligand effects on monomers and nanocrystals', *Chem. Mat.* **15**(22): 4300–8.
57. Talapin, D.V., *et al.* (2001) 'A novel organometallic synthesis of highly luminescent CdTe nanocrystals', *J. Phys. Chem. B* **105**(12): 2260–3.
58. Hines, M.A. and Guyot-Sionnest, P. (1998) 'Bright UV-blue luminescent colloidal ZnSe nanocrystals', *J. Phys. Chem. B* **102**(19): 3655–7.
59. Singh, S., Rama, N. and Rao, M.S.R. (2006) 'Influence of d-d transition bands on electrical resistivity in Ni doped polycrystalline ZnO', *App. Phys. Lett.* **88**(22).
60. Lee, H., Holloway, P.H. and Yang, H. (2006) 'Synthesis and characterization of colloidal ternary ZnCdSe semiconductor nanorods', *J. Chem. Phys.* **125**(16).
61. Yang, H.S., Lee, H. and Holloway, P.H. (2005) 'Anisotropic growth of luminescent Eu³⁺- or Er³⁺-doped Gd₂O₃ nanocrystals', *Nanotech.* **16**(12): 2794–8.
62. Battaglia, D. and Peng, X.G. (2002) 'Formation of high quality InP and InAs nanocrystals in a noncoordinating solvent', *Nano Lett.* **2**(9): 1027–30.
63. Zhu, J.J., Koltypin, Y. and Gedanken, A. (2000) 'General sonochemical method for the preparation of nanophasic selenides: Synthesis of ZnSe nanoparticles', *Chem. Mat.* **12**(1): p. 73–8.
64. Qian, H.F., Li, L. and Ren, J.C. (2005) 'One-step and rapid synthesis of high quality alloyed quantum dots (CdSe-CdS) in aqueous phase by microwave irradiation with controllable temperature', *Mat. Res. Bull.* **40**(10): 1726–36.

65. Wang, L.C., *et al.* (2006) 'A hydrothermal method to prepare the spherical ZnS and flower-like CdS microcrystallites', *Mat. Lett.* **60(29–30)**: 3627–30.
66. Frank, F.C. and van der Merwe, J.H. (1949) *Proc. Roy. Soc. London A* **198**: 205.
67. Volmer, M. and Weber, A. (1926) *Z. Phys. Chem.* **119**: 277.
68. Stranski, I.N. and Krastanow, V.L. (1939) *Akad. Wiss. Lit. Mainz Math.-Natur. Kl. IIB* **146**: 797.
69. Eaglesham, D.J. and Cerullo, M. (1990) 'Dislocation-Free Stranski–Krastanow Growth of Ge on Si(100)', *Phys. Rev. Lett.* **64(16)**: 1943–6.
70. Tsukamoto, S., Bell, G.R. and Arakawa, Y. (2006) 'Heteroepitaxial growth of InAs on GaAs(001) by in situ STM located inside MBE growth chamber', *Microelect. J.* **37(12)**: 1498–504.
71. Jiao, Y.H., *et al.* (2006) 'MBE InAs quantum dots grown on metamorphic InGaAs for long wavelength emitting', *Physica E-Low-Dim. Syst. & Nanostruct.* **35(1)**: 194–8.
72. Lobo, C. and Leon, R. (1998) 'InGaAs island shapes and adatom migration behavior on (100), (110), (111) and (311) GaAs surfaces', *J. App. Phys.* **83(8)**: 4168–72.
73. Ozgur, U., *et al.* (2005) 'A comprehensive review of ZnO materials and devices', *J. App. Phys.* **98(4)**.
74. Wang, Z.L. (2004) 'Zinc oxide nanostructures: growth, properties and applications', *J. Phys.-Cond. Matt.* **16(25)**: R829–58.
75. Djuricic, A.B. and Leung, Y.H. (2006) 'Optical properties of ZnO nanostructures', *Small* **2(8–9)**: 944–61.
76. Djuricic, A.B., *et al.* (2004) 'Visible photoluminescence in ZnO tetrapod and multipod structures', *App. Phys. Lett.* **84(14)**: 2635–7.
77. Cheng, H.M., *et al.* (2006) 'Size dependence of photoluminescence and resonant Raman scattering from ZnO quantum dots', *App. Phys. Lett.* **88(26)**.
78. Lu, J.G., *et al.* (2006) Self-assembled ZnO quantum dots with tunable optical properties', *App. Phys. Lett.* **89(2)**.
79. Norberg, N.S. and Gamelin, D.R. (2005) 'Influence of surface modification on the luminescence of colloidal ZnO nanocrystals', *J. Phys. Chem. B* **109(44)**: 20810–16.
80. Cross, R.B.M., De Souza, M.M. and Narayanan, E.M.S. (2005) 'A low temperature combination method for the production of ZnO nanowires', *Nanotech.* **16(10)**: 2188–92.
81. Abrarov, S.M., *et al.* (2005) 'Effect of photonic band-gap on photoluminescence of ZnO deposited inside the green synthetic opal', *Opt. Comm.* **250(1–3)**: 111–9.
82. van Dijken, A., Makkinje, J. and Meijerink, A. (2001) 'The influence of particle size on the luminescence quantum efficiency of nanocrystalline ZnO particles', *J. Lumin.* **92(4)**: 323–8.
83. Xiu, F.X., *et al.* (2006) 'p-Type ZnO films with solid-source phosphorus doping by molecular-beam epitaxy', *App. Phys. Lett.* **88(5)**.
84. Viswanatha, R., *et al.* (2006) 'Blue-emitting copper-doped zinc oxide nanocrystals', *J. Phys. Chem. B* **110(45)**: 22310–12.
85. Wang, Y.S., Thomas, P.J. and O'Brien, P. (2006) 'Optical Properties of ZnO Nanocrystals Doped with Cd, Mg, Mn, and Fe Ions', *J. Phys. Chem. B* **110(43)**: 21412–15.
86. Hirate, T., *et al.* (2005) 'Effects of laser-ablated impurity on aligned ZnO nanorods grown by chemical vapor deposition', *Thin Sol. Films* **487(1–2)**: 35–9.
87. Liu, S.M., Liu, F.Q. and Wang, Z.G. (2001) 'Relaxation of carriers in terbium-doped ZnO nanoparticles', *Chem. Phys. Lett.* **343(5–6)**: 489–92.
88. Cheng, B.C., *et al.* (2004) 'Controlled growth and properties of one-dimensional ZnO nanostructures with Ce as activator/dopant', *Adv. Funct. Mat.* **14(9)**: 913–19.
89. Ishizumi, A. and Kanemitsu, Y. (2005) 'Structural and luminescence properties of Eu-doped ZnO nanorods fabricated by a microemulsion method', *App. Phys. Lett.* **86(25)**.
90. Wu, G.S., *et al.* (2006) 'Synthesis and photoluminescence of dy-doped ZnO nanowires', *Physica E-Low-Dim. Syst. & Nanostruct.* **31(1)**: 5–8.

91. Zhang, X.T., *et al.* (2003) 'Structure and photoluminescence of Mn-passivated nanocrystalline ZnO thin films', *J. Cryst. Growth*. **254**(1–2): 80–5.
92. Xu, C.X., *et al.* (2005) 'Manganese-doped zinc oxide tetrapods and their photoluminescent properties', *J. Appl. Phys.* **98**(11).
93. Yang, L.W., *et al.* (2005) 'In situ synthesis of Mn-doped ZnO multileg nanostructures and Mn-related Raman vibration', *J. Appl. Phys.* **97**(1).
94. Ronning, C., *et al.* (2004) 'Manganese-doped ZnO nanobelts for spintronics', *App. Phys. Lett.* **84**(5): 783–5.
95. Foreman, J.V., *et al.* (2006) 'Time-resolved investigation of bright visible wavelength luminescence from sulfur-doped ZnO nanowires and micropowders', *Nano Lett.* **6**(6): 1126–30.
96. Shen, G.Z., *et al.* (2005) 'Synthesis and optical properties of S-doped ZnO nanostructures: Nanonails and nanowires', *J. Phys. Chem. B* **109**(12): 5491–6.
97. Han, L.L., *et al.* (2006) 'Synthesis of high quality zinc-blende CdSe nanocrystals and their application in hybrid solar cells', *Nanotech.* **17**(18): 4736–42.
98. Oey, C.C., *et al.* (2006) 'Polymer-TiO₂ solar cells: TiO₂ interconnected network for improved cell performance', *Nanotech.* **17**(3): 706–13.
99. Olson, D.C., *et al.* (2006) 'Hybrid photovoltaic devices of polymer and ZnO nanofiber composites', *Thin Sol. Films* **496**(1): 26–9.
100. Michler, P., *et al.* (2000) 'Quantum correlation among photons from a single quantum dot at room temperature', *Nature* **406**(6799): 968–70.
101. Cui, D.H., *et al.* (2006) 'Harvest of near infrared light in PbSe nanocrystal-polymer hybrid photovoltaic cells', *App. Phys. Lett.* **88**(18).
102. O'Regan, B., *et al.* (2000) 'Electrodeposited nanocomposite n-p heterojunctions for solid-state dye-sensitized photovoltaics', *Adv. Mat.* **12**(17): 1263.
103. Bereznev, S., *et al.* (2005) 'Hybrid CuInS₂/polypyrrole and CuInS₂/poly(3,4-ethylenedioxythiophene) photovoltaic structures', *Synth. Met.* **152**(1–3): 81–4.
104. Beek, W.J.E., Wienk, M.M. and Janssen, R.A.J. (2004) 'Efficient hybrid solar cells from zinc oxide nanoparticles and a conjugated polymer', *Adv. Mat.* **16**(12): 1009.
105. Yang, P., *et al.* (2001) 'ZnS nanocrystals co-activated by transition metals and rare-earth metals – a new class of luminescent materials', *J. Lumin.* **93**(2): 101–5.
106. Qu, S.C., *et al.* (2002) 'Photoluminescence properties of Eu³⁺-doped ZnS nanocrystals prepared in a water/methanol solution', *App. Phys. Lett.* **80**(19): 3605–7.
107. Suyver, J.F., *et al.* (2001) 'Synthesis and photoluminescence of nanocrystalline ZnS : Mn²⁺', *Nano Lett.* **1**(8): 429–33.
108. Bhargava, R.N., *et al.* (1994) 'Optical-Properties of Manganese-Doped Nanocrystals of ZnS', *Phys. Rev. Lett.* **72**(3): 416–19.
109. Bol, A.A. and Meijerink, A. (1998) 'Long-lived Mn²⁺ emission in nanocrystalline ZnS : Mn²⁺', *Phys. Rev. B* **58**(24): R15997–6000.
110. Su, F.H., *et al.* (2003) 'Pressure dependence of Mn²⁺ luminescence in differently sized ZnS : Mn nanoparticles', *J. Phys. Chem. B* **107**(29): 6991–6.
111. Khosravi, A.A., *et al.* (1995) 'Manganese-Doped Zinc-Sulfide Nanoparticles by Aqueous Method', *App. Phys. Lett.* **67**(17): 2506–8.
112. Beermann, P.A.G., *et al.* (2004) 'EPR spectra of Mn²⁺-doped ZnS quantum dots', *Chem. Mat.* **16**(5): 915–8.
113. Bol, A.A. and Meijerink, A. (2001) 'Luminescence quantum efficiency of nanocrystalline ZnS: Mn²⁺. I. Surface passivation and Mn²⁺ concentration', *J. Phys. Chem. B* **105**(42): 10197–202.
114. Hattori, Y., *et al.* (2005) 'Luminescent properties of ZnS:Mn²⁺ nanocrystals/SiO₂ hybrid phosphor synthesized by *in situ* surface modification co-precipitation', *J. Lumin.* **113**(1–2): 69–78.
115. Becker, W.G. and Bard, A.J. (1983) 'Photo-Luminescence and Photoinduced Oxygen-Adsorption of Colloidal Zinc-Sulfide Dispersions', *J. Phys. Chem.* **87**(24): 4888–93.

116. Baral, S., *et al.* (1986) 'Photochemistry and Radiation-Chemistry of Colloidal Semiconductors. 12. Intermediates of the Oxidation of Extremely Small Particles of Cds, Zns, and Cd₃p₂ and Size Quantization Effects (a Pulse-Radiolysis Study)', *J. Amer. Chem. Soc.* **108(3)**: 375–8.
117. Dunstan, D.E., *et al.* (1990) 'Importance of Surface-Reactions in the Photochemistry of Zns Colloids', *J. Phys. Chem.* **94(17)**: 6797–804.
118. Bhargava, R.N. (1996) 'Doped nanocrystalline materials – Physics and applications', *J. Lumin.* **70**: 85–94.
119. Bol, A.A. and Meijerink, A. (2001) 'Luminescence quantum efficiency of nanocrystalline ZnS : Mn²⁺. 2. Enhancement by UV irradiation', *J. Phys. Chem. B* **105(42)**: 10203–9.
120. Cao, L.X., *et al.* (2002) 'Luminescence enhancement of core-shell ZnS: Mn/ZnS nanoparticles', *App. Phys. Lett.* **80(23)**: 4300–2.
121. Jin, C.M., *et al.* (1995) 'Luminescence of Mn²⁺ doped ZnS nanocrystallites', *Journal of Luminescence* **66–7(1–6)**: 315–18.
122. Reiss, P., *et al.* (2004) 'Luminescent ZnSe nanocrystals of high color purity', *Mat. Chem. Phys.* **84(1)**: 10–13.
123. Karanikolos, G.N., *et al.* (2004) 'Synthesis and size control of luminescent ZnSe nanocrystals by a microemulsion-gas contacting technique', *Langmuir* **20(3)**: 550–3.
124. Shavel, A., Gaponik, N. and Eychmuller, A. (2004) 'Efficient UV-blue photoluminescing thiol-stabilized water-soluble alloyed ZnSe(S) nanocrystals', *J. Phys. Chem. B* **108(19)**: 5905–8.
125. Xiang, B., *et al.* (2003) 'Green-light-emitting ZnSe nanowires fabricated via vapor phase growth', *App. Phys. Lett.* **82(19)**: 3330–2.
126. Chen, H.S., *et al.* (2005) 'White-light emission from organics-capped ZnSe quantum dots and application in white-light-emitting diodes', *App. Phys. Lett.* **86(13)**.
127. Thantu, N. (2005) 'Second harmonic generation and two-photon luminescence upconversion in glasses doped with ZnSe nanocrystalline quantum dots', *J. Lumin.* **111(1–2)**: 17–24.
128. Chen, H.S., *et al.* (2004) 'Colloidal ZnSe, ZnSe/ZnS, and ZnSe/ZnSeS quantum dots synthesized from ZnO', *J. Phys. Chem. B* **108(44)**: 17119–23.
129. Kim, Y.G., *et al.* (2003) 'Temperature-dependent photoluminescence of ZnSe/ZnS quantum dots fabricated under the Stranski-Krastanov mode', *App. Phys. Lett.* **83(13)**: 2656–8.
130. Zu, L.J., *et al.* (2006) 'Impact of ripening on manganese-doped ZnSe nanocrystals', *Nano Lett.* **6(2)**: 334–40.
131. Norris, D.J., *et al.* (2001) 'High-quality manganese-doped ZnSe nanocrystals', *Nano Lett.* **1(1)**: 3–7.
132. Suyver, J.F., *et al.* (2000) 'Luminescence of nanocrystalline ZnSe : Mn²⁺', *Phys. Chem. Chem. Phys.* **2(23)**: 5445–8.
133. Norman, T.J., *et al.* (2003) 'Optical and surface structural properties of Mn²⁺-doped ZnSe nanoparticles', *J. Phys. Chem. B* **107(26)**: 6309–17.
134. Geng, B.Y., *et al.* (2006) 'One-step synthesis and enhanced blue emission of carbon-encapsulated single-crystalline ZnSe nanoparticles', *App. Phys. Lett.* **89(3)**.
135. Darugar, Q., Qian, W. and El-Sayed, M.A. (2006) 'Observation of optical gain in solutions of CdS quantum dots at room temperature in the blue region', *App. Phys. Lett.* **88(26)**.
136. Cao, H.Q., *et al.* (2006) 'Growth and optical properties of wurtzite-type CdS nanocrystals', *Inorg. Chem.* **45(13)**: 5103–8.
137. Kim, D., *et al.* (2005) 'Strong enhancement of band-edge photoluminescence in CdS quantum dots prepared by a reverse-micelle method', *J. App. Phys.* **98(8)**.
138. Demchenko, D.O. and Wang, L.W. (2006) 'Optical transitions and nature of Stokes shift in spherical CdS quantum dots', *Phys. Rev. B* **73(15)**.
139. Nandakumar, P., Vijayan, C. and Murti, Y. (2002) 'Optical absorption and photoluminescence studies on CdS quantum dots in Nafion', *J. App. Phys.* **91(3)**: p. 1509–14.

140. Ni, Y.H., *et al.* (2006) 'Preparation, characterization, and optical, electrochemical property research of CdS/PAM nanocomposites', *J. Phys. Chem. B* **110(35)**: 17347–52.
141. Wu, X.C., Bittner, A.M. and Kern, K. (2005) 'Synthesis, photoluminescence, and adsorption of CdS/dendrimer nanocomposites', *J. Phys. Chem. B* **109(1)**: 230–9.
142. Bryant, G.W. and Jaskolski, W. (2005) 'Surface effects on capped and uncapped nanocrystals', *J. Phys. Chem. B* **109(42)**: 19650–6.
143. Jeang, E.H., *et al.* (2004) 'Fabrication and optical characteristics of CdS/Ag metal-semiconductor composite quantum dots', *Bull. Korean Chem. Soc.* **25(6)**: 9346.
144. Je, K.C., *et al.* (2006) 'Local field-induced optical properties of Ag-coated CdS quantum dots', *Opt. Exp.* **14(17)**: 7994–8000.
145. Mohanta, D., *et al.* (2006) 'Scanning probe microscopy, luminescence and third harmonic generation studies of elongated CdS : Mn nanostructures developed by energetic oxygen-ion-impact', *Eur. Phys. J. App. Phys.* **35(1)**: 29–36.
146. Dridi, C., *et al.* (2006) 'Spectroscopic investigations on hybrid nanocomposites: CdS : Mn nanocrystals in a conjugated polymer', *Mat. Sci. & Eng. C-Biom. and Supramol. Syst.* **26(2–3)**: 415–20.
147. Kim, D., Miyamoto, M. and Nakayama, M. (2005) 'Photoluminescence properties of CdS and CdMnS quantum dots prepared by a reverse-micelle method', *J. Elect. Micro.* **54**: I31–4.
148. Yang, H. and Holloway, P.H. (2003) 'Enhanced photoluminescence from CdS : Mn/ZnS core/shell quantum dots', *App. Phys. Lett.* **82(12)**: 1965–7.
149. Santra, S., *et al.* (2005) 'Synthesis of water-dispersible fluorescent, radio-opaque, and paramagnetic CdS : Mn/ZnS quantum dots: A multifunctional probe for bioimaging', *J. Amer. Chem. Soc.* **127(6)**: 1656–7.
150. Yang, H. and Holloway, P.H. (2004) 'Efficient and photostable ZnS-Passivated CdS : Mn luminescent nanocrystals', *Adv. Funct. Mat.* **14(2)**: 152–6.
151. Bera, D., Holloway, P.H. and Yang, H. (2006) 'Efficient and Photostable ZnS-passivated CdS: Mn Quantum dots'. In: *Joint International Meeting of Electrochemical Society*. Cancun, Mexico: The Electrochemical Society.
152. Yang, Y.A., *et al.* (2006) 'Radial-position-controlled doping in CdS/ZnS core/shell nanocrystals', *J. Amer. Chem. Soc.* **128(38)**: 12428–9.
153. Steckel, J.S., *et al.* (2004) 'Blue luminescence from (CdS)/ZnS core-shell nanocrystals', *Ange-wandte Chemie-International Edition* **43(16)**: 2154–8.
154. Yang, H.S. and Holloway, P.H. (2003) 'Electroluminescence from hybrid conjugated polymer – CdS : Mn/ZnS core/shell nanocrystals devices', *J. Phys. Chem. B* **107(36)**: 9705–10.
155. Holloway, P.H., *et al.* (2006) 'Nanophosphor: PL, EL, and Biological Markers'. In: *Proceedings of 13th International Display Workshops, IDW'06 Otsu, Japan*.
156. Holloway, P.H., *et al.* (2006) 'Nanophosphor: PL, EL, and Biological Markers'. In: *Proceedings of 3rd International Symposium on Display & Lighting Phosphor Materials, ISDLPMW'06 Yokohama, Japan*.
157. Toth, E., *et al.* (2005) 'Water-soluble gadofullerenes: Toward high-relaxivity, pH-responsive MRI contrast agents', *J. Amer. Chem. Soc.* **127(2)**: 799–805.
158. Rohrer, M., *et al.* (2005) 'Comparison of magnetic properties of MRI contrast media solutions at different magnetic field strengths', *Invest. Radiol.* **40(11)**: 715–24.
159. Pierre, V.C., Botta, M. and Raymond, K.N. (2005) 'Dendrimeric gadolinium chelate with fast water exchange and high relaxivity at high magnetic field strength', *J. Amer. Chem. Soc.* **127(2)**: 504–5.
160. Tan, W.B. and Zhang, Y. (2005) 'Multifunctional quantum-dot-based magnetic chitosan nanobeads', *Adv. Mat.* **17(19)**: 2375.
161. Reiss, P., Bleuse, J. and Pron, A. (2002) 'Highly luminescent CdSe/ZnSe core/shell nanocrystals of low size dispersion', *Nano Lett.* **2(7)**: 781–4.

162. Han, M.Y., *et al.* (2001) 'Quantum-dot-tagged microbeads for multiplexed optical coding of biomolecules', *Nat. Biotech.* **19**(7): 631–5.
163. Sukhanova, A., *et al.* (2004) 'Biocompatible fluorescent nanocrystals for immunolabeling of membrane proteins and cells', *Anal. Biochem.* **324**(1): 60–7.
164. Dahan, M., *et al.* (2003) 'Diffusion dynamics of glycine receptors revealed by single-quantum dot tracking', *Science* **302**(5644): 442–5.
165. Dubertret, B., *et al.* (2002) 'In vivo imaging of quantum dots encapsulated in phospholipid micelles', *Science* **298**(5599): 1759–62.
166. Bowers, M.J., McBride, J.R. and Rosenthal, S.J. (2005) 'White-light emission from magic-sized cadmium selenide nanocrystals', *J. Amer. Chem. Soc.* **127**(44): 15378–9.
167. Jose, R., *et al.* (2006) 'White-light-emitting CdSe quantum dots synthesized at room temperature', *App. Phys. Lett.* **89**(1).
168. Chen, W., Joly, A.G. and McCready, D.E. (2005) 'Upconversion luminescence from CdSe nanoparticles', *J. Chem. Phys.* **122**(22).
169. Derfus, A.M., Chan, W.C.W. and Bhatia, S.N. (2004) 'Probing the cytotoxicity of semiconductor quantum dots', *Nano Lett.* **4**(1): 11–18.
170. Liu, Y.C., *et al.* (2006) 'Highly luminescent, stable, and water-soluble CdSe/CdS core – Shell dendron nanocrystals with carboxylate anchoring groups', *Langmuir* **22**(14): 6341–5.
171. Palaniappan, K., *et al.* (2006) 'Water-soluble, cyclodextrin-modified CdSe-CdS core-shell structured quantum dots', *Chem. Mat.* **18**(5): 1275–80.
172. Wang, Q.A., *et al.* (2006) 'Luminescent CdSe and CdSe/CdS core-shell nanocrystals synthesized via a combination of solvothermal and two-phase thermal routes', *J. Lumin.* **118**(1): 91–8.
173. Dabbousi, B.O., *et al.* (1997) '(CdSe)ZnS core-shell quantum dots: Synthesis and characterization of a size series of highly luminescent nanocrystallites', *J. Phys. Chem. B* **101**(46): 9463–75.
174. McBride, J., *et al.* (2006) 'Structural basis for near unity quantum yield core/shell nanostructures', *Nano Lett.* **6**(7): 1496–501.
175. Jin, T., *et al.* (2006) 'Control of the optical properties of quantum dots by surface coating with calix[n]arene carboxylic acids', *J. Amer. Chem. Soc.* **128**(29): 9288–9.
176. Lu, Z.X., *et al.* (2005) 'Core/shell quantum-dot-photosensitized nano-TiO₂ films: Fabrication and application to the damage of cells and DNA', *J. Phys. Chem. B* **109**(47): 22663–6.
177. Xie, R.G., *et al.* (2005) 'Synthesis and characterization of highly luminescent CdSe-Core CdS/ZnO.5CdO.5S/ZnS multishell nanocrystals', *J. Amer. Chem. Soc.* **127**(20): 7480–8.
178. Talapin, D.V., *et al.* (2004) 'CdSe/CdS/ZnS and CdSe/ZnSe/ZnS core-shell-shell nanocrystals', *J. Phys. Chem. B* **108**(49): 18826–31.
179. Xu, J.F. and Xiao, M. (2005) 'Lasing action in colloidal CdS/CdSe/CdS quantum wells', *App. Phys. Lett.* **87**(17).
180. Coe-Sullivan, S., *et al.* (2005) 'Large-area ordered quantum-dot monolayers via phase separation during spin-casting', *Adv. Funct. Mat.* **15**(7): 1117–24.
181. Li, Y.Q., *et al.* (2006) 'Bright white-light-emitting device from ternary nanocrystal composites', *Adv. Mat.* **18**(19): 2545.
182. Erwin, S.C., *et al.* (2005) 'Doping semiconductor nanocrystals', *Nature* **436**(7047): 91–4.
183. Dahan, M., *et al.* (2001) 'Time-gated biological imaging by use of colloidal quantum dots', *Opt. Lett.* **26**(11): 825–7.
184. Medintz, I.L., *et al.* (2003) 'Self-assembled nanoscale biosensors based on quantum dot FRET donors', *Nat. Mat.* **2**(9): 630–8.
185. Wang, Q., *et al.* (2006) 'Luminescent properties of water-soluble denatured bovine serum albumin-coated CdTe quantum dots', *J. Phys. Chem. B* **110**(34): 16860–6.
186. He, Y., *et al.* (2006) 'Microwave-assisted growth and characterization of water-dispersed CdTe/CdS core-shell nanocrystals with high photoluminescence', *J. Phys. Chem. B* **110**(27): 13370–4.

187. Schops, O., *et al.* (2006) 'Recombination dynamics of CdTe/CdS core-shell nanocrystals', *J. Phys. Chem. B* **110**(5): 2074–9.
188. Lee, H.S., Park, H.L. and Kim, T.W. (2006) 'Effect of ZnTe buffer layer on the structural and optical properties of CdTe/ZnTe quantum dots', *J. Cryst. Grow.* **293**(1): 27–31.
189. Wang, C.H., *et al.* (2006) 'Photoluminescence properties of CdTe/CdSe core-shell type-II quantumdots', *J. App. Phys.* **99**(12).
190. Kim, S., *et al.* (2004) 'Near-infrared fluorescent type II quantum dots for sentinel lymph node mapping', *Nat. Biotech.* **22**(1): 93–7.
191. Zhang, Y., *et al.* (2006) 'Time-dependent photoluminescence blue shift of the quantum dots in living cells: Effect of oxidation by singlet oxygen', *J. Am. Chem. Soc.* **128**(41): 13396–401.
192. Wolcott, A., *et al.* (2006) 'Silica-coated CdTe quantum dots functionalized with thiols for bioconjugation to IgG proteins', *J. Phys. Chem. B* **110**(11): 5779–89.
193. Boldt, K., *et al.* (2006) 'Comparative examination of the stability of semiconductor quantum dots in various biochemical buffers', *J. Phys. Chem. B* **110**(5): 1959–63.
194. Roither, J., *et al.* (2006) 'Two- and one-dimensional light propagations and gain in layer-by-layer-deposited colloidal nanocrystal waveguides', *App. Phys. Lett.* **89**(11).
195. Guldi, D.M., *et al.* (2006) 'CNT-CdTe versatile donor-acceptor nanohybrids', *J. Am. Chem. Soc.* **128**(7): 2315–23.
196. Williams, D.P., Andreev, A.D. and O'Reilly, E.P. (2006) 'Dependence of exciton energy on dot size in GaN/AlN quantum dots', *Phys. Rev. B* **73**(24).
197. Pan, G.Q., Kordesch, M.E. and Van Patten, P.G. 'New pyrolysis route to GaN quantum dots', *Chem. Mat.* 2006. **18**(17): 3915–17.
198. Barik, S., *et al.* (2006) 'Selective wavelength tuning of self-assembled InAs quantum dots grown on InP', *App. Phys. Lett.* **88**(19).
199. Steckel, J.S., *et al.* (2003) '1.3 μm to 1.55 μm tunable electroluminescence from PbSe quantum dots embedded within an organic device', *Adv. Mat.* **15**(21): 1862–6.
200. Choudhury, K.R., Sahoo, Y. and Prasad, P.N. (2005) 'Hybrid quantum-dot-polymer nanocomposites for infrared photorefractivity at an optical communication wavelength', *Adv. Mat* **17**(23): 2877.

3 Color Conversion Phosphors for LEDs

Jack Silver and Robert Withnall

BRUNEL UNIVERSITY, Uxbridge, Middlesex UB8 3PH, UK

3.1 Introduction	75
3.2 Disadvantages of using LEDs without color conversion phosphors	76
3.3 Phosphors for converting the color of light emitted by LEDs	79
3.4 Survey of the synthesis and properties of some currently available color conversion phosphors	83
3.5 Multi-phosphor pcLEDs	102
3.6 Quantum dots	103
3.7 Conclusions	104
Acknowledgements	104
References	104

3.1 INTRODUCTION

In this chapter we have not sought to present an exhaustive review of the literature, but rather to present the reader with an overview of the problems that currently need to be addressed by the light emitting diode (LED) and phosphor manufacturers. To do this we will focus on some of the major phosphors being developed by some of the major industrial players and their present drawbacks as color conversion materials. First we will present a brief history of LED development and the needs for color conversion phosphors. We will then discuss the photoluminescent phosphors that are currently being developed.

'Electroluminescence' was first reported by Henry Joseph Round in 1906, while he was experimenting with SiC (carborundum), and the first light emitting diode (LED) was effectively fabricated. Little progress followed in the next 50 years until concerted research into semiconductors began. In the 1950s, academic and industrial researchers carried out many experiments to generate light emission at the p-n junction of diodes using a number of materials. The results were disappointing as light emission was low in intensity, the LEDs were expensive and only a few colors were available. In his recent book, *Light-Emitting Diodes*, Schubert [1] documents many of the historical and technical aspects of the progress of LED research, and this provides greater detail on the evolution of LEDs. Only a brief

synopsis is given here to put this review of phosphors for LEDs into context with the still existing shortcomings of LEDs.

During the early 1960s, Texas Instruments sold 870nm LEDs for \$130 US, and GE launched red LEDs for around \$260 US. Hence these early LEDs were expensive and sold only in low volumes. In 1964, IBM used GaAsP LEDs on circuit boards in an early main-frame computer as on-off indicator lights: this was perceived as a significant breakthrough as it provided lighting in a new role to both manufacturer and end-user. The beauty of this innovation was that the LED could be mounted directly onto the circuit board, it used little power, and had a long lifetime thereby eliminating maintenance. These attributes are the ones used today to maneuver LEDs into replacing other light sources as the LEDs have become more efficient, cheaper and brighter.

Thus, although infra-red and red LEDs have been around for over 40 years, it was only the arrival of bright blue LEDs that heralded the genesis of the present solid state lighting revolution.

Research that led to the development of the blue LEDs followed from reports on III –V nitrides that allowed the production of high-quality crystals of GaN, AlGaIn, GaInN, and of p-type conduction in GaN and AlGaIn [2, 3]. In the early 1990s, Nakamura and co-workers followed up this work to develop low-resistive p-type GaN and AlGaIn using Mg-doping, which were produced after growth and thermal annealing in N₂ (which facilitated the reactivation of the Mg acceptors) [4]. This then allowed the bright blue GaInN/AlGaIn LEDs to be prepared, along with blue-green LEDs [5–9]. This was followed with the fabrication of bluish-purple laser diodes [10–18]. These innovations by Nakamura *et al.* led advances in the InGaIn LED technology, which were to initiate the wide-scale commercialization of blue and green solid-state sources as well as the development of white LEDs. A full range of colored LEDs was then available and this facilitated their use in many colored lighting applications displacing more traditional lighting methods.

Around 1997, prototype white solid state lighting was demonstrated at international conferences based on using red, green and blue LEDs. However, it was rapidly realized that the three different LEDs would age at different rates, causing the white light to take on colored hues. In addition, the color rendering index that could be achieved from three narrow band-emitting LEDs was poor and left much to be desired. A further problem was that the light was not bright, as the green LEDs were not bright (see green window below). It was then proposed that better white light could be produced from a combination of a blue LED and either two wide-band phosphors (green and red) each excited by the blue, or by a combination of a blue LED and a broad-band yellow emitting phosphor. These phosphor-converted LEDs, pcLEDs, have been rapidly developed over the last few years and are being widely used in a broad variety of lighting applications.

Here the development of the phosphors used in the pcLEDs will be reviewed, the properties desired in these phosphors will be discussed, and the problems that have yet to be overcome to achieve them will be outlined.

3.2 DISADVANTAGES OF USING LEDS WITHOUT COLOR CONVERSION PHOSPHORS

It is obvious to ask: ‘Why is it necessary to convert the beautiful colors emitted by LEDs?’ This question is particularly relevant when it is realized that the whole palette of colors is available (Figures 3.1 and 3.2).

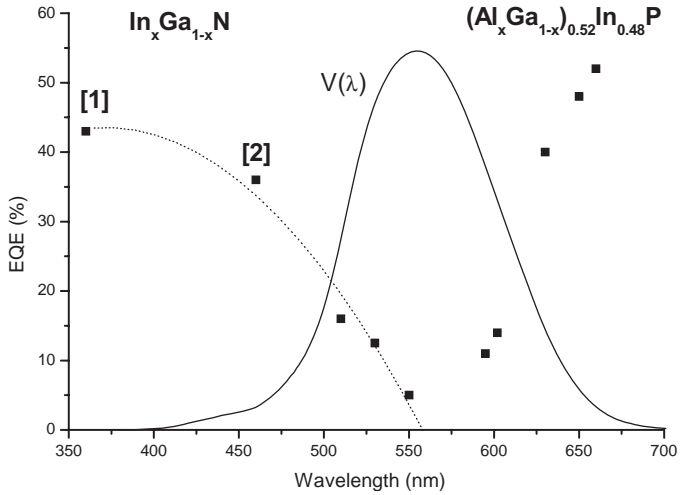


Figure 3.1 Plot of the external quantum efficiency (EQE) of LEDs vs. emission wavelength. The data points for wavelengths $\leq 550\text{nm}$ have been fitted to a polynomial function (dotted curve), and the photopic eye response function, $V(x)$, is shown for comparison. Data for points [1] and [2] were reported in 2004 by Nichia Chemical Co. and Cree, respectively; the other data have been reported by Philips Lumileds Lighting Company for high power ($>1\text{ W}$) LEDs @ 350mA , 70A/cm^2 and 25°C (adapted from N.F. Gardner, ECS 210th meeting, abstract 313, Cancun, Mexico, 2006)

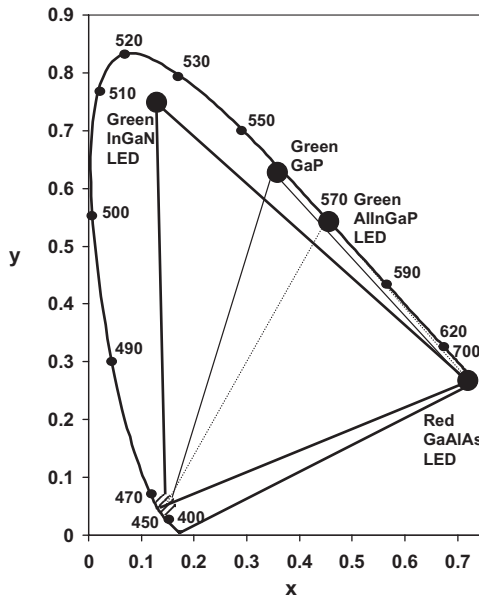


Figure 3.2 CIE chromaticity diagram showing color triangles based on some of the currently available LEDs

Although it is possible to obtain a full spectrum of colors from III-V LEDs and related compounds, there are a number of problems associated with LEDs:

- These include different working lifetimes of LEDs having different emission wavelengths, leading to different ageing of different color LEDs.
- Varying brightness of the different wavelength emitting LEDs. This is known as the *Green Window* problem, and is caused by the lack of good external quantum efficiency, EQE, values in the deep green to yellow region of the spectrum (Figure 3.1).
- There is a temperature dependence of the emission wavelength of some LEDs. Although for some LEDs the shift of the emission wavelength is small with temperature, for others it is larger. This can be readily addressed by the use of a phosphor which has an excitation band that is wider than the emission band of the LED. Even if the LED emission undergoes a wavelength shift with temperature, the excitation band of the phosphor may span the change so that the phosphor's emission band is not wavelength sensitive or at least much less so than that of the LED.

Where the highest reported values [19–25] of internal quantum efficiencies are plotted against wavelength for blue and near ultraviolet emitting LEDs, it is apparent that the highest efficiencies are in the 380 nm to 410 nm range (Figure 3.3). This can be compared to Figure 3.1; allowing for the fact that the latter is based on EQE values, it appears that in addition to the green window there is also a problem with LED performance at wavelengths shorter than 360 nm in the near ultra-violet region of the electromagnetic spectrum.

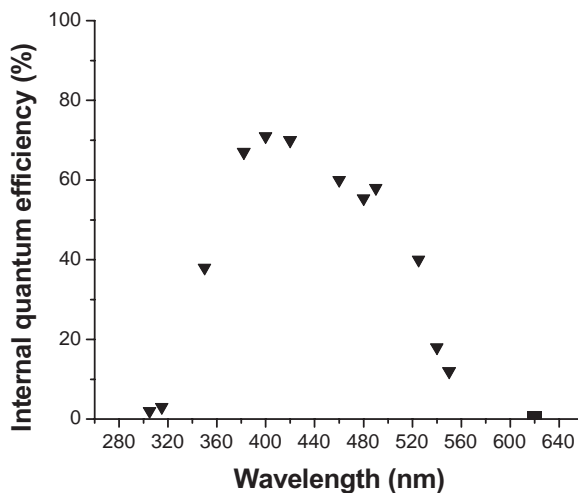


Figure 3.3 Highest literature values of internal quantum efficiencies as a function of emission wavelength

3.3 PHOSPHORS FOR CONVERTING THE COLOR OF LIGHT EMITTED BY LEDs

3.3.1 General considerations

It can be seen from the foregoing discussion, that there are several reasons for needing phosphor color converters. Phosphors are a well established technology, with many display and lighting applications based on their use. Although there are a large number of phosphors that emit light in the visible region of the spectrum, there are only a few photoluminescent phosphors that can be excited efficiently by blue and near ultraviolet LEDs. This means that there are presently a limited set of colors and spectral widths available, but there is much scope for further research into new host lattices to extend the color palette.

The use of phosphors will, of course, involve loss of energy due to a Stokes shift, arising from the fact that the energy of a photon of emitted light is less than that of a photon of the exciting light. The energy difference is known as the quantum deficit.

Properties required by the phosphor for specific use with LEDs depend on the desired applications, which are exemplified by the following:

- Conversion from blue to a specific color, e.g. green;
- Single phosphor white, e.g. a blue-emitting LED in conjunction with a complementary yellow-emitting phosphor;
- Multi-phosphor white, e.g. a UV-emitting LED in conjunction with red-, green- and blue-emitting phosphors;
- The physical location of the phosphor converter, i.e. whether it is deposited directly onto the LED chip, e.g. as a suspension in a binder, or if it used remotely from the LED, e.g. printed on a screen. In the former case it is desirable that the phosphor emission is not thermally quenched at its operating temperature (which is higher than room temperature due to heating by the LED itself), whereas in the latter case the operating temperature of the phosphor is close to room temperature so thermal quenching is not an appreciable problem.

3.3.2 Requirements of color conversion phosphors

When producing white light from an artificial source, it is important to match the light to the requirements of the user. If the white light is required to view colored objects in a commercial or domestic situation then the better the color rendering index of the light the better the consumer will appreciate it. However, if the light is only to illuminate a black and white page of a book for reading, then color rendering is not so important. For 100% color rendering, the spectral output of the light needs to match the blackbody radiation of the Sun. This is difficult to achieve in practice and color rendering indices (CRIs) of 80% or more are usually acceptable for domestic use.

In specific cases, such as light for illuminating a medical operation, the higher the CRI the better, as in most cases the surgeon wants to see as much contrast and detail of internal tissues as possible.

Where the solid state lighting may be replacing existing lighting for navigation lights on aeroplanes or in backlights for military displays, the properties of the lights have previously been defined and the customer will only accept solid state lighting that matches the previously accepted specifications. However, in most cases, the customer will also require higher brightness.

These are great challenges for the phosphor developer/manufacturer, as usually new phosphors have to be designed.

The properties required by the phosphor may include the following attributes:

- Its excitation spectrum must include bands that overlap the exciting emission from the blue LED.
- Its emission should be in the desired part of the visible spectrum.
- It should have high quantum efficiency when emitting light of the desired wavelength.
- It needs to have its grain size optimized to reduce/eliminate scattering.
- It should be chemically stable over its entire operating temperature range and over the lifespan of the pcLED. This might mean that if the host lattice of the phosphor is a metal sulfide or oxysulfide then it has to be protected with an oxide layer. Ideally it will be stable to at least 200 °C.
- Its emission intensity in the visible should not be drastically temperature dependent over the operating temperature range. Many LEDs that may have the phosphor applied in the LED package in front of the emitting surface reach temperatures of 125 °C or more, and the phosphor must be an efficient emitter at such temperatures. Ideally it will be stable to at least 200 °C.
- It should have a good particle morphology and narrow particle size distribution for easy incorporation into silicones or epoxy resins.
- For many of these properties, it is necessary to optimize the phosphor composition and crystallinity.
- Low production cost would also be useful.
- IP protection can also be desirable when commercialization is under consideration.

For white light a choice of the wavelength of the blue exciting LED needs to be made. Currently the maximum efficiency reported is at 410 nm (Nichia Chemical Company conference presentation at the International Workshop on Nitride Semiconductors 2004, Pittsburgh, USA). However, depending on the phosphor(s) used, other blue wavelengths may be preferable to achieve a desired CRI and color temperature.

The choice of the wavelength of the blue emission may ultimately be dictated by the wavelength range of the excitation spectra of the phosphor converter(s), or may be a compromise between this and the emission wavelengths of the most efficient exciting blue LEDs available. Therefore, it should be stated that not all the light emitting phosphors that can be excited by near UV or blue radiation will be excited with equal probability by all wavelengths of the exciting light (see below).

3.3.3 Commonly used activators in color conversion phosphors

Much of the research on phosphors for color converting LEDs has concentrated on the use of two activators, Ce^{3+} and Eu^{2+} , because of a number of the attributes of their emission properties.

Advantages of Ce^{3+} and Eu^{2+} activated phosphors include:

- These ions emit visible light when they undergo $d \rightarrow f$ rather than $f \rightarrow f$ electronic transitions.
- The emissions arising from $d \rightarrow f$ electronic transitions are generally more intense than those originating from $f \rightarrow f$ transitions, because the former are orbitally allowed and consequently have higher oscillator strengths than the latter, which are orbitally forbidden.
- The emissions arising from $d \rightarrow f$ electronic transitions are broader than those originating from $f \rightarrow f$ transitions, because the d -orbital is more sensitive to the environment of the ion than the f -orbital and the local environment of the ion changes during metal-ligand vibrations.
- The emissions due to $d \rightarrow f$ electronic transitions are more wavelength tuneable than those originating from $f \rightarrow f$ transitions because, as mentioned above, the d -orbital is more sensitive to its environment than the f -orbital. Thus, wavelength tuneability of the emission can be achieved by altering the crystal field splitting of the d -orbitals of the activator ion by changing the host lattice of the phosphor.

3.3.4 Strategies for generating white light from LEDs

There are a number of different approaches which can be used for generating white light from LEDs or a combination of color conversion phosphors and LEDs (pcLEDs). The approach that will be used will depend largely on the application, because there is a trade-off between the color rendering index (CRI) and luminous efficacy. Four different strategies for obtaining white light are given below, along with an assessment of their relative CRI vs. luminous efficacy attributes:

- a) A combination of red, green and blue LEDs. This approach has been discussed already in Section 3.2 above, where it was mentioned that drawbacks arise from differential ageing of the LEDs, poor CRI of the white light (due to narrow wavelength ranges of emissions) and the ‘green window’. On the other hand, the luminous efficacy is relatively high, because of the absence of color conversion phosphors and the quantum deficit that they necessarily introduce.
- b) A pcLED consisting of a blue LED and two color conversion phosphors, which emit in the green and red regions of the visible spectrum. This approach uses only a single LED so there is no problem with differential ageing of LEDs. Furthermore, the green and red emitting phosphors can have broad emission wavelength ranges, so the CRI is higher than for (a), above. There is obviously a quantum deficit involved in converting the blue LED emission to green and red by means of the phosphors, however, so the overall luminous efficacy of the pcLED is lower than for (a).

- c) A pcLED consisting of a blue LED and a single color conversion phosphor, which emits in the yellow-orange region. This approach uses only a single phosphor, so the phosphor emission needs to cover a broad wavelength range in the orange-yellow region in order to achieve a CRI in the 70–80% range. Nevertheless, there are wavelength regions in the red and between the LED and phosphor emissions where there is little or no light output, so a maximum CRI of only around 80% is achievable for a pcLED with a single phosphor. Although the CRI is less than what can be obtained for (b) above, the luminous efficacy can be higher because the quantum deficit is lower than for (b), where there is a large loss in energy in converting blue light into red. Consequently, pcLEDs with a single phosphor do not have sufficiently high CRIs for them to replace incandescent bulbs or fluorescent lights for general white light applications, but they are used instead for niche applications, e.g. for car headlamps.
- d) A pcLED consisting of a UV LED and three phosphors, which emit in the blue, green and red regions. This ‘color by neutral’ approach can achieve a higher CRI than (a)–(c) above, because the blue, green and red phosphor emissions can cover the whole visible region. However, there is a trade-off in luminous efficacy, which is lower than for (a)–(c) above, on account of the high quantum deficit in converting the UV radiation into visible light.

3.3.5 Outstanding problems with color conversion phosphors for LEDs

Although the general approach of using color conversion phosphors in combination with LEDs has been widely adopted, there are still outstanding problems with the phosphors that need to be addressed:

- The excitation spectrum of the color conversion phosphor needs to overlap the emission wavelength range of the pump LED. At present there are a number of phosphors that can be excited in the blue/violet and emit efficiently at longer wavelengths in the visible (see Section 3.4 below).
- The particle sizes of the phosphors need to be optimized in order to reduce light loss by scattering.
- The light that is emitted back towards the LED chip needs to be re-directed in the forward direction in order to maximize the light output from the pcLED.
- The LED emission is angle dependent, whereas the phosphor has an emission that is close to Lambertian. Thus phosphor coatings need to be deposited on the LED chip that minimize any angle dependent shift of the color point of the pcLED.
- The phosphor needs to be deposited homogeneously on the LED chip or other remote substrate in a controlled way.
- The binder in which the phosphor is suspended should not be photo-degraded by the LED light. Many epoxy resins yellow over time when illuminated by blue LED light and, even more so, by UV LED light. Silicone type binders are often used in preference due to their better photo-stability.

- YAG:Ce is commonly used for pcLEDs with a single phosphor, but it has a high color correlated temperature (CCT); other efficient, broad-band emitting phosphors with lower CCTs are required for white light pcLEDs that have a ‘warmer’ white in order to satisfy consumer preferences.

It is now useful to review some individual phosphors, and discuss their properties.

3.4 SURVEY OF THE SYNTHESIS AND PROPERTIES OF SOME CURRENTLY AVAILABLE COLOR CONVERSION PHOSPHORS

3.4.1 Phosphor synthesis

The synthesis of inorganic phosphors has been the subject of intensive research for well over 80 years. Much of the work has been carried out in industry and not in the public domain. Thus, literature on the manufacturing methods for industrial phosphors tend to be confined to specialist books rather than research journals, and the reader is referred to the well-known texts by Ropp [26, 27] that contain preparative details. Almost all were synthesized by solid-state reactions between very pure inorganic compounds at high temperature. It is impossible here to discuss every aspect of synthesis from its inception to the present day, so priority has been given to discoveries and developments appearing in the last five years to new phosphors developed specifically for use as color converters for LEDs. The structures of most of the host lattices used for phosphors have been described and correlated by Wells [28] and others [29], and the host lattice will, of course, determine the coordination environment of the dopant guest, which can influence its emission behavior.

The general properties of luminescent materials have been discussed in several texts [26, 27, 30, 31].

3.4.2 Metal oxide-based phosphors

3.4.2.1 Yttrium aluminium garnet activated by trivalent cerium (YAG:Ce³⁺ or Y₃Al₅O₁₂:Ce³⁺)

The first mention of this phosphor was in 1967 as a cathodoluminescent phosphor, though in the same paper its photoluminescent properties are described [32]. The use of this phosphor and many others for fluorescent lighting was reviewed in 1987 [33]. Methods of making this phosphor have been well documented elsewhere [26, 27].

This phosphor is referred to in many patents for use as a color converter using blue LED excitation and emitting yellow light, which when combined with more blue light from the LED gives a passable white light. Although many are referenced here, no attempt has been made to find them all [34–45].

The excitation spectrum of YAG:Ce³⁺ has its peak at around 470 nm (Figure 3.4). In the same figure the emission spectrum is shown to be asymmetrical as it is made up of two transitions $5D \rightarrow {}^2F_{5/2}$ and $5D \rightarrow {}^2F_{7/2}$; both the asymmetry and the position of this band varies, depending on the Ce³⁺ concentration, though the center of the peak is usually around

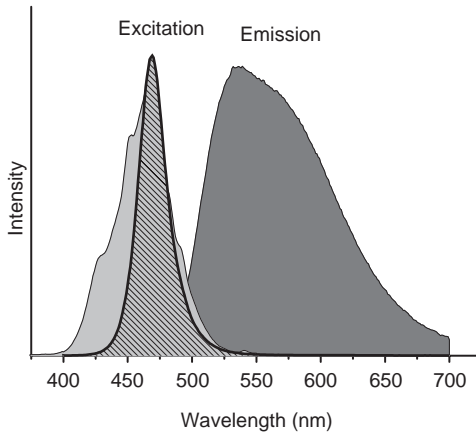


Figure 3.4 The excitation and emission spectra of $\text{YAG}:\text{Ce}^{3+}$. The hatched peak depicts an exciting emission from a blue LED emitting at 470 nm. The match of the exciting blue radiation to the excitation band of the phosphor is excellent

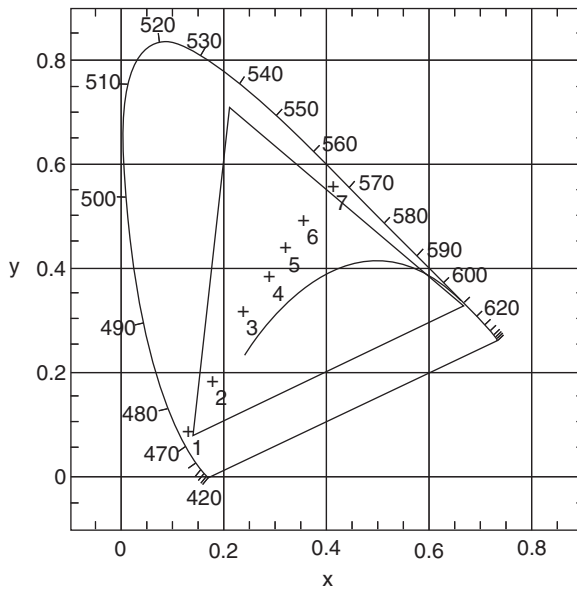


Figure 3.5 CIE chromaticity diagram showing the position of the emission of $\text{YAG}:\text{Ce}^{3+}$ phosphor (point 7) and the emission of a blue 470 nm LED (point 1). The other points 2 to 6 are explained in the text. The continuous curved line in the center of the diagram is known as the Planckian, which is the locus of blackbody emitters

550 nm. Also, Figure 3.4 shows the optimum position of an exciting blue emission (as from a blue LED emitting at 470 nm) [46–48].

In Figure 3.5 the position of the color coordinates of $\text{YAG}:\text{Ce}^{3+}$ are shown at point 7, whereas those of the exciting blue LED light are shown at point 1. Points 2 to 6 are gener-

ated by putting layers of $\text{YAG}:\text{Ce}^{3+}$ phosphor particles on glass and exciting them with blue light so some blue light also comes through the phosphor layer along with the yellow emission. Point 2 is created by one layer of $\text{YAG}:\text{Ce}^{3+}$ particles, point 3 is created by two layers and so on to point 6, which contains five layers [46–48].

Clearly, in Figure 3.5, points 3 and 4 are close to the white color point ($x = 0.33$, $y = 0.33$) and a line between these points represents the best ‘whites’ that can be generated from a blue LED emitting at 470 nm and $\text{YAG}:\text{Ce}^{3+}$ phosphor particles. To improve these whites it is necessary to chemically modify the $\text{YAG}:\text{Ce}^{3+}$ phosphor particles. The line between points 1 and 7 is known as the mixing line for varying phosphor thickness and blue LED light [46–48].

3.4.2.2 Yttrium aluminium garnet co-activated by trivalent cerium and praseodymium ($\text{YAG}:\text{Ce}^{3+},\text{Pr}^{3+}$ or $\text{Y}_3\text{Al}_5\text{O}_{12}:\text{Ce}^{3+},\text{Pr}^{3+}$)

There are several ways this can be done, as shown in Figure 3.6 [47]. It can be seen that by adding Pr^{3+} cations to $\text{YAG}:\text{Ce}^{3+}$, an emission peak around 620 nm (in the red) is added to the emission spectrum of $\text{YAG}:\text{Ce}^{3+}$. Also by adding some Gd^{3+} to replace some Y^{3+} , this moves the main $\text{YAG}:\text{Ce}^{3+}$ emission towards the red and as seen in the same figure, both these effects can be engineered in the same phosphor particles [47–49].

The color coordinates generated by the emission from the phosphors shown in Figure 3.6 are shown in the CIE chromaticity diagram in Figure 3.7 [49].

The color coordinates generated by the emission from the phosphors shown in Figure 3.6 are also shown in the CIE chromaticity diagram in Figure 3.7. The solid line crossing the Planckian from point 3 to point 4 (in Figure 3.7) shows how a real white can now be generated from the blue LED and the $(\text{Y,Gd})_3\text{Al}_5\text{O}_{12}:\text{Ce}^{3+},\text{Pr}^{3+}$ phosphor [49]. The particular white can be described by its color coordinates or by its color temperature.

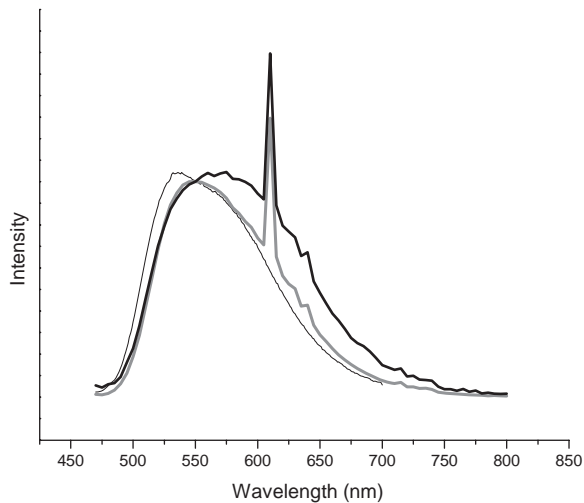


Figure 3.6 The Emission spectra of $\text{YAG}:\text{Ce}^{3+}$ (thin black line), $\text{Y}_3\text{Al}_5\text{O}_{12}:\text{Ce}^{3+},\text{Pr}^{3+}$ (gray line) and $(\text{Y,Gd})_3\text{Al}_5\text{O}_{12}:\text{Ce}^{3+},\text{Pr}^{3+}$ (thick black line) [49]

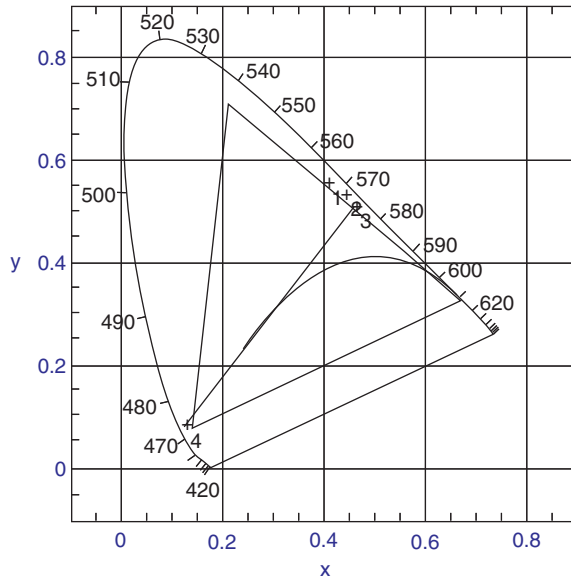


Figure 3.7 CIE color chromaticity diagram showing the position of the emission of YAG:Ce³⁺ phosphor (point 1), the emission of Y₃Al₅O₁₂:Ce³⁺,Pr³⁺ (point 2) and of (Y,Gd)₃Al₅O₁₂:Ce³⁺,Pr³⁺ (point 3). The emission of a blue 470 nm LED is also shown (point 4). The solid line crossing the Planckian from point 3 to point 4 shows how a real white can now be generated from the blue LED and the (Y, Gd)₃Al₅O₁₂:Ce³⁺,Pr³⁺ phosphor [49]

An empirical rule has been put forward for Ce³⁺ luminescence in Y₃Al₅O₁₂:Ce³⁺:

‘Increasing the diameter of the ion on the dodecahedral (Y³⁺) site increases the crystal field splitting, while increasing the diameter on the octahedral (Al³⁺) site has the reverse effect’ [50,51].

Thus on the dodecahedral site there is a wavelength shift on going from 550 nm for Y³⁺ to 585 nm for the larger Gd³⁺ ion, and a shift from 550 nm for Y³⁺ to 510 nm for the smaller Lu³⁺ ion. This is apparent for the (Y,Gd)₃Al₅O₁₂:Ce³⁺,Pr³⁺ in Figure 3.6.

In contrast, when the cation is located on the octahedral site, there is a wavelength shift from 550 nm for Al³⁺ to 505 nm for the larger Ga³⁺ ion. However, substituting Ga³⁺ for Al³⁺ reduces the emission intensity.

The basic YAG:Ce lattice can accommodate more than 60 different elements so many different combinations are possible. In order to consider some of the issues with blue LEDs exciting phosphors such as YAG:Ce³⁺, it is worth considering the calculation and measurement of some luminous efficacies.

Theoretical limit of luminous efficacies of YAG:Ce phosphors The luminous efficacy, η_{LE} , for the conversion by the YAG:Ce phosphor of blue (470 nm) LED light into yellow emission is given by

$$\eta_{LE} = \eta_{LO} \cdot \eta_{QD} \cdot \eta_{QE} \cdot \eta_{SC} \quad 52,53$$

where η_{LO} is the lumen equivalent

η_{QD} is the quantum deficit

η_{QE} is the quantum efficiency

η_{SC} is the screening efficiency.

The quantum deficit is ca. 0.80 and the quantum efficiency is ca. 0.95. Thus:

$$\eta_{LE} = 456 \times 0.80 \times 0.95 \times \eta_{SC} = 347 \cdot \eta_{SC} \text{ lm/W}$$

The luminous efficacies of YAG:Ce phosphor powders under 470 nm and 430 nm excitation were measured as a function of Ce concentration and also of firing temperature.

Clearly, the luminous efficacies for YAG:Ce phosphors are Ce activator concentration dependent (Figure 3.8).

Plotting the Ce activator concentration for YAG:Ce phosphors vs. luminous efficacy (see Figure 3.9 below, in which 470 and 430 nm excitations are compared), it is apparent that the luminous efficacies are also wavelength dependent [52–55]. The lower values for the 430 nm excitation are mainly due to the quantum deficit caused by the wavelength difference between the excitation and emission wavelengths.

Hence for YAG:Ce phosphors the luminous efficacy values are concentration and excitation wavelength dependent [52–54]

The luminous efficacies also reach maximum values in the YAG:Ce phosphors at a firing temperature of around 1500 °C, as seen in Figure 3.10 (where they are plotted for two different excitation wavelengths).

At lower concentrations of Ce, the luminous efficacy approaches the theoretical value (Figure 3.11). However, phosphors made at these lower concentrations do not perform well for two reasons. The first is that more phosphor is necessary to convert the correct proportion of the incoming exciting light; and the second is that the low concentrations reflect more of the exciting radiation, as is apparent from Figure 3.12 [52, 55].

Less blue light is absorbed for a Ce concentration of 0.1 mol%. η_{LE} is higher for this Ce concentration since:

$$\eta_{LE} = \text{no. lumens/power absorbed}$$

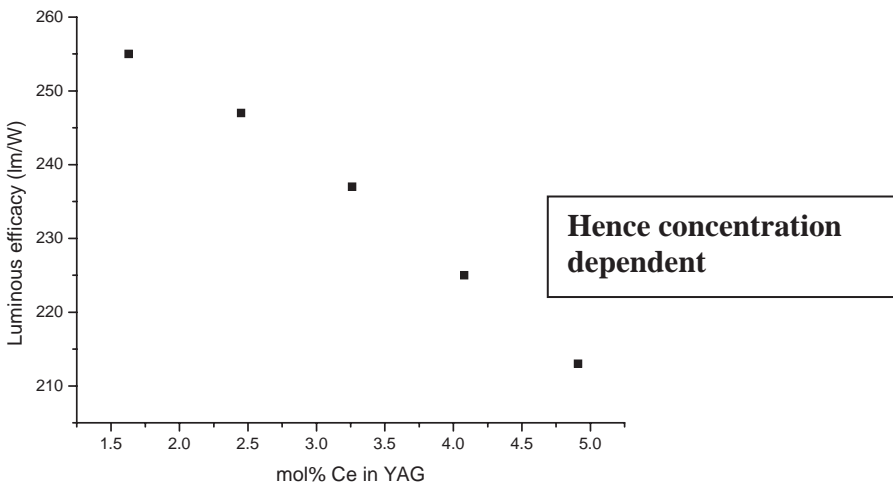


Figure 3.8 Plot of Ce activator concentration in YAG:Ce vs. luminous efficacy (470 nm excitation)

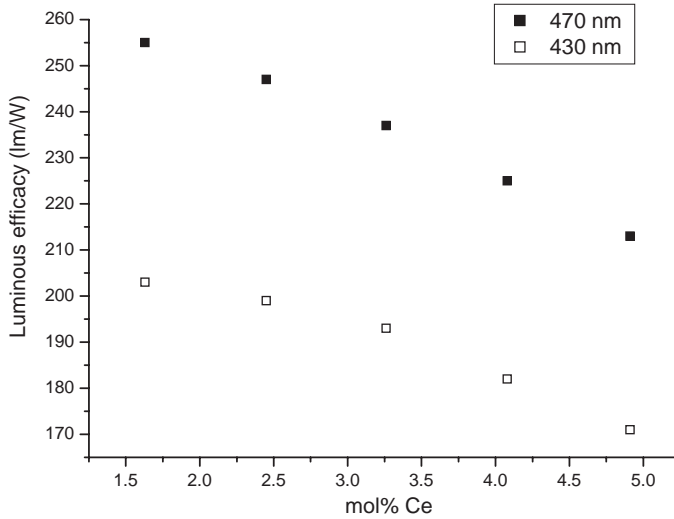


Figure 3.9 Plot of Ce activator concentration in YAG:Ce vs. luminous efficacy (comparison of 470 and 430 nm excitation)

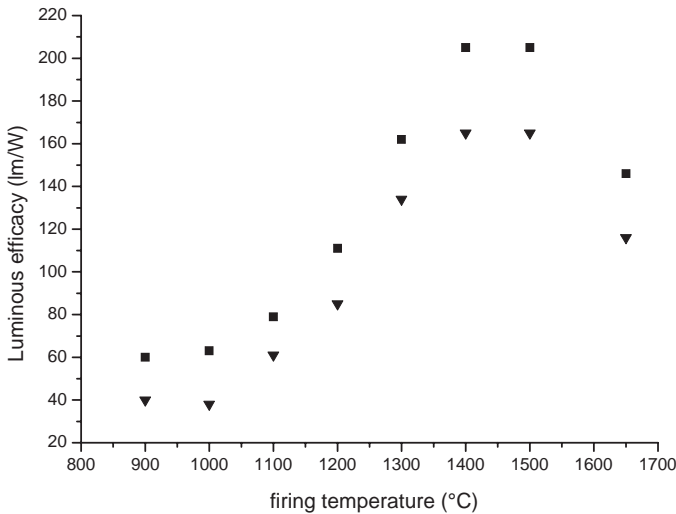


Figure 3.10 Plot of firing temperature vs. luminous efficacy of YAG:Ce phosphors (▼ = 430 nm and ■ = 470 nm excitation)

Table 3.1 gives the luminous efficacies and quantum efficiencies for the low concentration Ce YAG:Ce phosphors, compared to a commercial sample [52]. The values for the latter are similar to the values we obtained for 1.5 and 2.5 mol% Ce, as seen in Figure 3.11.

Color points and luminous efficacies ($\lambda_{\text{exc}} = 470 \text{ nm}$) of YAG:Ce and YAG:Ce,Pr phosphors (Pr concentration in range 1–5 mol%) are plotted in Figure 3.13. η_{LE} values of the YAG:Ce,Pr phosphors are very poor [52].

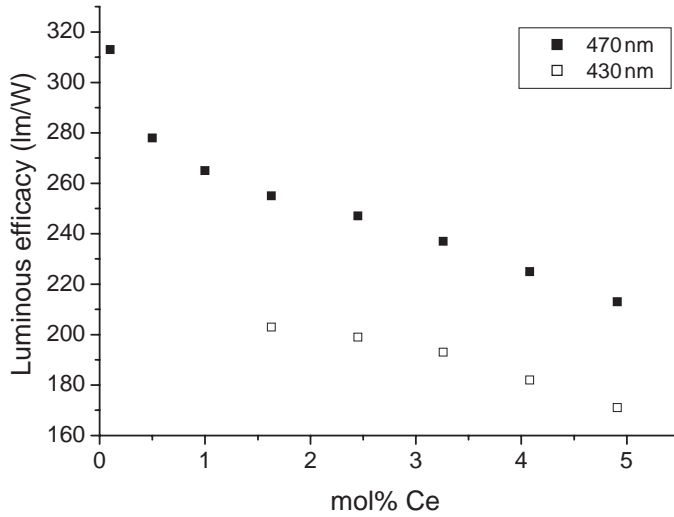


Figure 3.11 Plot of Ce activator concentration in YAG:Ce phosphors vs. luminous efficacy (extended down to lower Ce concentrations)

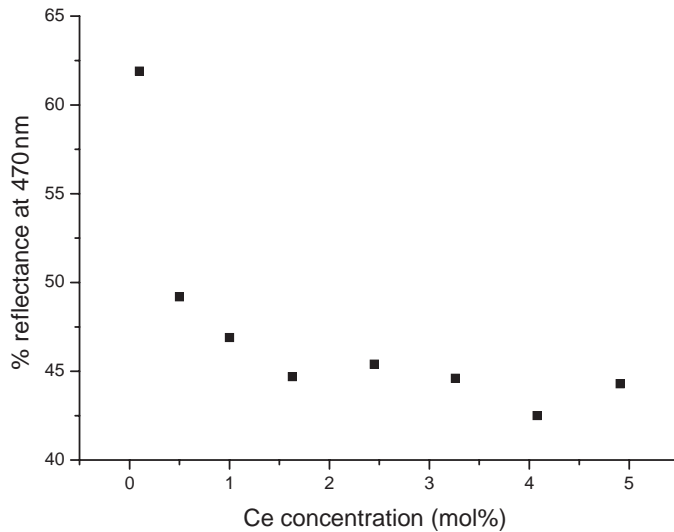


Figure 3.12 Percentage reflectance of YAG:Ce at 470nm as a function of mol% Ce in YAG:Ce phosphors

This is probably due to one of two reasons:

1. The Pr takes the exciting light from the LED preferentially (instead of the Ce) and downconverts it less efficiently than the Ce; or
2. The Pr uses the Ce emission as excitation and does not emit it efficiently [52].

Table 3.1 Luminous efficacies (LE) and quantum efficiencies (QE) for in-house synthesized YAG:Ce phosphors having different Ce concentrations, along with the values for a commercial sample

Ce conc. (mol%)*	LE (470 nm exc.) (lm/W)	QE (470 nm exc.) (%)
0.1	313	78
0.5	278	69
1.0	265	66
Commercial sample 470 nm	242	62

*The YAG:Ce phosphors were made via a solid state route and fired at 1500 °C

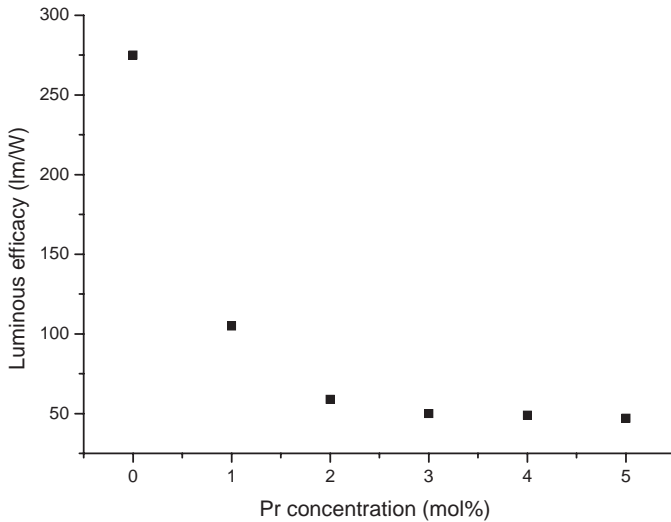


Figure 3.13 Plot of Pr co-activator concentration in YAG:Ce,Pr phosphors vs. luminous efficacy. The Ce concentration was 2.4 mol% in each case

Hence adding Pr as an additional activator in $Y_3Al_5O_{12}:Ce^{3+}$ to make $Y_3Al_5O_{12}:Ce^{3+},Pr^{3+}$ is not a sensible path to follow as the luminous efficacy falls dramatically although the CIE coordinates of the white may be better.

3.4.2.3 Yttrium/Gadolinium aluminium garnet activated by trivalent cerium (YAG:Ce³⁺ or Y₃Al₅O₁₂:Ce³⁺)

The alternate approach of preparing (Y_xGd_{1-x})AG:Ce (0 ≤ x ≤ 1) phosphors is also problematic [52]. A plot of luminous flux vs. wavelength ($\lambda_{exc} = 470$ nm) for the (Y_xGd_{1-x})AG:Ce (0 ≤ x ≤ 1) phosphors is shown in Figure 3.14.

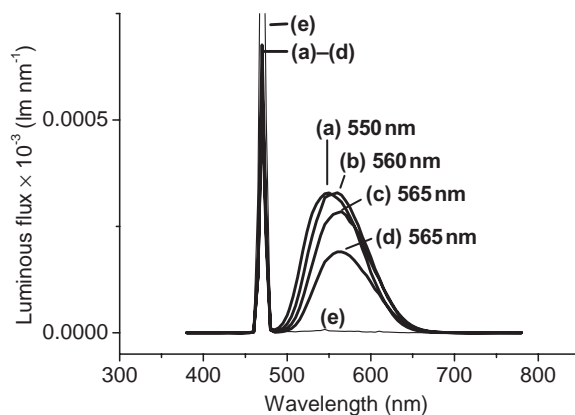


Figure 3.14 Plots of luminous flux vs. wavelength for $(Y_xGd_{1-x})AG:Ce$ phosphors with x equal to (a) 1.00, (b) 0.75, (c) 0.50, (d) 0.25 and (e) 0. The Ce concentration was 2.45 mol% and the excitation was centered on a wavelength of 470 nm (seen in the figure due to partial reflection by the phosphors)

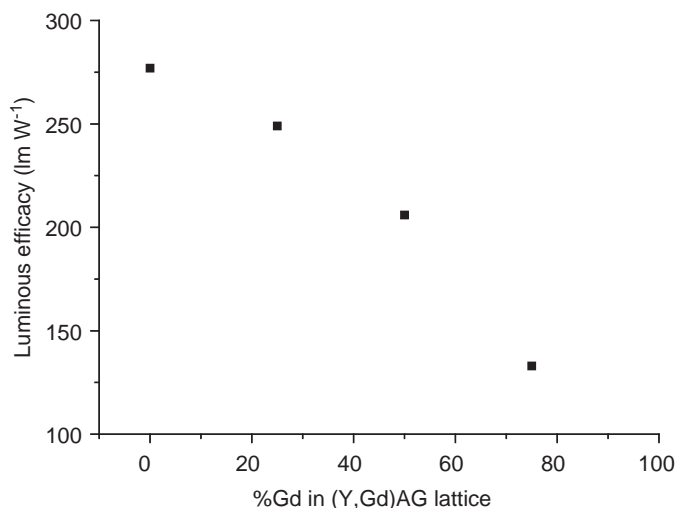


Figure 3.15 Luminous efficacies ($\lambda_{exc} = 470$ nm) of $(Y_xGd_{1-x})AG:Ce$ ($0.25 \leq x \leq 1$) phosphors

The emission band shifts to the red on substituting Y for Gd and the emission intensity decreases for $x = 0.50$ and $x = 0.75$. No emission is observed from $GdAG:Ce$ under 470 nm excitation (Figures 3.14 and 3.15). To investigate why the latter material does not emit, we examined the excitation bands of these phosphors [52].

From the Figure 3.16 it is apparent that all the $(Y_xGd_{1-x})AG:Ce$ ($0.25 \leq x \leq 1$) phosphors have an excitation band centered on ca. 470 nm, which does not extend below ca. 400 nm [52]. It is evident that the drop in luminous efficacy, as Gd is progressively substituted into the lattice, does not affect the excitation spectra. The most likely explanation is that as Gd is added the energy gap between the valence band and conduction band decreases so that

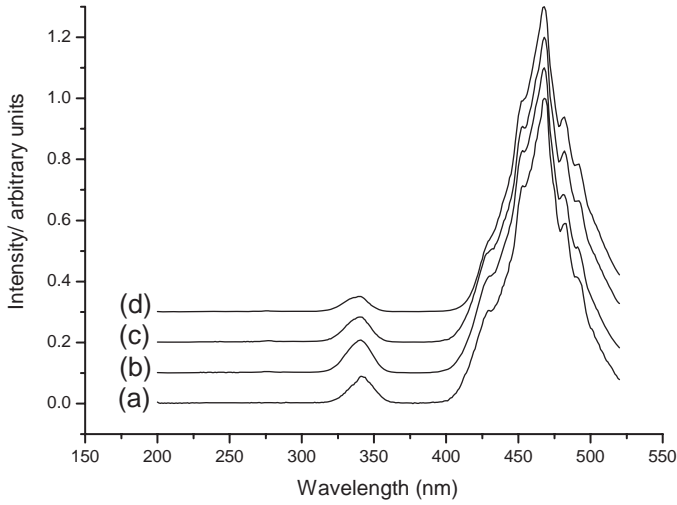


Figure 3.16 Observed Excitation Spectra of $(Y_xGd_{1-x})AG:Ce$ ($0.25 \leq x \leq 1$) phosphors when monitoring emission at 550 nm. (a) $x = 1.00$, (b) $x = 0.75$, (c) $x = 0.50$ and (d) $x = 0.25$

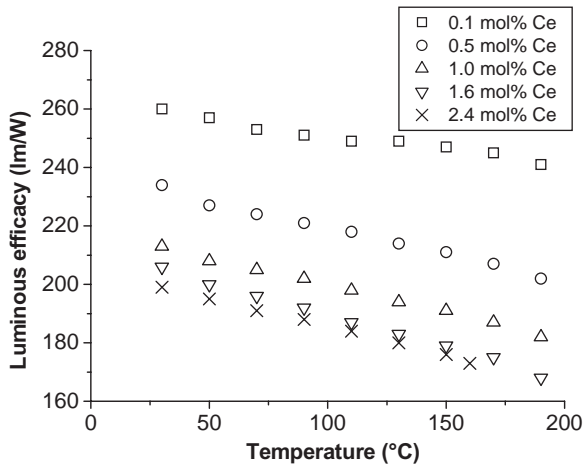


Figure 3.17 Plot of luminous efficacy vs. temperature for YAG:Ce phosphors (Ce = 0.1 to 2.4 mol %)

for the pure GdAG:Ce the excitation promotes the electron from the Ce directly into the conduction band, and this relaxes nonradiatively [52].

The temperature dependence of YAG:Ce phosphors prepared by a solid state mixing method are presented in Figure 3.17. It is apparent that there is a drop in efficacy with temperature that is roughly parallel for the YAG phosphors presented by this method for all the Ce concentrations studied. In all but the lowest Ce concentration the effect of a rise of 160 °C is a drop in efficacy of around 15%. This averages to a reduction in efficacy of ca. 1% with every rise of 10 °C [52].

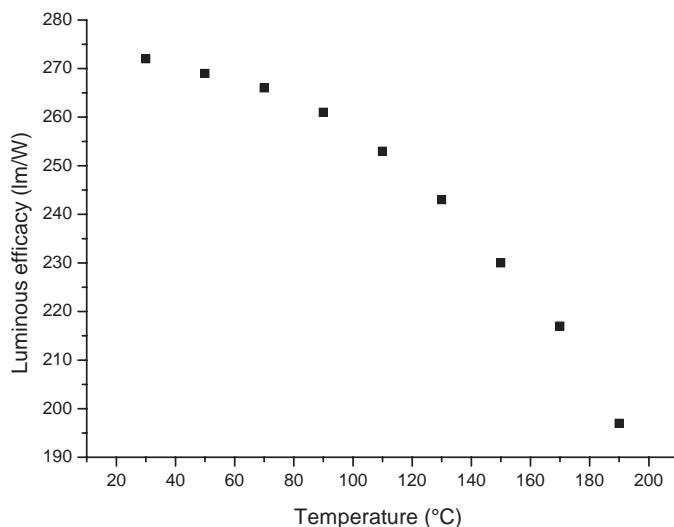


Figure 3.18 Plot of luminous efficacy vs. temperature for YAG:Ce phosphor (Ce 5.0 mol %)

However, if the YAG:Ce is prepared in other ways, such as being fired in a reducing atmosphere, then the temperature dependence can be different, as seen in Figure 3.18 [52].

In this case the YAG:Ce, which starts with a significantly higher efficacy, drops by 38% in the temperature range of 30 to 190 °C. This is around a 2.5% drop in efficacy for every 10 °C rise, although the drop is less (1.5% for each 10 °C rise) in the range 30 to 100 °C. These temperature dependent efficacies are important as LED junction temperatures and LED arrays can become very hot when in operation and phosphors that have poor thermal properties will not be useful as LED color converters [52].

So, in summary, garnet phosphors based on YAG:Ce are currently the best color converters for combining with blue LEDs to generate white light, providing there is no requirement for a high color rendering index.. The parent YAG:Ce is a very easily substituted lattice permitting wide variation in its elemental makeup.

3.4.2.4 Silicate garnets and related phosphors

$\text{Ca}_3\text{Sc}_2\text{Si}_3\text{O}_{12}:\text{Ce}$ is excited at 446nm and emits a broad band similar to that of YAG:Ce around 570nm [56]. A related phosphor system is $\text{BaY}_2\text{SiAl}_4\text{O}_{12}:\text{Ce}$. In a patent [57], a wide range of substitution is claimed based on the host lattice general formula $\text{MLn}_2\text{QR}_4\text{O}_{12}$, where:

- M is at least one element selected from the group consisting of Mg, Ca, Sr and Ba;
- Ln is at least one rare earth element selected from the group consisting of Sc, Y, La, Ce, Pr, Nd, Sm, Eu, Gd, Tb, Dy, Ho, Er, Tm, Yb and Lu;
- Q is at least one element selected from the group consisting of Si, Ge, Sn and Pb; and

- R is at least one element selected from the group consisting of B, Al, Ga, In and Tl [57].

The luminescence of the vanadate garnet, $\text{Ca}_2\text{NaMg}_2\text{V}_3\text{O}_{12}:\text{Eu}^{3+}$ has been evaluated and discussed as a potential ultraviolet light-emitting diode (UV-LED) phosphor [58]. This single phosphor has been claimed to be capable of converting the ultraviolet emission of a UV-LED into white light with good luminosity and color-rendering index. The luminescence of this material at elevated temperatures is of interest, because the junction temperatures of typical LEDs can be greater than 100 °C. Indeed, it has been reported [58] that there is significant thermal quenching of this phosphor and an emission color shift at temperatures greater than 100 °C. This has been explained as energy migration and transfer to non-radiative traps and Eu^{3+} within the host lattice [58].

3.4.2.5 $(\text{Y}_{2-x-y}\text{Eu}_x\text{Bi}_y)\text{O}_3$

Red phosphors based on $(\text{Y}_{2-x}\text{Eu}_x)\text{O}_3$ have been developed where the Bi is used to change the excitation spectrum by introducing absorption bands in the 340–370 nm region (due to the Bi $6s^2$ – $6s6p$ transition), which with the 4f-4f Eu^{3+} transition, gives a continuous excitation band extending between 340 and 410 nm [59]. The red emission is due mainly to energy transfer from Bi^{3+} to Eu^{3+} . Compositions that were studied include $\text{Y}_{1.84}\text{Eu}_{0.16}\text{O}_3$, $\text{Y}_{1.82}\text{Eu}_{0.16}\text{Bi}_{0.02}\text{O}_3$, $\text{Y}_{1.78}\text{Eu}_{0.16}\text{Bi}_{0.06}\text{O}_3$ and $\text{Y}_{1.72}\text{Eu}_{0.16}\text{Bi}_{0.12}\text{O}_3$, with the latter giving the best red emission [59].

3.4.2.6 $\text{Na}_2\text{Gd}_2\text{B}_2\text{O}_7:\text{Ce}^{3+},\text{Tb}^{3+}$

This is a new green emitting phosphor that transfers energy from Ce^{3+} to Tb^{3+} prior to emission. The Ce^{3+} is thermally quenched above 100 °C [60].

3.4.2.7 $\text{YCa}_3\text{M}_3\text{B}_4\text{O}_{15}:\text{Eu}^{3+}$

The photoluminescence properties of the red-emitting $\text{YCa}_3\text{M}_3\text{B}_4\text{O}_{15}:\text{Eu}^{3+}$ ($\text{M} = \text{Al}$ or Ga) phosphors under UV (395 nm) irradiation have been reported. A strong emission at 622 nm and several weaker peaks near this emission were observed [61]. The emission intensity increased with increasing Eu^{3+} content up to $x = 0.75$ in $\text{Y}_{1-x}\text{Eu}_x\text{Ca}_3\text{M}_3\text{B}_4\text{O}_{15}$. The authors claim these phosphors are better reds than $\text{CaS}:\text{Eu}^{3+}$ for LED applications [61].

3.4.2.8 Alkaline earth metal silicates $(\text{Ba}_{1-x-y}\text{Sr}_x\text{Ca}_y)\text{SiO}_4:\text{Eu}^{2+}$

Barry [62] has reported that the incorporation of Eu^{2+} in the compounds $\text{Ca}_3\text{MgSi}_2\text{O}_8$, $\text{Sr}_3\text{MgSi}_2\text{O}_8$, and $\text{Ba}_3\text{MgSi}_2\text{O}_8$ produces phosphors of high luminescence yield. The peak of the emission band occurs at progressively shorter wavelength and narrows as the radius of the major alkaline earth ion (Ca, Sr or Ba) is increased. A 1200 °C isotherm on compositions

intermediate to $\text{Sr}_3\text{MgSi}_2\text{O}_8$ and $\text{Ba}_3\text{MgSi}_2\text{O}_8$ shows a complete series of crystalline solutions to exist at this temperature. Using an orthorhombic cell, the d-spacings of the (222) reflections vary continuously from 1.956 Å for $\text{Sr}_3\text{MgSi}_2\text{O}_8:\text{Eu}^{2+}$ to 2.012 Å for $\text{Ba}_3\text{MgSi}_2\text{O}_8:\text{Eu}^{2+}$. However, the emission spectra of these samples vary in a discontinuous manner. In general, broadening of spectral energy distributions is observed as compositions move into the ternary section. All the compositions prepared resulted in phosphors of relatively high efficiency [62]. Following on from this work, a complete series of solid solution, for example, in the $\text{Ba}_2\text{SiO}_4\text{--Sr}_2\text{SiO}_4$ system with a continuous shift of luminescent color from green ($\lambda_{\text{max}} = 505 \text{ nm}$) to nearly orange ($\lambda_{\text{max}} = 575 \text{ nm}$) for the europium doped materials, Starick *et al.* [63], reported interesting phosphors in the ternary $(\text{Ba}_{1-x-y}\text{Sr}_x\text{Ca}_y)\text{SiO}_4:\text{Eu}^{2+}$ system. In contrast to Barry's work [62], isothermal run for all prepared phosphors, they preferred an individual optimisation of the preparation conditions for every promising member of the series [62].

It was found that the luminescent properties of these phosphors strongly depend on the conditions of their synthesis. Critical factors for getting high product quality include:

- a careful selection of suitable raw materials (purity, reactivity);
- selection of good flux materials;
- control of the firing atmosphere (N_2/H_2);
- optimization of the heating and cooling regimes;
- the post-treatment.

Phosphors with high crystal perfection, a favorable particle size distribution and with improved luminescent efficiencies are claimed. Their excitation spectra are broad and cover from below 300 nm to 500 nm, while their broad-band emission spectra range from 525 nm green to 595 nm orange.

These alkaline earth metal silicates of the general formula $\text{M}_2\text{SiO}_4:\text{Eu}^{2+}$ (where M = Ba, Sr or Ca) are color tuneable (by suitable combinations of Ba, Sr and Ca) green to yellow phosphors. Quantum efficiencies of more than 90% are said to be feasible. They have narrow emission bands for green phosphors but they suffer from low quenching temperatures and are not stable at ambient temperatures [64–67].

White light-emitting phosphors with a nominal composition of $(\text{Sr}_{2.55}\text{Ba}_{0.4})\text{MgSi}_{1.7}\text{O}_8:\text{Eu}^{2+}$ that can be excited in the near-UV have been reported recently. Their emission spectra consist of two bands in the visible region (one a blue band at 460 nm and the other a yellow band at 575 nm); these are thought to originate from Eu^{2+} in both $\text{Sr}_3\text{MgSi}_2\text{O}_8$ and in Sr_2SiO_4 , respectively. A white LED was fabricated from combining this phosphor with a near-UV InGaN chip ($\lambda_{\text{em}} = 405 \text{ nm}$). The LED is claimed to manifest high CRI (>80), high color stability, very good color coordinates (CIE, $x = 0.34$, $y = 0.33$) and high luminous efficiency (14.31 lm/W) [68].

3.4.3 Metal sulfide-based phosphors

Metal sulfide type phosphors have been used as cathodoluminescent and electroluminescent phosphors since the 1930s [69, 70]. More modern methods of making these types of phos-

phosphors have aided their development for use as color converters for LEDs. These methods are based on precipitation of the precursor phosphor from solution, and are important for both metal sulfides and selenides [71–75].

There are two general methods. The first involves treatment of aqueous metal salts, with or without added dopant, with hydrazine hydrate and either sulfur or selenium. This method has been successfully employed to synthesize metal chalcogenide phosphors, such as ZnS:Ag, ZnSe, Zn(S,Se), CdS, ZnS:Cu, ZnS:Cu,Al,Au [73], (Zn,Cd)S:Cu and Zn(S,Se):Cu [71–73] and this method was also extended to the synthesis of ternary metal-sulfide phosphors, such as $\text{Sr}_{0.97}\text{Ga}_2\text{S}_4:\text{Eu}_{0.3}$, $\text{Sr}_{0.985}\text{Ga}_2\text{S}_4:\text{Ce}_{0.015}$, $\text{Zn}_{0.98}\text{Ga}_2\text{S}_4:\text{Mn}_{0.02}$, $\text{Ca}_{0.8}\text{Ga}_2\text{S}_4:\text{Eu}_{0.2}$ and $\text{Ba}_2\text{Zn}_{0.985}\text{S}_3:\text{Mn}_{0.015}$ [74]. The second method utilized the decomposition of thiourea dioxide in aqueous solution at elevated temperatures in the presence of metal acetates, and has been used to prepare ZnS phosphors [75]. The advantage of these new methods is that the elaborate techniques necessary for the removal of toxic gases or vapors (H_2S and CS_2) commonly in solid state reactions are no longer required [71].

3.4.3.1 MS:Eu²⁺ (M = alkaline earth metal)

The MS:Eu²⁺ (M = Alkaline earth metal) phosphors have been explored for their use with LEDs by a number of groups [76–80].

Mixed alkaline earth metal sulfide lattices have also been studied, for example, strontium calcium sulfide activated with divalent europium ($\text{Sr}_x\text{Ca}_{1-x}\text{S}:\text{Eu}$), which has been reported as a red-emitting phosphor for LED white light generation. The host lattice, a solid solution of alkaline earth metal sulfides, can take various values of x between 0 and 1 [76–79]. The emission wavelength is then adjustable in the range 635 nm, which is the pure SrS:Eu, and 655 nm, which correspond to the pure CaS:Eu. The phosphor can be efficiently excited with blue and green light (in the range from 400 to 580 nm).

The phosphors with the formulation $\text{Sr}_x\text{Ca}_{1-x}\text{S}:\text{Eu}$ have low photoluminescent efficiencies due to a thermalization process, and are therefore not useful for blue LED excitation. However, it has been reported that co-doping in $\text{Sr}_x\text{Ca}_{1-x}\text{S}:\text{Eu}$ with a halide ion increases the emission efficiency. These phosphors are synthesized as follows: the precursor of the phosphor, strontium calcium sulfate is precipitated out of a strong acid solution containing the constituent metal ions by neutralizing the solution with ammonium hydroxide [78].

Wet chemical preparation of precursors:



After pulverization and drying, it is then fired at 600 °C for 3 hours.

High temperature reduction:



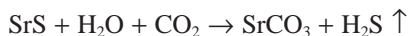
After grinding and milling, it is then fired in H_2S at 1000 °C for 6 hours.

Then activation with halide doping [78]:

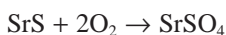


The quantum efficiency was measured to be 80%. The dependence of the emission intensity on the halide content was found to be linear in the range from 0.1 to 2%. The stability of this phosphor in a moist environment is not good. Hydrogen sulfide is liberated when the phosphor reacts with trace water. The emission efficiency is said to deteriorate to a very low level within a day [78].

Hydrolytic decomposition:



Oxidative decomposition:



To counter this, a SiO_2 coating was added to the phosphor particles to protect them from degrading in moist air [79].

As this phosphor can be excited by both blue and green light its use in a mixed system to generate white light with a green emitting phosphor and a blue emitting LED is not straightforward. Careful control of the amount of the red emitting phosphor present is important to balance whether the phosphor will be excited by blue and or green light. Alternatively the red phosphor could be covered with a blue or red filter to facilitate the balance of the system.

SrS:Eu sub-micrometre particles have been synthesized by a solvothermal method using ethylenediamine as the solvent. The reaction was carried out in a high-pressure autoclave at relatively low temperatures (<200 °C). A range of capping groups were explored and cubic crystallites in the size range 100 nm to 1000 nm were prepared [80].

3.4.3.2 Alkaline earth metal thiogallates, $\text{MGa}_2\text{S}_4:\text{Eu}^{2+}$ (M = alkaline earth metal)

Alkaline earth metal thiogallates were disclosed in the past as cathodoluminescent phosphors for display screens, and for use in electroluminescent displays [81–88]. The phosphors were synthesized by solid state reaction from alkaline earth sulfide, gallium sulfide and rare earth sulfide. These phosphors manifest good saturation properties, but their emission efficiency was said to be low (around 30% of other metal sulfide phosphors). In recent years, the photoluminescent properties of strontium thiogallate activated with divalent europium ($\text{SrGa}_2\text{S}_4:\text{Eu}^{2+}$) have been developed targeting high efficiency LED white light.

The $\text{SrGa}_2\text{S}_4:\text{Eu}^{2+}$ phosphor has a broad absorption band centered at 470 nm and stretches into the near ultraviolet, and it emits a green light peaking around 535 nm, as shown in Figures 3.19 and 3.20. Various solution preparation methods involving homogeneous precipitation followed by reduction firing have proved to significantly improve the emission efficiency [71–75].

One preparation uses a wet chemical reaction between a soluble strontium salt (SrSO_4) and europium nitrate in a strong acid medium [78]. This is followed by neutralization with ammonium hydroxide, which results in a suspension of strontium sulfate fine particles mixed with europium hydroxide:



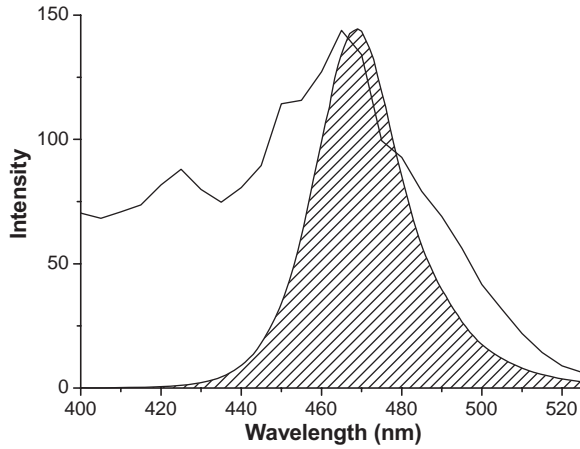


Figure 3.19 Excitation spectrum of $\text{SrGa}_2\text{S}_4:\text{Eu}^{2+}$ with 470 nm LED emission superimposed

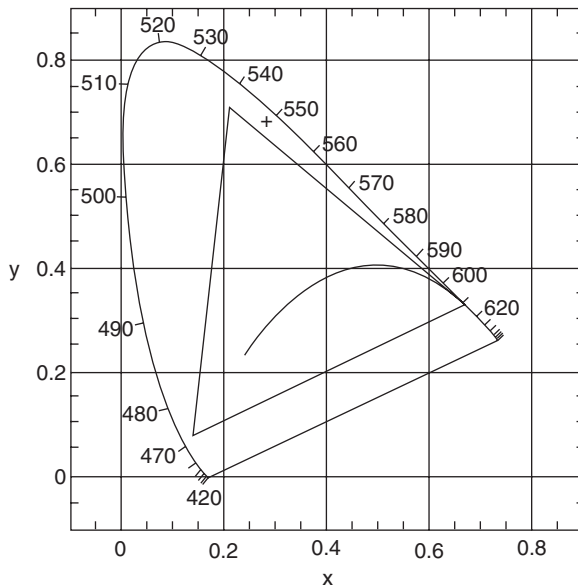


Figure 3.20 Chromaticity diagram showing CIE coordinates of $\text{SrGa}_2\text{S}_4:\text{Eu}^{2+}$

The adding of a Pr^{3+} is optional, depending on whether a red component is desired. The reaction temperature, the concentration of the soluble salt solution and additives such as an organic solvent, controls the particle size of the precipitates. Heating the equivalent acidic solution containing gallium makes a solution of an acid soluble gallium salt:



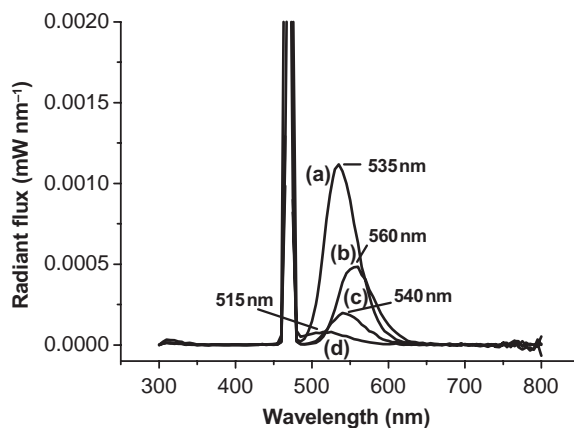
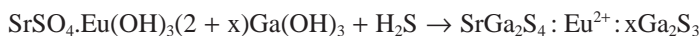


Figure 3.21 Photoluminescent emission spectra of thiogallate phosphors $\text{MGa}_2\text{S}_4:\text{Eu}^{2+}$: (a) $M = \text{Sr}$, (b) $M = \text{Ca}$, (c) $M = \text{Ba}$ and (d) $M = \text{Zn}$

Since gallium oxide is difficult to convert to an oxide-free sulfide with hydrogen sulfide, it is not used. The gallium nitrate solution is added to the resultant precipitates in a sufficient amount so as to produce an excess of gallium sulfide product. After combining these solutions and bringing the mixture to a neutral pH with ammonia, or by carrying out a precipitation of gallium using urea, a fine white powder is precipitated. This phosphor precursor is dried, ground and fired in hydrogen sulfide at about 800°C for approximately 5 hours.



A 2-step firing was reported, with the second firing being at 900°C . The resultant phosphor had an average particle size of $7\text{--}9\ \mu\text{m}$ and emits green light with a quantum efficiency of $80\text{--}97\%$. The parameter is $x = 0.7\text{--}7\%$. This high efficiency phosphor is achieved as a non-stoichiometric formulation, with gallium sulfide being a separate phase in the crystalline powder. It is claimed that if an organic solvent is added to the mixture during the precipitation, the average particle size will be smaller ($\sim 4\text{--}6\ \mu\text{m}$). However, the size control method needs careful control of the firing conditions (temperature and duration) [78].

The emission of $\text{MGa}_2\text{S}_4:\text{Eu}$ shifts to a longer wavelength when Sr is substituted by Ca and Ba, and to a shorter wavelength when Sr is substituted by Zn (Figure 3.21).

The temperature dependence of a $\text{SrGa}_2\text{S}_4:\text{Eu}$ phosphor prepared by a solid state mixing method is presented in Figure 3.22. It is apparent that there is a drop in luminous efficacy with temperature; the effect of a rise of 110°C is a drop of in efficacy of around 95%. This is about a 20.0% drop in luminous efficacy for the first 60°C rise, averaging to about 3.5% for every 10°C . However, above 90°C the luminous efficacy drops dramatically. So unlike $\text{YAG}:\text{Ce}$, this phosphor has very poor luminous efficacy above 100°C and such poor thermal properties will not make it a useful as an LED color converter above this temperature.

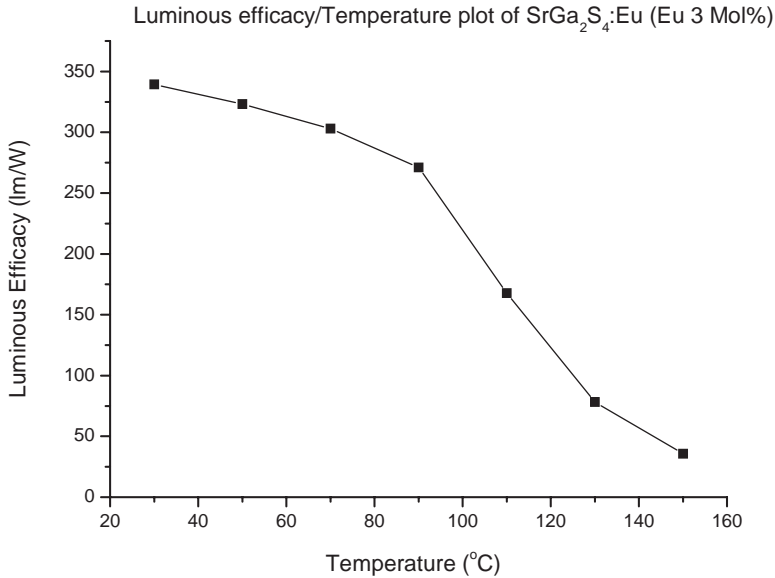


Figure 3.22 Plot of luminous efficacy vs. temperature for $\text{SrGa}_2\text{S}_4:\text{Eu}$ phosphor (Eu = 3 mol %)

Table 3.2 Various M-Si-N phases that have been studied as host lattices for color conversion phosphors

M-Si-N	[M = (Mg, Ca, Sr, Ba, Ln, Y)]
MSiN_2	M_4SiN_4
$\text{M}_5\text{Si}_2\text{N}_6$	MSi_3N_5 $\text{Y}_2\text{Si}_3\text{N}_6$ $\text{Y}_6\text{Si}_3\text{N}_{10}$
$\text{M}_2\text{Si}_4\text{N}_7$	$\text{M}_2\text{Si}_5\text{N}_8$
$\text{M}_3\text{Si}_6\text{N}_{11}$	$\text{M}_4\text{Si}_6\text{N}_{11}$ $\text{MSi}_7\text{N}_{10}$ $\text{SrSi}_7\text{N}_{10}$ $\text{M}_9\text{Si}_{11}\text{N}_{23}$

3.4.4 Metal nitrides

Some advantages of nitrides over oxides and sulfides are:

- higher charge density between activator and nitride ligands;
- large red-shift (allows phosphor to emit towards the red end of the spectrum);
- highly condensed anionic networks (this leads to the next three advantages);
- high density;
- good chemical stability;
- greater hardness (tough materials).

A number of M-Si-N phases have been studied [89] in the quest to synthesize metal nitride host lattices for phosphors, many of which are listed in Table 3.2.

3.4.4.1 $M_2Si_5N_8$ (M = Ca, Sr, Ba, Eu)

These phosphors have aroused much interest for their use with LEDs and several major players in the LED marketplace (such as Osram [90]) have discussed their merits at conferences [89–91].

Eu^{2+} -doped $M_2Si_5N_8$ (M = Ca, Sr, Ba) has been investigated. Although XRD analysis proved that Eu^{2+} -doped $Ca_2Si_5N_8$ forms a limited solid solution with a maximum solubility of about 7 mol% having a monoclinic lattice, the Eu^{2+} ion can be totally incorporated into $Sr_2Si_5N_8$ and $Ba_2Si_5N_8$, forming complete solid solutions with orthorhombic lattices. $M_2Si_5N_8:Eu^{2+}$ (M = Ca, Sr) manifests typical broad-band emission in the orange to red spectral range (600–680 nm), depending on the type of M and the europium concentration. $Ba_2Si_5N_8:Eu^{2+}$ emits in the yellow to red with maxima from 580 to 680 nm with increasing Eu^{2+} content. The long-wavelength excitation and emission was attributed to the effect of a high covalency and a large crystal-field splitting on the 5d band of Eu^{2+} in the nitrogen environment. With increasing Eu^{2+} concentration, the emission band manifests a red-shift for all $M_2Si_5N_8:Eu^{2+}$ compounds due to changing Stokes shift and the re-absorption by Eu^{2+} cations. The conversion (i.e. quantum) efficiency increases going from Ca to Ba and Sr under excitation at 465 nm. $Sr_2Si_5N_8:Eu^{2+}$ is reported to have a quantum efficiency of 75–80% and a thermal quenching of only a few percent at 150 °C; it is thought to be a highly promising red-emitting conversion phosphor for white-LED applications [91].

The crystal structures of $Eu_2Si_5N_8$ and $EuYbSi_4N_7$, which both contain highly condensed Si-N networks, have been reported [92].

Recently Philips [93] reported red-emitting phosphors based on the $M_2Si_5N_8$ (M = Ca, Sr, Ba, Eu) structures; $Eu_2Si_5N_8$ emits at 640 nm. However, they did not give the composition of their best phosphors, but suggested that their new nitride reds could be used in combination with $SrGa_2S_4:Eu^{2+}$ and a blue LED to give a CRI of 85–95 and a range of color temperatures between 2700 and 8000 °C.

3.4.4.2 $CaAlSiN_3:0.8\%Eu^{2+}$

Nitride phosphors in the system Ca_3N_2 -AlN- Si_3N_4 have been studied and a new red phosphor has been found, $CaAlSiN_3:0.8\%Eu^{2+}$. This was compared to an earlier red $Ca_2Si_5N_8:0.8\%Eu^{2+}$ and found to have superior high temperature performance [94]. The excitation spectrum of $CaAlSiN_3:0.8\%Eu^{2+}$ spans the range 300–600 nm and the emission spectrum is broad and centered at 650 nm [94, 95].

A new red phosphor, $CaAlSiN_3:Eu^{2+}$, has a broad excitation band extending from the UV region to 590 nm [96]. At the optimum Eu^{2+} concentration of 1.6 mol%, the quantum output is 7 times higher than for a conventional red phosphor, $La_2O_2S:Eu^{3+}$, under 405 nm excitation. The phosphor is also reported to be more efficient than $CaSiN_2:Eu^{2+}$ or $Ca_2Si_5N_8:Eu^{2+}$ at any excitation wavelength. One reason for the high room temperature efficiency is the small thermal quenching, which is probably related to the rigid network of $[SiN_4]$ and $[AlN_4]$ tetrahedra. The phosphor is also chemically stable and said to be a promising material for warm white light-emitting diodes [96]. Cheetam [89] has also reported routes for synthesizing $Ca_xAl_ySi_zN_3;Ce$ (yellow emitter (585 nm)), and $CaSiN_2:Ce$ (red emitter (630 nm)), but did not report performance data.

3.4.5 Alkaline earth metal oxo-nitrides

Alkaline earth metal oxo-nitrides are color tuneable (by suitable combinations of Ba, Sr and Ca) green to orange and red phosphors [64]. They have good thermal behavior, broad excitation bands and are efficient phosphors with QE values >90% thought to be feasible [64]. Their drawbacks are that they are difficult to manufacture, and the broad reds have low luminous efficacies [64].

The crystal structure of one of the possible host lattices ($\text{SrSiAl}_2\text{O}_3\text{N}_2$) has been reported [97] and from it a nine-coordinate Sr site is apparent, which could accommodate Eu^{2+} .

The α -SiAlON phosphor ($(\text{Sr,Ca})_{p/2}\text{Al}_{p+q}\text{Si}_{12-p-q}\text{O}_q\text{N}_{16-q}:\text{Eu}$) has a broad excitation band stretching from below 350 nm to above 490 nm and emits a broad band centered around 575 nm. When this phosphor is combined with a blue LED and a red nitride phosphor, it is said to give a warm white at 3200 K on the Planckian locus [56].

A Sialon-type phosphor has been reported in the form of a powder $(\text{Ca}_x\text{M}_y)(\text{Si,Al})_{12}(\text{O,N})_{16}$ (where M is at least one metal selected from the group consisting of Eu, Tb, Yb and Er, $0.05 < (x + y) < 0.3$, $0.02 < x < 0.27$ and $0.03 < y < 0.3$) and having a structure such that Ca sites are partially substituted by the other metal [98]. Another patent taken on this type of phosphor covers a Sialon-based phosphor having a high photoluminescent intensity, which can realize a high brightness LED, particularly a white LED using a blue LED as the light source, and production of the Sialon-based phosphor is also covered. The alpha-Sialon based phosphor of this invention has the formula $\text{Li}_x\text{M}_y\text{Ln}_z\text{Si}_{12-(m+n)}\text{Al}_{(m+n)}\text{O}_n\text{N}_{16-n}$, where M is at least one metal selected from Ca, Mg and Y, Ln is at least one lanthanide metal selected from Eu, Dy, Er, Tb, Yb and Ce, $x + ay + bz = m$ (assuming that the valence of metal M is a and the valence of lanthanide metal Ln is b), $0 < x \leq 0.8$, $0 < y$, $0 < z$, $0.3 \leq m < 4.5$ and $0 < n < 2.25$ [98].

3.5 MULTI-PHOSPHOR pcLEDs

Having looked at the most important phosphors used or potentially of use for color converters for LEDs, we now briefly consider some of the commercial approaches currently used in achieving white light from blue LEDs that involve the use of more than one phosphor. This allows the fabrication of single-chip white LEDs with higher color rendition than can be achieved by single phosphor pcLEDs.

At this point we will briefly review the use of some diphosphor combinations for LEDs. We have tabulated below some current approaches using a blue InGaN LED, with green- and red-emitting phosphors.

blue LED	+‘green’ phosphor	+‘red’ phosphor	Company
InGaN	$\text{SrGa}_2\text{S}_4:\text{Eu}^{2+}$	$\text{MS}:\text{Eu}^{2+}$	Lumileds ^{76,100}
InGaN	$\text{Y}(\text{Al,Ga})\text{G}:\text{Ce}^{3+}$	$\text{M}_2\text{Si}_5\text{N}_8:\text{Eu}^{2+}$	OSRAM ⁹⁰ , Nichia ¹⁰¹
InGaN	$\text{YAG}:\text{Ce}$	$\text{CaS}:\text{Eu}^{2+}$	Lumileds ¹⁰²
InGaN	$\text{SrSi}_2\text{O}_2\text{N}_2:\text{Eu}^{2+}$;	$(\text{Sr}_{1-x-y}\text{Ba}_x\text{Ca}_y)_2\text{Si}_5\text{N}_8:\text{Eu}^{2+}$	Lumileds ¹⁰²

The first two systems are limited in the color temperatures and CRI values that can be achieved. The approach of Lumileds [102] for a warm white was to add a red emitter to the

Table 3.3 Color conversion phosphors that can be excited by UV or blue LEDs

Phosphor	Activator	Emission Color	Excitation Wavelength in nm	Reference
YAG	Ce ³⁺	yellow	470	51
SrGa ₂ S ₄	Eu ²⁺	green	460	51
SrS	Eu ²⁺	red	450	51
(Ca,Mn) ₅ (PO ₄) ₃ Cl	Eu ²⁺	orange	415	103,104
Sr ₂ Si ₅ N ₈	Eu ²⁺	red	400	51
ZnS	Ag ⁺	blue	400	51
(Zn,Cd)S	Cu ⁺ ,Al ³⁺	green	<400	51
SrAl ₂ O ₄	Eu ²⁺	green	400	51
SrAl ₁₄ O ₂₅	Eu ²⁺	cyan	<00	103,104
(Y _{2-x-y} Eu _x Bi _y)O ₃	Eu ³⁺	red	360–410	59
Gd ₂ O ₂ S	Eu ³⁺	red	380	51
Sr ₅ (PO ₄) ₃ Cl	Eu ²⁺	blue	375	51
Sr ₅ (PO ₄) ₃ Cl	Eu ²⁺	blue	375—00	103,104
BaMgAl ₁₀ O ₁₇	Eu ²⁺	blue	375	51
YBO ₃ , Y ₂ SiO ₅	Ce ³⁺ ,Tb ³⁺	green	350	51

plain (cold) white of blue +YAG:Ce. They chose CaS:Eu²⁺. More red gives lower CCT, and more blue gives higher CCT. With this combination, all CCTs from 2700 to 5500K, with excellent CRI Ra >90, can be achieved.

An all nitride white diphosphor system has also been developed by Lumileds {102} that can be used to generate a wide range of whites by changing composition and/or Eu²⁺ concentration.

The third approach is to use a UV LED and three phosphors (triphosphors) emitting in the visible region of the electromagnetic spectrum. This also allows the fabrication of single-chip white LEDs with high color rendition. However, when the UV is down-converted into the visible region, there is a large loss of energy (quantum deficit). This is particularly important for the red emission. However, this approach is still attractive if efficiency is not a problem.

Three phosphors that emit respectively in the blue, cyan and orange are: (Sr,Eu)₅(PO₄)₃Cl, (Sr,Eu)₄Al₁₄O₂₅ and (Ca,Eu,Mn)₅(PO₄)₃Cl. (Table 3.3 for excitation bands) [103, 104]. When these three phosphors are combined with a UV LED, color correlated temperatures between 3000 °C.and 6500 °C can be achieved.

3.6 QUANTUM DOTS

Many claims have been made and there has been much hype about the possible use of quantum dots (semiconductor nano-particles) as color converters for LEDs. The claims are because their band gaps can be tuned by size, resulting in the occurrence of size-dependent, tuneable emission (and absorption). The ‘bright idea’ is to mix different sizes of quantum dot to increase spectral width across the visible region and so get ‘perfect white’ [105].

However, a serious drawback arises from the overlap of absorption and emission bands. This causes serious re-absorption at finite concentrations, which in turn moves the emission further to the red, and as long as the $QE < 1$ in highly diluted suspensions leads to a decrease of QE with concentration; this occurs at concentrations well below those desired for use in current LEDs [105].

A further drawback is that the number of compounds emitting in the visible is limited and many of the elements used in the fabrication of quantum dots are poisonous, such as Cd, Se, etc.

3.7 CONCLUSIONS

We have explained many of the challenges still to be met before ideal color converting phosphors can be fabricated for use with UV and blue-emitting LEDs. We have chosen not to cover the many academic papers that refer to color conversion as a reason for their work on phosphors, and have only covered the systems that have been used or researched by the major industrial players. We believe that this exciting field will stimulate much academic work to find new color conversion phosphors for industrial applications in the next decade. Indeed it must be stated that some of tomorrow's practical color converting phosphors for LEDs may currently be being explored in academic laboratories, but as yet they have not yet been recognized for their future potential.

ACKNOWLEDGEMENTS

We are grateful to the DTI (and many Industrial Partners) for substantial financial support in the form of DTI Technology programs 'Nanophosphor' under the Nano/Micro Initiative and the 'Novelets' part of the Photonics and Electronics program. We are also grateful to the DTI and Enfis Ltd for a KTP program.

Thanks are due to present and past members of the Centre for Phosphors and Display Materials, including A. Lipman, E. Barrett, D.A. Davies, R. Ellis, G. Fern, P. Harris, T. Ireland, P.J. Marsh, B. Patel, J.A. Rose, R. Stone and N. Wilstead.

REFERENCES

1. Schubert, E.F. (2003) *'Light emitting Diodes'*, Cambridge: Cambridge University Press.
2. Amano, H., Kito, M., Hiramatsu, K. and Akasaki, I. (1989) 'P-Type Conduction in Mg-Doped GaN Treated with Low-Energy Electron Beam Irradiation (LEEBI)', *Jpn. J. Appl. Phys.* **28**: L2112–14.
3. Strite, S., Lin, M.E. and Morkoc, H. (1993) 'Progress and prospects for GaN and the III–V nitride semiconductors', *Thin Solid Films* **231**: 197–210.
4. Nakamura, S., Iwasa, N., Senoh, M. and Mukai, T. (1992) 'Hole Compensation Mechanism of P-Type GaN Films', *Jpn. J. Appl. Phys.* **31**: 1258–66.
5. Nakamura, S. (1994) 'Nichia I Cd blue LED paves way for full-color display', *Nikkei Electron. Asia* **6**: 65–9.

6. Nakamura, S., Mukae, T. and Senoh, M. (1994) 'High-brightness InGaN/AlGaIn double-heterostructure blue-green-light-emitting diodes', *J. Appl. Phys.* **76**: 81–9.
7. Nakamura, S., Mukae, T. and Senoh, M. (1994) 'Candela-class high-brightness InGaN/AlGaIn double-heterostructure blue-light-emitting diodes', *Appl. Phys. Lett.* **64**: 1687–9.
8. Nakamura, S., Senoh, M., Iwasa, N. and Nagahama, S. (1995) 'High-Brightness InGaN Blue, Green and Yellow Light-Emitting Diodes with Quantum Well Structures', *Jpn. J. Appl. Phys.* **34**: L797–9.
9. Nakamura, S., Senoh, M., Iwasa, N., Nagahama, S., Yamada T. and Mukai, T. (1995) 'Super-bright Green InGaN Single-Quantum-Well-Structure Light-Emitting Diodes', *Jpn. J. Appl. Phys.* **34**: L1332–5.
10. Nakamura, S., Senoh, M., Nagaham, S. *et al.* (1996) 'InGaN-Based Multi-Quantum-Well-Structure Laser Diodes', *Jpn. J. Appl. Phys.* **35**: L74–6.
11. Nakamura, S., Senoh, M., Nagaham, S. *et al.* (1996) 'InGaN Multi-Quantum-Well-Structure Laser Diodes with Cleaved Mirror Cavity Facets', *Jpn. J. Appl. Phys.* **35**: L217–20.
12. Nakamura, S., Senoh, M., Nagaham, S. *et al.* (1996) 'InGaN multi-quantum-well structure laser diodes grown on MgAl₂O₄ substrates', *Appl. Phys. Lett.* **68**: 2105–7.
13. Nakamura, S., Senoh, M., Nagaham, S. *et al.* (1996) 'Characteristics of InGaN multi-quantum-well-structure laser diodes', *Appl. Phys. Lett.* **68**: 3269–71.
14. Nakamura, S., Senoh, M., Nagaham, S. *et al.* (1996) 'Ridge-geometry InGaN multi-quantum-well-structure laser diodes', *Appl. Phys. Lett.* **69**: 1477–9.
15. Nakamura, S., Senoh, M., Nagaham, S. *et al.* (1996) 'Optical gain and carrier lifetime of InGaN multi-quantum well structure laser diodes', *Appl. Phys. Lett.* **69**: 1568–70.
16. Nakamura, S., Senoh, M., Nagaham, S. *et al.* (1996) 'Continuous-wave operation of InGaN multi-quantum-well-structure laser diodes at 233 K', *Appl. Phys. Lett.* **69**: 3034.
17. Nakamura, S., Senoh, M., Nagahama, S. *et al.* (1996) 9th Annual Meeting of IEEE Lasers and Electro-Optics Society, Boston, PD1.1. Nov. 18–21.
18. Nakamura, S. (1996) Materials Research Society Fall Meeting, Boston, N1.1, Dec. 2–6.
19. Harris, J.C., Someya, T., Hoshino, K., Kako, S. and Aarakawa, Y. (2000) 'Photoluminescence of GaN Quantum Wells with AlGaIn Barriers of High Aluminium Content', *Phys.Stat.Sol.(a)* **180**: 339–43.
20. Fuhrmann, D., Retzlaff, T., Rossow, U. *et al.* (2006) 'Large internal quantum efficiency of In-free UV-emitting GaN/AlGaIn quantum-well structures', *Appl. Phys. Lett.* **88**: 191108 (3 pages).
21. Akasaka, T., Gotoh, H., Saito, T. and Makimoto, T. (2004) 'High luminescent efficiency of InGaIn multiple quantum wells grown on InGaIn underlying layers', *Phys. Lett.* **85(15)**: 3089–91.
22. Hangleiter, A., Fuhrmann, D., Grewe, M. *et al.* (2004) 'Towards understanding the emission efficiency of nitride quantum wells', *Phys. Stat. Sol. (a)* **201(12)**: 2808–13.
23. Sun, Y., Cho Y.H., Kim, H.M. and Kang, T.W. (2005) 'Formation of Ru nanocrystals by plasma enhanced atomic layer deposition for nonvolatile memory applications', *Appl. Phys. Lett.* **87**: 093115 (3 pages).
24. Fuhrmann, D., Rossow, U., Netzel, C. *et al.* (2006) 'Optimizing the internal quantum efficiency of GaInN SQW structures for green light emitters', *Phys. Stat. Sol. (c)* **3(6)**: 1966–9.
25. McAleese, C. and Humphries, C. (2006) Materials Dept., Cambridge University. (pers. comm.)
26. Ropp R.C. (1993) *The Chemistry of Artificial Lighting Devices*, Amsterdam, London, New York: Elsevier Science Publishing, pp. 1–664.
27. Ropp, R.C. (1991) *Luminescence and the Solid State*, Amsterdam, New York: Elsevier Science Publishing, pp. 1–453.
28. Wells, A.F. (1975) *Structural Inorganic Chemistry*, 4th edn, Oxford: Clarendon Press. pp. 1–1095.

29. Leskela, M. and Ninisto, L. (1986) 'Inorganic Complex Compounds I', In: *Handbook on the Physics and Chemistry of Rare Earths* (Gschneidner, K.A. Jr and Eyring, L., eds.), Chapter 56, Amsterdam: Elsevier Science Publishers BV. pp. 203–334.
30. Garlick, G.F.J. (1949) *Luminescent materials*. Oxford: The Clarendon Press. pp. 1–254.
31. Shinoya, S. and Yen, W.M. (eds) (1998) *Phosphor Handbook*. London: CRC Press. pp. 1–921.
32. Blasse, G. and Brill, A. (1967) 'A new phosphor for flying-spot cathode-ray tubes for colour television: Yellow-emitting, $Y_3Al_5O_{12}-Ce^{3+}$ ', *App. Phys. Lett.* **11**(2): 53–5.
33. Smets, B.M.J. (1987) 'Phosphors based on rare-earths, a new era in fluorescent lighting', *Mat, Chem. Phys.* **16**: 283–99.
34. Butterworth, M. and Helbing, R.P. (1997) 'Fluorescent dye added to epoxy of light emitting diode lens', US Pat. 5,847,507, July 14.
35. Shimizu, Y., Sakano, K., Noguchi, Y. and Moriguchi, T. (1997) 'Light-emitting device having a nitride compound semiconductor and a phosphor containing a garnet fluorescent material', US Pat. 5,998,925, July 29.
36. Lowery, C.H. (1998) 'Multiple encapsulation of phosphor-LED devices', US Pat. 5,959,316, Sept. 1.
37. Shimizu, Y., Sakano, K., Noguchi, Y. and Moriguchi, T. (1999) 'Light-emitting device with blue light LED and phosphor components', US Pat. 6,614,179, Dec. 10.
38. Holn, K., Debray, A., Schlotter, P., Schmidt, R. and Schneider, J. (2000) 'Wavelength-converting casting composition and its use', US Pat. 6,066,861, May 23.
39. Holn, K., Debray, A., Schlotter, P., Schmidt, R. and Schneider, J. (2000) 'Wavelength-converting casting composition and light-emitting semiconductor component', US Pat. 6,245,259, Aug. 29.
40. Ellens, A. and Zwaschka, F. (2000) 'Phosphor for light sources, and associated light source', US Pat. 6,552,487, Oct. 23.
41. Reeh, U., Holn, K., Stath, N. *et al.* (2000) 'Light-radiating semiconductor component with a luminescence onversion element', US Pat. 6,812,500 B2, Dec. 6.
42. Reeh, U., Holn, K., Stath, N. *et al.* (2000) 'Light-radiating semiconductor component with a luminescence conversion element', US Pat. 6,576,930 B2, Dec. 7.
43. Srivastava, A.M., Setlur, A.A. and Comanzo, H.A. (2001) 'Broad-spectrum terbium-containing garnet phosphors and white-light sources incorporating the same', US Pat. 6,596,195, June 1.
44. Ellens, A., Jermann, F., Kummer, F., Ostertag, M. and Zwaschka, F. (2002) 'Led-based white-emitting illumination unit', US Pat. 6,504,179, Jan. 17.
45. Reeh, U., Holn, K., Stath, N. *et al.* (2005) 'Light-radiating semiconductor component with a luminescence conversion element', US Pat. 7,126,162, March 15.
46. Withnall, R., Silver, J., Rose, J. *et al.* (2004) 'Phosphor Screens Excited by Blue LEDs as a White Light Source for Full Colour Head Up Displays in Automobiles', Proc. of EL 2004, Sept. 20–23, Toronto, Canada. pp. 325–8.
47. Silver, J., Withnall, R., Rose, J.A. *et al.* (2005) 'Broad-band Green Phosphor Screens as a Light Source for Head Up Displays in Moving Platforms', Technical Abstracts, *Opto Ireland*, April 4–6, Dublin, Ireland. p. 87.
48. Silver, J., Withnall, R., Rose, J.A. *et al.* (2005) 'Broad-band Green Phosphor Screens as a Light Source for Head Up Displays in Moving Platforms', Proc. SPIE, *Opt. Sens. Spectro.* **5826**: 537–44.
49. Silver, J. (2006) 'Phosphors for LEDs, Current state of the Art, Problems, and Needs.' Invited lecture, conference entitled 'The Future of LEDs', June 26–27, London.
50. Robertson, J.M., van Tol, M.W., Smits W.H. and Heynen, J.P.H. (1981) *Philips J. Res.* **36**(1): 15–30.

51. Rossner, W. (2003) 'Trivalent Rare Earth Activated Phosphors for Wavelength Conversion in LEDs: Possibilities and Limitations', *Phosphor Global Summit*, Scottsdale, AR, USA. Conference Paper 14, pp. 1–18.
52. Silver, J., Withnall, R., Fern, G., Ireland, T., Catherall, C. and Lipman, A. (2007) 'Efficiency Measurements on Phosphors for LEDs. (Efficacy Measurements relative to Blue exciting light)', *Phosphor Global Summit*, Seoul, Korea. Conference Paper 7, pp. 1–18.
53. Withnall, R., Silver, J. and Lipman, A. (2006) 'Measurements of luminous efficiencies of conversion phosphors for blue emitting LEDs', *Proceedings of the 13th International Display Workshop (IDW)*, Otsu, Japan, **1**: 431–2.
54. Silver, J., Withnall, R., Fern, G. and Lipman, A. (2007) 'White light production from blue LEDs: the synthesis of small particle YAG:Ce type phosphors for solid state lighting', *ASID 07*, **1**: 306–10.
55. Withnall, R., Silver, J. and Lipman, A. (2007) 'Measurements of luminous efficiencies of conversion phosphors for blue emitting LEDs', *ASID 07*, **1**: 1074–8.
56. Zachau, M. (2006) 'Phosphors, Patents, and Products for LEDs', *Phosphor Global Summit*, San Diego, CA, USA. Conference Paper 12, pp. 1–17.
57. Hirakata, S.O. (2003) 'Inorganic oxide and phosphor', US Pat. 7,029,602 B2, Sept. 25.
58. Setlur, A.A., Comanzo, H.A., Srivastava, A.M. and Beers, W.W. (2005) 'Evaluation of a White Light Phosphor for UV-LEDs— $\text{Ca}_2\text{NaMg}_2\text{V}_3\text{O}_{12}:\text{Eu}^{3+}$ ', *J. Electrochem. Soc.* **152**: H205–8.
59. Liu, R.S. (2005) 'Efficiency Enhancement for Bi-Doped $\text{Y}_2\text{O}_3:\text{Eu}$ Red Phosphors of UV LEDs', *Global Summit 2003*, San Diego, CA, USA. Conference Paper 19, pp. 1–12.
60. Srovastava, A. (2006) 'A New Green Emitting Phosphor for UV LEDs', *Phosphor Global Summit*, San Diego, Ca, USA. Conference Paper 13, pp. 1–10.
61. Lee, D.-W., Kwak, C.H. and Jung, H.K. (2006) 'Photoluminescence properties of red-emitting $\text{YCa}_3\text{M}_3\text{B}_4\text{O}_{15}:\text{Eu}^{3+}$ ($\text{M} = \text{Al}$ or Ga) phosphors under UV irradiation: A recent advance in EL, Displays and Lighting', JeJu, Korea, *Tech. Digest* pp.363–4.
62. Barry, T.L. (1968) 'Equilibria and Eu^{2+} Luminescence of Subsolidus Phases Bounded by $\text{Ba}_3\text{MgSi}_2\text{O}_8$, $\text{Sr}_3\text{MgSi}_2\text{O}_8$, and $\text{Ca}_3\text{MgSi}_2\text{O}_8$ ', *J. Electrochem. Soc.* **115**: 733–8.
63. Starick, D., Kempfert, W., Limberg, H.-J. (2003) 'Silicate Phosphors and their Performance in White LEDs', *Phosphor Global Summit*, Scottsdale, AR, USA. Conference Paper 19, 1–3.
64. Meyer, J. (2006) 'Novel Garnet Phosphors for LEDs', *Phosphor Global Summit*, San Diego, CA, USA. Conference Paper 9, 1–13.
65. Levinson, L.M. and Srivastava, A.M. (1998) 'Light emitting device with $\text{Ba}_2\text{MgSi}_2\text{O}_7:\text{Eu}^{2+}$, $\text{Ba}_2\text{SiO}_4:\text{Eu}^{2+}$, or $(\text{Sr}_x\text{Ca}_y\text{Ba}_{1-x-y})(\text{Al}_z\text{Ga}_{1-z})_2\text{Sr}:\text{Eu}^{2+}$ phosphors', US Pat. 6,429,583, Nov. 30.
66. Ota, K., Hirano, A., and Ota, A. *et al.* (2000) 'Light emitting device having phosphor of alkaline earth metal silicate', US Pat. 6,943,380, Dec. 28.
67. Tasch, S., Pacher, P., Roth, G., Tews, W., Kempfert, W. and Starick, D. (2003) 'Light source comprising a light-emitting element', US Pat. 6,809,347, Dec. 22.
68. Jae, C.-K., Park, J.P., Kim, K.N., Kim, C.H. and Kim, H.K. (2006) 'White light-emitting diodes of InGaN-based $(\text{SrBa})_3\text{MgSi}_{1.7}\text{O}_8:\text{Eu}$ ($2.0 \leq x \leq 1.7$) and the luminescent properties: A recent advance in EL, Displays and Lighting', JeJu, Korea, *Tech. Digest* pp. 334–5.
69. Leverenz, H.W. (1950) *An Introduction to Luminescence of Solids*, New York: John Wiley & Sons.
70. G. Destriau, G. (1936) 'Recherches sur les scintillations des sulfures de zinc aux rayons', *J. Chemie Phys.* **33**: 587–625.
71. Vecht, A., Davies, D.A. and Smith, D. (1998) 'A Novel Method for the Preparation of Sulfides and Selenides and its Application for Phosphor Synthesis', *Mat. Res. Innovat.* **2**: 17680.
72. Davies, D.A., Vecht, A., Rose, J.A. *et al.* (1999) 'Improved Zinc-Sulfide type Phosphors by a Novel Synthetic Method'. *SID 99 Digest*, **30**: 1018–21.

73. Davies, D.A., Vecht, A., Silver, J., Marsh, P.J. and Rose, J.A. (2000) 'A Novel Method for the Preparation of Inorganic Sulfides and Selenides. Part 1: Binary Materials and Group II-VI Phosphors', *J. Electrochem. Soc.* **147**: 765–71.
74. Marsh, P.J., Davies, D.A., Silver, J., Smith, D.W., Withnall, R. and Vecht, J. (2001) 'A Novel Method for the Clean Syntheses of Sulfides/Selenides. Part 2 Ternary Sulfides/Selenides', *J. Electrochem. Soc.* **148**: D88–93.
75. Davies, D.A., Silver, J., Vecht, A., Marsh, P.J. and Rose, J.A. (2001) 'A Novel Method for the Synthesis of ZnS for use in the Preparation of Phosphors for CRT Devices', *J. Electrochem. Soc.* **148**: H143–8.
76. Mueller-Mach, R. and Mueller, G.O. (2000) 'White light-emitting diodes for illumination', *Proc. SPIE* **3938**: 30–41.
77. Van Haecke, J.E., Smet, P.F., Michelena, E. and Poelman, D. (2006) 'Solvothermal synthesis of europium-doped submicron SrS: A recent advance in EL, Displays and Lighting', *JeJu, Korea, Tech. Digest* 353–5.
78. Tian, Y. (2003) 'Phosphor Development for LED lighting Devices', *Phosphor Global Summit*, Scottsdale, AR, USA. Conference Paper 10, 1–7 and 1–3 of handout.
79. Juestel, T., Schmidt, P.J., Busselt, W. (2003) 'Novel phosphors and phosphor blends for white LEDs', *Phosphor Global Summit*, Scottsdale, AR, USA. Conference Paper 15, 1–13.
80. Kim, K.N., Park, J.K., Choi, K.J., Kim, J.-M and Kim C.H. (2006) 'Luminescent Properties of europium doped alkaline earth selenide phosphors: A recent advance in EL, Displays and Lighting', *JeJu, Korea, Tech. Digest* p334–5.
81. Peters, T.E. and Baglio J.A. (1972) 'Luminescence and Structural Properties of Thiogallate Phosphors Ce⁺³ and Eu⁺²-Activated Phosphors', Part I, *J. Electrochem. Soc.* **119**: 230–6.
82. Donohue, P.C. and Hanlon, J.E. (1974) 'The Synthesis and Photoluminescence of M^{II}M₂^{III}(S,Se)₄', *J. Electrochem. Soc.* **121**: 137–42.
83. Davolos, M.R., Garcia, M.R., Fouassier, C. and Hagenmuller, P. (1989) 'Luminescence of Eu²⁺ in strontium and barium thiogallates', *J. Solid State Chem.* **83**: 316–23.
84. Kobayashi, T., Uheda, K., Naruke, H. and Yamase, T. (1996) 'A Novel Preparation of Thiogallate-based Rare-earth Phosphors', *Chem. Lett.* **26**: 567.
85. Eichenauer, L., Jarofke, B., Mertins, H.-C. *et al.* (1996) 'Optical characterization of europium and cerium in strontium thiogallate thin films and powders', *Phys. Stat. Sol. A* **153**: 515–27.
86. Yang, S., Stoffers, C., Zhang, F., Jacobson, S.M., Wagner, B.K. and Summers, C.J. (1998) 'Green phosphor for low-voltage cathodoluminescent applications: SrGa₂S₄:Eu²⁺', *Appl. Phys. Lett.* **72**: 158–60.
87. Barthou, C. and Benoit, J. (1998) 'SrGa₂S₄: RE phosphors for full colour electroluminescent displays', *J. Alloy and Comp.* 275–7, 709–15.
88. Sastry, I.S.R., Bacalski, C.F. and McKittrick, J. (1999) 'Preparation of Green-Emitting Sr_{1-x}Eu_xGa₂S₄ Phosphors by a Solid-State Rapid Metathesis Reaction', *J. Electrochem. Soc.* **146**: 4316–9.
89. Cheetham, A.K. (2006) 'Novel Phosphors for Solid State Lighting', *Phosphor Global Summit*, San Diego, CA, USA. Conference Paper 7, 1–13.
90. Bogner, G., Botty, G., Braune, B., Hintzen, H.T., van Kreveld, J.W.H. and Waitl, G. (2003) 'Light source using a yellow-to-red-emitting phosphor', US Pat. 6,649,946, Nov. 18.
91. Yi, Y.Q., van Steen, J.E.J., van Kreveld, J.W.H. *et al.* (2006) 'Luminescence properties of red-emitting M₂Si₃N₈: Eu²⁺ (M = Ca, Sr, Ba) LED conversion phosphors', *J. Alloys Compd.* **417**: 273–9.
92. Huppertz, H. and Schnick, W. (1997) 'Eu₂Si₃N₈ and EuYbSi₄N₇. The First Nitridosilicates with a Divalent Rare Earth Metal', *Acta Cryst.* **C53**: 1751–3.
93. Meyer, J. (2006) 'From Garnets to Novel LED Phosphors', *Phosphor Global Summit*, San Diego, CA, USA. Conference Paper 9, 1–13.

94. Uheda, K. and Yamamoto, H. (2005) 'Nitride Phosphors in the System $\text{Ca}_3\text{N}_2\text{-AlN-Si}_3\text{N}_4$ ', *Phosphor Global Summit*, San Diego, CA, USA. Conference Paper 21, 1–5.
95. Miyamoto, Y., Yamamoto, H., Hirotsuki, N. and Uheda, K. (2006) 'Luminescence decay characteristics of a red nitride phosphor $\text{CaAlSiN}_3\text{:Eu}^{2+}$ for white light-emitting diodes: A recent advance in EL, Displays and Lighting', JeJu, Korea, *Tech. Digest*, 339–40.
96. Uheda, K., Hirotsuki, N., Yamamoto, Y. Naito, A., Nakajima, T. and Yamamoto, H. (2006) 'Luminescence Properties of a Red Phosphor, $\text{CaAlSiN}_3\text{:Eu}^{2+}$, for White Light-Emitting Diodes', *Electrochem. So. State Lett.* **9**: H22–5.
97. Lauterbach, R. and Schnick, W. (1998) 'Synthese, Kristallstruktur und Eigenschaften eines neuen Sialons - $\text{SrSiAl}_2\text{O}_3\text{N}_2$ ', *Z. Anorg. Allg. Chem* **624**: 1154–8.
98. Mitomo, M., Endo, T., Ueda, K. and Momatsu, M. (2002) 'Oxynitride phosphor activated by a rare earth element, and sialon type phosphor', US Pat. 6,632,379, June 6.
99. Sakata, S.-I. and Yamada, T. (2004) 'Sialon-based phosphor and its production method', US Pat. EP 1,498,466, July 15.
100. Craford, G. (2003) 'Solid State Lighting: The promise and Challenges For LEDs', *Phosphor Global Summit*, Scottsdale, AR, USA. Conference Paper 13, 1–36.
101. Yamada, M., Naitou, T., Izuno, K. *et al.* (2003) 'Red-Enhanced White-Light-Emitting Diode Using a New Red Phosphor', *Jpn. J. Appl. Phys.* **42**: L20–3.
102. Mueller, G. (2005) 'Set the Pace in the White Space: White LEDs for illumination and back-lighting', *Phosphor Global Summit*, San Diego, CA, USA. Conference Paper 18, 1–15.
103. Radkov, E. (2005) 'High Quality White Light with Near-UV LED chips', *Phosphor Global Summit*, San Diego, CA, USA. Conference Paper 17, 1– 9.
104. Radkov, E. (2003) 'White Light with UV LEDs', *Phosphor Global Summit*, Scottsdale, AR, USA. Conference Paper 20, 1–19.
105. Mueller, G. (2006) 'Colour Conversion of LED light', *Phosphor Global Summit*, San Diego, CA, USA. Conference Paper 11, 1–14.

4 Development of white OLED technology for application in full-color displays and solid-state lighting

T. K. Hatwar and Jeff Spindler

Eastman Kodak Company, Rochester, NY 14650-2011, USA

4.1 Introduction	111
4.2 Generation of white light	112
4.3 White OLEDs for display applications	122
4.4 White OLED tandem architecture	130
4.5 White OLEDs based on triplets	140
4.6 White OLEDs based on conjugated polymers	142
4.7 White OLEDs for solid-state lighting	143
4.8 Advanced manufacturing of large-area coatings	149
4.9 Future outlook	155
Acknowledgements	156
References	156

4.1 INTRODUCTION

Efficient electroluminescence (EL) from organic thin films was reported nearly 20 years ago by Tang and Van Slyke at the Eastman Kodak Company [1, 2]. The promise of a new display technology – with features of wide viewing angle, fast response time, high contrast ratio, excellent color reproduction, and wide temperature range operation – generated significant excitement, resulting in worldwide corporate as well as academic research and development activities. Starting with the introduction of passive matrix (PM) displays in 1995 (Pioneer Electronics, the first to licence the Kodak technology), the PM display market has grown to about \$500M per year (2006). Limited to about 100 rows, primarily as a consequence of capacitance issues, PM displays have been incorporated into products such as cellular telephone sub-displays, MP3 players and automobile after-market audio components. Although requiring a more complex substrate, active matrix OLED (AMOLED) displays are scaleable to larger sizes and are more suited for high-resolution full-color applications. Small

AMOLED displays (<3.5-inch diagonal) have been commercialized [3–5] and are expected to become widespread for mobile applications (cellular phones, digital cameras, PDAs), as well as eventually for larger applications, such as televisions, in the next few years.

Key to the widespread adoption of OLED technology is the basic performance of the OLED emission process and the manufacturability of the display format. For example, it has been determined that the conventional method of depositing small molecule OLED materials through a fine metal mask, in order to pattern the individual red, green and blue emitters, is problematic due to mask integrity, mask cost and inability to scale the mask to be compatible with large substrates that will eventually be used in high-volume manufacturing (one square meter and larger). An unpatterned white-emitting OLED layer in combination with color filters patterned on the substrate, prior to the OLED deposition process and avoids the use of fine metal mask. With a white emitter and a four sub-pixel (RGBW) configuration, highly efficient, stable and manufacturable AMOLED displays have been demonstrated [3, 6]. It is expected that this display format will be utilized in small as well as large OLED displays and will solve many of the problems that have been associated with fine metal masks as well as other emitter patterning technologies.

White OLED emission is suitable for solid-state lighting applications as well as display applications. Understandably, there is significant interest by lighting companies as well as National Governments in any emission technology that can be utilized to improve the efficiency of general lighting. In fact, government-supported initiatives in the USA supported by DOE as well as Europe (OLLA) are underway to investigate solid-state lighting technologies, including OLED. Many of the technical requirements for lighting applications are similar to the requirements for OLED displays, including high efficiency, long lifetime, low cost and emission covering the visible spectrum. For these reasons, white OLED technology is being considered and actively developed for lighting applications.

In this chapter, we will describe the status as well as the future outlook of white OLED technology in relationship to requirements for display and lighting applications. In addition, supporting technologies, such as vacuum thermal evaporation and thin-film encapsulation, are also briefly reviewed.

4.2 GENERATION OF WHITE LIGHT

Light can be described by chromaticity coordinates on a Commission International d'Eclairage (CIE) chromaticity diagram. The horseshoe-shaped diagram defines all the colors within the visible spectrum. Figure 4.1 shows the well-known 1931 CIE diagram. Included in the diagram is an arc (called the Planckian Locus) along with equivalent color temperatures. The arc defines the color coordinates of a blackbody radiator from 2500 to about 10000 K. For display (and lighting) applications, the range of required white color temperatures is from about 3000 to 9300 K. The lower color temperatures are usually termed 'warm' and the higher temperatures are termed 'cool' white. For many typical display applications, the white point is targeted to be near 6500 K (called D65) to 10,000 K, which corresponds to color coordinates of about (0.31, 0.33) and (0.27, 0.29), respectively. For general lighting applications, color-correlated temperatures are typically lower, between 3000 and 6000 K.

An OLED device producing white light was reported by Kido *et al.* [9]. The device has three emission layers, which emit blue, green and red light individually, but combine to

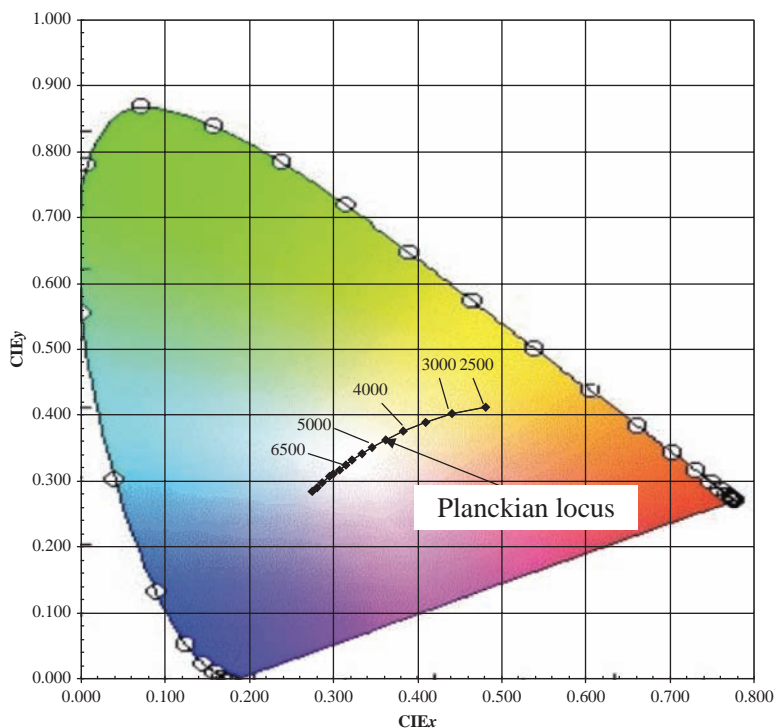


Figure 4.1 Chromatic diagram defining Planckian locus

produce light that is white in color. Several other researchers have tried variations of this structure [10–12]. Although these reference devices have good electroluminescent characteristics, the EL properties change significantly with small changes in dopant concentrations. Also, the low dopant concentrations (between 0.12–0.25%) used in these formulations are difficult to control in a manufacturing environment. Another structure using red, blue, and green luminescent layers separated by a hole-blocking layer has also been reported [13]. The emission color of this device varies significantly as a result of small changes in the dopant concentration as well as in the current density. High-performance white structures, based on small molecule singlet fluorescent materials for both high efficiency and high operational stability, have been demonstrated at the Eastman Kodak Company [14–17]. The details of the device structure, method of optimizing the color, efficiency and operational stability are discussed in the sections to follow. White OLEDs also can be obtained by using small molecule triplet phosphorescent materials and polymer materials; the results of devices based on these materials will be discussed in Sections 4.5 and 4.6, respectively.

4.2.1 High-performance 2-layer white OLED architecture

The white OLED structure based on two-light-emitting layers is shown in Figure 4.2. It is similar to that used for producing monochrome colors, such as blue, green or red, except that it contains two light-emitting layers, yellow and blue. Both the blue-emitting and

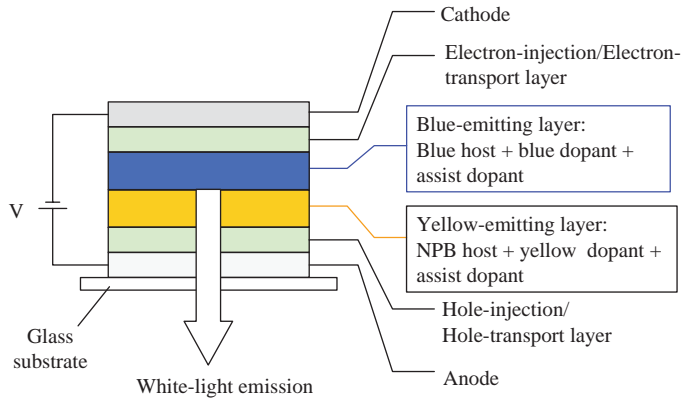


Figure 4.2 Schematic of the two-layer white OLED formulation

yellow-emitting layers incorporate host and dopant materials. In the case of the yellow layer, an NPB (4,4'-bis[*N*-(1-naphthyl)-*N*-phenylamino]biphenyl) host with a rubrene-type yellow-emitting dopant and an anthracene derivative as an assist host/dopant are used. For the blue-emitting layer, an anthracene host and blue dopant combination is used, and similar to the yellow layer, an assist dopant is incorporated. The function of the assist dopant in both cases is to facilitate energy transfer from the excited host to the dopant molecules. The hole transport layer (HTL) and an electron transport layer (ETL) consist of NPB and Alq (tris-(8-hydroxyquinolino) aluminium III), respectively. The device has indium tin oxide (ITO) as the anode, aluminium as the cathode, fluorocarbon (CF_x) as hole injection layer (HIL) and lithium fluoride (LiF) as the electron-injection layer (EIL). The details of the structure are:

- Glass substrate/
- Anode: ITO (60 nm)/
- HIL: CF_x (1 nm)/
- HTL: NPB (150 nm)/
- Yellow EML: (40 nm)/
- Blue EML: (30 nm)/
- ETL: Alq (10 nm)/
- EIL: LiF (0.5 nm)/
- Cathode: Al (100 nm).

The various materials used in the above structure are given elsewhere [17].

4.2.2 Optimization of white color-two emitting layer (yellow/blue) configuration

White emission is obtained by appropriately mixing the emissions from the adjacent blue- and yellow-emitting layers in the OLED multilayer stack. Varying the yellow and blue dopant concentrations results in first-order optimization of the color. Figure 4.3 shows the

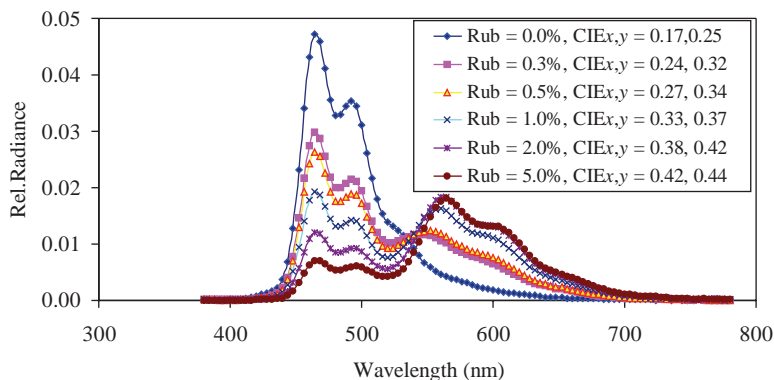


Figure 4.3 White OLED obtained by mixing the blue and yellow emissions in two separate layers

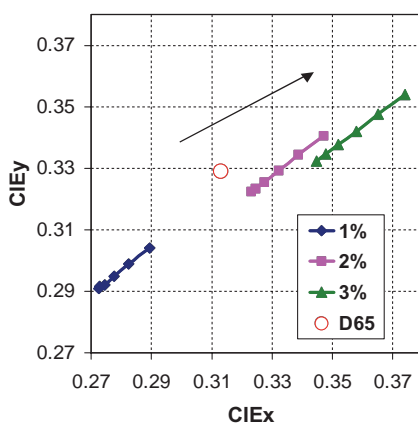


Figure 4.4 Effect of yellow dopant concentration on chromaticity as a function of current density

variation of the EL spectrum as a function of the yellow dopant (in this case, rubrene) concentration and demonstrates the mechanism of white emission. Without any yellow dopant, the device emits blue with color coordinates of $\text{CIE}_{x,y} = (0.17, 0.25)$. With 0.3% rubrene (Rub) concentration, the color coordinates change to $(0.24, 0.32)$. A white color close to D65 can be obtained with rubrene concentrations between 0.5–1.0%. When rubrene concentrations are higher, the color shifts to yellowish white, such as $(0.38, 0.42)$ at 2% rubrene and $(0.42, 0.44)$ at 5% rubrene. Mechanistically, charge recombination in the blue-emitting layer results in the formation of the blue dopant excited state that emits directly, or transfers excited-state energy to the yellow-emitting layer, which subsequently emits. Partitioning of charge-carrier recombination between the blue and yellow layers may also occur to some extent. However, regardless of the exact mechanism, the result is emission of both blue and yellow light, which when combined, results in white emission. Detailed fabrication processes of these white OLED devices are discussed elsewhere [17].

The hue of the emission can be modified by varying the OLED structure (dopant concentrations, layer thicknesses, etc.) and by tuning to the desired color temperature. Figures 4.4–4.6 show the chromaticity variations as a function of concentration for the yellow, blue and yellow assist dopants, respectively. In all three plots, the chromaticity was determined

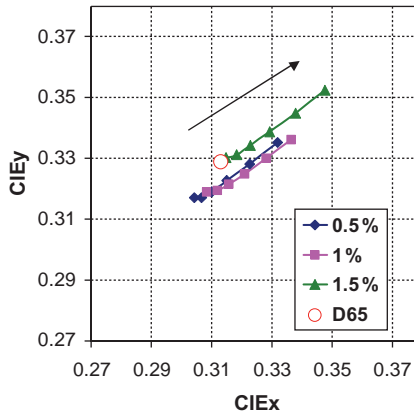


Figure 4.5 Effect of blue dopant concentration on chromaticity as a function of current density

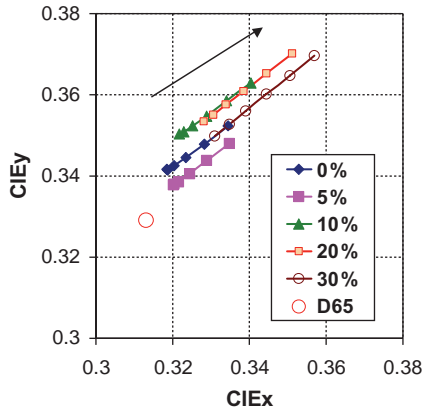


Figure 4.6 Effect of yellow assist dopant concentration on chromaticity as a function of current density

at 1, 2.5, 5, 10, 20 and 40 mA/cm². A progressive yellow shift was observed for each device configuration with increasing current density. As shown in Figure 4.4, the yellow dopant concentration has a large effect on the white point (at a particular current density), and the optimum concentration (nearest to the D65 point) is at about 2%. The chromaticity is much less sensitive to the blue dopant concentration (Figure 4.5). In this case, the optimum concentration appears to be in the 0.5–1% range. As with the yellow dopant, as the concentration of the blue dopant is increased, the chromaticity change with the current density also increases. With the yellow assist dopant (Figure 4.6), the optimum concentration from the standpoint of stability and efficiency is in the 20–30% range. In this range, the chromaticity change with current density is about the same as without incorporation of the assist dopant. All three of these dopants show a similar trend in terms of the chromaticity change with current density. That is, as the dopant concentrations increase, the magnitude of the color shift increases. In all three graphs, the color shifts from left to right as the current density

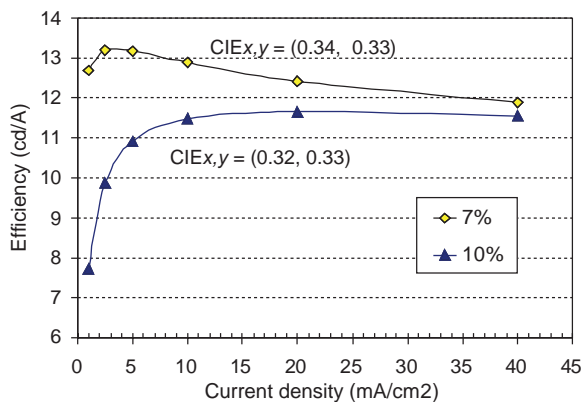


Figure 4.7 Effect of assist dopant concentration in the blue layer on luminance efficiency as a function of current density

increases from 1 to 40 mA/cm². The assist dopant in the blue-emitting layer does not affect the color of the spectrum, but is important for the efficiency. The luminance efficiency as a function of current density is given in Figure 4.7 for an optimized white structure at two concentrations of the blue assist dopant.

4.2.3 White OLED device performance

4.2.3.1 Color stability as a function of current density for an optimized structure

As seen above the white color chromaticity varies with the concentrations of dopants/assist dopants. However, it is possible to fabricate a two-emitting layer white which has good color stability as good color stability as a function of current density, as well as in operational aging. Figure 4.8 shows the EL spectra at various current densities. The EL spectra and CIE coordinates of these white OLEDs change little as a function of current density over the practical range from 40 down to 1 mA/cm². This feature is most valuable in applications requiring variable intensity. It is also potentially valuable in constant-intensity applications; otherwise, different applications that demand different intensities may require different compositions for optimum ‘whiteness’.

4.2.3.2 Operational stability at ambient conditions

The white structures described previously have excellent operational luminance and voltage stability under direct current (DC) conditions. The half-life times (time required to reach half of the starting luminance level) were measured by driving the test samples at varying current densities of 5, 10, 20 and 80 mA/cm². It was found that both the yellow and blue assist host/dopant concentrations are important for both the color and device operational stability. The assist host in the yellow layer is a non-emitting blue host material that has a negligible effect on the white emission chromaticity change with the current density, but it has a strong effect on the operational stability and the luminance efficiency. Figure 4.9 shows the effect of a blue anthracene co-host, in the yellow emitting layer on the luminance

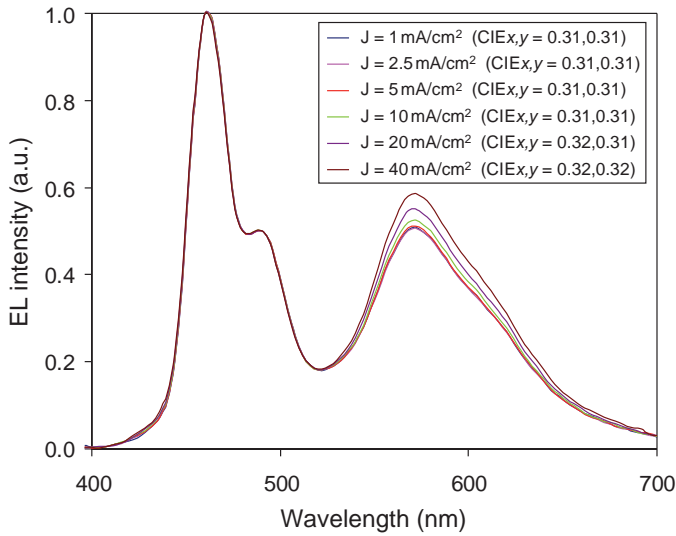


Figure 4.8 White EL spectra as a function of current density

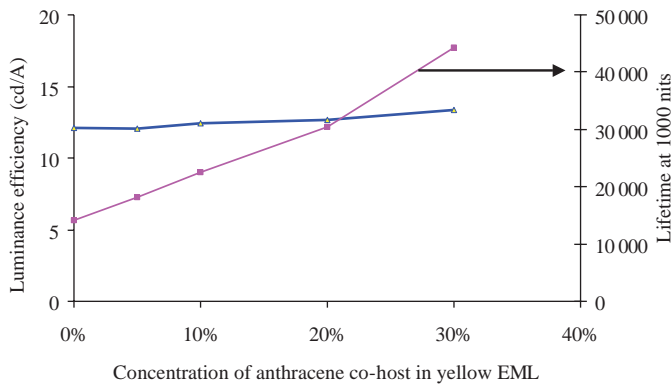


Figure 4.9 Effect of co-host concentration in the yellow layer on operational stability and luminance efficiency

efficiency and the operational lifetime. A dramatic improvement in the operational stability is observed with the increase of anthracene co-host concentrations, accompanied by a modest increase in luminance efficiency. It is known that, similar to Alq3 cations, NPB anions have a negative effect on device stability. With anthracene co-doping in the NPB-containing yellow layer, it is likely that the formation of the NPB anion is significantly reduced, which contributes to an increase of device stability [18].

Figure 4.10 shows the extrapolated half-lives at room temperature, as a function of initial luminance. With operation at a constant current, the extrapolated lifetime with an initial luminance of 2500 cd/m² is approximately 15 000 h; and with an initial luminance of 1000 cd/m², it is approximately 50 000 h. These lifetimes are certainly adequate for OLED full-color displays as well as lighting applications.

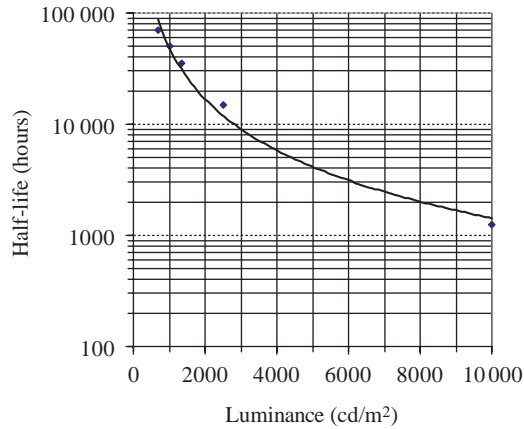


Figure 4.10 Operational half-life as a function of luminance

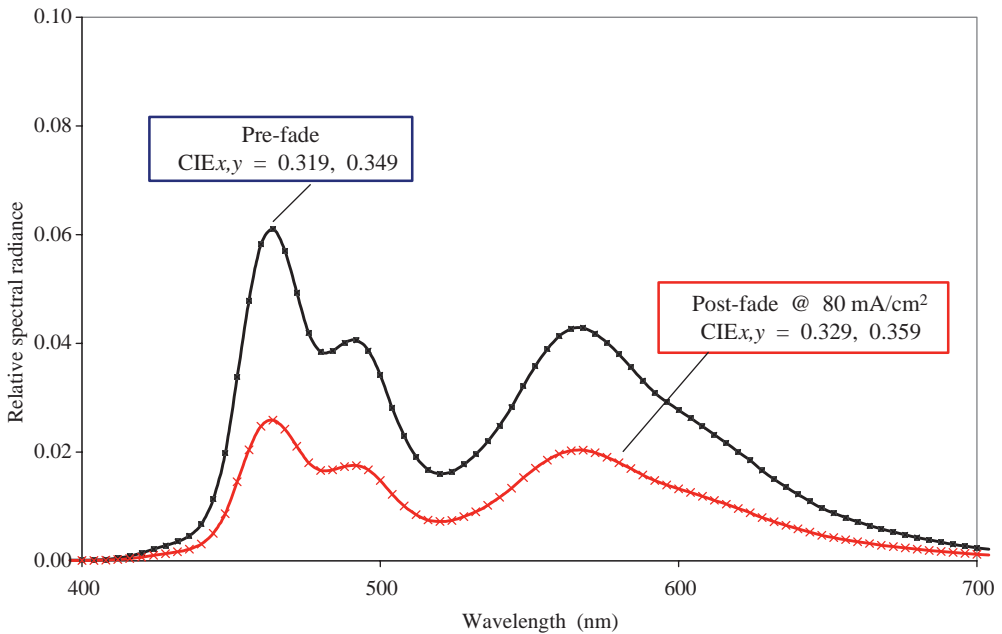


Figure 4.11 EL spectra of a stable 2-layer white device before and after operational fade (50% decay in luminance) at 80 mA/cm² DC testing

These devices have excellent color stability as the device ages during operation. Figure 4.11 shows EL spectra for a white OLED device before and after 50% operation at 80 mA/cm² current density. The EL spectra and the CIE coordinates are virtually unchanged (changes ≤ 0.003 CIE unit) during the operational stability. In fact, this is one of the important features of white OLEDs that are being considered for uses in display applications as shown in the later part of this chapter.

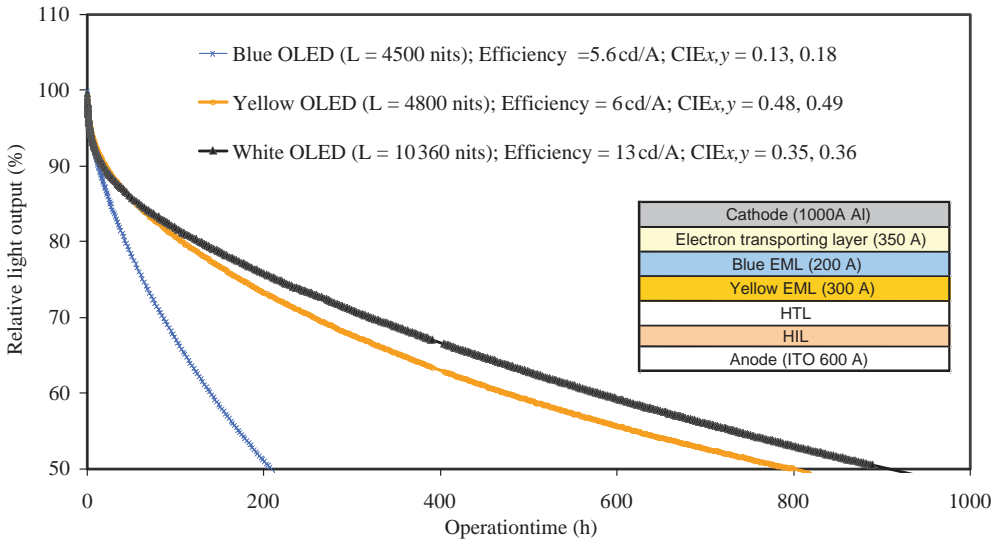


Figure 4.12 Accelerated aging of blue, yellow and white devices at constant current density (80 mA/cm^2) showing differences in operation stability. White structure is shown in inset. Blue device has only blue emitting layer and yellow device has only yellow emitting layer. The other layers are common

4.2.4 White stability comparison with other colors and the mechanism of operational stability

It is important to understand why white OLEDs have higher stability than other colors such as blue, green or yellow. Figure 4.12 shows the relative luminance loss as a function of time when blue, yellow and white devices were operated at a constant current density of 80 mA/cm^2 . The operational stability of the white OLED is relatively higher than other colors, even though the layer architecture is the same for all three devices. Earlier studies described two major degradation mechanisms influencing OLED stability. One is extrinsic, such as dark spot growth that is due to moisture/oxygen permeation, which may be controlled by a good encapsulation/desiccant methodology, described later in this chapter. The other is the intrinsic stability that relates fundamentally to device architecture, including the interfaces, carrier transport and materials stability. For green emitting devices, Aziz *et al.* have improved the stability by co-doping the hole-transporting material into the Alq3 emission layer. Aziz demonstrated that tris(8-hydroxyquinoline) aluminum cationic species formed by the excess of holes residing on Alq3 causes device instability. NPB doping into the Alq3 layer suppresses the accumulation of holes on the Alq3 molecule [19, 20]. However, this methodology has not worked well for the blue-emitting OLED and so blue has the lowest operational stability.

There are other reports where blue emitters have been stabilized to some degree by the uniform doping of the hole-transporting layer by an anthracene host [21]. In terms of the white OLED, even though the blue layer separately is very unstable, the two-layer white OLED, using the blue and yellow layers adjacent to each other, provide a very stable device. As described earlier, white emission is obtained by appropriately mixing the emission from the adjacent blue- and yellow-emitting layers in the OLED multilayer stack, as a result of

energy transfer from blue to yellow. The emission zone is hypothesized to be widely distributed in both the yellow and blue EML [22]. The spreading of the emission zone is the most probable cause for improved stability and efficiency. Also, because of the energy transfer from blue to yellow emitters, both emitters decrease at the same rate and the ratio of blue to yellow remains the same. This provides a stable color as a function of aging time. This is one of the important considerations for a full-color display and minimizes the effects on color balance and gray scale for the RGB and RGBW formats. Kanno *et al.* proposed the energy level diagram for the two-layer white OLED structure [18]. It is hypothesized that the non-emitting assist dopants, such as anthracene, which was doped in the hole transporting yellow emitting layer, has electron-transporting properties and adjusts the carrier balance to enhance emission. A similar effect occurred when the hole-transporting NPB assist dopant was added to the blue emission layer. The recombination zone was adjusted with the assist dopants in the interface between the orange and blue EML, which resulted spreading out of the electron-hole recombination zone.

4.2.5 Method of emitter selection to obtain suitable white color

Many combinations of emitters can be implemented to obtain a particular white point (e.g. D65). A method was developed to choose the component colors that make up the white OLED emitter. A simple method for making this selection is illustrated in Figure 4.13. As shown, the individual emitters can be plotted as a single point on the CIE 1931 x,y chromaticity (or CIE 1976 u',v' uniform chromaticity scale) diagram and connected by a line. If the line intersects the desired white point, the white point can be obtained by the appropriate combination of the two emitters by adjusting the relative peak heights. For example, Blue X (actually a blue-green color), in combination with Red X (a pure red), can provide

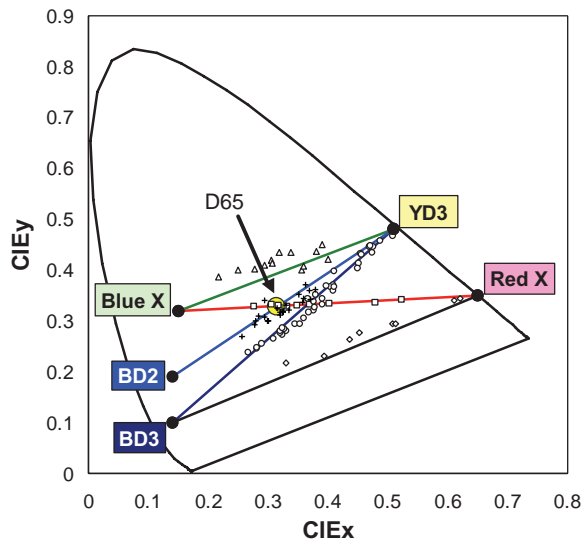


Figure 4.13 Combination of emitters to obtain D65 white point

the target D65 white point by adjusting the relative peak heights of these two emitters in the white emitting structure. Similarly, BD2 (another blue dopant from the Eastman Kodak Company) and YD3 (yellow dopant which is a derivative of rubrene) can be used to attain D65. However, the combination of BD3 (a pure blue emission) with Red X cannot achieve D65 and is a poor candidate for any system using a white emitter with color filter arrays (in this case, there is insufficient green). Slight changes in chromaticity coordinates may be made by adjusting the thickness of the layers to take advantage of cavity effects. However, these adjustments can only be used to fine tune the emission chromaticity coordinates and cannot be used to correct for major differences in the chromaticity coordinates from the target-display white point. This technique has been experimentally verified, as shown by the many data points (each representing a particular test device that was fabricated) plotted on the CIE 1931 x,y chromaticity diagram in Figure 4.13.

4.3 WHITE OLEDS FOR DISPLAY APPLICATIONS

Steady progress has been made towards producing full-color displays. Prototypes have been demonstrated by a number of organizations taking different fabrication approaches. Full-color displays can be achieved several ways, and the choice of technique mainly depends upon the display performance, such power consumption, lifetime and manufacturability [23–26]. Here, we will briefly review three main techniques that have been commonly used for patterning the individual colors in full-color OLED displays.

4.3.1 Methods of color patterning

The first patterning technique for defining the R-, G-, and B-emitting pixels is by precision shadow masking as shown in Figure 4.14. It uses a thin metal shadow mask (<50 μm thick) that is positioned in close contact with the substrate in order to define depositions within the appropriate regions of the substrate. The mask is aligned appropriately with the electrodes (typically ITO), and red, green and blue emitting layers are deposited. Three separate alignments/depositions are required and each of these steps may require 30 seconds to 2 minutes of process time. This method produces the highest efficiency and good color gamut, but it has significant disadvantages (process time, thermal expansion of the mask causing misalignment, defect generation caused by necessary contact with the substrate and high

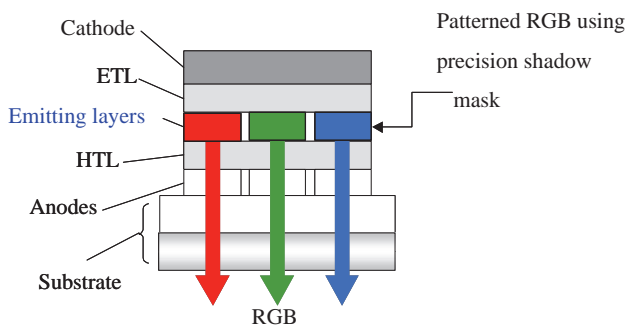


Figure 4.14 Methods of color patterning by R, G, B pixelation

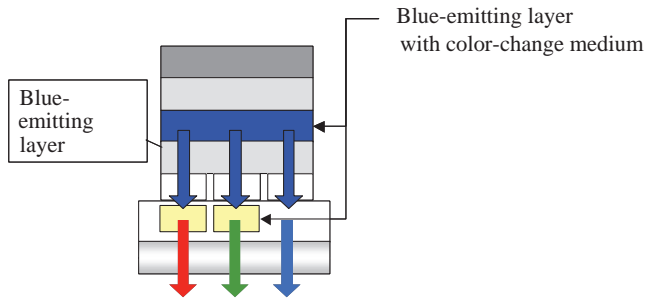


Figure 4.15 Method of color patterning using blue-emitting layer with color change medium

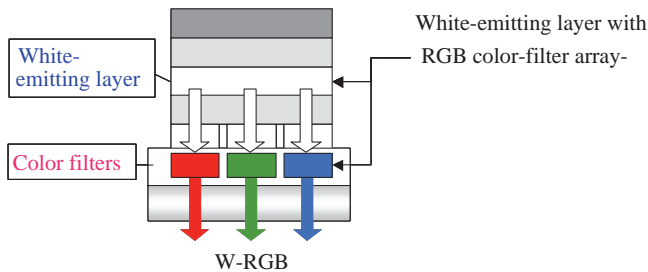


Figure 4.16 Method of color patterning using a white-emitting layer and color filters

cost. It is also difficult to manufacture masks with small apertures and scaling up to large substrate sizes is difficult. It is currently thought that the Gen4 size is the approximate maximum). This technique also becomes impossible for fabricating micro displays where the subpixels are only a few micrometers in size. Another major disadvantage is the differential aging of the R, G, and B pixels. In spite of technological innovations to improve the blue stability, blue is still the least stable emission color and it is difficult to maintain color balance over time because blue ages at a higher rate compared to blue and red. Other techniques to pattern individual R, G, and B emitting are being investigated, such as laser transfer and inkjet printing, but so far these techniques have not been proven to be manufacturable and scalable.

The second method is that of depositing an unpatterned blue-emitting layer and using a color filter array or a color change medium (Figure 4.15). It does not require a precision shadow mask, since blue emission is absorbed through the color conversion layer or color filters and is converted to either green or red light. As mentioned before, blue emitters typically have poor stability and efficiency, which may inhibit the usefulness of this technique, and consequently this approach is significantly disadvantaged for applications requiring high stability.

The third method is to provide the R, G and B emissions through the implementation of a white emitter combined with color filters (Figure 4.16). In the case of the white OLED with color filter arrays, it is expected that the manufacturing yield will be higher, and scalability to larger substrate sizes will be possible. Although the color filtering drastically reduces the transmitted light intensity, the high efficiency of the white OLED has led to performance that can be comparable to displays of the first-generation pixelated R, G and B emitters. An extension of this method that provides much power efficiency in display applications is described in section 4.3.3.



Figure 4.17 15-inch AMOLED (1280 × RGB × 720) using white technology and a color filter array on poly-Si TFT

4.3.2 OLED full color displays

The third method (described above), a non-shadow mask approach using a white emitter with R, G and B color filters formed on a substrate was demonstrated on a 15" display format on a poly-Si thin film transistor (TFT) backplane through a joint development effort between Sanyo and Kodak [15, 28]. The display using this method is shown in Figure 4.17. In addition to the avoidance of the precision mask, it has other attractive benefits, such as:

- reduction in the number of manufacturing steps (one or two emitting-layer depositions, rather than three separate depositions);
- more uniform degradation of the emission (red, green and blue emitters degrade at different rates); and
- it is enabled by the high-efficiency, stable white OLED formulations that have been recently developed in Eastman Kodak Company [29, 30].

White OLEDs are being used for manufacturing micro-displays. The micro-display format (size 0.72") allows the user to view a very large virtual video screen using goggles with appropriate optics. In 2001, eMagin Corporation introduced a high-resolution full-color active-matrix top-emitting micro-display on a silicon substrate for near-to-eye applications using a top-emitting white OLED and color filter array, with the color filter array being processed on the OLED structure.

There are other methods of color patterning, such as inkjet printing and laser thermal printing that do not require precision shadow masking. Inkjet printing technology is used for the patterning of soluble amorphous OLED materials. Successful implementation of inkjet patterning for AMOLEDs requires modification of the receptor substrate, such as a hydrophilic/hydrophobic surface patterning to confine the jetted drops. Although this method was used for small molecule OLEDs, it is mainly advantageous for polymer OLEDs.



Figure 4.18 Micro-displays by eMagin corporation. 0.72-inch AMOLED on silicon (800×600) using top-emitter white OLED and color filters. It is ideal for head mounted application. Information Display 2006, Vol. 22, No. 2, Amal Ghosh, Steven Van Slyke, 'The Challenges Ahead', p. 27, Copyright (2006). Reproduced by permission of The Society for Information Display

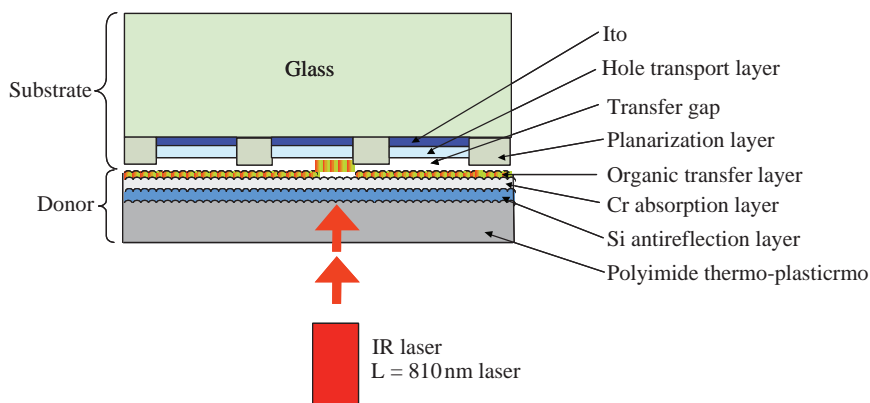


Figure 4.19 Schematic representation of the radiation-induced sublimation transfer (RIST) process. Information Display 2005, Vol. 36, Michael Boroson et al., 'Schematic of RIST Process p.972, Copyright (2006). Reproduced by permission of The Society for Information Display

Eastman Kodak Company and 3M Corporation developed laser thermal printing [31, 32]. This was meant for high-resolution digital patterning for potential applications, such as patterning OLED emitters, organic thin-film transistors and color filters. This process is similar to thermal printing where a donor sheet (blanket coated with appropriate emitting material) is placed adjacent to the substrate, and a laser is used to pattern-wise transfer the emitting material from the donor to the substrate. A schematic representation of the radiation-induced sublimation transfer (RIST) process developed by Boroson *et al.*, Eastman Kodak Company, is shown in Figure 4.19. In this example, the radiation source is an 810 nm laser diode beam, which is modulated into individually addressable channels to create 256 laser spots, $8.5 \times 20 \mu\text{m}$ in size. The donor includes a polyimide support ($75 \mu\text{m}$), a silicon anti-reflection layer (50 nm), a chromium absorption layer (40 nm) and an organic transfer layer (20–60 nm). The total reflectivity of the donor at the laser wavelength is $<7\%$ (including the air/polymer interface), resulting in highly efficient conversion of the laser energy to heat to sublime the organic transfer layer. In the RIST process, the organic material is

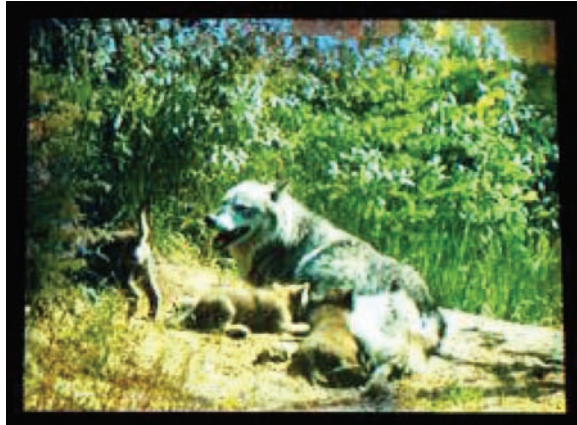


Figure 4.20 2.4-inch near QVGA AMOLED using RIST technology. SID 2005 Digest, Michael Boroson et al., 'Active matrix OLED patterned by the RIST process, p. 972, Copyright (2005). Reproduced by permission of The Society for Information Display

transferred to the substrate by vacuum sublimation; therefore, the donor and active portion of the substrate are spaced apart within the vacuum system to maintain a transfer gap of 1–10 μm . Radiation is applied only to the areas where material transfer is desired. The organic transfer layer (emissive layer in this example) sublimates and re-condenses on the substrate. Singlet and triplet dopants and hosts, as well as mixtures of multiple dopants and hosts, can be coated onto the donor for transfer by RIST.

Figure 4.20 shows a photograph of a 2.4-inch near-QVGA AMOLED (190K pixels) patterned by the RIST process. Sub-pixel pitch for this display was $57 \times 165 \mu\text{m}$. The hole-injection layer, hole-transport layer, electron-transport layer and cathode were evaporation-deposited over the entire display area. The red, green and blue emission layers were patterned using the non-contact RIST process. Individual pixels looked uniform under magnification, indicating no misalignment or cross-contamination of the emission layers. This technique eliminates the need to precision shadow mask. However, the operational luminance stability of these devices is lower than those fabricated using conventional thermal evaporation technique. Also some of the luminance materials were found to be degrading during the transfer process, thus limiting the usefulness of this non-contact process.

4.3.3 Development of RGBW 4-pixel pattern

Although white plus color filter technology does not require precision shadow masking, much of the emitted white light is absorbed by the color filters in the white – RGB (W-RGB) approach, resulting in low luminance efficiency of the R, G, and B light. This leads to much lower display efficiency compared to the directly patterned RGB format, especially given that significantly improved performance of R, G and B emitters have been demonstrated recently [33,34]. Therefore, it is difficult to envision a state-of-the-art full-color OLED display that uses a white OLED in combination with RGB color filters and that is as efficient as displays fabricated with direct-patterned emitters. Recently, it was shown that full-color AMOLED displays that use a white emitter with an RGBW pixel pattern (W-RGBW) provide a substantial reduction in power consumption for imaging applications compared to analogous displays that use a white emitter and an RGB (W-RGB) pixel pattern. Power

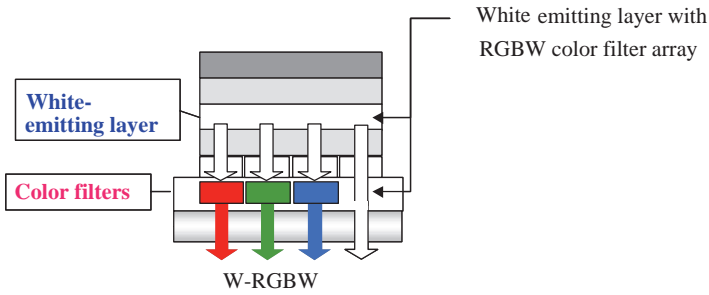


Figure 4.21 4-pixel RGBW patterning using white OLED and color filters

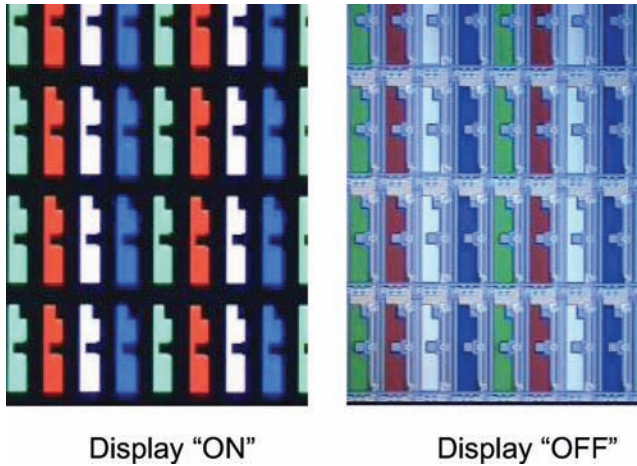


Figure 4.22 RGBW displays showing ‘ON’ and ‘OFF’ pixels

consumption is important for AMOLED TV applications because lower power leads to lower operating temperatures, which results in longer lifetimes of the OLED layers. Figure 4.21 shows the RGBW pixel pattern. The unfiltered W subpixel enables the reduction in power consumption because most images contain a large portion of unsaturated color, and the highly efficient white pixel is, consequently, used frequently. This results in a power consumption of about one-half that of the analogous W-RGB display. The key to the reduced power of the W-RGBW format is a high-efficiency white emitter that is optimized to the target display white point (e.g. D65). It was shown that, for minimum power consumption, the white OLED emission should match the white point of the display (e.g., D65) because a large amount of the scene content for imaging applications is nearly neutral in color and, therefore, heavily utilizes the unfiltered white subpixels [23–26].

4.3.4 Full-color displays based on the RGBW format

Full-color displays, both in small and large size, were demonstrated in the W-RGBW format. Recently, Sanyo Electric introduced a 2.2-inch AMOLED Xacti HD1 digital camera based on the W-RGBW concept [18, 35, 36]. Figure 4.21 shows a typical W-RGBW pixel pattern in a 2.2-inch AMOLED display prototype. Both ON and OFF states are shown in Figure 4.22.



Figure 4.23 40-inch OLED display demonstrated by Samsung Electronics at SID 2004. Chung *et al.* “Development of 40-inch display” *IMID* 2005, p. 781. Copyright (2005). Reproduced by permission of The Society for Information Display

The 4-pixel W-RGBW pattern was also used to fabricate a large 40” OLED television (TV) (Figure 4.23). This demonstration for a large-sized display has shown that the AMOLED technology based on white OLED is ready for commercialization and is ready to enter the TV size display market that is currently dominated by the liquid crystal display (LCD) and the plasma display panels (PDP).

4.3.5 White OLED structures for improved color gamut

As described above, a white structure consisting of a two-emission-layer configuration, based upon separate yellow- and blue-emitting regions, has excellent stability and efficiency. However, the two-layer Y/B white structure is deficient in the green color. By replacing the yellow layer with green- and red-emitting layers, a three-emitting layer white structure was prepared. The device architecture and the emission spectrum are shown in Figure 4.24. Separate red, green and blue emission peaks were designed to match RGB color filters, resulting in excellent color gamut. The performance of this three-emitting layer white structure was further improved by inserting a thin (10–40 Å) yellow-emitting layer between the red- and blue-emitting layers. This four-emitting layer white structure and the EL spectrum are shown in Figure 4.25. Compared to the three-emitting layer structure, the four-emitting layer white OLED structure provides higher efficiency and similar color gamut as compared to three-layer white structure.

4.3.6 Low-voltage white OLEDs

The major contribution to power efficiency is the operating voltage needed to drive OLED at the required brightness, thus lowering the drive voltage is important for minimizing the

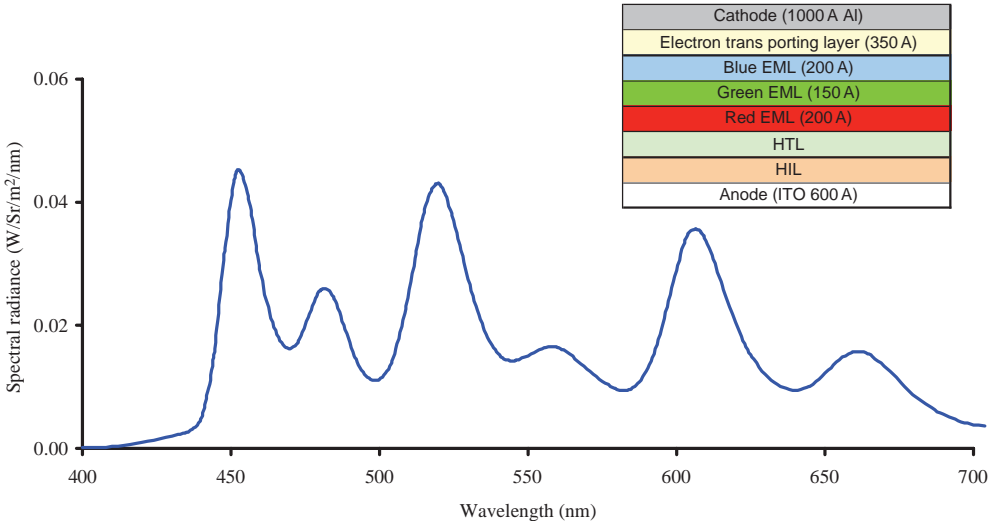


Figure 4.24 Three-layer white formulation for improved green color

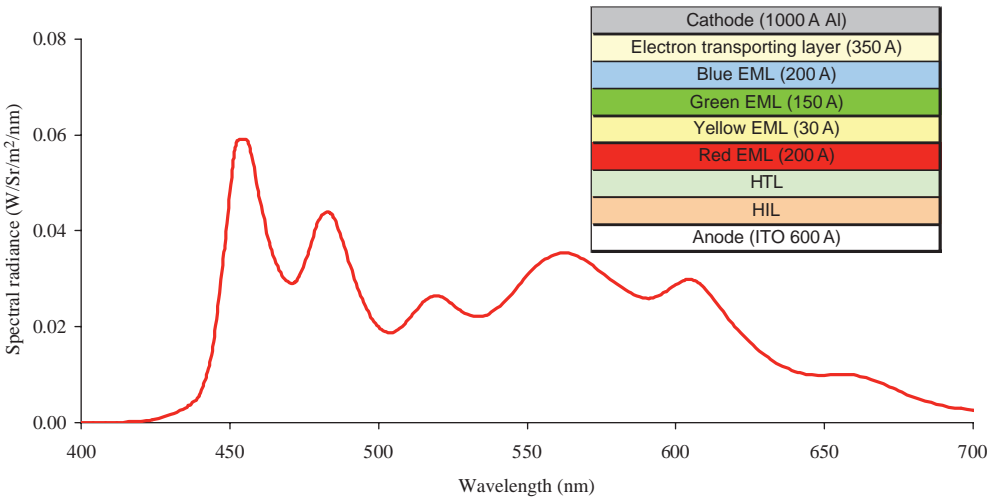


Figure 4.25 Four-layer white formulation for improved green color and efficiency

display power consumption. A minimum threshold voltage is needed for the generation of light at a certain wavelength, which is given by the energy wavelength relation, such as E (eV) = 12.3194/wavelength (nm). Additional voltage drop occurs due to contact resistance and space charge limitations for the common OLED design. OLED voltage reduction has been achieved by several techniques, such as doping the hole-transporting and electron-transporting layers with p- and n-type dopants, respectively, and improving the hole injection and electron injection by incorporating interface layers such as the HIL between the ITO anode and HTL, and the EIL between the ETL and cathode [37–43]. Figure 4.26 shows the current density as a function of drive voltage for a low voltage white OLED and a

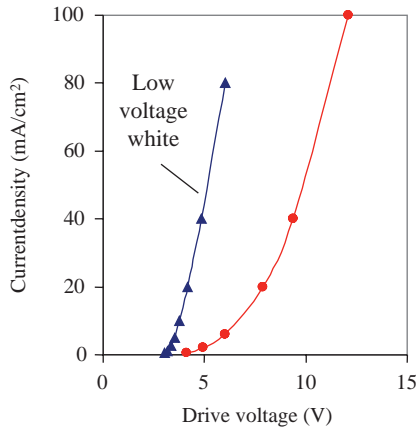


Figure 4.26 Low drive voltage white OLED

conventional control device. The low voltage device has 10.7 cd/A luminance efficiency at 4.2 V and 20 mA/cm² current density. In identical conditions, the control device has 11 cd/A luminance efficiency at 8 V. The white colors for these devices were close to D65. The low voltage white OLED operates at relatively low voltage as a result of minimizing the layer thickness, the use of new electron transport layer, and incorporating a more conductive blue host into the device structure.

4.4 OLED TANDEM ARCHITECTURE

OLEDs are current driven devices and with the luminance proportional to the current density. In order to achieve high brightness required for TV display applications, the OLED has to be operated at a relatively high current density, which shortens its lifetime. Thus, it is critical to improve luminance efficiency of the OLED device while operating at the lowest possible current density that is required for intended luminance level. Clearly, in order to lower the current density and the power consumption further, an increase in the white OLED efficiency is necessary. Of course for white OLEDs, any white efficiency increase must be accomplished while maintaining the required white spectrum, with emission peaks matching the R, G, and B color filters. This improvement in luminance efficiency and color gamut of the white-emitting structure can be achieved by utilizing a tandem format, where two or more low-voltage white units (stacks) are joined by a ‘PN’ connector. Tandem structures can also be optimized to obtain the highest efficiency as well as a white point close to D65. As noted above, obtaining the D65 white point with the unfiltered emitter is critical for minimizing the power consumption in the RGBW full-color display format. Matsumoto *et al.* [44] and Liao *et al.* [45] have shown that high efficiency at lower current density could be obtained with tandem structures, where multiple electroluminescent (EL) units (stacks) are connected electrically in series using an optically transparent PN connector between adjacent EL units. With this format, since each of the emitting units is connected in series, the drive voltage increase is expected to be linearly proportional to the number of units included in the structure. The quantum efficiency (photons emitted per electron

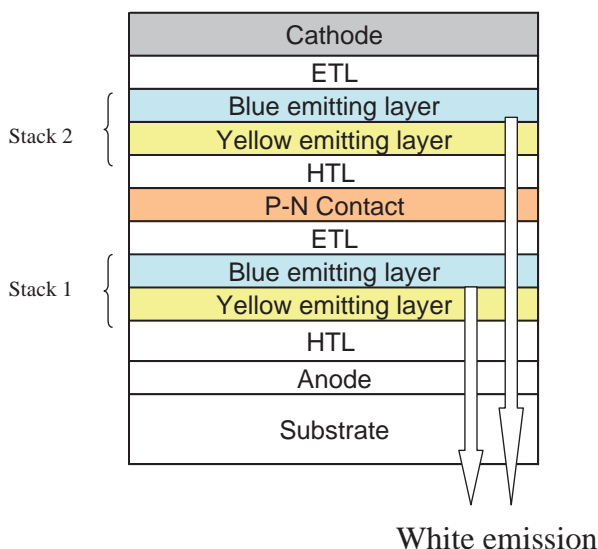


Figure 4.27 Schematic of the 2-stack tandem white OLED

injected) is also expected to increase linearly with the number of EL units, which results in a significant improvement in the operational stability (from the same initial luminance) as a result of the reduced current density required with the more efficient structures. In the Liao's work, it was found that the drive voltage, efficiency and stability behaved in this manner. Efficiencies of 32 and 136 cd/A were demonstrated for green fluorescent and phosphorescent devices, respectively, with three EL-unit tandem architecture, but with drive voltages greater than 20 V.

4.4.1 White OLED tandem architecture

In order for the tandem architecture to be useful for display applications, the drive voltage should be as low as possible. This means that the voltage drop across each of the emitting units must be reduced so that the overall drive voltage (obtained by summing the voltage drop across each EL unit) is within an acceptable range, compatible with the drive electronics and the power consumption specification for the display. Low-voltage two-emitting layer white structures consisting of blue- and yellow-orange-emitting layers within each EL unit were used for the tandem structures based on white OLEDs (Figure 4.27). The PN connector was an organic and optically transparent material designed to provide the required carrier injections with essentially no voltage loss [46].

4.4.2 Optimization of tandem stacks

It was found that, unlike the monochrome green device, the luminance efficiency of the white tandem device does not linearly increase with the number of white-emitting EL units

Cathode	
ETL	350 Å
White EL unit	400 Å
HTL	→ 0 - 1200 Å
P-N contact	100 Å
ETL	350 Å
White EL unit	400 Å
HTL	600 Å
Anode	200 Å
Substrate	

Figure 4.28 Optimization of two-stack white tandem

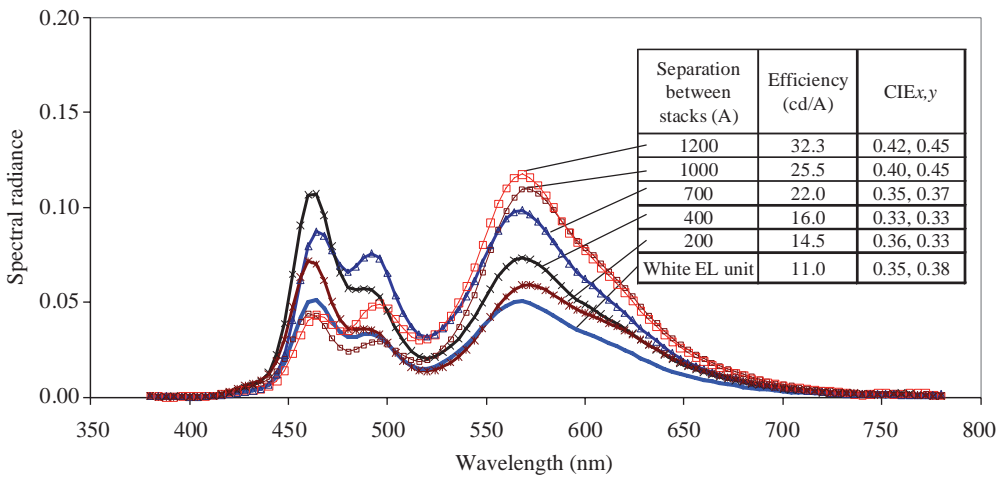


Figure 4.29 Variation of EL spectrum with varying separation between two white units of the tandem

in the stack. Both the luminance efficiency and the white point of the tandem structure depend strongly on the separation between the EL units. Figure 4.28 shows the device architecture and Figure 4.29 shows the EL spectra of two EL-unit tandem devices where the separation (D) between the two units was varied between 0 and 1400 Å by adjusting the HTL thickness as shown. In fact, varying the HTL thickness within each EL unit is the best way to optimize the emission because the drive voltage is relatively unaffected by thickness of this layers. The single-EL unit control is shown by the solid curve and has a luminance efficiency of 11 cd/A at 20 mA/cm², with CIE x,y coordinates of 0.35, 0.38. Both the luminance efficiency and color varied significantly with the separation distance. In this example, the efficiency was as high as 32.3 cd/A and as low as 14.5 cd/A, but the chromaticity was not constant. This effect is caused by the complex optical interference that occurs within the structure, with the most important factors being the distance between the emitting units and the reflective cathode and between the emitters and the ITO/glass interface [47]. As discussed, it is important to optimize the white emission to D65 for displays with the RGBW format, and the optical stack was optimized to provide a two-stack tandem white with an emitting color near the D65 point.

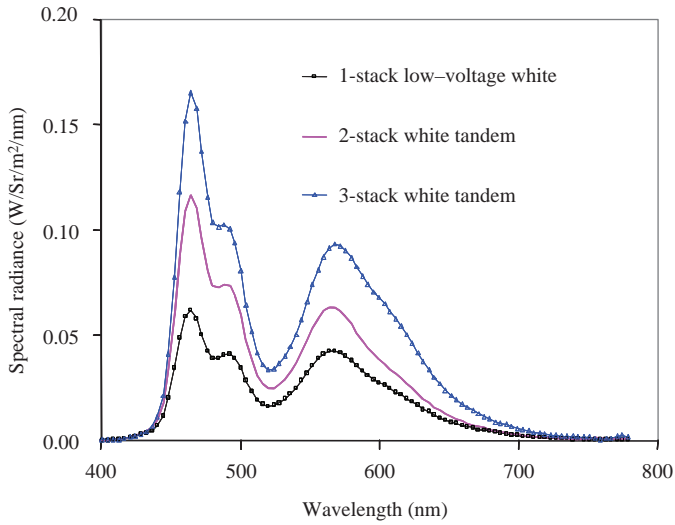


Figure 4.30 EL spectra for 1-, 2- and 3-unit white tandems optimized for D65 white point

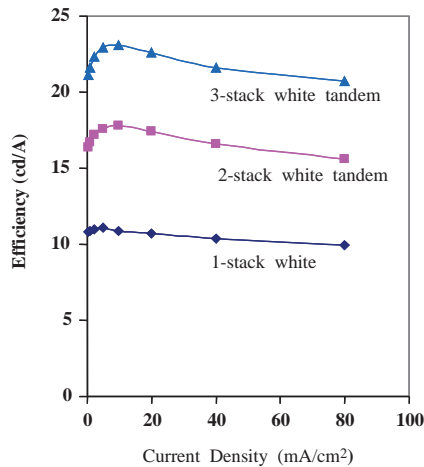


Figure 4.31 Luminance efficiency as a function of current density for 1-, 2- and 3-unit white tandems

4.4.3 Performance of tandem structure

Figure 4.30 shows the EL spectra of 1-, 2- and 3-unit tandem structures with chromaticity near D65 (measured at 20 mA/cm^2). The luminance efficiency vs. current density curves for these devices are shown in Figure 4.6. The single-stack device has an efficiency of 10.7 cd/A , a drive voltage of 4.2 V , and CIE x,y of $0.32, 0.35$. The 2-stack tandem device has an efficiency of 17.4 cd/A , drive voltage of 8.7 V , and CIE x,y of $0.30, 0.34$ and the 3-stack device has an efficiency of 24.6 cd/A , drive voltage of 13.1 V , and CIE x,y of $0.32, 0.34$.

Table 4.1 Performance of white tandem OLEDs

White Structure	Number of stacks in white tandem	Drive voltage (V)	Luminance efficiency (cd/A)	CIE _x	CIE _y	RGBW Power (mW)	RGB Power (mW)	NTSC _{XY} Ratio
2-layer white	1	8.0	11.0	0.33	0.33	289	657	61%
2-layer low voltage white	1	4.2	10.7	0.32	0.35	228	527	63%
2-layer low voltage white	2	8.7	17.4	0.30	0.34	194	448	63%
2-layer low voltage white	3	13.1	24.6	0.32	0.34	172	409	62%
4-layer white	1	4.3	9.9	0.32	0.35	236	557	71%
4-layer white	2	8.6	17.5	0.33	0.37	216	451	70%

These results give approximately 1.7X and 2.3X improvement in efficiency for the 2-unit stack and 3-unit tandem structures, respectively. However, the drive voltage shows a linear increase with increasing number of stacks, which is similar to monochrome green devices. The lack of linearity in the efficiency with the stack number is primarily due to the difficulty in optimizing both the yellow and blue-green portions of the emission spectrum at essentially the same emitting planes within the structure.

Table 4.1 shows the performance of the one, two and three EL-unit tandem white OLED structures at 20 mA/cm² and the predicted power consumption modeled for 2.16-inch diagonal AMOLED displays with both the RGB and RGBW formats. The power consumption was predicted using a model developed to evaluate the performance of the various white formulations, using the white efficiency and spectral data, as well as the drive voltage at the required current density as input to calculate the average power consumption required for a set of 13000 digital camera images. In all cases, the target display white point was D65, the luminance was 180 cd/m², and the calculations included a circular polarizer with 44% transmittance. The details of the power calculation model are given elsewhere [25]. As shown, the improved luminance efficiency (cd/A) of the white emitter as the number of EL units increases results in lower power consumption, even though the efficiency does not increase linearly with the number of EL units in the OLED stack. This results, in part, from the fact that the drive voltage required to provide the same display luminance does not scale linearly with the number of stacks (the current density required is lower for the higher efficiency configurations). In fact, the increase in the drive voltage required to provide the same luminance is more than offset by the lower current density required, hence the reduced power consumption with the higher efficiency formats.

These structures also show good operational stability for both luminance decay and voltage rise. Simple test devices (0.1 cm²) were operated under DC conditions at initial luminance level of 1000 cd/m². Figure 4.32 shows the luminance stability as a function of operational time for the three devices shown in Figure 4.6. The stability of the new low-voltage white OLED is similar to earlier published white structures [17], which operated at approximately twice the drive voltage at equivalent luminance levels. The luminance stabil-

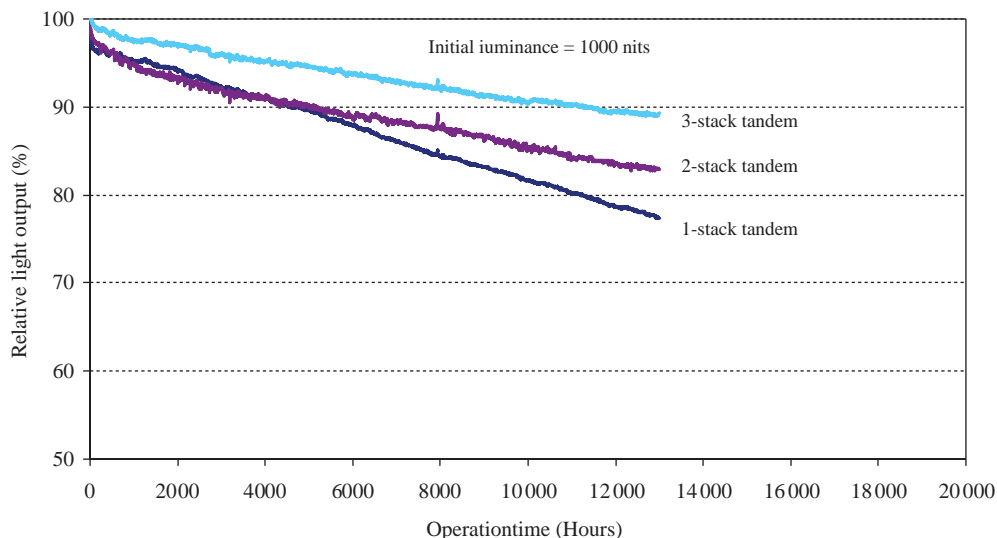


Figure 4.32 Operational luminance stability of 1-, 2- and 3-stack white tandems

ity is significantly improved for the tandem structures because of the lower current density required for the same luminance level. After operating for over 13 000h, the extrapolated half-life time at 1000 cd/m² for the ‘single-stack’ low-voltage white OLED is expected to be >50 000h. For the two EL-unit tandem structure, it is expected to exceed 70 000h and for the three EL-unit tandem structure, it is expected to exceed 110 000h. It is also noteworthy that the drive voltage increases very slowly for all of these configurations, with an expected increase of less than 1 V when the luminance has decayed to half of the initial level. It is important to recognize that the luminance stability is dependent upon both the OLED efficiency change with operation and the backplane changes during operation that reduce the current being supplied to the OLED structure (thus reducing the luminance output). By selecting the proper tandem stack and the stable TFT backplane display, a lifetime target of >50 000h can be achieved, which is better than or equivalent to LCDs and plasma display technologies.

4.4.4 Tandem structures for improved color gamut

As described in Section 4.3.5, the three-layer and four-layer white OLEDs provide higher color gamut than the two-layer white. Figure 4.33 shows the EL spectra of the four-layer white (single EL-unit) and two-stack tandem structures designed for improved color gamut expressed in terms of NTSC ratio. This is the ratio of the area of the triangle defined by the primary colors of interest divided by the area of the triangle defined by the primary colors recommended by the National Television System Committee (NTSC) of USA. The NTSC recommended color coordinates (CIE_{x,y}) are: red: (0.67, 0.33); green: (0.21, 0.71); and blue: (0.14, 0.08). The emission peaks in the blue, green and red portions of the spectrum (Figure 4.33) result in an improved color gamut relative to the two-peak white devices described

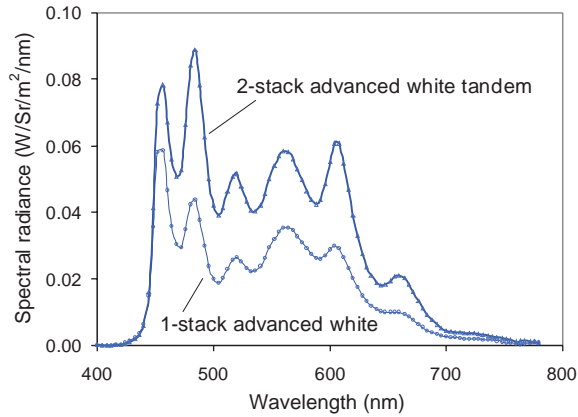


Figure 4.33 One- and two-stack white tandem structure for improved color gamut



Figure 4.34 14.1-inch a-Si RGBW AMOLED display using tandem white technology

above for the same filter set. The color gamut using typical LCD TV color filters was calculated to be greater than $>76\%$ NTSC $_{x,y}$. Thus, for a RGBW full-color display, a color gamut of $>76\%$ NTSC $_{x,y}$ ratio is achievable with the combination of OLED emission (Figure 4.33) and typical LCD TV color filters.

4.4.5 Full-color displays using white OLED tandems

A 14.1-inch prototype (307.2 mm \times 184.3 mm) W-RGBW AMOLED display (Figure 4.34) was demonstrated on an a-Si backplane, in a joint collaboration by the Eastman Kodak Company and Samsung Electronics, Korea [48]. This display used the tandem white architecture (with conventional LCD color filters) on an a-Si backplane. The OLED structure was deposited on 300 \times 400 mm size substrates, using an in-line pilot machine in collaboration with the ULVAC Company, Japan. The deposition tool was equipped with linear sources for the organic layer depositions. The details of the evaporation sources are described

later in Section 4.8.1. These high-resolution bottom-emitting WXGA (1280×768) displays showed excellent performance, with a peak luminance of 500 cd/m^2 , and had average 15 W power consumption while showing video (approximately 18% ON), and color gamut at 78% NTSC ratio. Other features of this display were:

- white emission point: $\text{CIEx,y} = 0.32, 0.34$;
- display thickness: 1.8 mm;
- subpixel size: $120 \mu\text{m} \times 120 \mu\text{m}$ (106 ppi);
- wide viewing angle ($>170^\circ$); and
- darkroom color contrast ratio >20000 .

4.4.6 White tandem and improved color filters for wide color gamut

As described above, the color gamut using the white tandem and typical color filters is approximately the same as LCD displays with cold cathode fluorescent (CCFL) backlights (approximately 72–78% NTSC ratio) for TV applications. While a well-tuned white OLED spectrum can achieve decent color gamut, it is difficult to achieve $>80\%$ NTSC ratio by tuning of the white emission peaks alone. This is primarily due to the broad nature of the commercially available LCD color filters. The large overlap in the transmission between the different colors limits the color purity of the individual color through the color filters. The LCD industry is increasing the color gamut by improving the backlight technology, for example, by using LED backlight, which has characteristically very narrow emission peaks. In order to achieve better color gamut for the AMOLED display, both the white OLED spectra and the color filters must be improved. This section describes the development of a tuned tandem OLED white and a set of color filters that were developed at the Eastman Kodak Company to achieve wider color gamut, i.e. greater than 100% NTSC ratio.

Curves (a), (b) and (c) in Figure 4.35 are EL spectra of two-stack tandems that can be produced based on the two-, three- and four-emitting layer white OLEDs, respectively. Curve (d) is the two-stack tandem using the combination of two-emitting layer white and three-layer white OLEDs. Results indicated that the two-stack tandem based on two-emitting layer (Y/B) white and three-layer (R/G/B) white combination provided the best efficiency and color gamut [49]. This two-stack tandem was then optimized for D65 color and used in combination with the new color filters developed at the Eastman Kodak Company. In all of the following discussions, “color filters” developed at the Eastman Kodak Company are films prepared by spin coating aqueous dispersions of pigment blends desired to achieve high gamut when cascaded with a typical 4-emitting layer two stack tandem OLED. It should be kept in mind that these dispersions must be formulated into color resist for processing on an appropriate OLED backplane.

The new color filter transmission spectra are shown as dark color curves, along with emission from the white tandem OLED, in Figure 4.36. The new color filters have been developed based on the use of new color-forming chemistries and micro-milling processes and are used to alter the optical characteristics of color pigments [50]. Figure 4.36 also shows typical LCD color filters (light color curves). These improved color filters, when matched with the AMOLED emission spectrum, result in an increase in the color gamut to 102% (NTSC x,y ratio). Higher purity G, B and R colors are obtained when the white OLED

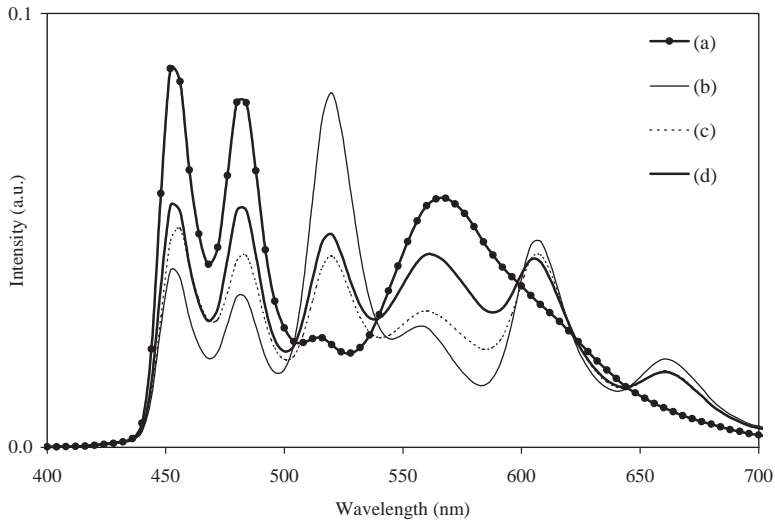


Figure 4.35 EL spectra of two-stack tandems of various white combinations

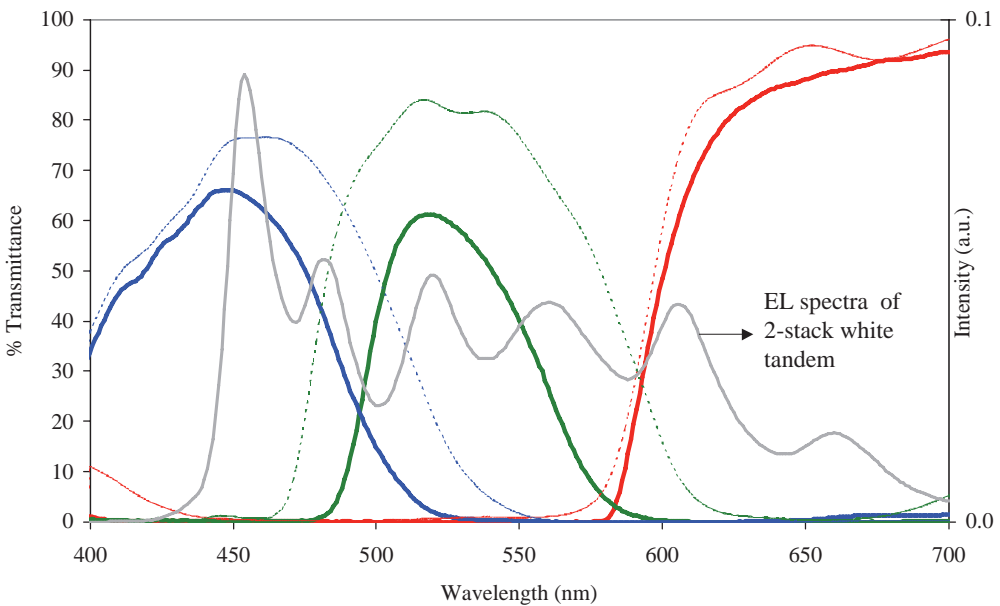


Figure 4.36 White emission spectrum and transmittance of commercial LCD color filters (light color curves) and Kodak's improved color filters (dark color curves)

spectrum is transmitted through these filters due to narrow bandwidth of the B and G filters and sharper cutting edge of the R filter. The R, G and B emission spectra, obtained by cascading the white spectrum through the filter spectrum, can be seen in Figure 4.37. The bandwidth of the transmitted green and blue peaks (solid curves shown in Figure 4.37) is

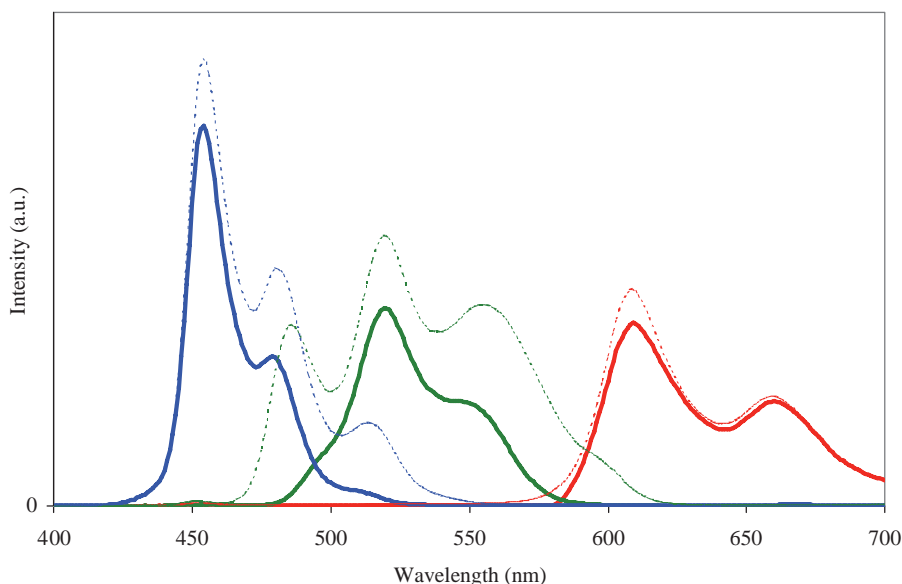


Figure 4.37 RGB emission spectra obtained from commercial LCD color filters and Kodak's improved color filters

Table 4.2 RGB chromaticity and color gamut obtained from commercial LCD color filters and Kodak's improved color filters

Color filter set	Red (CIE _x , CIE _y)	Green (CIE _x , CIE _y)	Blue (CIE _x , CIE _y)	%NTSC _{xy} Ratio
LCD TV filters	(0.647, 0.343)	(0.276, 0.592)	(0.130, 0.111)	67.7
Kodak's filters	(0.663, 0.332)	(0.208, 0.708)	(0.139, 0.057)	101.2

much narrower with Kodak's improved color filters, as compared to that obtained using LCD filters (light curve shown in Figure 4.37). The chromaticity in the 1931 CIE diagram and color gamut obtained with these primaries are shown in Table 4.2. The color gamut of 101.2% NTSC ratio is obtained using Kodak's improved color filters, whereas it is only 67.7% NTSC ratio with the LCD filters.

Figure 4.38 shows the 1931 CIE chromaticity diagram with the color triangles obtained from a combination of the tandem white OLED with the LCD color filters and with the improved filters designed by Kodak. The NTSC primaries are also shown. The green and blue primaries are dramatically improved using Kodak's filters, resulting in a larger area triangle. This demonstrates that the use of white tandem technology, combined with properly designed color filters, can provide AMOLED displays with color gamut exceeding 100% NTSC ratio. Note that the best color gamut that can be obtained by patterned RGB emitters without color filters (and without the use of enhancement techniques such as the microcavity effect) is 80–85% NTSC ratio. This is another key advantage of the white OLED plus color filter technology.

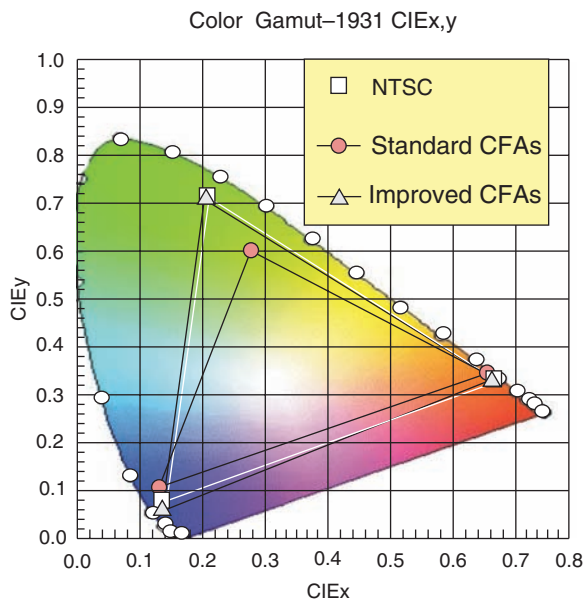
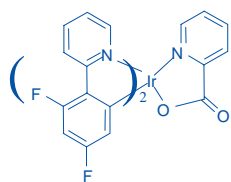


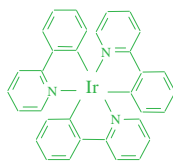
Figure 4.38 CIE_{x,y} plot showing enhanced color gamut using a combination of tandem white OLEDs and improved color filters to give color gamut >100 % NTSC_{x,y} ratio

4.5 WHITE OLEDS BASED ON TRIPLETS

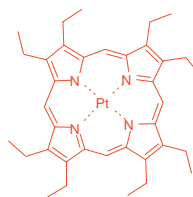
As described in the previous sections, fluorescent-based singlet white OLED systems have demonstrated pure colors, good efficiency, excellent lifetime and their usefulness both for display and SSL applications. However, their power efficiency is still lower than the phosphorescent triplet materials. Fluorescent emitters can have internal quantum efficiencies of up to 25%, which is the theoretical maximum value based on well-known spin statistics. However, the phosphorescent emitters can have the internal quantum efficiency of 100%, as they harvest both singlet and triplet excitons. Significant progress has been made in demonstrating the usefulness of monochrome phosphorescent materials as green and red emitters. Some of the most commonly used phosphorescent dopants are shown below.



Irpic



Ir(ppy)₃



PtOEP

These molecules have an efficient intersystem crossing between the singlet and triplet states, and they have a short (<ms) recombination lifetime. External quantum efficiencies of 30% are easily obtained at low current densities (0.1 to 1 mA/cm²), and power efficiencies of 20lm/W are easily obtained at a 1000 nits level. The progress of these monochrome phosphorescent dopants is reviewed in several prior publications (51–54).

4.5.1 White based on fluorescent and phosphorescent emitters

Baldo *et al.* [55] and D'Andrade *et al.* [56] reported high-efficiency electrophosphorescent white-emitting devices with a triple-doped emissive layer [57]. Red, green and blue phosphorescent dopants are doped in wide band-gap host materials. Three dopants in EML are: 2 wt% iridium (III) bis(2-phenyl quinolyl-N,C^{2'}) acetylacetonate (PQIr) providing red emission, 0.5 wt% fac-tris(2-phenylpyridine) iridium (Ir(ppy)₃) for green emission, and 20 wt% bis(4',6'-difluoro-phenylpyridinato)tetrakis(1-pyrazolyl)borate (Fir6) for blue emission, all doped into a wide energy gap p-bis(triphenylsilyl)benzene (UGH2) host. Varying the dopant concentration ratios, typically with blue having the highest concentration followed by green and red, controlled the balance between the three emission colors.

The device has a power efficiency of >20 lm/W at 1000 cd/m² by optimizing the thickness of the layers for low voltage, efficiently confining charge and excitons within the emission layer, and using direct-triple-exciton formation on a blue dopant. The power efficiency of these OLEDs can further be enhanced by the use of p and n doping based on the intentional doping of the charge carrier transport layers. Reduction of the operating voltage by the use of an intentionally doped transport layer leads to higher power efficiencies. Power efficiencies of 35 lm/W at 100 cd/m² and 25 lm/W at 1000 cd/m² brightness were obtained [58]. No operational stability data was reported for these devices. Therefore, the utilization of phosphorescent emitters for white suffers from lack of suitable blue phosphorescent emitter materials that combine a deep blue color, high current efficiencies and lifetimes suitable for commercial applications. However, the high efficiencies achieved with a phosphorescent white OLED set the benchmark for future approaches for all triplets for white light generation.

In the absence of a suitable stable blue phosphorescent emitter, a hybrid white OLED system was developed where a blue fluorescent dopant, together with red and green phosphorescent, was used in the EML. In this device, the blue fluorescent dopant harvests singlet excitons, and the lower energy triplets diffuse through the conductive host to directly excite the green and red phosphors.

4.5.2 Hybrid tandem-white OLEDs

Another approach for high efficiency is to use a stacked electrophosphorescent element that is connected by a charge-generating layer [57–60]. Recently tandem white OLEDs based on the combination of fluorescent (F) and phosphorescent (P) emitters were reported. A charge generation layer of transparent MoO_x is used as a connecting layer. The structure of a two-stack hybrid white tandem is shown in Figure 4.39. External quantum efficiency of 33% and power efficiency of 20 lm/W was obtained for a two-stack tandem. For a three-stack tandem, external quantum efficiency of 53% and power efficiency of 22 lm/W was

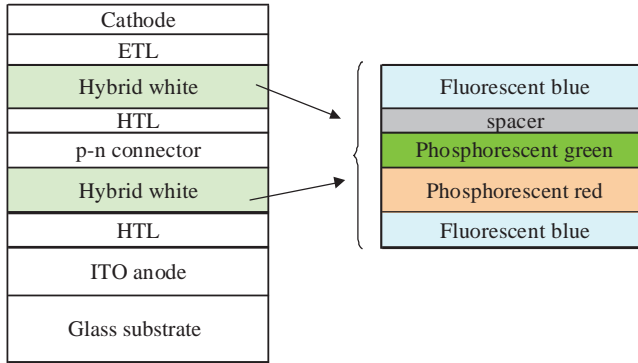


Figure 4.39 Two-stack tandem using white OLED obtained by combination of fluorescent blue and phosphorescent red

obtained. The color coordinates of these tandem are CIE $x,y = 0.38, 0.44$. These results demonstrate that white electrophosphorescent tandem OLEDs constitute a promising route to achieving high brightness and an efficient source for indoor lighting, if the stability of these can be increased to the specifications set forth in Section 4.7. Further enhancement in power efficiencies is possible with the p and n doping technology and an out-coupling layer (Section 4.7.3).

4.6 WHITE OLEDs BASED ON CONJUGATED POLYMERS

Electroluminescence from devices based on poly(p-phenylenevinylene) (PPV) was invented just after the discovery of small molecule OLEDs [61]. The manufacturing simplicity of polymer light-emitting diodes (PLEDs) provided an incentive for possible low-cost manufacturing. The PLED device structure also contains fewer layers than the small molecule OLED structure. With solution processing, one can think about large-area displays that do not require precision shadow masking for pixel patterning. This approach was validated when a 40" OLED display was fabricated by Seiko Epson using a Gen 5 inkjet patterning system and was shown at SID 2005. However, the inkjet printing displays did not provide the sufficient lifetime required for display applications. Introduction of a new hole-injection layer material by Dupont provided both improved efficiency and stability [62]. Progress in white PLEDs is slower than the small molecule white OLEDs, due to lack of efficient blue-emitting polymers. White polymer OLEDs were fabricated by spin coating or inkjet printing and by blending blue- and red-emitting polymers [63–65]. In the blending system, the dopant can be excited directly by capturing the charge carriers or by an energy transfer from the host to the guest. As a result, light emission can come from both the host and the guest, the combined effect being high efficiency. Incomplete energy transfer from the host to the dopant is necessary to achieve a white light. However, white PLEDs made by polymer blending show color variation that is due to well-known phase separation and results from different turns on voltages of red and blue polymers. A two-layer system, using the emission layers of a polyfluorene-based (PFO) blue and a MEH-PPV polymer-blended layer, was

employed. The white device had modest efficiencies of 4.7-cd/A-luminance efficiency and 2-lm/W-power efficiency [65]. Kwon *et al.* reported a successful development of WOLEDs using a single polymer: polyfluorene derivatives with 1,8-naphthalimide chromophores chemically doped onto a polyfluorene backbone [66]. Optimization of the relative content of 1,8-naphthalimide derivatives in the polymer resulted in white light emission with $CIE_{x,y} = 0.32, 0.36$ from a single polymer. The performance of the ITO/PEDOT:PSS/polymer/Ca/Al, again, gave a modest efficiency of 3.8 cd/A and 2.1 lm/W power efficiency. It is apparent that the efficiency and stability of the white polymer OLED is still an issue and the performance is significantly lower than the device using singlet and phosphorescent dopants.

4.7 WHITE OLEDs FOR SOLID-STATE LIGHTING

The drive towards the use of white-emitting solid-state lighting was mainly based upon the initiatives from the US Department of Energy (DOE) [7]. Inorganic LEDs are effective 'point source' lights, whereas OLEDs are excellent 'diffuse' large-area light emitters. Because of their thin device structure and low turn-on voltage, OLED lights can be integrated into ceiling fixtures. OLEDs can also be used in less demanding lighting applications, such as specialty colored lighting, low-to-medium backlights for portable electronics, interior signage, and headgear and footwear lighting. If a large-area white-light-emitting OLED could potentially provide a solid-state diffuse light source that could compete with conventional lighting technologies in performance and cost, and if OLED technology could be successfully transitioned to lighting applications, the possible impact would be enormous and could substantially reduce dependence on natural global energy resources (crude oil and coal) and minimize carbon dioxide emissions that threaten the global ecosystem.

4.7.1 Performance and cost goals for OLED lighting

The potential for OLED lighting is dependent upon the white OLED source fulfilling certain key requirements for operational lifetime, power conversion efficiency, CRI, and unit cost of manufacturing. For OLEDs to effectively compete with fluorescent lighting:

- power efficiency should be $>30 \text{ lm/W}$ at 1000 cd/m^2 white;
- the CRI should be greater than 80 for the color temperature between 3000 to 6000 K on the black body locus;
- the lifetime should be greater than 20 000 h of operation (2–3 years of continuous usage); and
- the cost of manufacturing should be competitive with traditional light sources ($<\$6$ per kilo lumen and $<\$40/\text{m}^2$ at 1000 cd/m^2).

Figure 4.40 shows the comparison of luminance efficiency of the current light sources with OLED devices. Also included are the efficiencies obtained from the OLED devices using R, G, B and white colors. White OLED power efficiency of $\sim 30 \text{ lm/W}$ exceeds the $\sim 15 \text{ lm/W}$ power efficiency of a 60 W general light bulb. Similarly green phosphorescent OLED power

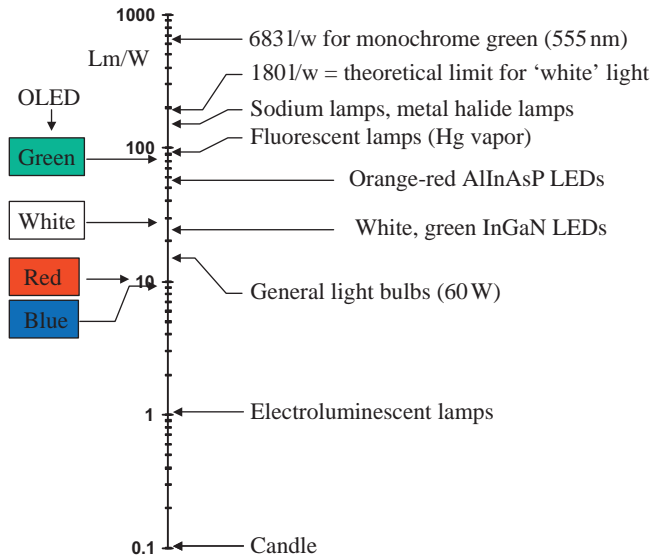


Figure 4.40 OLED luminous efficiency compared to other light sources

efficiency of ~ 80 lm/W is approaching 90 lm/W power efficiency of a fluorescent mercury vapor lamps.

Another question is how much light is required for typical office lighting? On average, there are two fluorescent tube fixtures ($48'' \times 12''$) covering 20% of ceiling areas. Each tube gives off 2900 lumens per tube (GE T12). Considering 100% reflector efficiency, the luminance at the diffuser is equal to $(2900 \text{ lumens}) \times 2/0.38 \text{ m}^2/\pi = 4860 \text{ cd/m}^2$. Given that the light fixture covers 20% of the ceiling area, the light output is equal to $4860 \text{ cd/m}^2 \times 0.20 = 972 \text{ cd/m}^2$. The OLED target, according to the DOE, calls for 1000 cd/m^2 [7].

OLEDs are available in almost any wavelength in the visible region, and the spectrum of the white OLEDs can be designed as described earlier. This availability of wide emission color is one key advantage that differentiates between OLED solid-state lighting and traditional discharge lamps, the spectra of which depends upon available phosphors and emissions from gas. For customer acceptance, light sources need to be as close as possible to blackbody radiation, and the color of the illumination source should be within 0.01 CIE x,y units from the blackbody locus. In addition, color-rendering index should be greater than 80%. The color-rendering index (CRI) is a quantitative measure of color rendition that determines the illumination quality of light source or how 'true' different colored objects appear when illuminating by the light source.

4.7.2 Color rendition improvement using tandem white

Color rendering is determined solely from the spectrum of the source and is better achieved by broadband spectra distributed throughout the visible spectra. The two-emitter white OLED spectrum (Section 4.2.1) has a low color-rendering index of <50 , whereas the three- and four-layer white OLED structures have higher CRI (>70). Another approach to increase

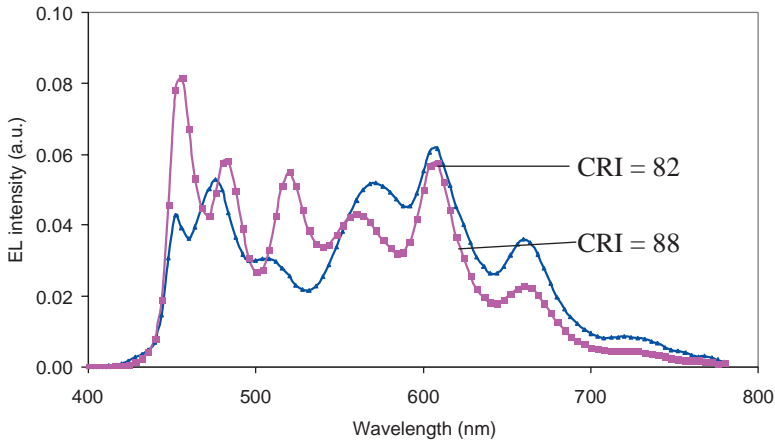


Figure 4.41 Improved color-rendering index (CRI) for white lighting

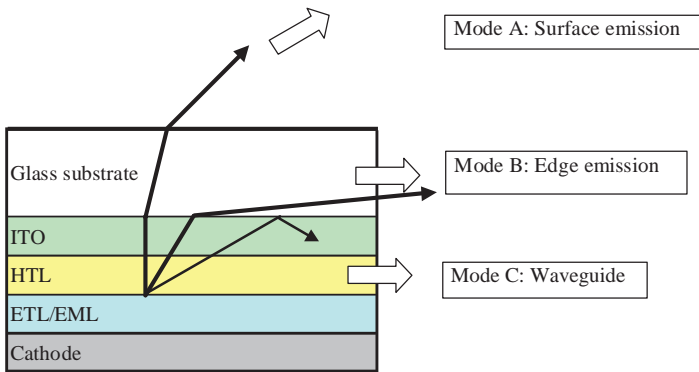


Figure 4.42 Three modes of OLED emission and efficiency-loss mechanism

CRI is based on the tandem structure and using two different white OLEDs. Combined broadband emission spectra can be obtained by properly selecting the white OLEDs with different emission peaks. Figure 4.41 shows the tandem spectra that were obtained using two-stack white OLEDs and having a CRI from 82–88. In this case, two individual stacks of the tandem structure were based on the two-layer (Y/B) white and three-layer (R/G/B) white OLED.

4.7.3 Light extraction and enhancement using scattering layer

One of the significant issues facing these devices is low out-coupling efficiency of OLEDs [68, 69]. In a conventional OLED structure, photons emitted at the recombination zone are coupled into three types of modes (Figure 4.42):

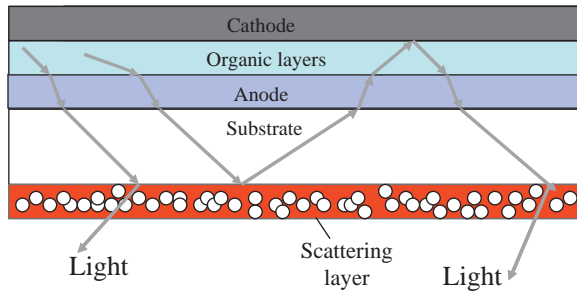


Figure 4.43 External scattering layer that is spin coated on the substrate

- Mode A – surface emission mode, corresponding to direct transmission to the air;
- Mode B – edge emission mode, representing the edge emission, which is due to the total reflection at the glass/air interface; and
- Mode C – explained by the waveguide transmission within the high-refractive index ITO and the organic layer owing to the total reflection at ITO/glass interface, causing light to be trapped in the organic layers and the transparent electrode.

On the assumption of Lambertian light sources, the fraction of total emitted photons in these three modes has been estimated at 0.2, 0.3 and 0.5, respectively. Eighty percent of total light emission is trapped within the OLED and the glass substrate. Several different techniques have been proposed to reduce the loss due to Modes B and C and to realize high-luminance efficiency. One method involves the use of a scattering layer (Figure 4.43) [67–69].

A scattering layer was spin-coated onto the substrate of a bottom-emitting OLED demonstration device. Light that is emitted from the organic layers will bounce off the scattering particles and either leave the OLED device, or will bounce back towards the reflective electrode. It is again reflected back to the scattering layer and possibly emitted. Thus, the light will bounce back and forth until it is either emitted or absorbed. Efficiency enhancement greater than 50% has been obtained by the use of the scattering layer.

4.7.4 Top-emitting white with scattering layer

The scattering layer can also be deposited onto the OLED layers, as shown for the top-emitting device architecture in Figure 4.44. Figure 4.45 shows the performance obtained from the two-stack top-emitting white tandem with a 500-nm-thick TiO_2 scattering layer. A power efficiency of 23.4 lm/W and a lifetime of >50 000h was obtained at 1000 nits luminance level. In comparison, the device without the scattering layer only had a power efficiency of 10 lm/W. The emission was yellowish white for both devices, with correlated color temperatures between 3000–3500 K, which is suitable for lighting applications.

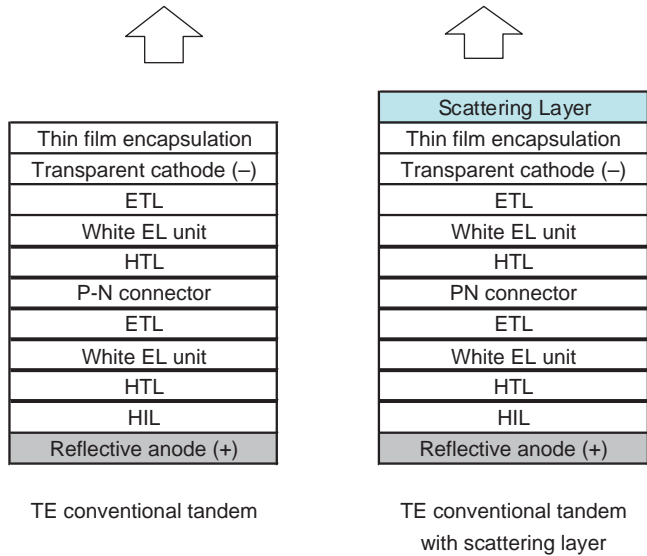


Figure 4.44 Top-emitting white OLED structure with and without a scattering layer

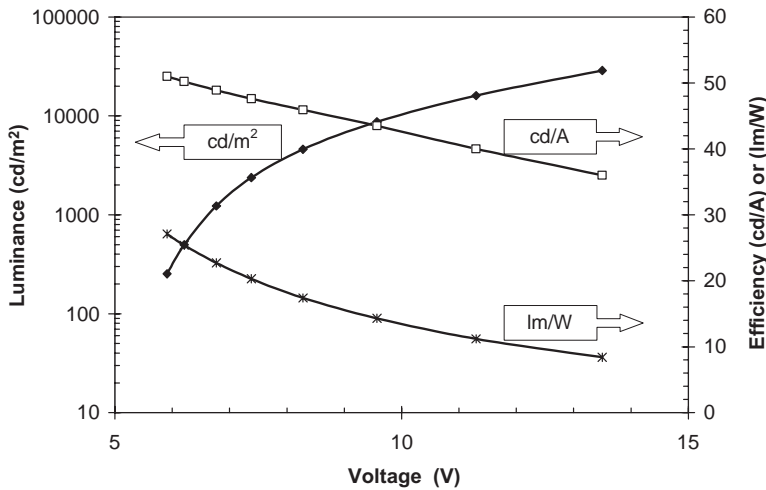


Figure 4.45 Performance of two-stack tandem white structure with scattering layer

4.7.5 Prototypes of SSL panels

Prototype panels were demonstrated at the General Electric Company and are shown in Figures 4.46 and 4.47. White emission was obtained using a device architecture consisting of a blue-emitting polymer OLED with down-conversion layers optically coupled to the OLED substrate. The down-conversion layers were chosen to absorb the blue OLED emission and then re-emit at longer wavelengths. Specifically, three down-conversion layers



Figure 4.46 4' × 4' white OLED SSL panel showing high CRI (Courtesy: Dr Anil Duggal, General Electric Corp.)



Figure 4.47 4' × 4' white OLED SSL panel showing high CRI (Courtesy: Dr Anil Duggal, General Electric Corp.)

were based on perylene-based orange and red organic dyes with high photoluminescence efficiency, and an inorganic phosphor. The thickness and/or concentration of each layer are chosen to ensure that the combination of non-absorbed blue OLED emission and the down-converted emission results in white light [8, 70–73].

4.8 ADVANCED MANUFACTURING OF LARGE-AREA COATINGS

For any new technology to be adopted in the marketplace, the unit manufacturing cost (UMC) is the most important issue. In order to attain a unit manufacturing cost for AMOLED displays that is competitive with AMLCDs, it is necessary to implement an efficient, high-throughput OLED manufacturing system that utilizes advanced OLED deposition technologies. Similarly, the cost of the OLED SSL panels has to be competitive with the current light sources for similar applications. Both ‘cluster type’ and ‘in-line’ manufacturing systems have been widely used for OLED manufacturing. The cluster type system includes a glass loading chamber, a pretreatment chamber, deposition chambers and unloading chambers. In the center of the system there is a buffer chamber for the glass substrate to be transferred to each process chamber, by using a robot. Two or more cluster-connected systems are generally used to reduce the cycle time and improve manufacturing throughput. The in-line system uses a continuous substrate flow. The glass is loaded into the load chamber, and subsequently the substrate is transferred into the chambers that are needed for each particular organic layer. These layers are finalized with a cathode metal deposition. The cycle time for completing a device is adjusted by equalizing the deposition time of various layers within each of the chambers. Both of these types of manufacturing systems are suitable for a rigid substrate, such as glass. For low-cost manufacturing of SSL panels, the adoption of a roll-to-roll manufacturing method is most likely (Figure 4.48).

However, there are many supporting technologies that need to be developed to enable continuous manufacturing. Two of these key technologies are uniform and high rate deposition of organic layers and encapsulation, which will be described in this section.

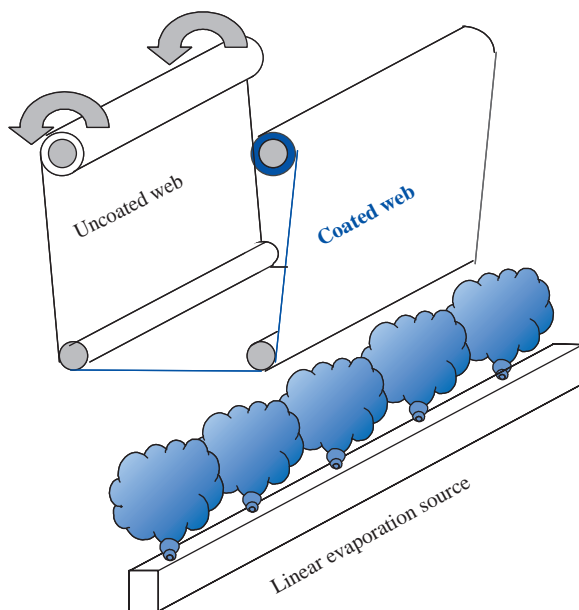


Figure 4.48 Schematic of the roll-to-roll coating for advanced manufacturing

4.8.1 Vacuum-thermal evaporation using linear sources

In order to attain a low unit manufacturing cost for displays or lighting panels, it is necessary to implement an efficient, high-throughput OLED manufacturing system that utilizes advanced OLED deposition technologies. Of critical importance is the OLED deposition source. There are several types of deposition sources that have been developed to replace the conventional point sources. We will describe the three main large-area sources that were developed in the Eastman Kodak Company. All of these advanced linear source technologies enable an ‘in-line’ machine, where each layer requires only one source, and the substrate is transported above the source assembly in one pass in order to deposit all of the organic layers required in the OLED structure. This design is particularly suitable using the white OLED format, and there is no need to stop to change masks (such as used for RGB pixelation) during the OLED deposition, thus reducing the TAC time required.

A key requirement for fabrication of OLED displays is uniform film deposition over large areas, because of the sensitivity of emission color and efficiency on the film thickness. Conventional deposition using point sources is unattractive because it requires a large separation between the source and substrate. This also contributes to very low materials utilization, which is typically 5–8%. A novel, extended linear deposition has been developed that offers significant advantages over the conventional point-source deposition approach [74]. Figure 4.49 is a schematic drawing of a linear source. The deposition rate is established in a position that is remote from the substrate, and the source is scanned under the substrate. Uniformity in the y-axis direction is achieved by appropriate design of the linear source so that a uniform vapor flux is attained along its length. Thickness uniformity within $\pm 5\%$ can be obtained on a 350×350 mm substrate using a linear source of 500 mm in length. Figure 4.50 shows the deposition uniformity for evaporating an Alq host film on a 350 mm \times 350 mm substrate. The deposition rate of Alq at the substrate is very high. Material utiliza-

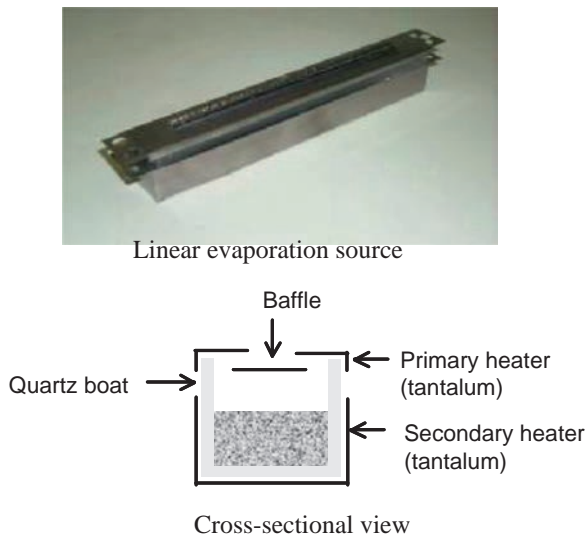


Figure 4.49 Next-generation deposition technology using extended linear evaporation source

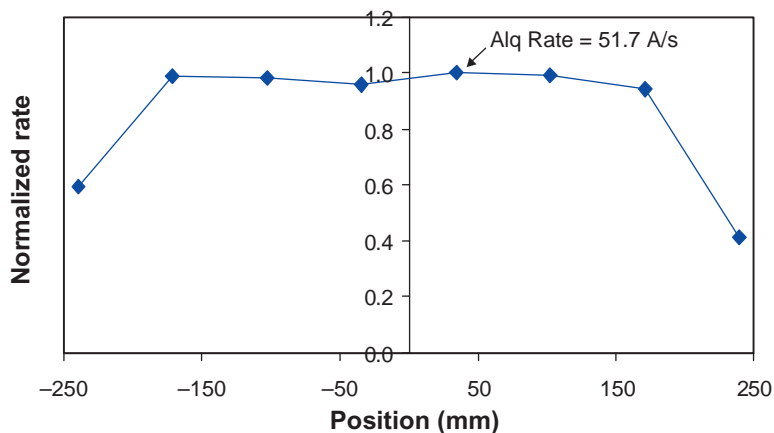


Figure 4.50 Linear source uniformity for evaporating Alq host (deposition at substrate ~ 52 A/s) (boat length = 500 mm, aperture = 440 mm)

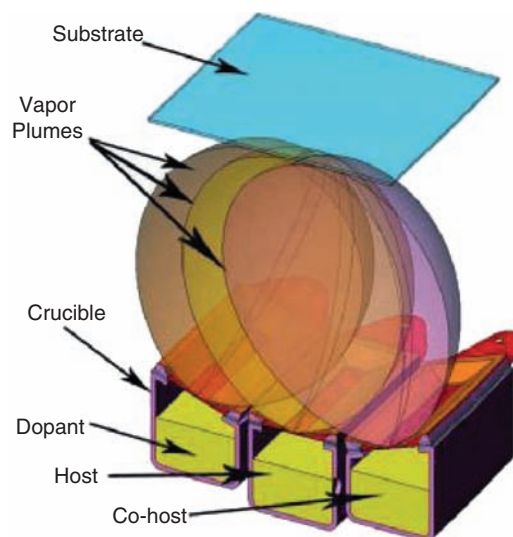


Figure 4.51 Next-generation deposition technology using vacuum thermal evaporation linear sources. Three sources placed adjacent to each other are used for host/dopants co-deposition (courtesy: Dr Michael Long)

tion up to 30% can be obtained. For an organic layer containing either one host or two dopants or two-hosts and one dopant, three linear sources (one for each component) are arranged in close proximity for uniform mixing of the host-dopant vapor. The three linear source configuration is shown in Figure 4.51. Therefore, each of the different materials requires a different source to be operated at different evaporation temperatures to control the appropriate mixing ratio.

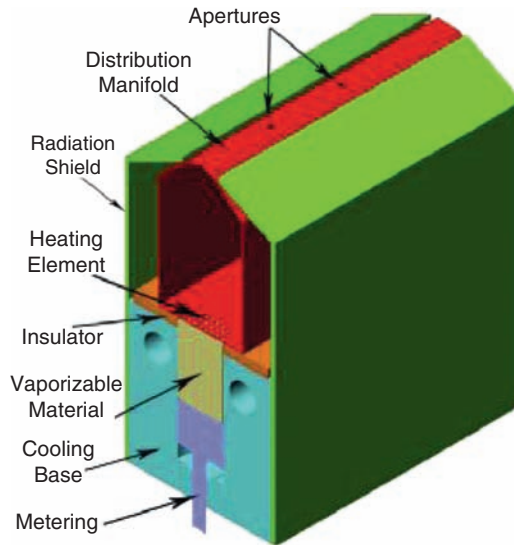


Figure 4.52 Next-generation deposition technology using flash evaporation single source for deposition of mixed layer (SID 2006, courtesy: Dr Michael Long). SID 2006, M. Leng et al., 'Thermal Evaporation . . .', p. 1474, Copyright (2006). Reproduced by permission of The Society for Information Display

4.8.2 Flash evaporation sources

Improved advanced linear sources have been developed by Kodak that enable OLED material usage efficiencies greater than 50% and that also incorporate novel technology allowing for the introduction of multiple materials into the same manifold. Conceptually shown in Figure 4.52, the high material utilization largely results from implementation of a short source-to-substrate distance. An advanced vacuum thermal evaporation source for OLED manufacturing, recently published, is based on the principle of flash evaporation [75]. These vacuum thermal evaporation source sources reduce the number of organic deposition sources, which substantially increase the material utilization and increase the rate of deposition without thermally degrading the organic materials while reducing the cycle time. The evaporation source uses the blended organic materials (mixed in the correct host/dopant proportion) that reduce the number of sources required and demonstrate material utilization efficiencies greater than 50%. The architecture of the source is shown in Figure 4.51 and includes heat shields surrounding a heated vapor distribution manifold. The heat shields are in contact with a cooled base element that principally serves to maintain the organic material at essentially room temperature. The organic material is metered towards a permeable heating element at the bottom of the distribution manifold, across a narrow gap, which is defined by an insulating element. As the top surface of the organic material vaporizes, the vapor passes through the permeable heating element, is distributed along the length of the vapor distribution manifold, and exits through numerous apertures. The apertures distribution and conductance is tailored such that good thickness uniformity within $\pm 1\%$ can be obtained in the deposited film. A single-source co-deposition has been demonstrated to vaporize a mixture of different components. The composition of the input blended mixture

is accurately maintained in the deposited film. The other advantage of this deposition technology is that size and complexities of the manufacturing tool are significantly minimized. The result is a high material-usage efficiency, low TAC time (high throughput) and cost-effective (simple, small) manufacturing equipment that achieves a competitive unit manufacturing cost.

4.8.3 Thin-film encapsulation

Encapsulation is needed to protect sensitive OLED devices from attack by water and air. Currently, most OLED devices are encapsulated using either a glass plate or a metal can glued to the substrate. The bottom glass substrate provides a rigid and protective barrier, and the top plate provides a hermetic barrier. For roll-to-roll manufacturing, the use of polymeric substrates will be required, but they are too permeable to use as protective barriers for active layers. Similarly, the thin-film encapsulation against the conventional rigid glass or metal will be required. To understand the thin film encapsulation technology, the conventional encapsulation technique is shown in Figure 4.53 for a typical bottom-emitter device. The cover glass can have a pocket that is etched into it. The desiccant is placed inside this pocket so as to avoid its physical contact with the OLED device. The two substrates are aligned and sealed using a UV-curable epoxy. The devices are then scribed into individual panels, ensuring that the electrical contact leads are sufficiently exposed for testing purpose.

Thin-film encapsulation (Figure 4.54) has a lot of advantages over the existing glass lid/metal can technology. It would make the device less than half its thickness and it would reduce the cost. Thin-film encapsulation also is particularly suitable for top-emitting architectures, where entire TFT circuitry is below the OLED layer and a larger pixel aperture ratio is possible. It can provide good protection from moisture so that the color filters can be directly patterned over the OLED layers, thereby minimizing pixel-to-pixel optical crosstalk, especially for high-resolution displays.

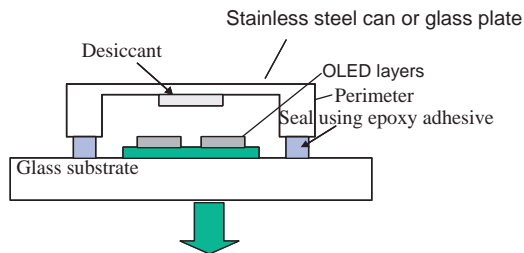


Figure 4.53 Current device architecture of OLED encapsulation of a bottom-emitting device

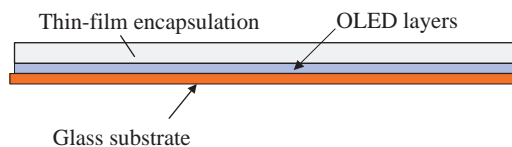


Figure 4.54 Device architecture using thin-film encapsulation without desiccant

Although thin-film encapsulation would be an attractive feature, thin-film layers should be highly transparent, have no pinholes, be crack free, have low permeability, have no reactivity to the cathode layer, have strong adhesion to the cathode, be easy to process at low cost at low processing temperatures (preferably below 100 °C and at a maximum limit of approximately 130 °C), be highly conformed so that small particles can be well encapsulated, have minimal UV or sputter-like process damage, and have a deposition material that is able to withstand thermal cycling as specified by the product requirements. The permeability to water should be $<10^{-6}$ g/m²/day, and to oxygen should be $<10^{-3}$ cc/m²/day. It should also provide protection of the OLED device against the physical damage in the pixel area.

A simple thin-film encapsulation using thin-film technology is shown in Figure 4.54. The thin film can be a bi-layer of the inorganic films and a polymer film or a multilayered film of such combination. Inorganic film provides lower permeability and protection against physical damage, whereas polymer layers provide flatness and compensation for pinholes and cracks that occur in inorganic layers. The inorganic film made from materials such as SiO, SiN or AlN is relatively thin at <100 nm, whereas polymer film has thicknesses between 20–100 μ m.

Vitex has proposed a new process for thin-film encapsulation of OLEDs using multilayers of organic and inorganic layers, called Barix. One of the thin-film encapsulation multilayered structures developed by Vitex is shown in Figure 4.55 [76]. The multilayer consists of thicker (0.25 to 4 μ m) polymer layers alternated by thin (200–500 nm thick) layers of oxide or nitride. The polymer layers are deposited in vacuum as a thin liquid film of an acrylate monomer, which is polymerized with UV light. These layers planarize the substrate and provide the almost ideal surface to grow defect-free oxides. The polymer layer also covers particles, decoupling defects in the oxide layer so that they are not aligned and function as a stress-release layer. The thin films of oxide serve as the barrier layers to oxygen and water.

The Barix multilayer structure (Figure 4.55) consists of two to five bi-layers of inorganic/organic materials. The organic layer provides a continuous surface for the impervious oxide layer. Lifetimes of 500h at extremely aggressive high-temperature/high-humidity conditions have been demonstrated (60 °C and 90% RH) giving the possibility that thin-film encapsulation will be adequate throughout the display lifetime.

Based on a multilayered structure similar to Vitex, OTB developed another thin-film encapsulation using a plasma enhanced chemical vapor deposition (PECVD) silicon nitride (SiN_x) layer instead of sputtered Al₂O₃ [77]. The conformal characteristics of the PECVD process provide a better moisture barrier. The polymer layer is spin-coated. The encapsulation layer structure used by OTB (Figure 4.56) may contain one to three bi-layers of (SiN_x + polymer) layers.

Instead of the above thin-film multilayer stacks, there also is another method known as atomic layer deposition (ALD) that is used for thin film encapsulation. This method of deposition produces the most conformal coatings and is, therefore, a single layered coating with a thickness between 100–200 nm, which is expected to give the best protection results for a moisture barrier. ALD deposits films use pulses of gases that produce one atomic layer at a time. For Al₂O₃ conformal coatings, gas mixtures of tri-methyl aluminum (TMA) and ozone (O₃) for Al₂O₃ films are generally used. Within wide process windows, the deposited film thickness is only dependent upon the number of deposition cycles, providing extremely high uniformity and thickness control. Commercial equipment from Sundew Technologies and ASM Microchemistry, AKT, is available. The ALD process was found to provide

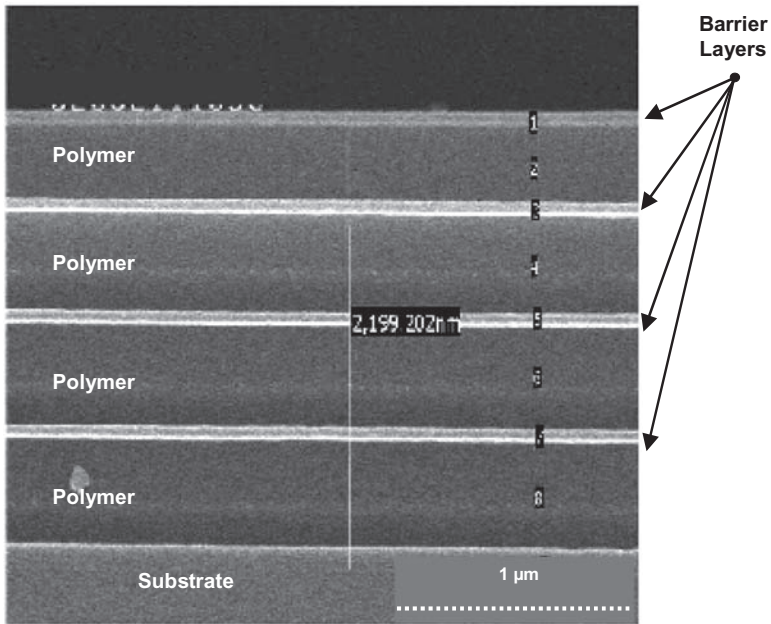


Figure 4.55 SEM cross-section of a typical Barix multilayer coating. Oxide layers typically are between 30–100nm and polymer layers are 0.25–4 μm (Courtesy: Dr Robert Visser, Vitex)

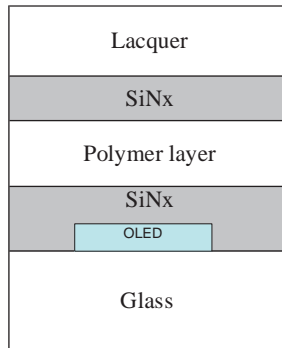


Figure 4.56 Thin-film encapsulation developed by OTB

protection up to 2000h without any dark spot growth at 85 °C and 85% RH test conditions. However, the process is very slow (~1 A/sec deposition rate as against ~10–100 A/s for sputtering or PECVD). For high throughput and low-cost manufacturing, however, the ALD processing rate will need to be increased to make it practical.

4.9 FUTURE OUTLOOK

As described above, significant progress has been made in developing white OLED technology for both display and lighting applications. White OLEDs based on small molecule

singlet based materials demonstrated high efficiency and high stability. Their emission color can be easily tuned for both display and lighting applications. Tandem architecture is shown to be useful for increasing efficiency and decreasing power consumption for full-color displays. The operational stability was also found to increase with an increasing number of stacks. The white tandem technology, combined with optimized color filters, can provide AMOLED displays in RGBW formats with low power consumption at high peak luminance ($>400\text{cd/m}^2$), wide color gamut ($>100\%$ NTSC_{x,y}) and long lifetimes ($>50\,000\text{h}$, which is equivalent to a 15-year lifetime with an average of 8 h/day usage). The large-area prototypes based on OLED tandem white technology demonstrate that they are ready for manufacturing and are easily scalable to large-sized displays (such as 32–47-inch TVs). With its natural performance advantage of very high contrast, thin architecture and excellent off-axis viewability, OLED display technology is poised to compete successfully with other flat-panel display technologies, such as LCD and PDP.

OLEDs based on phosphorescent materials have shown the potential of increasing luminance and power efficiency. Record power efficiencies have been achieved, approaching levels required for solid-state lighting applications. If stable blue triplet materials can be developed, tandem white structures, using triplet materials in combination with low voltage technology, will surpass the needs both for the large-area displays and solid-state lighting.

Polymer white OLEDs have the potential for low-cost manufacturing, but efficiency and stability are still low, and significant progress in the stability of co-polymers is required before they can be used for any practical applications in either full-color displays or in lighting applications.

The success of the OLED technology depends upon its manufacturability. The selection of white technology, the development of new OLED deposition sources, and the introduction of large-scale production equipment have made it possible to lower unit manufacturing costs to the level of comparable LCD displays. Other complementary technologies, such as a-Si backplane, deposition of organic layers and thin-film encapsulation, will need to be perfected for low-cost manufacturing. Although no details were covered in this chapter, driving electronics will also play a huge role in determining unit manufacturing costs.

ACKNOWLEDGEMENTS

We would like to acknowledge the help and contributions of several colleagues who were instrumental in developing the white OLEDs and related technologies in Kodak. They include Steven Van Slyke, Dr G. Rajeswaran, Dr Ralph Young, Michele Ricks, Dr Willy Begley, Dr Chris Brown, Dr Margaret Helber, Dr Larry Liao, Dr J. Ramon Vargas, Dr S. Krishnamurthy and Dr Michael Long. We also would like to acknowledge the contribution and association with Dr Yuji Hamada during the Kodak-Sanyo joint development program.

REFERENCES

1. Tang, C.W. and Van Slyke, S.A. (1987) *Appl. Phys. Lett.* **51**: 913.
2. Van Slyke, S.A., Chen, C.H. and Tang, C.W. (1996) *Appl. Phys. Lett.* **69**: 2160.
3. Rajeswaran, G., Itoh, M., Boroson, M. *et al.* (2000) *SID Int. Symp. Digest* 974.

4. Wakimoto, T., Murayama, R., Nagayama, K., Okuda, Y., Nakada, H. and Tohma, T. (1996) *SID Int. Symp. Digest* 849.
5. Tsujimura, T. *et al.* (2003) 'A 20-inch OLED Display Driven by Super-Amorphous-Si Technology', *SID Digest* 6.
6. Chung, K. *et al.* (2005) *IMID Digest*, 781.
7. OLEDs for general illumination, *OIDA report 2002*.
8. Duggal, A.R., Foust, D.R., Nealon, W.F. and Heller, C.M. (2004) 'OLEDs for lighting: New approaches', *SPIE Proc.* **5214**: 241.
9. Kido, J. Hongawa, H., Okuyama, K. and Nagai, K. (1994) *Appl. Phys. Lett.* **64**: 815.
10. Ali, A.A., Ghosh, A.P. and Howard, W.E. (1999) *SID Digest* 442.
11. Hosokawa, C., Toshio, S., Fukuoka, K. *et al.* (2001) *SID Digest* 522.
12. Yamamoto, H. *Electronic Journal*, 6th FPD Seminar, 31.
13. Deshpande, R.S., Bulovic, V. and Forrest, S.R. (1999) *Appl. Phys. Lett.* **75**: 888.
14. Hatwar, T.K., Young, R.H., Rajeswaran, G., Hamada, Y. and Takahashi, H. (2001) 'White OLEDs with Excellent Stability and Manufacturability', *Proc. Asia Display/IDW* 1771–2.
15. Mameno, K., Suzuki, K., Ichikawa, S. *et al.* (2002) 'Active Matrix Full Color OLED Displays with High Efficiency White OLEDs and ON-Chip Color Filter', Abstract G-06, *The 8th IUMRS Int. Conf. on Electronic Materials*, June 10–14.
16. Hatwar, T.K., Spindler, J.P., Ricks, M.L. *et al.* (2003) *SPIE* **5214**: 233.
17. Hatwar, T.K., Spindler, J.P. and Van Slyke, S.A. (2004) 'High Performance White OLEDs for Full Color Displays', *Proc. EL Toronto*.
18. Kanno, H., Hamada, Y., Nishimura, K. *et al.* (2006) 'Reduction in power consumption for full color active matrix OLEDs', *Jpn. J. Applied Phys.* **45**: L947–50.
19. Popvic, Z., Aziz, H., Hu, N.X., Ioannidis A. and d. Anjos, P.N.M. (2001) *J. J. App. Phys.* **89**: 467.
20. Aziz, H. and Popovic, Z.D. (2002) *Appl. Phys. Lett.* **80**: 2180.
21. Hatwar T.K. and Young, R.H. (2004) US Pat. 6,727,644 B2.
22. Jarikov, V., Young, R.H., Vargas, J.R., Brown, C.T., Klubek, K.P. and Liao, L.S. (2006) *J. Appl. Phys.* **100**: 094907 9.
23. Hatwar, T.K., Spindler, J., Ricks, M.L. *et al.* (2004) 'White OLED Structures Optimized for RGB and RGBW Formats', *Proc. ASIA Display* 25.4.
24. Arnold, A., Hatwar, T., Hettel, M. *et al.* (2004) 'Full-color AMOLED with RGBW Pixel Pattern', *Proc. ASIA Display* 25.2.
25. Arnold, A., Castro, P., Hatwar, T. *et al.* (2005) 'Full-color AMOLED with RGBW Pixel Pattern', *J. Soc. Info. Display* **13**(6): 525–35.
26. Lee, B., Park, C., Kim, S. *et al.* (2003) 'TFT-LCD with RGBW color system', *SID Digest* 1212–15.
27. Hamer, J.W., Yamamoto, Y., Rajeswaran G. and Van Slyke, S.A. (2005) *SID Symp. Digest* **34**: 1902
28. Consumer Electronics Show, Japan, April (2002).
29. Hatwar, T.K., Spindler, J. and Van Slyke, S.A. (2006) *SID Digest* 71.2.
30. Spindler, J.P., Hatwar, T.K., Miller, M.E. *et al.* (2005) 'Lifetime and power enhanced RGBW displays based on White OLEDs', *SID Digest* 36–9.
31. Lee, S., Chin, B., Kim, M. *et al.* (2004) 'A Novel Patterning Method for Full-Color Organic Light-Emitting Devices: Laser Induced Thermal Imaging (LITI)', *SID Digest* 1008–11.
32. Boroson, M., Tutt, L., Nguyen, K., Preuss, D., Culver, M. and Phelan, G. (2005) *SID Digest*.
33. Brown, C.T., Owczarczyk, B., Hatwar T.K. and Kondakov, D. (2003) *Infor. Disp. Res. Conf.* 42.
34. Liao, L.S., Klubek, K.P., Helber, M.J., Cosimbescu, L. and Comfort, D. (2006) *Proc. SID Digest* 1197.

35. Miller, M.E., Murdoch, M.J., Kane, P.J. and Arnold, A.D. (2005) 'Image Quality Impact of Pixel Patterns and Image Processing Algorithms for RGBW OLED Displays,' *SID Digest* 398-401.
36. Chung, H.K. *et al.* (2005) 'Development of 40 inch Full Color OLED Display', *IMID Digest* 781.
37. Kido, J. and Matsumoto, T. (1998) *Appl. Phys. Lett.* **73**: 2866
38. Hung, L.S., Zheng, L.R. and Mason, M.G. (2001) *Appl. Phys. Lett.* **78**: 673.
39. Kishigami, Y., Tsubaki, K., Kondo, Y. and Kido, J. (2001) *Proc. Asia Display/IDW* 549.
40. Iwakuma, T., Aragane, T., Hironaka, Y. *et al.* (2002) *Proc. SID* 598.
41. Endo, J., Matsumoto T. and Kido, J. (1998) *Appl. Phys. Lett.* **73**: 2866.
42. Pfeiffer, M., Beyer, A., Fritz T. and Leo, K. (1998) *Appl. Phys. Lett.* **73**: 3202.
43. Zhou, X., Blochwitz, J., Pfeiffer, M., Nollau, A., Fritz, T. and Leo, K. (2001) *Adv. Mat.* **11**: 310.
44. Matsumoto, T., Nakada, T., Endo, J. *et al.* (2003) *SID Digest* 979.
45. Liao, L.S., Klubek, K.P. and Tang, C.W. (2004) *Appl. Phys. Lett.* **84**: 167.
46. Liao, L.S., Slusarek, W., Hatwar, T.K., Ricks, M. and Comfort, D. (2007) 'Tandem OLED using hexaazatriphenylene hexacarbonitrile in the intermediate connector' *Advanced Materials* (to appear 2007).
47. Chang, C., Chen, J., Hwang, S. and Chen, C.H. (2005) Highly efficient OLED devices based on tandem architecture, *Appl. Phys. Lett.* **87**: 253501.
48. Hatwar, T.K., Spindler, J. and Van Slyke, S.A. (2006) 'High Performance Tandem OLEDs for Large Area Full Color AM Displays and Lighting Applications', *IMID Digest* 1582.
49. Spindler J. and Hatwar, T.K. (2007) 'Development of tandem white architecture for large-sized AMOLED displays with wide color gamut', *SID Digest* Abstract 8.2.
50. Helber, M., Alessi, P., Burberry, M *et al.* (2007) 'Color Filter Formulations for Full-Color OLED Displays: High Color Gamut Plus Improved Efficiency and Lifetime', *SID Digest*.
51. Brown, J.J., Kwong, R., Tung, Y.-J., Adamovich, V., Weaver, M. and Hack, M. (2004) 'Recent Progress in High-Efficiency Phosphorescent OLED Technology', *J. Soc. Info. Display* **12**: 329-34.
52. Hack M. and Brown, J. (2004) 'OLED Excitement', *J. SID* **12**: 6.
53. Adamovich, V., Brooks, J., Tamaya, A. *et al.* (2002) *New. J. Chem.* **26**: 1171.
54. Brown, J.J., Kwong, R., Tung, Y.J., Adamovich, V., Weaver, M. and Hack, M. (2004) *J. Soc. Info. Display* **12**: 329.
55. Baldo *et al.* (1998) *Nature* **395**.
56. D'Andrade, W., Holmes, R.J. and Forrest, S.R. (2004) 'Efficient electro phosphorescent white LED with a triple doped emissive layer', *Adv. Mater.* **6**: 624.
57. Sun, Y., Giebink, N., Kanno, H., Ma, B., Thompson, M.E. and Forrest, S.R. (2006) 'Management of singlet and triplet excitons for efficient white OLED', *Nature* **908**.
58. Murano, S., Burghart, M., Birnstock, J. *et al.* (2005) 'Highly efficient white OLEDs for lighting applications', *SPIE Proc.* 5937.
59. Kanno, H., Giebink, N., Sun, Y. and Forrest, S.R. (2006) 'Stacked white OLEDs based on a combination of fluorescent and phosphorescent emitters', *Appl. Phys. Lett.* **89**: 023503.
60. Kanno, H., Holmes, R.J., Sun, Y., Cohen, S.K. and Forrest, S.R. (2006) 'White OLEDs employing MoO₃ as charge generating layer', *Adv. Mater.* **18**: 339.
61. Burroughs, J.H. *et al.* (1990) *Nature* **347**: 539.
62. Kim, S.H., Hsu, C., Zhang, C. *et al.* (2004) 'Degradation of PLEDs and a way to improve device performance', *Asia Display, IMID* 183.
63. Gong, X., Moses, D. and Heeger, A.J. (2005) 'White electrophosphorescence from semiconducting polymer blend', *SPIE* **5519**: 82.
64. Tash, S., List, E.J.W., Ekstrom, O., Craupner, W. and Leising, G. (1997) *Appl. Phys. Lett.* **71**: 20.

65. Buchhauser, D., Scheffel, M., Rogler, W. *et al.* (2004) 'Characterization of white emitting copolymers for PLED-displays', *SPIE* 5519.
66. Kwon, S.K. *et al.* IMID/IDMC (2006). Recently, Tu, G., Mei, C., Zhou, Q. *et al.* (2004) *Adv. Funct. Mater.* **16**: 101.
67. Tung, Y.J., Ngo, T., Hack, M. *et al.* (2003) *J. SID Digest* 967.
68. Cok, R.S. (2005) 'Scattering layer for light extraction in OLEDs', *Eur. SID* 13.4.
69. Huang, W.K., Wang, W.S., Kan, H.C. and Chen, C.F. (2006) 'Enhanced light out coupling efficiency of OLEDs with self-organized micro lens arrays', *Proc. SID* 961.
70. Bulovic, V., Khalfin, V.B., Gu, G., Burrows, P.E., Garbuzov, D.Z. and Forrest, S. (1998) *Phys. Rev. B* **58**: 3730.
71. Madigan, C.F., Lu, M.H. and Sturm, J.C. (2000) 'Improvement of output coupling efficiency of OLED by backside substrate modification', *Appl. Phys. Lett.* **76**: 1976.
72. Duggal, A.R. (2005) 'OLED devices for Solid State Lighting', in *Organic Electroluminescence*, Kafafi, Z.H. ed., New York: CRC Press, p. 437.
73. Van Slyke, S., Pignata, A., Freeman, D. *et al.* (2002) 'Linear source deposition of organic layers for full color display', *SID Digest* 886.
74. Long, M., Grace, J., Freeman, D.R., Redden, N.P. and Koppe, B.E. (2006) 'New Capabilities in Vacuum Thermal Evaporation Sources for Small Molecule OLED Manufacturing', *SID Digest* 1474.
75. Moro, L.M., Chu, X., Hirayama, H., Krajewski, T. and Visser, R.J. (2006) *IMID/MMM Digest* 317.
76. Hemerik, M., Ligter, M., Lange, R., Veheijen, J. and Rens, B.V. (2006) *IMID/IDMC Digest* 1769.

5 Polymer Light-Emitting Electrochemical Cells

Jun Gao

QUEEN'S UNIVERSITY, Kingston, Ontario, ON K7L 3N6, Canada

5.1 Introduction	161
5.2 Operating mechanism and device characteristics of LECs	168
5.3 LEC materials	176
5.4 Frozen-junction LECs	183
5.5 Planar LECs	188
5.6 Conclusions and outlook	201
Reference	202

5.1 INTRODUCTION

Electroluminescence (EL) is the generation of light, other than black body radiation, by a solid-state luminescent material in response to electrical excitation. EL can be generated by either 'impact ionization' (Destriau effect) or 'field ionization' (Zener effect) under a high electrical field, or by injection of charge carriers (injection EL). EL devices, based on inorganic semiconductors, have achieved broad technological applications in lighting, information display, telecommunication, consumer electronics and xerographic printing. The last two decades have seen the emergence of novel EL devices based on thin films of organic metal complexes and conjugated polymers. Organic and polymer semiconductors are relatively new and less well understood than conventional semiconductors. But the significant cost benefit and novel functionalities promised by these materials have spurred tremendous research and development effort in both academia and industry alike. With commercialization already begun, organic and polymer light-emitting diode (LED) technologies are perceived as likely candidates for next-generation flat-panel display and lighting applications. This chapter discusses the materials and device physics aspects of polymer light-emitting electrochemical cells (LECs). Like polymer LEDs, LECs are solid-state polymer light-emitting devices, but are highly unique in their operating mechanisms and device characteristics among polymer-based devices, which closely resemble those of a conventional p-n junction diode. LECs provide an alternative approach to achieving efficient EL from luminescent polymers and are rich in intriguing sciences yet to be explored.

5.1.1 EL from organic small molecules

EL from organic materials was first demonstrated by Pope *et al.* in 1963 [1]. Single crystals of anthracene 10 to 20 microns thick were contacted on opposite faces by identical electrodes. With silver paste electrodes, EL was observed when a DC voltage bias above 400 V was applied along the c' axis of the crystal. The excitation mechanism of the EL was thought to be that of impact ionization.

Using asymmetrical liquid electrodes for electron and hole injection, Helfrich and Schneider first demonstrated injection EL from anthracene single crystals in 1965 [2]. The large thickness of the sample (5 mm) allowed the blue EL to be imaged through a polished side of the crystal. The observation of a bright emission zone reaching 2 mm into the crystal clearly indicated that EL was originating from the crystal, rather than the crystal/electrode interfaces.

In the 20 years following these initial reports, organic EL was mainly studied for scientific curiosity as an interesting phenomenon associated with certain organic semiconductors. The mechanism of organic EL had been studied via transient [3], low temperature [4, 6], current vs. voltage vs. light intensity [6–11] and spectroscopy [12] measurements. A majority of organic EL observations can be ascribed to carrier injection through the electrode interfaces and the subsequent radiative recombination of the injected charge carriers. Excitation by impact ionization is difficult because charge carriers are not likely to obtain enough kinetic energy due to the low carrier mobility in molecular crystals [13].

While early organic EL research focused mainly on anthracene [1–6, 7, 14–17] or doped anthracene [6, 9, 10, 2, 16, 18–20], EL was also demonstrated with tetracene [21], pyrene [22] and naphthalene [8] crystals. The inconvenient liquid electrodes were gradually replaced by a variety of solid electrodes, and eventually by evaporated metals with a large work function difference, in order to facilitate dual injection of electron and holes. Despite these early successes, organic EL devices were generally regarded as impractical for potential lighting and display applications. Not coincidentally, the overall intensity and impact of early organic EL research was low, as evidenced by the relatively small number of journal publications and the lack of commercial development of organic EL devices. The main obstacle to the realization of more practical organic EL devices was the high operating voltage, due to the large thickness of the EL specimen, which can be tens of microns or even millimeters. The high voltage bias severely limits the power efficiency of the device.

However, it should be mentioned that organic EL with a much lower operating voltage had indeed been achieved by using evaporated organic thin films as the active material, rather than single crystals. In 1977, Kampas and Gouterman reported an aluminium/octaethylporphyrin/silver sandwich cell fabricated on glass substrate [11]. The evaporated octaethylporphyrin layer was only several hundred nanometers thick. When the semi-transparent aluminium electrode was negatively biased, EL was now visible to the dark-adapted eye at a mere 15 V. Subsequently, in 1982, Vincett *et al.* successfully demonstrated EL from vacuum-deposited anthracene films [23]. The device was constructed on glass, with 50 nm of aluminium as the bottom electrode and 15 nm of gold as the top, semi-transparent electrode. The anthracene layer had a thickness ranging from 0.2 μm to about 3 μm . With the gold electrode biased positively, significant current (mA/cm^2) injection could occur at fairly moderate voltage levels (<100 V). Many cells exhibited strong EL, which was visible under normal room illumination when subjected to about 30 V or higher bias. For the thinnest samples (~ 0.18 μm), EL was visible in a darkened room at voltages as low as 12 V. Similar results were also obtained with perylene and 1,12-benzeperylene films. Despite the devices'

low external quantum efficiencies (up to 0.03–0.06%), the results clearly demonstrated the feasibility of low-voltage organic EL devices.

The real breakthrough came in 1987, when Tang and Vanslyke at Eastman Kodak invented a highly efficient organic EL diode with dramatically reduced driving voltage [24]. The ‘Tang cell’ is revolutionary because of its ‘bilayer’ device structure and because of the materials it uses. The cell was constructed on an indium tin oxide (ITO) coated glass substrate. ITO is a good anode material due to its high work function and good transmittance. On top of the ITO anode was an aromatic diamine layer ~75 nm thick, followed by a layer of 8-hydroxyquinoline aluminum (Alq₃) ~60 nm thick. The cathode was an alloy of magnesium and silver with an atomic ration of 10:1, deposited by co-evaporation. Again, the use of evaporated, ultra-thin organic layers and asymmetrical electrodes led to an extremely low driving voltage. Moreover, the insertion of an organic layer between the anode and the emissive layer had a dramatic effect on the efficiencies of the cell. Since the diamine layer was only capable of transporting holes (called a ‘hole-transport layer’, or HTL), the injected electrons were blocked at the diamine/Alq₃ interface. The recombination of injected electrons and holes therefore took place solely in the Alq₃ layer within about 30 nm of the interface. This carrier confinement effect prevented charge carriers passing through the device without recombination.

As a result of these innovative features, the Tang cell exhibited measurable EL from as low as 2.5 V under forward bias. The light output was linearly proportional to the input current from 0.1 to 100 mA/cm², and a high luminance of more than 1000 cd/m² was generated with a DC bias of less than 10 V. The device exhibited an external quantum efficiency of about 1%, a luminous efficiency of 1.5 lm/W and a power conversion efficiency of 0.46%.

The remarkable performance of Tang’s organic EL diode completely revived organic EL research. Research activity expanded rapidly from the late 1980s and remains strong until the present day. Tang’s original bilayer device structure has been further improved by Adachi *et al.* with the insertion of a separate ‘electron-transport layer’ (ETL) between the emitting layer (EML) and the cathode, resulting in a quantum well-like multilayer device structure of anode/HTL/EML/ETL/cathode [25]. With properly aligned energy levels at the interfaces, the unipolar HTL and ETL can now facilitate the efficient injection and transport of holes and electrons, respectively, into the EML. The recombination/emission process takes place entirely in the EML, whose position and thickness can be fine-tuned for improved efficiency. In less than 20 years, OLED technology has already been commercialized with consumer electronic devices such as cell phones, car audios, mp3 players and digital cameras, using OLED-based displays that have better contrast and response time than liquid-crystal displays.

5.1.2 Electroluminescence from conjugated polymers

Compared to organic small molecules, polymers as electroluminescent materials offer additional processing and structural advantages. Since most luminescent conjugated polymers or their precursor polymers are soluble in water or common organic solvents, standard solution processing techniques, such as spin-casting, screen printing or inkjet printing, can be used to fabricate large-area polymer films at low cost. It might even be possible to directly print polymer devices on a flexible substrate with roll-to-roll processing, so that roll-up TV monitors can be made. In addition, amorphous polymer films are less susceptible to recrystallization, which degrades the long-term stability of small molecule-based, thin-film, organic EL devices.

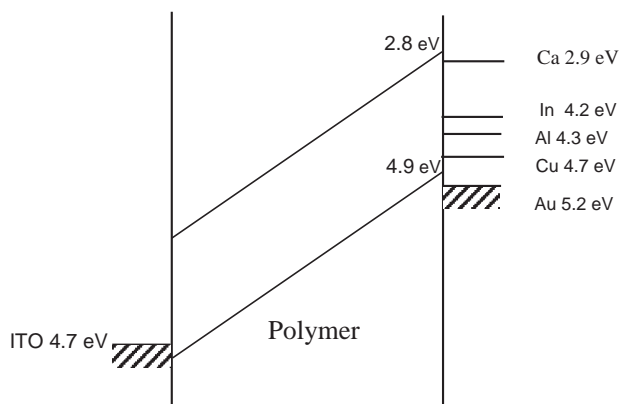
The first polymer light-emitting diode based on a luminescent conjugated polymer was demonstrated in 1990 by Burroughes and co-workers at Cambridge University [26]. The

polymer used was poly(*p*-phenylene vinylene), PPV, which is luminescent but not soluble in organic solvents. The PPV film was prepared from its solution-processable precursor polymer by thermal conversion. Ultra-thin (typically 100 nm), dense and homogenous film of PPV was formed on a suitable substrate (such as glass), which had been pre-coated with a transparent bottom electrode (e.g. indium oxide). The device was completed by the deposition of a top electrode (e.g. Al) on top of the PPV film. Substantial charge injection was achieved with a DC voltage bias of just below 14 V, with indium oxide electrode biased positive with respect to the aluminum electrode. The green-yellowish emission from the device could easily be seen under normal laboratory lighting. However, the quantum efficiency of the PPV devices was only up to 0.05%, much lower than the estimated photoluminescence (PL) quantum yield of about 8% for PPV.

The results of the Cambridge group were quickly confirmed by Braun and Heeger at UC Santa Barbara, with improved material processability and device performance [27, 28]. The Heeger group used a derivative of PPV, poly(2-methoxy, 5-(2'-ethylhexoxy)-1, 4-phenylene vinylene), or MEH-PPV, as the active material. MEH-PPV offers the advantage of being soluble in common organic solvents, such as tetrahydrofuran or xylene. MEH-PPV films approximately 120 nm thick were prepared by spin-casting onto a patterned ITO glass substrate. Calcium or indium cathodes were then deposited on top of the polymer film to complete the device. The diode with the indium cathode exhibited yellow-orange EL visible to the eye just below 9 V under forward bias (ITO positive). The quantum efficiency of the device at 1 mA was only about 0.05%. However, with calcium as the cathode, the quantum efficiency increased by 20-fold to about 1%, and EL was easily observed in a lighted room at a forward bias of only 4 V.

The intensive research and development activity in polymer LEDs mirrored that of organic LEDs in recent years. The research intensity is evidenced by the number of journal citations generated by the original paper published by the Cambridge group, which numbered more than 5000 up to 2007. The understanding of the fundamental sciences involved in polymer EL, as well as the performance of polymer LEDs, has advanced rapidly in the past 17 years. Commercialization of simple polymer-based displays began in 2002.

Figure 5.1 shows the energy level diagram of an MEH-PPV LED with ITO anode and various cathode materials [29]. Under forward bias, electrons and holes are injected from cathodes and anodes, respectively, and propagate by drift and/or diffusion until they capture one another to form singlet and triplet excitons. The radiative decay of singlet excitons gives rise to light emission. An obvious requirement for high efficiency and low driving voltage in a polymer LED is to have efficient and balanced charge carrier injection from the electrodes. The injection of holes from the ITO anode into the highest occupied molecular orbital (HOMO) of MEH-PPV requires the charges to overcome a potential energy barrier of ~0.2 eV (Figure 5.1). This hole-injection barrier is relatively small and matches well with electron injection from the calcium cathode into the lowest unoccupied molecular orbital (LUMO) of MEH-PPV. As a result, an ITO/MEH-PPV/Ca diode exhibits high efficiency and low driving voltage. However, when metals with higher work functions are used as the cathode, the device performance suffers due to poor electron injection. The effect of cathode work function on the quantum efficiency of polymer LEDs is shown in the table of Figure 5.1. In general, the injection of charge carriers in a polymer LED is achieved via field-assisted thermionic emission and/or quantum mechanical tunneling. Both injection mechanisms are sensitive to the barrier height at the electrode/polymer interfaces, as well as the electrical field within the device [13]. Efficient and balanced injection is achieved by using



Metal	Work function (eV)	Band offset (eV)	Efficiency (photons/hole)
Ca	2.87–3.00	~0.1	4×10^{-3}
In	4.12–4.20	1.3–1.4	1.6×10^{-4}
Ag	4.26–4.74	1.5–1.9	1.8×10^{-4}
Al	4.06–4.41	1.2–1.6	8×10^{-5}
Cu	4.65–4.70	1.9	8×10^{-6}
Au	5.1–5.47	2.3–2.7	5×10^{-7}

Figure 5.1 Band diagram of a polymer LED in forward bias for various cathode materials. The table compares the quantum efficiencies of polymer LEDs with various cathode materials (reprinted from reference 29 with permission. Copyright (1994) American Institute of Physics)

anode material with a large work function (such as ITO) and cathode material with a low work function (such as Ca). In addition, the active polymer layer is usually extremely thin (~100 nm) in order to maximize the electrical field and reduce the series resistance of the device. These attributes are universal to all polymer LEDs based on undoped conjugated polymers, and their implications will be discussed in Section 5.1.3.

Table 5.1 summarizes some representative work in the development of organic and polymer-based EL devices. An obvious trend is the reduction of driving voltage as the devices evolve. This can be mainly attributed to the decrease in device thickness. For example, by replacing thick single crystalline anthracene with evaporated polycrystalline anthracene less than a micron thick, the driving voltage has been reduced from hundreds of volts to less than 20 V. Further decrease in device thickness has been made possible with the use amorphous organic and polymer thin films, which eventually yielded a driving voltage of less than 10 V. The electrode materials used also evolved, from the initial inconvenient and inefficient liquid electrodes to symmetric metal electrodes, and eventually to transparent ITO anode and low work function metal cathodes for efficient and balanced charge carrier injection. In general, improved electrodes are responsible for the vastly superior quantum efficiencies of current devices. While a multilayer device structure is an essential feature of most state-of-the-art OLEDs, a vast majority of today's high-performance polymer LEDs retain a simple sandwich structure. This is probably due to the

Table 5.1 Some experimental results in the development of organic and polymer based electroluminescence

Specimen	Specimen thickness	Electrode contacts (positive/negative)	EL turn on voltage (V)	Quantum efficiency (ph/el)	References
Anthracene single crystals	10–20 μm	Silver paste or liquid electrolyte, symmetrical	400	Unspecified	[1]
Anthracene single crystals	1–5 mm	Electron and hole-injecting liquid electrodes	<100	Unspecified	[2]
Naphthalene single crystals	42 μm	Liquid electrolyte/liquid Na-K alloy	~300	Unspecified	[8]
Anthracene single crystals	0.5 mm	Silver/silver	600~1400	Unspecified	[17]
Octaethylporphin thin films	Several hundred nanometers	Silver/aluminium (Al)	15	Unspecified	[11]
Anthracene thin films	0.18–3 μm	Gold/aluminium	12	0.03–0.06%	[23]
Diamine/Alq3 thin films	75 nm/60 nm	Indium tin oxide/Mg:Al	~5	1%	[24]
PPV thin film	70 nm	Indium oxide/Al	~14	0.05%	[26]
MEH-PPV thin films	120 nm	Indium tin oxide/Ca	~4	1%	[27]

very low charge carrier mobility of most disordered luminescent polymers [30], which allows relative efficient electron-hole capture in an ultra-thin polymer layer.

5.1.3 Polymer light-emitting electrochemical cells

The evolution of organic and polymer light-emitting devices has established that the key to achieving high EL efficiency and low operating voltage is the use of an ultra-thin active layer and electrodes with a large work function difference. While these requirements are not hard to satisfy in a laboratory, they pose serious challenges in the development of commercially viable polymer LED-based displays and other devices. The ultra-thin film is prone to defects caused by pinholes and dust particles, which inevitably affect the product yield. The device efficiency can also suffer if the film is too thin, as the excitons generated within 20 nm of the metal electrode can transfer energy into the metal without undergoing radiative decay [31]. A low work function cathode, such as a calcium cathode, is highly reactive and will place stringent requirement on the encapsulation of the devices. Additionally, the matching of electrode work function with the LUMO and HOMO of the luminescent polymer becomes more difficult when the energy gap (E_g) of the polymer increases.

These limitations are intrinsic to all polymer LEDs and are not easily circumvented by simply improving the purity of the luminescent material or adopting a multilayer device structure. By contrast, conventional LEDs based on crystalline inorganic semiconductors are characterized by extremely low operating voltage and high quantum efficiency, even though the device is much thicker and no reactive metal is used for the electrodes. The following fundamental differences exist between a polymer LED and its inorganic counterpart.

Conventional LEDs are based on *doped* semiconductors and the formation of one or several *junctions* within the device, which give rise to the functionalities of the devices. The simplest inorganic LED is a p-n junction diode made with a direct band gap semiconductor such as GaAs or InGaN. The operation of a p-n junction LED involves the injection of 'minority charge carriers' across the p-n junction under forward bias. The subsequent radiative recombination of these minority charge carriers with the majority charge carriers in the vicinity of the junction gives rise to EL. Under a reverse bias, a large potential energy barrier exists for both electrons and holes at the reversely biased junction, which prevents significant current flow and gives the diode its unipolar conduction and light emission. The metal contacts in a p-n junction diode are low-resistance ohmic contacts.

Most polymer LEDs are based on pristine luminescent conjugated polymers without intentional doping. The active layer in a polymer LED is essentially an insulator, which must be kept extremely thin to minimize series resistance and maximize the electrical field when under bias. A polymer LED does exhibit diode rectification. For example, the Braun and Heeger MEH-PPV diode displayed a rectification ratio in excess of 10^4 [27]. However, this was entirely caused by the work function difference of the dissimilar electrodes, not by a p-n junction.

The obvious benefits of doping in the reduction of bulk and contact resistance inevitably led to the use of doped polymers in polymer LEDs. The most successful example was the use of conducting polyaniline [32, 33] and polythiophene derivatives [34] as hole-injecting materials in polymer LEDs. These solution-processable polymers are typically inserted as a thin layer between the ITO anode and the luminescent polymer layer. Polymer LEDs,

incorporating these conducting polymer layers, show lowered operating voltage, improved efficiency and longer operating lifetime. These beneficial effects have been attributed to the high work functions of these p-doped conducting polymers and (perhaps more likely) the diffusion of dopants into the luminescent polymer. Dopants such as FeCl_3 [35], I_2 [36] and LiClO_4 have also been introduced into the luminescent polymer itself to achieve chemical doping [37]. Efficiency increase and lowering of driving voltage have been observed. In addition, the rectification ratio of devices diminishes, and current flow and EL are typically observed under both forward and reverse bias. However, the direct and uniform chemical doping of the luminescent layer does not lead to the formation of a p-n junction and is limited to low concentrations in order to avoid significant quenching of the polymer photoluminescence.

Can one make a polymer analogue of an inorganic p-n junction LED? The answer is yes, since the demonstration of the so-called polymer light-emitting electrochemical cell (LEC) by Pei and Heeger in 1995 [38]. An LEC is based on a mixed ionic/electronic conductor consisting of a luminescent polymer and a solid-state polymer electrolyte. When a large enough voltage bias is applied, the luminescent polymer is *electrochemically* p-doped on the anode side and n-doped on the cathode side; and a light-emitting p-n junction is eventually formed when the expanding p- and n-doped regions meet within the device. Such *in situ* electrochemical doping leads to significantly reduced bulk and contact resistance in an LEC, and both high external quantum efficiency (~4%) and low operating voltage (<4 V) can be achieved, even with air stable electrodes. During the past 10 years, many researchers have made significant contributions to the understanding and optimization of LECs and related materials [39, 40].

5.2 LEC OPERATING MECHANISM AND DEVICE CHARACTERISTICS

Both qualitative and quantitative models have been developed to describe the operating mechanism of LECs [38, 41–44]. This section discusses the LEC operating mechanism and device characteristics qualitatively in terms of *in situ* electrochemical doping and p-n junction formation [38, 45].

5.2.1 LEC operating mechanism

The active material of an LEC is a blend of luminescent polymer and polymer electrolyte. A polymer electrolyte is a solid-state ionic conductor consisting of an ion-solvating/transport polymer and a molecular salt. The polymer electrolyte used in the original LECs is polyethylene oxide (PEO, with a repeating unit of $\text{CH}_2\text{CH}_2\text{O}$) complexed with lithium trifluoromethanesulfonate (LiTf , LiCF_3SO_3). The device configuration and photograph of a sandwich LEC based on MEH-PPV are shown in Figure 5.2.

By appearance, a working LEC is indistinguishable from a polymer LED based on the same luminescent polymer. However, the operating mechanism of an LEC is fundamentally different from that of a polymer LED. Before the application of a voltage bias, the solvated free cations (e.g. Li^+) and anions (e.g. CF_3SO_3^-) in the LEC film are randomly distributed between the metal electrodes (Figure 5.3 (a)). When a sufficiently large voltage bias (typically 2–4 V) is applied, electrons are injected from the negatively biased cathode, and holes

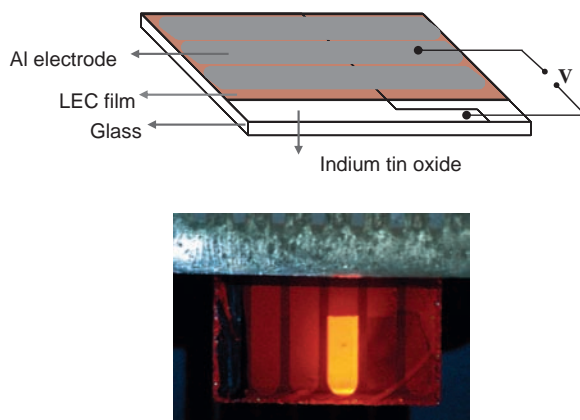


Figure 5.2 Schematic of a sandwich LEC (top) and the photograph of an operating sandwich LEC (bottom)

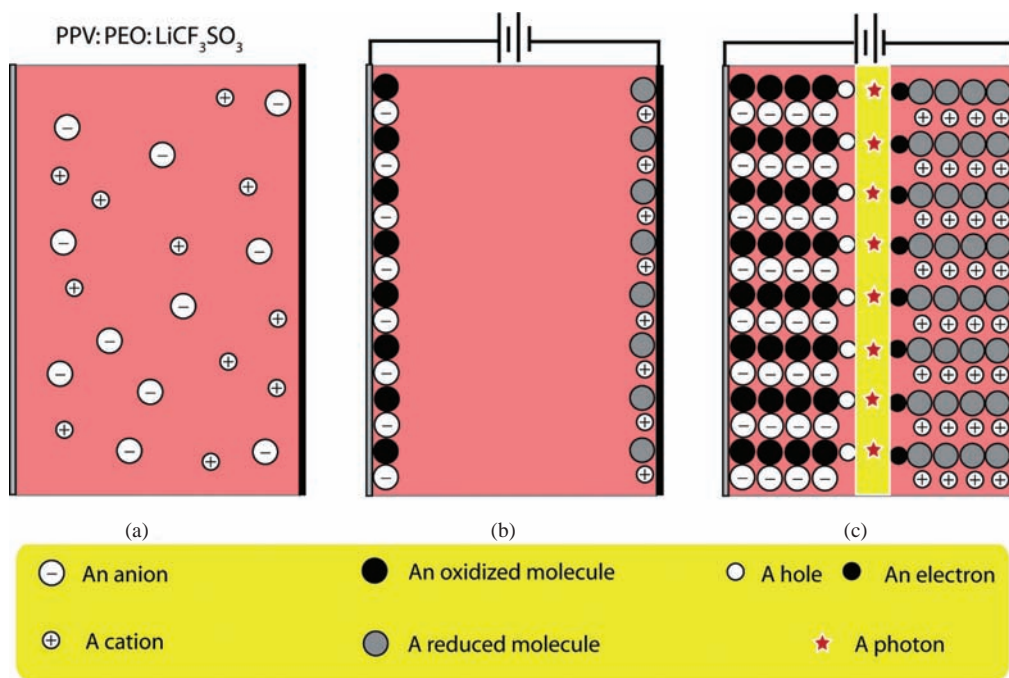


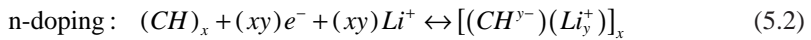
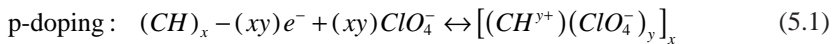
Figure 5.3 Schematic representation of LEC operation: (a) without bias; (b) doping initiation under a voltage bias; (c) electroluminescence from a fully formed p-n junction

are injected from the positively biased anode. As a result, the luminescent polymer is oxidized near the anode and reduced near the cathode. The injected electronic charges are ‘compensated’ by oppositely charged ionic species abundant throughout the polymer film. This leads to electrically neutral, but highly conductive, doped polymer near the electrode/polymer interfaces. The luminescent polymer is p-doped near the anode, and n-doped near the cathode (Figure 5.3 (b)). Under a constant bias, the *in situ* electrochemical doping

process continues with the injection of electronic charges and the redistribution of ionic charges, or counter-ions, causing the doping region to expand. Eventually the p- and n-doping fronts meet within the bulk of the LEC film to form a true semiconductor p-n junction. Only when a p-n junction is formed can EL be observed in an LEC, by the radiative recombination of the injected electrons and holes in the vicinity of the p-n junction (Figure 5.3 (c)). Several key issues involved in the LEC operation are discussed below in more detail.

5.2.1.1 Electrochemical doping

Electrochemical doping provides an alternative approach to chemical doping, to achieve highly conductive conjugated polymers in a more controllable fashion [46]. It is typically realized in a three-electrode electrochemical cell filled with a liquid electrolyte (e.g. a non-aqueous solution of lithium perchlorate, LiClO_4) [46, 47]. A polymer working electrode, which is insoluble in the electrolyte solution, is suspended in the electrolyte along with a counter electrode and a reference electrode. Upon application of a suitable potential difference, which is measured between the working electrode and the reference electrode, the polymer film is oxidized or reduced, and subsequently p- or n-doped when counter ions from the electrolyte enter the polymer. The electrochemical p- and n-doping reactions are described in the following, using polyacetylene $(\text{CH})_n$ as an example:



where y is doping level, and e^- represents an electron.

It should be stressed that in electrochemical doping, the dopants (i.e. counter ions) do not enter the polymer backbone by breaking covalent bonds. Instead, the ions are simply inserted between the polymer chains, which can be easily removed by reversing the polarity of the voltage bias applied. In addition, the doping level is easily controlled by the magnitude of the voltage bias applied. These features make electrochemical doping a more flexible doping technique than chemical doping. An LEC is a two-terminal solid-state electrochemical cell in which the polymer to be doped is mixed intimately with the electrolyte, also a polymer, which together form an interpenetrating network. Electrochemical doping occurs as a result of reduction/oxidation, ion insertion *and* the removal of ions that do not participate in the doping process. The electrochemical doping in an LEC is unique, in that p- and n-doping of the same luminescent polymer occurs simultaneously within the cell, and a light-emitting p-n junction is eventually formed as a result of the electrochemical doping process.

5.2.1.2 The electrode–polymer interface

The electrode–polymer interface in an LEC is assumed to be ‘ion-blocking’. That is, there is no ion exchange between the electrolyte and the metal electrodes. This assumption is consistent with experimental observations, especially due to the fact that the LEC operation

is insensitive to the electrode materials used. However, the initial electrochemical potential difference across the interface or an applied external bias will cause a build-up of net ionic charge at the electrode/electrolyte interface; and an electrical ‘double layer’ will form, consisting of ionic charge on the electrolyte side and an equal amount of opposite electronic charge on the electrode [48]. For LECs with sufficiently high salt concentration ($>10^{20} \text{ cm}^{-3}$), the thickness of the double layer, which extends mostly to the electrolyte side, is extremely small ($\sim 0.5 \text{ nm}$) [43]. As a result, electronic charges can easily tunnel through the double layer even under a moderate voltage bias, resulting in charge injection into the luminescent polymer. This ‘ionic space charge effect’ plays an important role in the initiation of electrochemical doping process [43]. However, once charge injection occurs, the polymer film near the electrodes is doped when the injected electronic charges are compensated by accumulated ionic charges. At a high level of doping, the electrode/polymer contacts in an operating LEC become ohmic and are capable of efficient charge carrier injection.

5.2.1.3 The nature of the electrical current in an LEC

The LEC film is a mixed ionic/electronic conductor, and we expect both ionic and electronic currents to be involved in the device operation. However, the ionic and electronic contributions to the total device current depend on the operating scheme and the various stages of device operation. When a constant voltage bias larger than the energy gap of the luminescent polymer ($V > E_g/e$) is applied to an LEC, electrochemical doping will occur. The device current will be initially of ionic nature, because the polymer film contains far more mobile ionic charges than electronic charges. However, once a p-n junction is formed, which creates a low resistance pathway for electronic charges, electronic current and EL will turn on sharply. Eventually, when doping is fully established with the device exhibiting maximum current and EL, the ionic current will cease. If the voltage bias is subsequently increased or decreased, further electrochemical doping or de-doping will occur due to the redistribution of ions, until a new steady state is reached, and the device current is again entirely of electronic nature. However, if a fast AC bias is superimposed on a DC bias that maintains the doping, it is possible to achieve higher device current of pure electronic nature without altering the level of doping [49]. In a ‘frozen-junction’ LEC (Section 5.5) with a stabilized doping profile, the device current is purely electronic, regardless of the amplitude and frequency of applied bias.

5.2.2 LEC device characteristics

The LEC operating mechanism described above is responsible for its unique device characteristics, which have both advantages and drawbacks compared to a polymer LED.

Figure 5.4 displays the current-voltage-light intensity (I-V-L) characteristics of an ITO/MEH-PPV + PEO + LiCF₃SO₃/Al sandwich LEC [38]. The voltage bias was scanned from 0 to 4 V under forward bias (ITO positive) and from 0 to -4 V under reverse bias (Al positive). The I-V curve is nearly anti-symmetrical about the origin. The lack of current rectification contrasts an LEC to both a conventional p-n junction diode and a polymer LED. More strikingly, the LEC exhibits strong EL under both forward and reverse bias, with brightness reaching greater than 100 cd/m^2 at a mere $\pm 4 \text{ V}$. Such ‘bipolar’ behaviors have

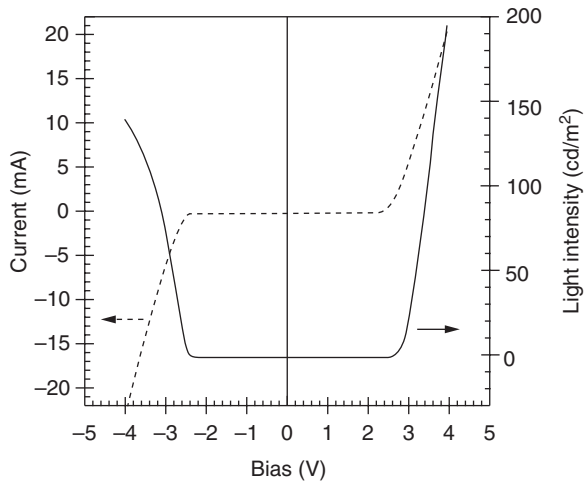


Figure 5.4 Current and light output vs. voltage for ITO/MEH-PPV:PEO:LiTf/Al LECs with the ITO contact wired as positive (reprinted with permission from [38]. Copyright (1995) AAAS)

been observed in a large number of LECs of various material compositions and device structures [38, 45, 50–60]. Although a single-layer polymer LED that uses identical electrodes can also exhibit anti-symmetrical current and bipolar EL, simply because the device structure is symmetrical [62], the device also exhibits extremely high operating voltage and low efficiency. The I-V-L characteristics shown in Figure 5.4 are the manifestation of LECs insensitivity to electrode work function. Regardless of the polarity of the applied voltage bias, mobile ions will redistribute in response to the electrical field. The accumulation of mobile ions at the electrode interface facilitates the initial injection of electronic charges via tunneling. In addition, the subsequent electrochemical doping of the polymer layer renders the electrode/polymer contact even more conductive. The current flow and EL turn-on in an LEC is therefore independent of the work function of the electrode.

Due to the low mobility of the counter-ions, the I-V-L characteristics of an LEC strongly depend on the scan rate and the biasing history. A voltage scan too fast to allow doping to reach steady state will result in a lower device current and a higher apparent EL turn-on voltage [45]. On the other hand, the I-V-L scan shows hysteresis behavior if applied to a previously biased device that has not fully discharged [45, 63, 64]. In fact, unipolar EL and a large diode rectification were observed when a fast voltage scan was applied to a fully turned-on LEC before it could discharge [65]. This is consistent with the fact that an LEC operates on the formation of a unipolar p-n junction.

LECs are characterized by a low EL turn-on voltage ($V_{\text{EL-on}}$), typically less than 4 V, which is largely independent of the electrode work function, and the thickness of the active layer, as well as the polarity of the voltage bias. For a well-made LEC, $V_{\text{EL-on}}$ is found to be approximately the same as the energy gap of the luminescent polymer, i.e. $V_{\text{EL-on}} \approx E_g/e$ [38]. This behavior is clearly illustrated in Figure 5.5, which displays the luminance vs. voltage curves of LECs made with PPV and MEH-PPV, respectively [66]. The $V_{\text{EL-on}}$ of the PPV and MEH-PPV based devices are 2.4 V and 2.1 V, respectively, indistinguishable from the materials' energy gaps determined from the onset of optical absorption. Agreement

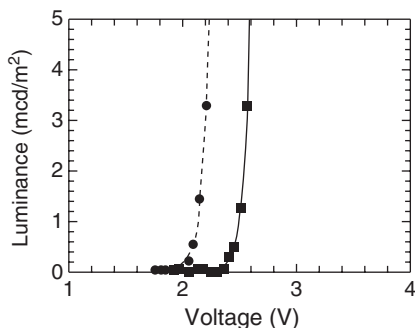


Figure 5.5 Luminance vs. voltage for LECs fabricated with PPV (■) and MEH-PPV (●) (reprinted from [66]. Copyright (1996), with permission from Elsevier)

between $V_{\text{EL-on}}$ and the ‘optical gap’ has also been observed in LECs made with larger-gap polymers emitting in yellow, blue-green or blue [60, 61, 67, 68]. This agreement is expected because an LEC, when fully turned on, is essentially a light-emitting p-n junction; and the minimum voltage to achieve and maintain such a p-n junction by electrochemical doping is equal to the energy gap of the luminescent polymer. In rare cases, $V_{\text{EL-on}}$ was observed to be 0.4~0.6V less than E_g/e [43, 69]. This phenomenon was probably caused by either the radiative recombination of injected holes with thermally excited electrons, or by the existence of sub-gap states, which lower the threshold for electrochemical doping and EL. A low $V_{\text{EL-on}}$ close to the energy gap of the luminescent polymer represents a highly desirable feature for LECs. LECs typically exhibit sharp EL increases beyond $V_{\text{EL-on}}$, and the luminance of the device can reach hundreds of cd/m^2 below 4V. The intrinsically low $V_{\text{EL-on}}$ is responsible for LEC low driving voltage and high power efficiency. For example, an LEC based on a polyfluorene derivative exhibits a maximum luminance of $190\text{cd}/\text{m}^2$ at a 3.1V, a power efficiency of 12 lumin/w , and an external quantum efficiency of 4% [70]. Generally speaking, LECs exhibit comparable or higher quantum efficiencies than polymer LEDs made with the same luminescent polymer, all without the use of reactive cathodes and ultra-thin films.

LECs are not without drawbacks. Since LEC operation involves the redistribution of ions and the doping of the luminescent polymer, an LEC generally displays slow response, due to the low mobility of ionic species. An LEC is often driven by a fixed voltage bias, and it typically takes seconds or even minutes for the device to reach maximum device current and EL intensity. Figure 5.6 displays the ‘turn on’ of the high-efficiency polyfluorene-based LEC mentioned above, after fixed voltage biases of 3.1V or 3.5V have been applied [70]. Both device current and EL intensity increased with time. At 3.1V, it took nearly 2h for both current and EL intensity to reach their respective maximum values of approximately 0.6mA and $190\text{cd}/\text{m}^2$. At 3.5V, the device turned on much faster, reaching current and luminance of $\sim 4\text{mA}$ and $1000\text{cd}/\text{m}^2$ after only 25min. The slow turn-on process is common to nearly all LECs and has often been used as a criterion to determine whether a device is a true LEC or simply a polymer LED.

The increase in device current and EL intensity with time under a constant bias, sometimes by many orders of magnitude, can only be explained by an increase in doping level during *in situ* electrochemical doping. It is obvious that electrochemical doping does not

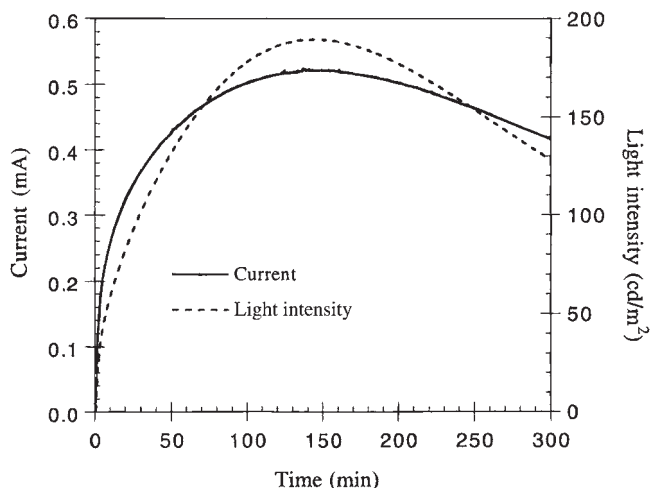


Figure 5.6 Current and light intensity as a function of time of an ITO/BDOH-PF + LiCF₃SO₃/Al LEC biased at 3.1V (reprinted with permission from [70]. Copyright (1996) American Chemical Society)

cease after the initial junction formation and the emergence of EL, but it continues to play an important role in bringing the device to a more useful operating point with maximum EL output. As a result the response time of an LEC, which is defined as the time it takes for EL to increase from 10% to 90% of its maximum value, is slow. In addition, a fully operational LEC exhibits a large open-circuit voltage or short-circuit current when the applied bias is removed (Figure 5.7) [45]. For this reason, an LEC can be regarded as a 'light-emitting battery'. The slow 'discharging' process of an LEC leads to hysteresis. Although the response time of an LEC depends on many factors and can be greatly improved by optimizing the phase morphology of the LEC film [69, 71], it generally lags far behind that of a polymer LED, which can be on the order of ns [72]. This drawback limits LECs application in displays that require a fast refresh rate.

Another major LEC drawback is its poor operating stability. Although above discussions have mentioned a purely electronic 'steady state' as the last stage of theoretical LEC operation, this is not the case in real LECs, due to the degradation of luminescent polymers. In fact, LECs typically exhibit a half-life on the order of 100 h or less [61, 68, 69, 73–75]. In contrast, half-lives in excess of 10 000 h have been achieved in polymer LEDs operated at display brightness [76, 77]. Considering that polymer LEDs and LECs commonly employ the same luminescent polymers and sandwich device configuration, the dramatic difference in stability can only be attributed to electrochemical doping itself. Carter *et al.* have shown that the oxidation of MEH-PPV is a highly reversible reaction, while the reduced form of MEH-PPV is unstable and the reaction irreversible. Even for p-doping, over-oxidation will occur for voltages higher than 1 V (vs. Ag/Ag⁺) and results in irreversible degradation in the polymer.

In addition, the stability of LEC is adversely affected by pronounced phase separation that is common to LEC films containing incompatible non-polar luminescent polymer and polar polymer electrolyte. The existence of large, phase-separated domains leads to highly

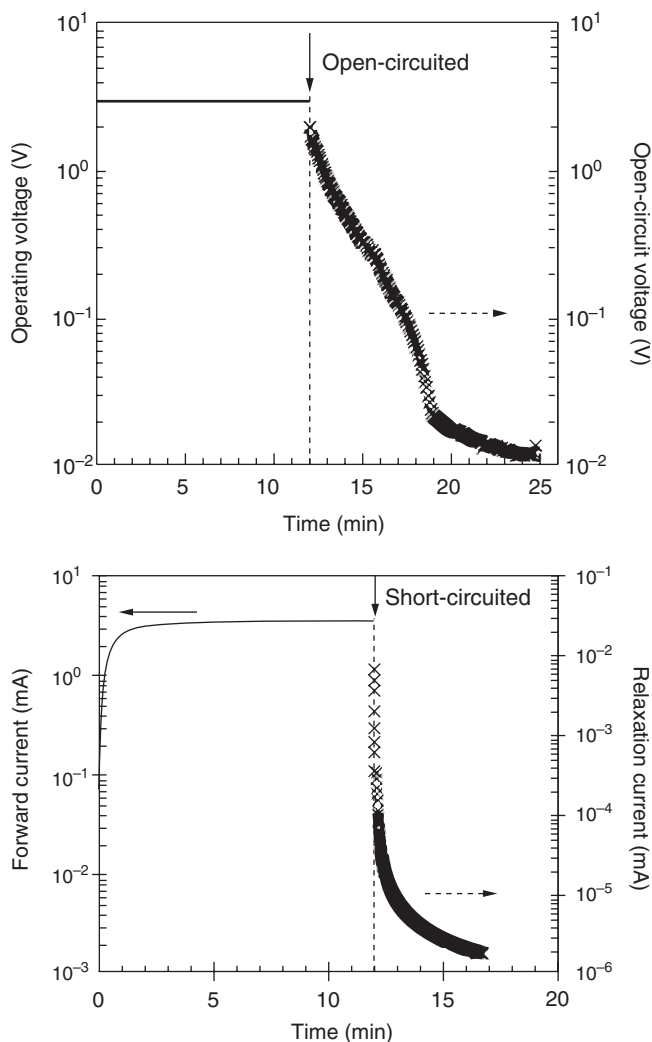


Figure 5.7 Decay of the open-circuit voltage of an ITO/PPV + PEO(Li)/Al cell after applying a 3 V bias for 12 min (top). Chrono-amperometric response at 3 V and the subsequent relaxation at 0 V (bottom) (reprinted with permission from [45] copyright (1996) American Chemical Society)

localized current that can accelerate the current-driven degradation process [78]. The ideal phase morphology of an LEC film is that of a bi-continuous, interpenetrating network with domain size on the order of nanometers [69]. Indeed, it has been shown that finer phase morphology, achieved either by the addition of a surfactant to a PEO-containing LEC or by using a low molecular weight electrolyte, can significantly improve both the turn-on response and the operating lifetime of LECs at room temperature [69, 73]. However, the ultimate solution to the drawbacks of a 'dynamic-junction' LEC is to operate the device in 'frozen-junction' mode, which will be introduced in Section 5.4.

5.3 LEC MATERIALS

The LEC film consists of a luminescent polymer, an ion-solvating/transporting polymer and a molecular salt. The latter two constitute a polymer electrolyte, which provides the mobile counter ions necessary for electrochemical doping. The complexity of the LEC film, as a mixed electronic/ionic conductor, and the unique LEC operating mechanism place stringent requirements on each LEC material component. In return, a well-made LEC has attractive attributes, such as insensitivity to electrode work function and device thickness, which are difficult to realize in polymer LEDs. This section introduces the structures and properties of common luminescent polymers and electrolyte materials, as related to their applications and performance in LECs.

5.3.1 Luminescent polymers

5.3.1.1 Conventional luminescent conjugated polymers

The first LECs were fabricated with the same luminescent polymers used in polymer LEDs, in particular PPV and its derivatives [38, 45]. This is not surprising, since common LED polymers already possess the redox activity required for electrochemical doping, in addition to being luminescent and processable. Figure 5.8 shows the chemical structures of common LED polymers that have also been successfully applied in LECs. With a backbone of alternating single and double bonds, these luminescent polymers are the so-called conjugated polymers or ‘semi-conducting polymers’ [79]. The small energy gap ($<3\text{ eV}$) between delocalized π and π^* states allows the conjugated polymers to be easily reduced or oxidized. If the reduction or oxidation of the polymer segments is accompanied by the insertion of counter ions contributed by either dopants or electrolytes, the polymer becomes n- or p-doped. Doped conjugated polymers can display metallic conductivity and are called ‘conducting polymers’ or ‘synthetic metals.’ PPV, PPP and polythiophene were all extensively studied in their highly doped form before they were used in light-emitting devices [80].

Unlike a polymer LED, an LEC utilizes both the intrinsic and extrinsic properties of the luminescent polymer. Highly luminescent in their pristine state and conductive in their doped state, the polymers displayed in Figure 5.8 were widely used in early LEC studies. With an energy gap ranging from 1.5 eV to 3 eV, these polymers give rise to EL emission spanning the entire visible spectrum. In addition, LECs based on these polymers exhibit extremely low EL turn-on voltage as well as high quantum efficiencies. On the other hand, a large quantity of polymer electrolyte, such as PEO:LiTf, must be added to these pure electronically conductive polymers in order to solvate and transport counter ions. The incompatible polarity between the luminescent polymer and the ion-conducting polymer often cause pronounced phase separation, which contributes to the slow response and poor stability of LECs.

5.3.1.2 Luminescent polymers with ion-conductive side groups

A logical solution to the problem of phase separation in an LEC is to employ a luminescent polymer that is both electronically and ionically conductive, so that the need for a separate

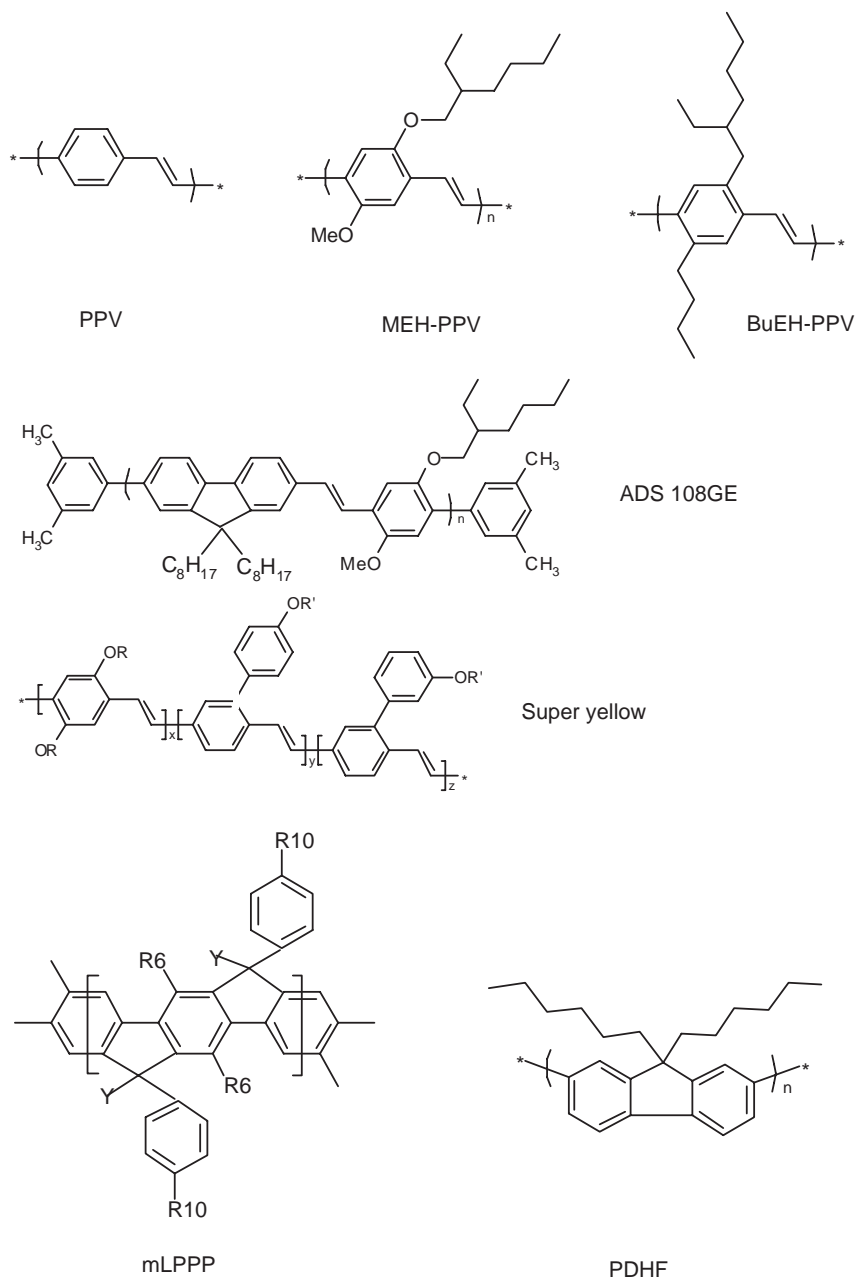


Figure 5.8 Chemical structures of luminescent conjugated polymers commonly used in LECs

ion-solvating polymer is eliminated. The first such polymer, poly[9,9-bis(3,6-dioxaheptyl)-fluorene-2,7,-diyl], or BDOH-PF, was synthesized by Pei [71, 81]. The conjugated polyfluorene main chain is capable of transporting electrons and holes, while the PEO-like bis(3,6-dioxaheptyl) side groups can solvate and transport ions. BDOH-PF is soluble in common organic solvents and exhibits a photoluminescence quantum efficiency of 73% in solid film, one of the highest among luminescent polymers. Single-layer LECs have been fabricated by sandwiching an emissive layer consisting of BDOH-PF and lithium triflate salt at a weight ratio of 5.6:1 between ITO and Al electrodes. The spin-cast BDOH-PF:LiTf films (~150 nm thick) are colorless and transparent. The BDOH-PF LECs exhibit by far the highest external quantum efficiency (4%) and luminous efficiency (12 lm/W) among all polymer LECs. At 3.5 V, the LEC displays a maximum luminance of 1000 cd/m² (Figure 5.6).

By comparison, the ITO/BDOH-PF/calcium LED (no LiTf added) turned on at 9 V and reached a luminance of 100 cd/m² at 30 V. The quantum efficiency of the diode was only 0.3%, even though low work function calcium was used as the cathode. These results clearly demonstrated that BDOH-PF did possess both ionic and electronic conductivity, and an LEC resulted without the addition of PEO. However, the BDOH-PF LEC still suffered from slow response and poor stability. In fact, the EL turn-on of the device was among the slowest, even when compared to LECs made with PEO (Figure 5.6). The bis(3,6-dioxaheptyl) side group, despite being PEO-like, is perhaps too short to efficiently solvate and transport counter ions. Indeed, the EL turn-on speed was significantly improved when a small amount (~10% by weight) of PEO was added to the BDOH-PF blend [81]. The device operating lifetime of the BDOH-PF LEC ranged from 10 to 20 hours, depending on the stress voltage. Furthermore, the emission color changed during continuous operation, from the initial sky blue to blue green and even white. This change was attributed to a morphology change that facilitated the formation of interchain excimers. The color stability of BDOH was greatly improved when end-capped and/or copolymerized with anthracene [82].

Since then, ion-solvating/transporting groups, such as oligo(ethylene oxide), OEO, or crown ether, have also been successfully grafted onto PPVs [50, 52–55, 83–88], polythiophenes [51], fluorene copolymers [68] and thienylene-phenylene copolymers [89], resulting in a new class of luminescent polymers with a conjugated backbone and ion-conducting side groups. The molecular structures of these materials, along with the aforementioned BDOH-PF polymers, are shown in Figure 5.9. The application of the above materials in LECs generally yields characteristic LEC behaviors, such as low EL turn-on voltage and bipolar EL and current flow. The oligo(ethylene oxide) side groups are optically inactive but improve the solubility of the polymer due to its flexibility.

As expected, the LEC films exhibit a smoother and finer surface morphology, due to the elimination of ion-conducting polymers such as PEO [52, 85]. Low EL turn-on voltage comparable to the polymer energy gap ($V_{on} \sim E_g/e$) has been observed in LECs made with BTEM-PPV, DB-BTEM-PPV, BDMOS-co-BTEM-PPV and BTEO-PPV-*alt*-PPV [50, 53, 55]. In addition, sub-millisecond or milliseconds response times have been observed in LECs made with BTEM-PPV and BTEO-PPV-*alt*-PPV [83, 85]. However, LECs made with 15C5-DMOS-PPV containing LiTf showed very slow response and a relatively high EL turn-on voltage of 3.8 V. The addition of PEO significantly improved the device performance, suggesting that the crown ether side group did not provide sufficient ion-solvation/transporting power [84]. In general, the grafting of ion-conducting side groups to a

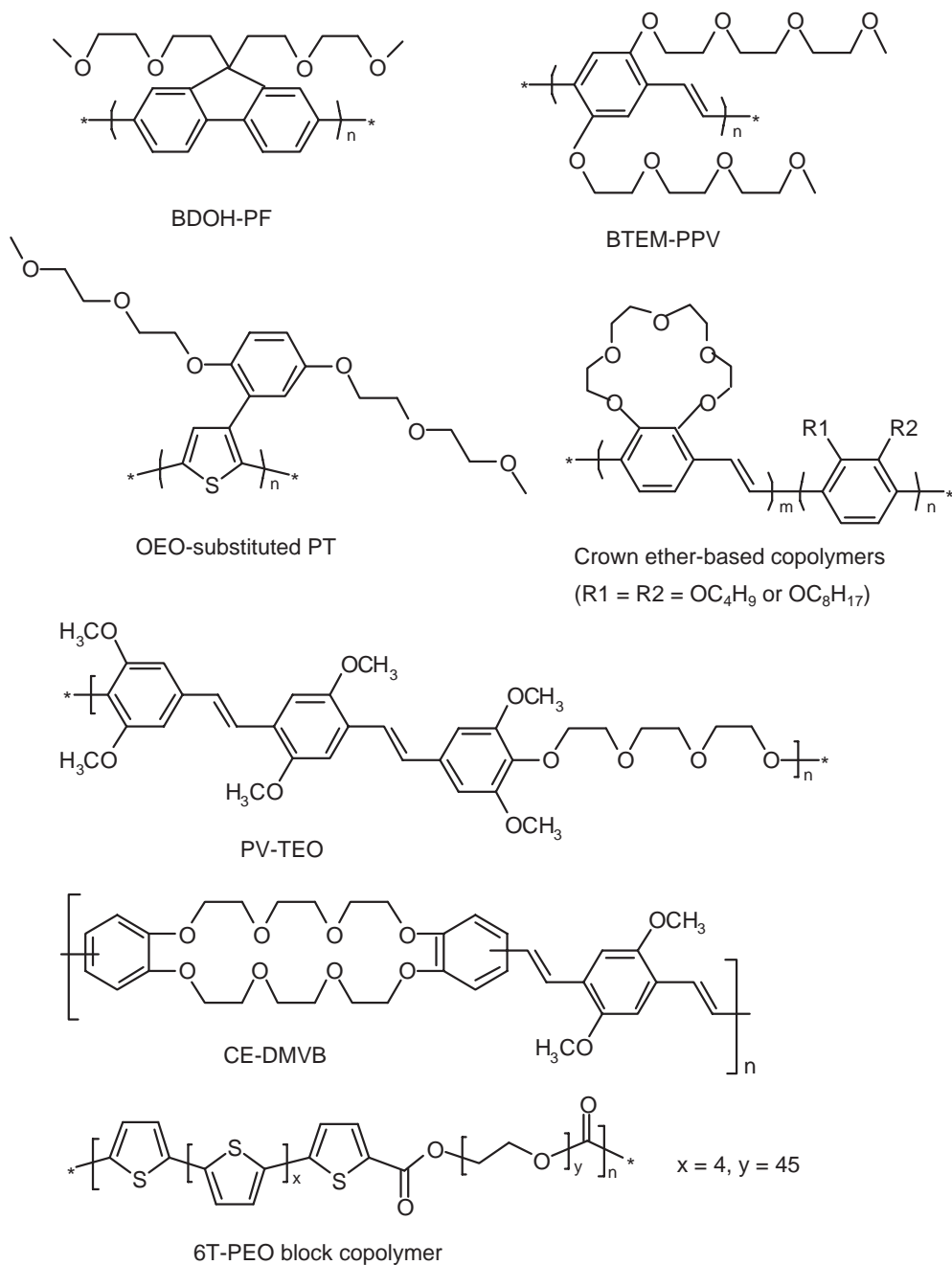


Figure 5.9 Chemical structures of some luminescent conjugated polymers with ion-conducting groups

semi-conducting luminescent polymer promote ion solvation and transport. True LEC behaviors are obtained using these materials without the addition of a separate ion-transport polymer. However, the device performance of these 'two-component' (polymer + salt) LECs is not superior to conventional 'three-component' LECs, with the exception of BDOH-PF-based LECs.

5.3.1.3 Block copolymers containing ion-conductive segments

Another approach that introduces ionic conductivity into luminescent conjugated polymers is the insertion of oligo(ethylene oxide) or crown ether segments into the backbone of the luminescent polymer [67, 90–95]. The molecular structures of some resulting copolymers are also shown in Figure 5.9. OEO groups were first inserted into the main chain of PPV to achieve blue emission by shortening the effective conjugation length [96]. Indeed, all PPV-based copolymers emit in blue or blue-green with relatively high quantum yield [90, 91, 94, 95]. However, the ionic conductivity of the copolymers appeared to be insufficient for demonstrating efficient 'two-component' LECs. In fact, the LECs made from these polymers also contained PEO in addition to LiTf salt. The three-component LECs showed low EL turn-on voltage close to the polymer energy gap, but the efficiencies and the luminance of the devices were low [67, 90, 91]. A perylene-based copolymer yielded a maximum luminance of only 1.6 cd/m^2 in LECs containing LiTf. The addition of PEO resulted in even lower performance [92]. As well, some copolymers were not characterized in LECs [93–95]. Apparently the copolymer approach so far has not generated viable materials for high performance LEC applications, and more research is needed to fully evaluate the potential of this class of materials.

5.3.2 Electrolyte materials

The active material of an LEC must contain the mobile ions necessary for electrochemical doping. This was first achieved by blending a polymer electrolyte into the luminescent polymer. A polymer electrolyte in its original sense is a solid-state ion conductor formed by dissolving salts in a high molecular weight polar polymer host. Therefore, a polymer electrolyte should be differentiated from a polyelectrolyte such as poly(sodium styrene sulfonate), which is a polysalt with an immobile polyanion. The poly(ethylene oxide), or PEO, used in the original LECs is the first and to date most studied electrolyte polymer that is able to solvate a wide range of salts. Ion solvation results from the strong interaction between the ether oxygen of PEO and the metal cations of the salt, which leads to the formation of coordination bonds. High molecular weight PEO is a semi-crystalline material with a melting point of $T_m = 65^\circ\text{C}$ and a glass transition temperature $T_g \approx -60^\circ\text{C}$ [97]. Ion transport in PEO mainly occurs in the amorphous phase at temperature above T_g . Since chain diffusion is negligible in high molecular weight hosts, the motion of ions strongly depends on the segmental motion of polymer chains that result from bond rotation, which creates a localized liquid-like environment.

In dynamic bond percolation theory (DBP) [98], cation motion is the continuous making and breaking of co-ordinate bonds with motion between coordinating sites, while anion motion is regarded as a hopping between an occupied site and a void that is large enough

to accommodate the ion. The assumption of different mechanisms responsible for cation and anion motion is consistent with the experimental observation in *a*PEO-LiPF₄, where the diffusion of Li⁺-based species and PF₆⁻-based species have different temperature dependencies [97]. Here the most important conclusion relevant to LEC application is that in PEO-based electrolytes, both cation and anions are mobile, making simultaneous p- and n-doping of the luminescent polymer possible. In addition, PEO-based electrolytes, such as PEO-LiCF₃SO₃, exhibit adequate room temperature ion conductivity ($\sim 10^{-6}$ S/cm) [45] and excellent electrochemical stability – attributes that are highly desirable for LEC applications. As a result, PEO-based electrolytes are still widely used in LEC research as the model electrolytes.

The main disadvantage of PEO is its poor compatibility with the luminescent polymer. All ion-solvating polymers, especially PEO, are strongly polar; they are soluble in polar solvents, such as water, acetonitrile and tetrahydrofuran, but not soluble in non-polar organic solvents, such as toluene and xylene, which are commonly used to dissolve solution-processable luminescent polymers. Thus, many highly luminescent conjugated polymers cannot be used in LECs, due to the lack of common solvents. Even when a common solvent is available, the resulting solvent-cast LEC films tend to be severely phase-separated due to the limited entropy gain when high molecular weight polymers are mixed. A variety of techniques have been used to compatibilize the components of LEC blends. Cao *et al.* first introduced a bi-functional additive octylcyanoacetate (OCA) into the LEC blend containing MEH-PPV and PEO: LiTf [69]. The surfactant-like OCA (polar on one end and non-polar on the other) improved the mixing of the luminescent polymer and electrolyte polymer by reducing the surface energy and enthalpy of mixing. The resulting LEC film showed bi-continuous interpenetrating network morphology with typical feature size in the range of 10–100 nm. The TEM micrograph of the OCA containing LEC film is shown in Figure 5.10. With the addition of OCA, the device exhibited an EL turn on voltage

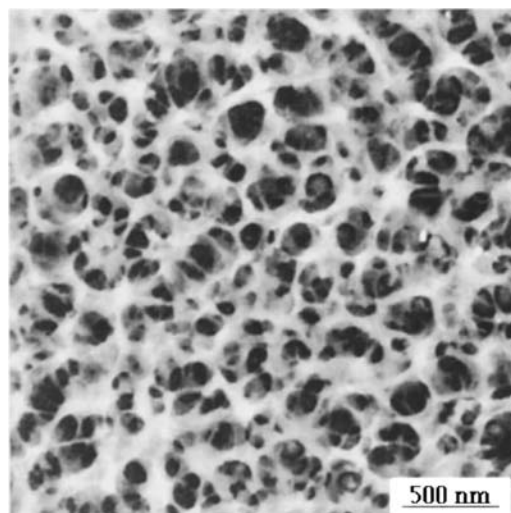


Figure 5.10 TEM micrograph of MEH-PPV + PEO + LiTf + OCA composite film (reprinted from [69] with permission. Copyright 1996 American Institute of Physics)

of only 1.5 V and a luminance of nearly 1000 cd/m² at 3 V, compared to a $V_{\text{EL-on}}$ of ~2.1 V and luminance of 10 to 20 cd/m² at 3 V without OCA. The addition of OCA also drastically improved the response time and operational lifetime of the device. The response time was approximately 20 ms, compared to approximately 1 s without OCA. At an initial luminance of 300 cd/m², continuous operation for more than 100 h resulted in less than 20% decrease in luminance. The MEH-PPV:PEO:LiTf LEC with OCA still represents the best device performance among LECs made with PEO-based electrolytes.

Subsequently, Cao *et al.* described LECs with crown ether as solid electrolyte, without the use of PEO [73]. Crown ethers are stronger complexing agents for alkali metal ions than their linear counterparts, and they have been used as plasticizers in polymer electrolytes to reduce cation–anion interactions by shielding the cations from nearby anions. Used alone, crown ethers exhibit moderate ion conductivity when complexed with lithium halide. However, the high efficiencies and low EL turn-on voltage of BDOH-PF:LiTf LECs described earlier suggest that even as pendant groups, crown ether is able to solvate Li cation. Cao's seminal work on crown ether-based LECs involves various luminescent conjugated polymers, Li salts and several commercially available crown ethers. With MEH-PPV as the luminescent polymer, a majority of the crown ether:Li salt combinations gave rise to LECs with low operating voltage and anti-symmetrical I-V curves. Among the five crown ethers tested, Dicyclohexano-18Crown-6 (DCH18C6) gave the best device performance, comparable to that of PEO-based LECs. The performance of MEH-PPV:DCH18C6-based LECs, on the other hand, depends on the anions of the salt. LECs made with Li-imide, Li-triflate, Li-methide and Li-perchlorate all achieved luminance of more than 100 cd/m² at a bias of 3–4 V; while LiCl-, LiPF₆- and LiOCCF₃-based devices returned little or no light, even at a bias of 30–40 V. The effects of anions on the kinetics and stability of LECs have also been noted in PEO-based LECs [61]. Overall, a green-emitting BuEH-PPV:DCH18C6:Li-imide-based LEC gave the best quantum efficiency of more than 1% and luminance of over 400 cd/m² at 4 V.

Crown ether-alkali metal complexes are soluble in non-polar solvents such as toluene and xylene. In addition, less phase separation is expected when luminescent polymers are blended with low molecular weight crown ether, due to larger entropy of mixing compared to the negligible entropy gain when high molecular weight polymers are mixed. Better film quality is believed to be responsible for the performance of a MEH-PPV:DCH18C6:Li-imide LEC, which displays a fast response and good operating lifetime, similar to those observed in the MEH-PPV:PEO:LiTf:OCA LEC. Wenzl *et al.* observed under AFM that blending mLPPP with DCH18C6 at a weight ratio of 1:1 had almost no influence on the surface RMS roughness in comparison with pristine mLPPP films (1.5 nm vs. 1 nm); whereas the mLPPP/PEO blend film surface was clearly structured due to more pronounced phase separation [56, 60]. Similar observations were also obtained by Edman *et al.* in LEC films based on a different luminescent polymer [99]. The better phase morphology of crown ether containing LEC film has led to the demonstration of LECs with sub-microsecond response [71, 100].

In spite of different molecular weight, both PEO and crown ether are solvents serving the crucial functions of ion solvation and transport in an LEC. Without PEO or crown ether, a ITO/PPV:LiTf/Al device functions like a typical ITO/PPV/Al LED [45]. Interestingly, characteristic LEC behaviors, such as low turn-on voltage, slow response speed and bipolar EL, have also been observed in polymer devices based on 'solvent-free electrolytes'. These include certain 'ionic liquids' or room temperature molten salts [63, 78, 101–103], single-

ion conducting ionomers [64, 104, 105] and luminescent conjugated polyelectrolytes (LCPE) [58, 59, 106–110]. Fluorescence imaging of a large planar LEC containing MEH-PPV and an ionic liquid 1-ethyl-3-methylimidazolium ethylsulfate directly confirmed the occurrence of electrochemical doping and junction formation in a solvent-free system. In the case of luminescent conjugated polyelectrolytes, the material is both an electronically conductive, luminescent, conjugated polymer and an ion-conductive electrolyte, although only one type of ion is mobile. LCPEs have the advantages of being soluble in more environmentally benign polar solvents, such as water and alcohol, and allowing the fabrication of ‘single-component’ LECs that do not suffer from phase separation. However, LECs based on these novel electrolytes display far inferior device performance to PEO- or crown ether-based LECs, especially in terms of quantum efficiency.

5.4 FROZEN-JUNCTION LECs

LECs possess some very attractive device characteristics that include low EL turn-on voltage, high quantum and power efficiencies, insensitivity to the thickness of the polymer film, the work functions of the electrodes and the energy gap of the luminescent polymer. On the other hand, due to the nature of their principal operating mechanism, being *in situ* electrochemical doping, LECs also suffer from the serious drawbacks of slow response and poor operational stability. The relaxation of a ‘charged’ LEC upon the removal of voltage bias also makes it difficult to study the electronic structure of the polymer p-n junction formed, and prevents application in photovoltaic and photoconductive devices. Both the response speed and the operational lifetime of an LEC can be improved, to some extent, by controlling the phase morphology of the LEC film. The advancement in LEC materials, as introduced in Section 5.3, largely reflects an attempt to achieve optimized phase morphology via the creation of multi-functional materials. The successful application of many novel luminescent polymers and electrolyte materials in LECs demonstrates the general nature of LEC operating mechanism. However, this pure chemistry approach had not yet yielded LECs that are fast and long-lasting.

In contrast, conventional inorganic p-n junction LEDs are prized for their fast response speed, extremely long operating lifetime and high efficiency in a wide variety of applications, such as traffic signals, automotive tail lights, general lighting and outdoor displays. While inorganic semiconductors possess much higher charge carrier mobility and chemical stability than their organic counterparts, an inorganic p-n junction’s speed and stability also has to do with its operating temperature. An inorganic p-n junction is commonly fabricated by a high temperature chemical doping process, where the dopant atoms enter the host material by thermal diffusion [111]. After necessary annealing and metalization procedures, the finished p-n junction diode is operated at near room temperature, where ionized donors and acceptors do not have sufficient energy to migrate out of the crystal lattice. The dopant distribution and the p-n junction are therefore permanent. As a result, the operation of a conventional p-n junction LED only involves electronic charges, and the turn-on speed is RC limited. By contrast, a polymer p-n junction in an LEC must be formed and operated at the same temperature. The finite mobility of solvated ions at room temperature is ultimately responsible for all the drawbacks of LECs.

This comparison suggests that the response speed and operational stability of the LEC might be significantly improved simply by cooling a fully formed p-n junction to freeze the

counter ions and all the electrochemical processes. This approach is indeed possible, because the ion transport in a polymer electrolyte such as PEO:LiTf is strongly temperature dependent. Below the glass transition temperature of the polymer electrolyte, the polymer chain segmental motion ceases and ions are immobilized. So-called frozen-junction LECs were first realized by Gao *et al.* in 1997 [112]. An ITO/MEH-PPV:PEO:LiTf/Al LEC was turned on at room temperature under a fixed voltage bias of 3 V. The fully turned-on LEC was then cooled to 100 K with the voltage bias on to prevent the p-n junction from relaxing during the cooling process. Once at 100 K, the 3 V 'pre-bias' was removed, and the device was tested to verify and characterize the stabilized p-n junction. Even at 100 K, the LEC exhibited efficient EL and low $V_{\text{EL-on}}$ close to the polymer energy gap.

On the other hand, frozen-junction LECs also displayed device characteristics that are dramatically different from dynamic-junction LECs operated at room temperature. For example, the current-voltage (I-V) curve showed rectifying behavior, and EL was only observed under forward bias that corresponds to the polarity of the 'prebias'. Moreover, the polarity of current flow and EL could be reversed by simply reversing the polarity of the 'pre-bias' and thereby the polarity of the p-n junction formed. This behavior is shown in Figure 5.11, where the I-V-L characteristics were obtained on the same device. The current rectification ratio displayed in Figure 5.11 is very modest due to the increased bulk resistance at low temperature. Significantly larger rectification ratio (~ 80) was observed in frozen-junction LECs operated at higher temperatures [113]. The I-V-L characteristics were independent of scan rate and free of hysteresis when the voltage was scanned cyclically, providing additional evidence that the p-n junction formed at room temperature was indeed frozen [113].

As expected for a frozen p-n junction, the EL turn-on response was also greatly improved. Figure 5.12 compares the temporal EL response of a frozen-junction LEC operated at 100 K

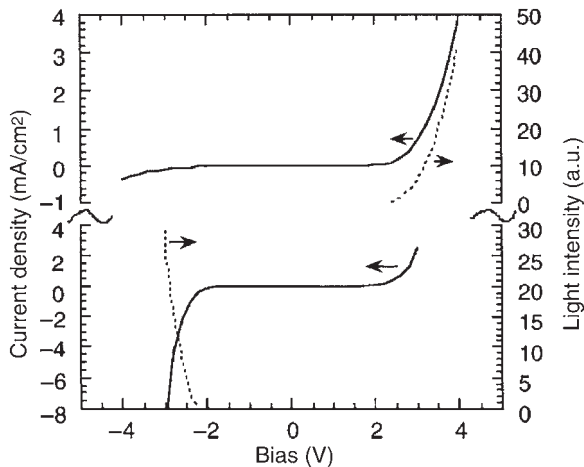


Figure 5.11 Current and light intensity vs. voltage characteristics of a frozen-junction LEC measured at 100 K. The LEC was initially turned on at 300 K by applying a +4 V bias, and then cooled to 100 K (upper curves). The same device was then warmed to 300 K and biased at -3 V before it was cooled to 100 K again (lower curves) (reprinted with permission from [112]. Copyright 1997 American Institute of Physics)

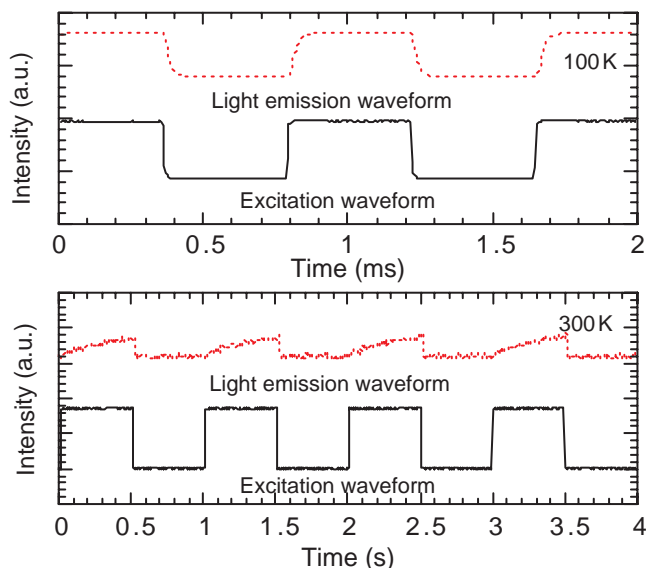


Figure 5.12 Comparison of EL response between a frozen-junction LEC at 100K and a dynamic-junction LEC at 300K (reprinted with permission from [112]. Copyright 1997 American Institute of Physics)

and a dynamic-junction operated at 300 K. At 300 K, the EL did not peak during the excitation cycle of 0.5 s, whereas the frozen-junction LEC displayed an EL turn-on time of approximately $40\ \mu\text{s}$, limited by the RC time constant of the photodiode amplifier. Using a faster photodetector, a turn-on time of 678 ns was later obtained on a similar frozen-junction LEC [113]. The nearly 10^8 -fold increase in response speed unambiguously confirmed the creation of a stabilized p-n junction whose operation involved only the fast electronic processes.

In addition, the freeze-out of ionic mobility also led to much better operational stability, as evidenced by a linear EL intensity vs. current curve up to a current density of $300\ \text{mA}/\text{cm}^2$ [113]. In contrast, the dynamic-junction LEC showed sublinear L-I characteristics and would self-destruct when driven at higher current density and voltage bias. A frozen p-n junction, therefore, allows an LEC to be operated well outside the electrochemistry stability window of the luminescent polymer. Preliminary study of the stability of a frozen-junction LEC driven at $5\ \text{mA}/\text{cm}^2$ showed a 5% drop in EL intensity after nearly 14 h. The frozen junction was found to be stable (frozen) at temperatures up to 200 K. However, at 250 K, the decrease in current rectification ratio with time, as well as the observation of ‘charging’ behavior under a constant bias, indicates that the p-n junction cannot be completely frozen at this temperature. The upper limit in frozen-junction operation temperature (200–250 K) is very close to the glass transition temperature of PEO [113].

Recently, the lifetime and degradation characteristics of frozen-junction LECs in a planar configuration (Section 5.5) have been systematically studied [114]. Two seemingly minor factors, the end group of the same luminescent polymer (MEH-PPV) and the type of substrate on which the device is constructed, have been shown to have profound effects on the stress behaviors of these devices when operated at a nominal temperature of 200 K. In

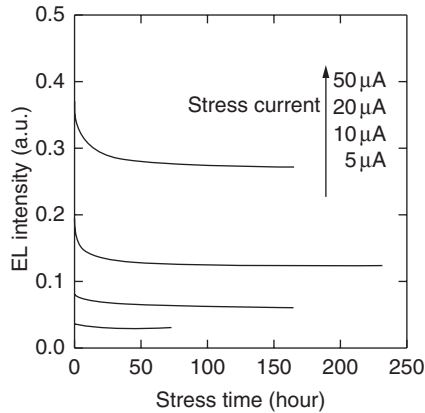


Figure 5.13 Time evolution of EL intensity for identical 0.6 mm frozen-junction LECs stressed at various currents at 200 K (reprinted from [114] copyright (2006) American Institute of Physics)

devices made on glass substrates, an anomalous increase in light intensity and driving voltage has been observed under constant current stress measurement. This increase was attributed to the relaxation of the electrochemical doping, which reduced photoluminescence quenching and increased resistance in the polymer film. The implications of doping relaxation will be discussed in Section 5.5. In general, the doping relaxation is accelerated by the poor thermal conductivity of glass substrate, which causes significant temperature rise in the device, due to self-heating. Evidence also suggests that doping relaxation can occur, even at temperatures below T_g of the polymer electrolyte. All devices were short-lived when operated at or above 250 K. However, devices made on sapphire substrates based on 3,5-dimethyl phenyl-terminated MEH-PPV were remarkably stable when operated at 200 K (Figure 5.13). At a constant stress of $50 \mu\text{A}$, which corresponds to a current density of 1 A/cm^2 due to the small cross-sectional area of planar configuration, the estimated half-life was approximately 700 h. During the 165-h stress at $50 \mu\text{A}$, $594\,000 \text{ C/cm}^2$ of charge passed through the film. The extremely high redox stability of the frozen-junction planar LEC is in fact comparable to that shown by a polymer LED with a half lifetime of 20 000 hours, stressed at 8.3 mA/cm^2 [76].

A true p-n junction at thermal equilibrium possesses a built-in potential V_{bi} and a built-in electrical field E_{bi} , due to the chemical potential (i.e. Fermi level) difference of p- and n-doped semiconductors. This E_{bi} can be exploited for energy conversion and light detection applications via the photovoltaic effect. In fact, the common silicon solar cell is essentially a p-n junction diode with a shallow, flat junction close to the illuminated surface. Indeed, an open-circuit voltage (V_{OC}) of 1.3 V and a short-circuit current (I_{SC}) of $3.5 \mu\text{A/cm}^2$ have been measured off a frozen-junction LEC under 20 mW/cm^2 illumination at 430 nm [112]. Moreover, the polarity of both V_{OC} and I_{SC} was reversed when the polarity of the ‘pre-bias’ was reversed. This suggests that the photovoltaic response in a frozen-junction LEC indeed originated from the p-n junction itself. By contrast, a polymer LED also exhibits photovoltaic response, but the built-in electrical field is the result of the electrode work function difference [115]. The power conversion efficiency of a frozen-junction LEC photovoltaic cell was low because the majority of the photogenerated charge carriers recombine.

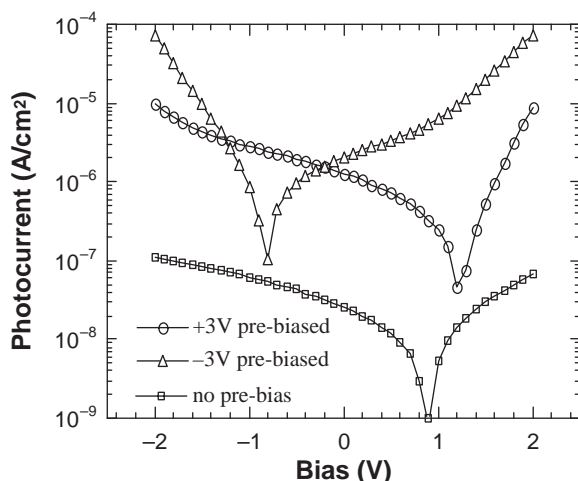


Figure 5.14 Photocurrent vs. voltage characteristics of a frozen-junction ITO/MEH-PPV:CN-PPV:PEO:LiTf/Al photovoltaic cell with various prebiases. The incident light intensity is 20 mW/cm^2 at 430 nm (reprinted from [116] with permission. Copyright Wiley/VCH 1998)

Higher conversion efficiency has been achieved by introducing a more electro-negative polymer into the polymer blend to facilitate charge separation by ‘photoinduced charge transfer’ [116]. Figure 5.14 displays the photocurrents vs. voltage bias of such a polymer p-n junction photovoltaic cell, which again shows reversible photovoltaic polarity depending on the polarity of the initial bias. A maximum I_{SC} of $83\ \mu\text{A/cm}^2$ was obtained. On the other hand, a control cell directly cooled to 100 K, without first being turned on at 300 K, only showed an I_{SC} of $0.26\ \mu\text{A/cm}^2$ with a fixed polarity. This illustrates the importance of doping and p-n junction for reducing the overall device resistance and providing a large built-in electrical field for photovoltaic conversion.

Frozen-junction LECs possess the complementary advantages of a dynamic-junction LEC and a polymer LED without suffering from any of their drawbacks. A stabilized polymer p-n junction opens up the possibility of a whole new class of high performance polymer-based photonic devices that may also include photodetectors, solar cells and diode lasers. The only remaining drawback of frozen-junction LEC is the low operating temperature, which is limited to below 200 K when PEO-based electrolyte is used. Frozen-junction operation has also been demonstrated with an ionic liquid electrolyte [103]. The MEH-PPV: ionic liquid LEC exhibits unipolar EL, fast response and improved lifetime when operated in frozen-junction mode. But like PEO-based LEC, the transition temperature for frozen-junction operation was also between 200 K and 250 K.

Frozen-junction LECs that can be operated at room temperature were first reported by Yu *et al.* in 1998 [117]. The LECs were based on soluble PPV derivatives and an electrolyte containing crown ether and LiTf. The green-emitting BuEH-PPV:CE:LiTf cell was inefficient at room temperature, with a quantum efficiency of 0.04% and a luminance of 20 cd/m^2 at 4 V. However, the device could be ‘activated’ by applying a fixed voltage bias of 3–4 V at an elevated temperature of 60–80 °C, or by applying a large voltage bias (15–20 V) at RT to induce self-heating. Once activated and cooled to RT, the device exhibited drastically

different device characteristics, consistent with those of a frozen-junction LEC. These include a low $V_{\text{EL-on}}$ of 2.1 V, a large current rectification ratio of 10^4 – 10^5 at 4 V, and a fast response time of 25–35 μs .

The activated device also displayed a vastly improved external quantum efficiency of 3% and a maximum luminous efficiency of 5.6%, both among the best reported for green-emitting devices. At 8 V, the luminance reached 21 400 cd/m^2 . The activated device was no doubt an LEC, and the activation process was the turn-on process during which a p-n junction was formed by *in situ* electrochemical doping. However, there was no mention of the stability of the frozen junction at room temperature. More recently, Edman *et al.* also observed room-temperature frozen-junction behavior in a planar LEC based on the luminescent polymer ‘superyellow’ and the same crown ether:LiTf electrolyte [99]. The device maintained fast current and EL response after being left under open-circuit condition for an hour. Since the activation temperature (60–85 °C) of these crown ether-based devices was very close to room temperature, the p-n junction is probably only quasi-frozen at room temperature. More detailed studies are needed to determine the stability of frozen junctions at room temperature. For LECs based on polymer electrolytes, frozen junction operation at elevated temperatures (e.g. RT) can be achieved either by the use of polymer electrolytes with high T_g , so that the ion conductivity at room temperature is negligible, or by the cross-linking of the low T_g polymer electrolyte once the p-n junction is formed.

5.5 PLANAR LECs

The DC resistance of a two-terminal device such as a polymer LED or LEC is the sum of contact resistance and bulk resistance. The overall device resistance must be small in order to achieve low operating voltage and high power efficiency. In a polymer LED, the contact resistance is minimized by employing electrodes with work functions matching the LUMO and HOMO of the luminescent polymer. To reduce the bulk resistance and facilitate charge injection due to the high resistivity of undoped conjugated polymer, an ultra-thin film must be used [118]. In an LEC, *in situ* electrochemical doping renders the LEC film highly conductive, which automatically reduces both the contact resistance and the bulk resistance of the device. Consequently, the performance of an LEC is highly insensitive to the choice of electrode materials and the thickness of the polymer film. This makes it possible to demonstrate LECs in a planar configuration with identical electrodes and a large interelectrode spacing. Such planar LECs have been realized and reported in the original LEC paper by Pei *et al.* [38]. The large interelectrode spacing, on the order of 10 μm , allows the planar devices to be imaged under a microscope, providing a unique cross-sectional view of the device operation.

Figure 5.15 shows the photomicrograph of a planar LEC fabricated with interdigitated gold electrodes (dark strips) [38]. The spacing between each pair of electrodes is 15 μm , and a 4 V bias was applied to turn on the devices. The extremely low turn-on voltage of these planar LECs, which had a thickness (inter-electrode spacing) of six times that of sandwich LECs, clearly demonstrated the LEC’s insensitivity to device thickness and electrode materials. EL from the planar LECs was observed in a narrow region 1 to 3 μm wide, consistent with the formation of a light-emitting p-n junction. Subsequently, Yu *et al.* demonstrated PPV- and MEH-PPV-based planar LECs with a smaller interelectrode spacing of 5 μm [119]. The devices can be operated with a luminance of 100 cd/m^2 at voltages below

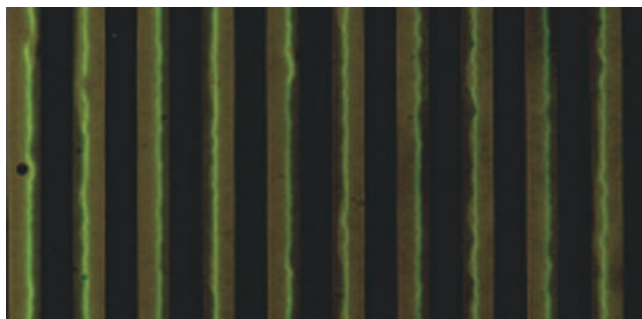


Figure 5.15 Photograph of a polymer LEC in a surface cell configuration with interdigitated gold electrodes (dark lines); the spacing between the electrodes is $15\mu\text{m}$. 4V is applied across each pair of electrodes (reprinted with permission from [38], copyright (1995) AAAS)

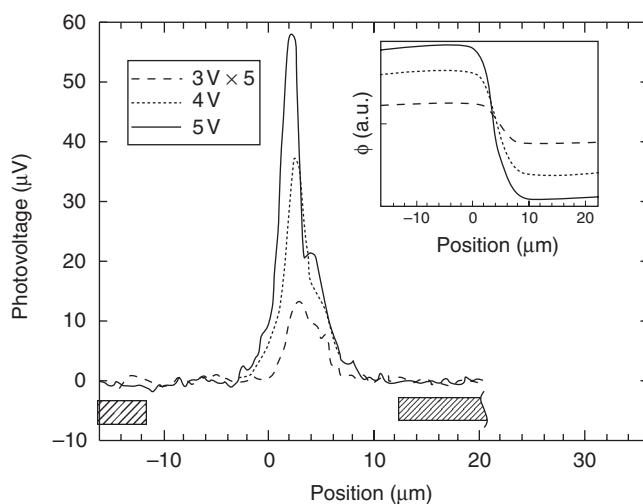


Figure 5.16 OBIC scans (photovoltage vs. position) showing the built-in electric field across a planar LEC. The spatial profile of the built-in potential is shown in the inset (reprinted with permission from [120], copyright (1996) Wiley-VCH)

5 V and a luminance of $\sim 720\text{cd/m}^2$ at 5 V. The quantum and luminous efficiencies of the planar devices are comparable to those observed in sandwich LECs.

A great benefit of the planar device configuration is its compatibility with interelectrode imaging and scanning techniques, which cannot be performed on a sandwich device. The study of planar LECs enables the device operating mechanism to be elucidated more directly and effectively. Dick *et al.* first utilized optical beam-induced current (OBIC) and spatially resolved PL scan to map the built-in potential and doping profile of a planar LEC [120]. In OBIC measurement, a focused laser beam was scanned across the entire inter-electrode spacing ($\sim 22\mu\text{m}$) of a PPV-based planar LEC, which was cooled to 250K to stabilize the junction. A photovoltage signal was measured as a function of position, which is zero in neutral p- and n-doped regions and maximum in the junction region (Figure 5.16). The photovoltage signal was then integrated to give the built-in potential distribution. It was

found that the higher the voltage bias at which the junction was formed, the larger the built-in potential and the narrower the junction. In the spatially-resolved PL scan, the PL intensity across the LEC film was measured, following the application of a 4 V bias at room temperature. The PL intensity of the polymer film decreased as a result of doping-induced quenching. It was also found that p-doping quenched the PL more strongly than n-doping, and the transition in PL intensity was used to determine the junction position. The junction position and width, as determined by OBIC and PL scans, were consistent with those determined by direct EL imaging. More recently, the PL scan has also been carried out on a 40 μm superyellow/crown ether-based planar LEC, and a similar PL quenching effect was observed, which could be attributed to doping [121]. These results strongly support electrochemical doping and p-n junction formation as the fundamental principle of LEC operation.

5.5.1 Planar LECs with millimeter interelectrode spacing

Despite their great potential as a useful and yet simple tool for studying the complex LEC processes, planar LECs were rarely studied following their initial demonstration. As a result, many important questions were left unanswered that could easily have been elucidated with a planar LEC configuration. The initial EL imaging was carried out on planar LECs already turned on and therefore did not provide information about the turn-on process. In addition, the imaging was performed under ambient light or white light, so the doping-induced PL quenching could not be directly observed, although slight darkening in the p-doped region was visible in some EL images [120]. All these limitations could be resolved by the time-lapse fluorescence imaging of planar LECs with a suitable inter-electrode spacing, which will help to answer important questions such as:

- Where is doping originated from?
- How does doping propagate and relax?
- How does junction width vary with inter-electrode spacing?
- Is the junction formed a p-n junction or a p-i-n junction?

Perhaps the most interesting question one can ask about an LEC is: How large can it be? Here 'it' refers to the inter-electrode spacing of a planar LEC, which we have shown could be at least tens of micrometers. Since the turn-on voltage of a 40 μm planar LEC is only 4 V, it should be possible to turn on planar LECs with even larger inter-electrode spacing, perhaps by applying a higher voltage bias. Knowing the scalability of a semiconductor device is fundamentally important for any device application. In addition, a much larger planar LEC offers a number of advantages over small, microplanar LECs. These include easy device fabrication and testing, better spatial resolution for imaging the fine details of junction structure and better temporal resolution for imaging the dynamic LEC process. In the remainder of section 5.5, results from author's group on extremely large planar LECs are summarized.

Planar LECs with millimeter-sized interelectrode spacing were first demonstrated and imaged by Gao and Dane in 2003 [65]. Figure 5.17 shows two 1.5 mm planar LECs fabricated on the same substrate and turned on simultaneously. The two devices were made with different luminescent polymers (MEH-PPV and ADS108GE) and hence emitted in different colors. The extremely large planar LECs were fabricated and operated inside a nitrogen-filled glove box and imaged through the glove box window with a digital camera.

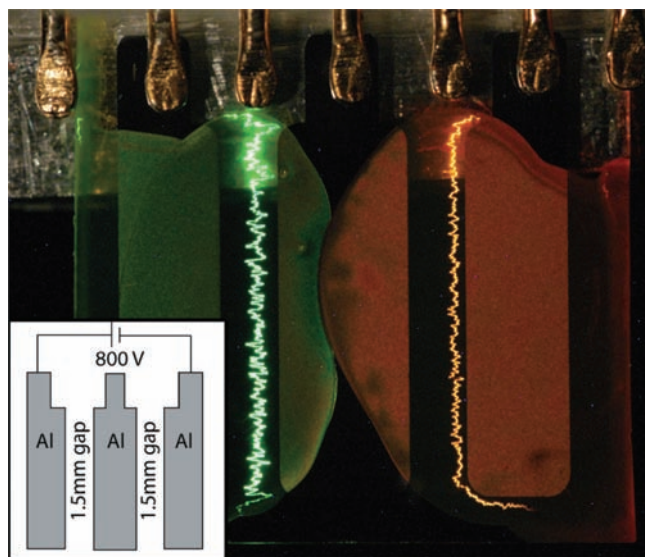


Figure 5.17 Photograph of two 1.5 mm planar LECs under 800 V. The inset shows the two devices are biased in series (reprinted with permission from [65]. Copyright 2003 American Institute of Physics)

To simultaneously turn on the two devices, a bias of 800 V was applied between the left- and right-most electrodes, while the center electrode was allowed to float. The equivalent interelectrode spacing of the configuration was therefore 3 mm. The large voltage bias was necessary to turn on the devices within a reasonable amount of time due to the extremely large interelectrode spacing. Once the device was turned on, the response was fast and EL could be detected at voltages as low as 5 V. The photograph in Figure 5.17 was taken after the device had been operated continuously for about 1 h at 800 V. EL came only from a narrow region between the electrodes, consistent with previous observations in microplanar LECs. However, the emission zone in both devices is found to be extremely wide ($\sim 70 \mu\text{m}$), although this zone only accounts for approximately 5% of the inter-electrode spacing. The width of the light-emitting junction alone is several times larger than the entire inter-electrode spacing of previously reported planar LECs. This indicates that the width of the p-n junction in an LEC is a function of the inter-electrode spacing. In addition, the junction position is closer to the cathode in both devices, and more so for the MEH-PPV-based LEC. This is contrary to the observations on PPV-based microplanar LECs, where the junction is seen to be closer to anode [38].

The photograph shown in Figure 5.17 was taken in a darkened room, with some back-lighting from a desk lamp or pen flashlight filled in during exposure to reveal the electrodes. Time-lapse imaging under UV illumination allows *in situ* electrochemical doping, manifested as photoluminescence quenching, as well as its time evolution to be visualized [122]. Figure 5.18 displays a 1.5 mm MEH-PPV planar LEC imaged with various time delays after a voltage bias was applied to turn on the device. Under UV illumination, the LEC film exhibits the characteristic orange-red photoluminescence of MEH-PPV. Also visible is dark, finger-like PL quenching, caused by electrochemical p-doping propagating from anode

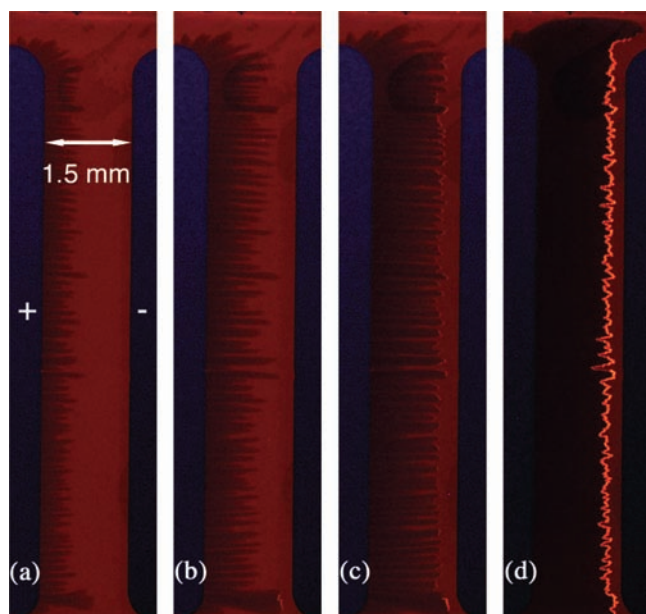


Figure 5.18 Time-lapse fluorescence imaging of a MEH-PPV-based planar LEC under 365 nm UV illumination. The device was tested at 310K under a voltage bias of 140 V. Time elapsed since the application of voltage bias: (a) 8 min; (b) 13 min; (c) 18 min; (d) 43 min (reprinted with permission from [122]. Copyright (2004) American Institute of Physics)

towards cathode. On the opposite side, subtle but discernable electrochemical n-doping propagates from cathode towards anode. Since p-doping propagates at a faster speed than n-doping, the p-n junction was formed closer to the cathode. Once, and only when the p- and n-doped regions met to form a p-n junction, EL could be observed in the junction region. Thus, an off-centered emitting junction closer to the cathode is the result of different p- and n-doping propagation speeds.

The exposure and time delay in the above time-lapse imaging were controlled by a computer. This allowed a large number of photographs to be taken with exactly the same time delay. The images were analyzed, and the average distance between the p-doping frontier and the edge of anode was extracted and plotted as a function of time. Under a constant bias of 140 V, p-doping initially propagated at a near constant speed of $\sim 65 \mu\text{m}/\text{min}$. Then the p-doping propagation came to a near stop when it had made full contact with the propagating n-doping, indicating the formation of a p-n junction. Coinciding with the junction formation were the emergence of EL and an exponential increase in current flow. The increase in current and EL suggested an increase in the doping level after the initial formation of p-n junction, as evidenced by the darkening of both p- and n-doped regions. When operated near peak current and luminance, the PL in the p-doped region was completely quenched, and EL was only from the partially quenched n-side of the p-n junction.

The time-lapse fluorescence imaging of the large planar LECs vividly illustrated the dynamic electrochemical p- and n-doping processes and provided unambiguous proof that doping and the formation of a p-n junction was the fundamental principle of LEC operation. *In situ* electrochemical doping indeed originates from the electrode–polymer interfaces and then

expands at a finite speed. The interior of the device was not immediately affected by PL quenching. In Dick's time-lapse PL scanning experiments on a $22\ \mu\text{m}$ planar LEC, the decrease in PL intensity was observed to occur simultaneously across the entire p- and n-doped regions, following the application of voltage bias. In the much smaller microplanar LEC, the junction was probably already formed before the first PL scan was conducted at 1 min after the application of a voltage bias. The slow turn-on time of extremely large millimeter planar LECs thus offers much better temporal resolution for studying the LEC dynamics.

With time-lapse fluorescence imaging, the average doping propagation speed can be extracted from the linear portion of the doping front position vs. time plots and can be evaluated as a function of applied voltage bias and operating temperature [123]. At a fixed temperature, the p-doping propagation speed was found to increase linearly with applied bias. Since p-doping is achieved by the oxidation of the luminescent polymer in the presence of anions (e.g. CF_3SO_3), cations (Li^+) must be spatially separated from anions during the process by drifting away from the anode. By assuming the p-doping front to be also receding from a region containing surplus cations, the cation mobility was calculated and found to be consistent with reported value. At a fixed voltage bias, the p-doping propagation speed increases with operating temperature according to $\ln V_p \propto \exp(E_d/kT)$. As shown in Figure 5.19, the p-doping propagation speeds increases from $\sim 5\ \mu\text{m}/\text{min}$ at 300 K to $\sim 390\ \mu\text{m}/\text{min}$ at 330 K. As a result, EL was observed from the 2-mm-planar LEC in less than 5 min at 330 K, while it took more than 1 h at 300 K.

The strong temperature dependence of doping propagation speed can be attributed to the temperature-dependent ion mobility and conductivity. This suggests it is possible to turn on

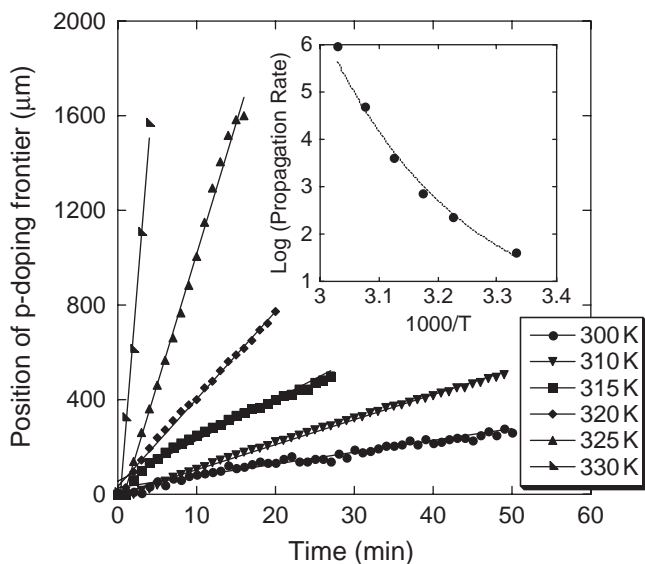


Figure 5.19 Average distance between p-doping frontier and anode as a function of time obtained from 2 mm MEH-PPV planar LEC operated at different temperatures under 200 V bias. Solid lines are linear fits to the data. The inset shows logarithmic p-doping propagation rate versus inverse temperature. The dashed line represents an exponential fit to the data (reprinted with permission from [123]). Copyright 2005 American Institute of Physics)

even large planar LECs by modestly heating the device to promote ion motion and accelerate the doping process. This simple approach worked extremely well, as planar LECs with an interelectrode spacing of 6–11 mm were successfully turned on at 330 K [122, 124]. At an inter-electrode spacing of 11 mm, the planar LECs are arguably the largest solid-state light-emitting devices ever reported. By heating the device to 360 K, which is above the melting temperature of the crystalline PEO domain, Edman *et al.* recently were able to turn on planar LECs with a 1 mm gap by applying only 5 V [125]. It is therefore entirely possible to turn on planar LECs with an even larger gap than 11 mm. These results underscore the importance of temperature in LEC operation, which can be used as a powerful control parameter to either freeze an already formed junction or turn on a large planar LECs. The extremely large 6–11 mm planar LECs offer unprecedented spatial and temporal resolution for fluorescence imaging. For the first time, the dedoping process upon the reversal of the applied bias, as well as interesting transient EL, were captured. The reversal of voltage bias polarity eventually led to the reversal of the doping profile and the formation of a new light-emitting p-n junction [122, 124, 126].

Figure 5.20 displays the time-lapse fluorescence imaging of an 11 mm planar Al/MEH-PPV:PEO:LiTf/Al LEC operated under 800 V bias at 340 K [126]. PL quenching from both

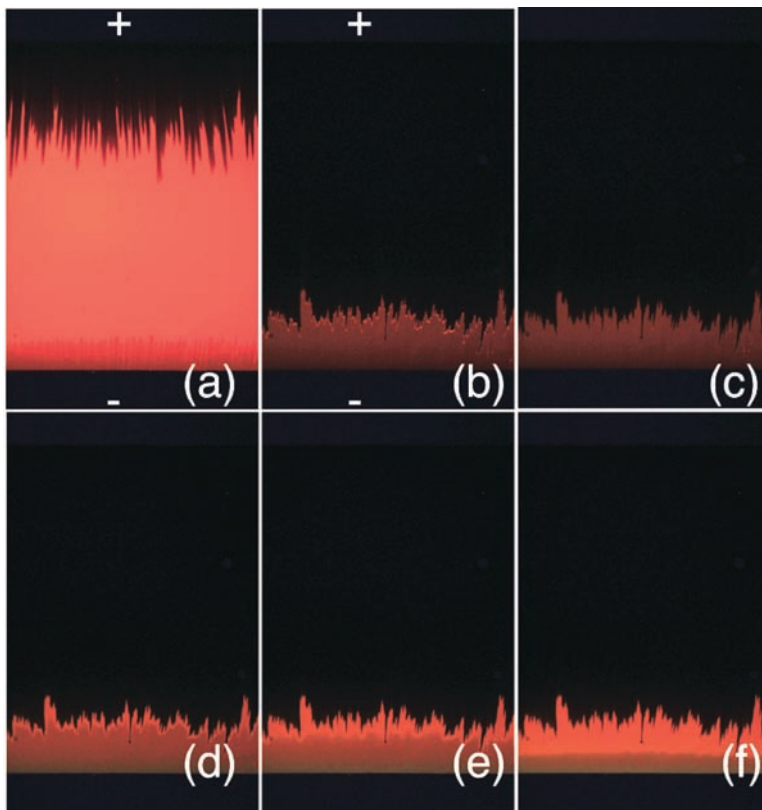


Figure 5.20 Time-lapse fluorescence imaging of an 11 mm MEH-PPV:PEO:LiCF₃SO₃ planar LEC at 340 K. Time since an 800 V bias was applied: (a) 40 s; (b) 116 s; Time since the 800 V bias is removed: (c) <4 s; (d) 16 s; (e) 22 s; (f) 32 s (reprinted with permission from [126]. Copyright 2006 American Institute of Physics. The contrast of the composite image has been enhanced)

p- and n-doping are clearly visible (Figure 5.20 (a)). The direct observation of n-doping proves that Li ion can effectively n-dope MEH-PPV, which was thought to be impossible in a traditional liquid electrochemical cell [47]. When the light-emitting p-n junction was fully formed (Figure 5.20 (b)), the 800 V bias was removed, and the cell was allowed to relax. Figure 5.20 (c) shows the doping profile immediately (~5 s delay) after the voltage bias was turned off. A very significant observation was the sharp junction between p- and n-doped regions. The absence of a less-quenched 'intrinsic region' suggests that the junction formed in an LEC is not a p-i-n junction, as has been previously postulated in a theoretical LEC study [42].

The fact that the homojunction formed in an LEC is a p-n junction, rather than a p-i-n junction, represents a serious drawback limiting the maximum EL efficiency achievable in an LEC. The absence of an 'intrinsic' region means that EL must come from a doped polymer, and the heavy PL quenching as a result of doping (Figure 5.20) severely degrades the EL intensity and efficiency of an LEC. However, a p-i-n junction can indeed form when a fully-established p-n junction is allowed to relax. Figures 5.20 (d)–(f) show the dynamic doping relaxation (i.e. dedoping) process after the voltage bias was removed. No change was immediately observed in the p-doped region, but n-doping could be seen to recede rapidly away from the junction, leaving a widening 'intrinsic' region with significantly weaker PL quenching between p- and n-doped regions. As a result, the ohmic contact was not immediately affected by the dedoping process. This suggests that we can overcome the adverse PL quenching by relaxing a p-n junction into a p-i-n junction to create a more efficient EL emission zone while maintaining the low resistance contact.

5.5.2 LECs with a relaxed p-n junction

The effects of doping relaxation were studied with planar LECs with an inter-electrode spacing of 0.6 mm [127]. This modest inter-electrode spacing allows spatially resolved imaging of EL and doping profile, as well as significant current flow and luminance at cryogenic temperatures. The devices were turned on at 315 K and subsequently cooled to 200 K to freeze the junction. Doping relaxation was realized by warming the device to above the glass transition temperature of the polymer electrolyte, holding for a period of several minutes, and finally cooling back to 200 K again. This procedure allows the frozen p-n junction to be relaxed in a controlled manner, with the degree of dedoping easily controlled by adjusting the temperature and duration of relaxation. Figure 5.21 shows light intensity vs. current (L-I) and current vs. voltage (I-V) characteristics of a frozen-junction LEC at 200 K before and after relaxation. The EL intensity was significantly higher after the simple doping relaxation procedure, with a percentage increase ranging from ~400% at 19.9 μA to 2600% at 2.4 μA . Note even at 2.4 μA , the current density was high (~50 mA/cm^2) due to the extremely small cross-sectional area of the planar device configuration. In addition, the relaxed device exhibited EL under both forward and reverse bias. But unlike a 'bipolar' dynamic-junction LEC operated at room temperature, the reverse bias EL observed in a frozen-junction LEC originated from the same emission zone as forward-bias EL. The origin of this reverse-bias EL is still unclear. The device resistance also increased significantly as a result of doping relaxation (Figure 5.21 (b)). The I-V curve of the fresh frozen junction is linear and symmetrical about the origin. The lack of current rectification, despite the existence of a unipolar p-n junction, is not surprising in these planar structures, due to the large bulk resistance.

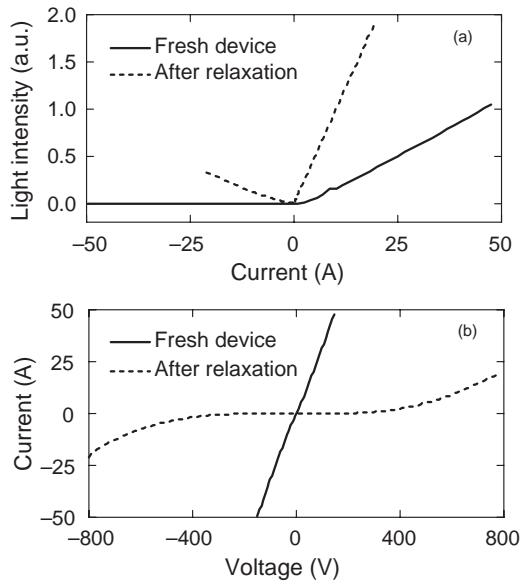


Figure 5.21 (a) Light intensity vs. current and (b) current vs. voltage characteristics of a frozen-junction planar LEC, measured before and after a doping relaxation cycle, during which the frozen-junction LEC was warmed from 200 K to 285 K and held at 285 K for 6 min without bias, and then cooled back to 200 K. All measurements were made at 200 K (reprinted with permission from [127]. Copyright 2006 American Institute of Physics)

The dramatic increase in EL efficiency by controlled doping relaxation can be attributed to the formation of a more efficient p-i-n junction, which is visualized by the direct imaging of EL and doping profiles of the planar LEC. Figures 5.22 (a) and (b) compare the EL before and after doping relaxation, imaged under a constant current of $30\ \mu\text{A}$. The EL of the fresh frozen junction appeared weak and scattered, partially due to the low throughput of microscope imaging and a relatively fast shutter speed. EL after relaxation was clearly much stronger. Figures 5.22 (c) and (d) compare the doping profiles measured before and after relaxation, illustrating the difference between a p-n and a p-i-n junction. The 285 K warming cycle had led to the formation of an ‘intrinsic’ region with much less PL quenching between heavily p- and n-doped regions. The ‘recovered’ PL in the intrinsic region was responsible for the greatly improved EL.

Although planar LECs were used in the proof-of-principle demonstration of the p-i-n junction LEC, the doping relaxation technique can also be applied to sandwich LECs. Preliminary results had shown a 100% increase in quantum efficiency with only a 10% increase in driving voltage. Improvement upon the already efficient sandwich LECs may lead to polymer light-emitting structures with record EL efficiencies suitable for achieving an electrically pumped polymer laser.

5.5.3 Polymer bulk homojunction LECs

The images shown in Figure 5.20 also revealed that the width of the light-emitting p-n junction was very small compared to the inter-electrode spacing (denoted as D) of the planar

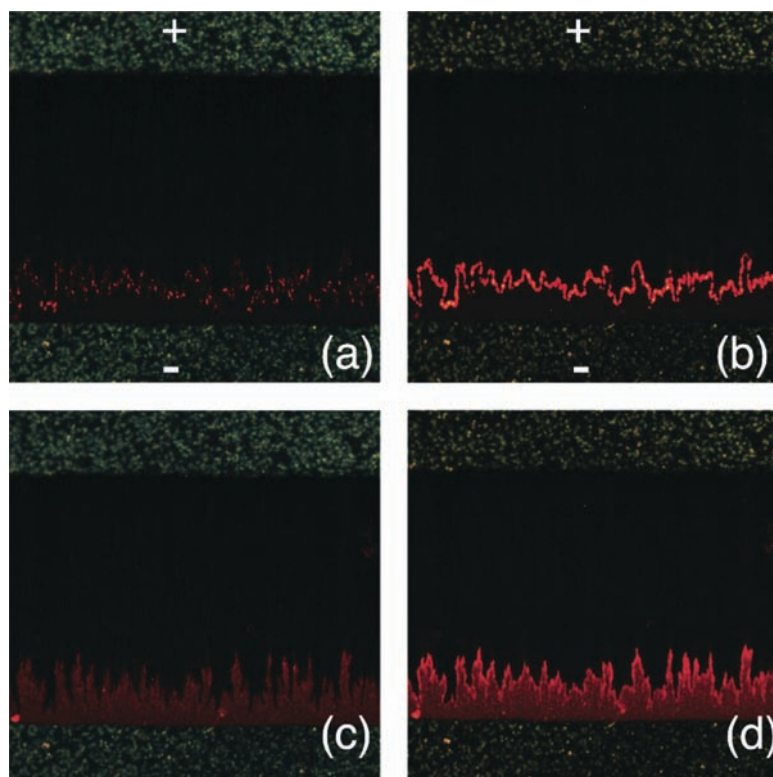


Figure 5.22 EL and doping profiles of a 0.6 mm frozen-junction LEC imaged before and after doping relaxation. The device was identical to the one shown in Figure 5.21 and subject to the same doping relaxation procedure: (a) EL before relaxation; (b) EL after relaxation; (c) doping profile before relaxation; (d) doping profile after relaxation. A driving current of $30\ \mu\text{A}$ was applied for EL imaging (reprinted with permission from [127]. Copyright 2006 American Institute of Physics)

LEC. The ratio of EL emission zone width and inter-electrode spacing, denoted as R_E , is in fact less than 1% for planar LECs, with $D = 6\ \text{mm}$ or $11\ \text{mm}$ [122, 124]. R_E increases as D decreases, reaching approximately 5% for $D = 1.5\ \text{mm}$ [65] and 6–20% for much smaller microplanar LECs with $D = 15 \sim 40\ \mu\text{m}$ [38, 120, 128, 129]. R_E is the largest in sandwich LECs, ranging from 10–80% (voltage dependent) as determined by capacitance measurement [130, 131]. A small R_E limits the maximum EL output from an LEC, since only a small portion of the polymer film actually contributes to EL.

Since R_E increases with decreasing D , a possible solution is to form multiple light-emitting p-n junctions of smaller dimensions, as opposed to a single junction for a given D or device area. The use of micro-fabricated inter-digitated electrodes of small spacing has indeed resulted in efficient and more uniform EL from a large emitting area of $5\ \text{mm} \times 5\ \text{mm}$ [119]. The device configuration is equivalent to many smaller LECs with a gap of $5\ \mu\text{m}$ wired in parallel. Alternatively, multiple planar LECs can be created *in situ* by depositing *floating* metallic strips between the two electrodes that define D . The equivalent circuit of such a device configuration is that of multiple LECs connected in series [132].

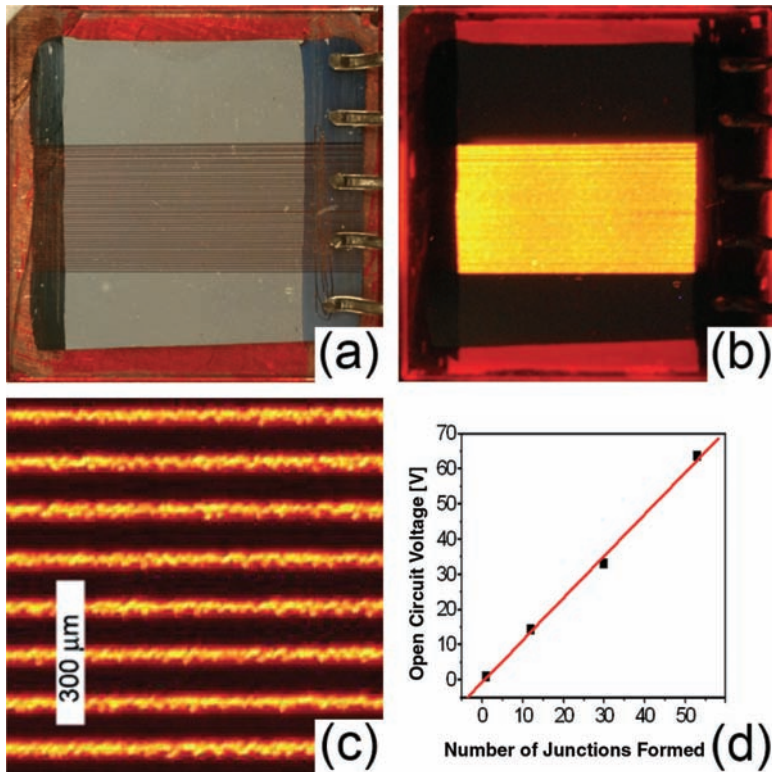


Figure 5.23 MEH-PPV planar LEC consisting of 52 electrically floating Al strips. The inter-electrode spacing between anode and cathode is 5.1 mm: (a) image of the device without bias; (b) image of the device taken under 565 V bias at 320 K; (c) close-up image showing light-emission from individual p-n junctions; (d) photovoltaic open circuit voltage vs. number of junctions formed in MEH-PPV-based planar LECs. All photovoltaic measurements were carried out under 40 mW/cm^2 illumination from a blue/UV laser at 200 K (reprinted with permission from [132]. Copyright 2005 American Institute of Physics)

Figure 5.23 shows a planar device structure consisting of 52 approximately equally spaced floating aluminium strips deposited between the two outer electrodes 5.1 mm apart (all metal deposition was carried out in a single step using a metal wire shadow mask). Without the inter-electrode strips, the device is a regular planar LEC in which only one narrow light-emitting p-n junction can be formed. However, the device with the aluminium strips exhibited nearly uniform EL across the entire device (Figure 5.23 (b)). At high magnification, both the $60 \mu\text{m}$ -wide aluminium strips and the light-emitting p-n junction between them can be seen (Figure 5.23 (c)). The polymer film between adjacent floating strips was approximately $40 \mu\text{m}$ wide. A total of 53 light-emitting p-n junctions were placed across the entire device, resulting in an EL uniform to the naked eye. The total light-emitting area was more than 20% of the entire device area between the biased electrodes. A larger percentage is expected if narrower Al strips are used, which block 60% of the polymer film.

The formation of multiple p-n junctions in series was verified by photovoltaic measurement at frozen-junction temperature (200 K), such that doping relaxation is negligible. An

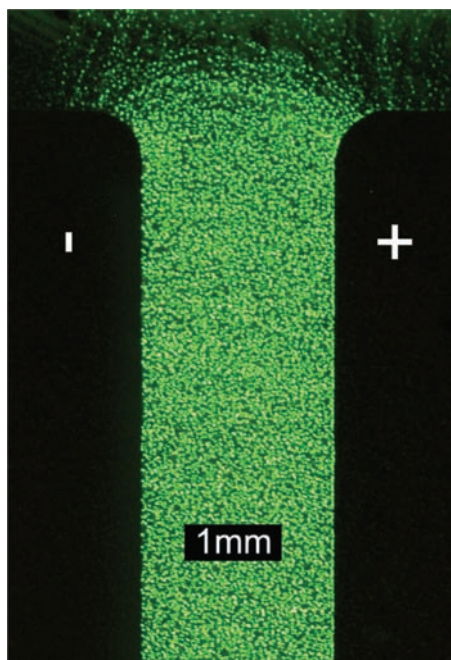


Figure 5.24 Green-emitting (based on ADS 108GE) planar device containing conductive ITO particles. The inter-electrode spacing was 2 mm. The device was turned on by applying an 800 V bias at 325 K. The image was taken in dark (reprinted from [132] with permission. Copyright 2005 American Institute of Physics)

open circuit voltage of 63.5 V was detected between the two terminal electrodes under 40 mW/cm^2 blue/UV light illumination, despite the device's completely symmetrical configuration. The giant V_{OC} , which is about 20 times of E_g/e for the polymer used, was obviously contributed by all 53 p-n junctions connected in series. A smaller V_{OC} was indeed measured when the number of strips was reduced. The open-circuit voltage showed a linear dependence on the number of junctions formed (Figure 5.23 (d)), with a slope of $1.19 \pm 0.04 \text{ V/junction}$ [132].

The formation of multiple p-n junctions in a planar LEC is greatly simplified by adding conductive ITO particles into the LEC film, resulting in the highly innovative 'bulk homojunction' LECs [132]. Figure 5.24 shows a 2-mm green-emitting bulk homojunction device imaged in darkness. EL was observed across the entire device, from cathode to anode, in the form of thousands of individual light-emitting dots. EL near the electrode edges clearly illustrates the electrical field lines reminiscent of those between two parallel conducting plates. Each light-emitting dot is in fact a tiny light-emitting p-n junction formed in the polymer film between nearby ITO particles. The large number of p-n junctions present in the device also gives rise to a large photovoltaic open circuit voltage of $V_{\text{OC}} = 25.5 \text{ V}$.

The overall light intensity from a bulk homojunction LEC is much stronger than that of a regular planar LEC of the same size, due to a much larger (>20 times) emitting area. This was verified by EL intensity measurement with an amplified photodiode [133]. Figure 5.25 displays EL intensity measured from two identical green-emitting bulk homojunction LECs

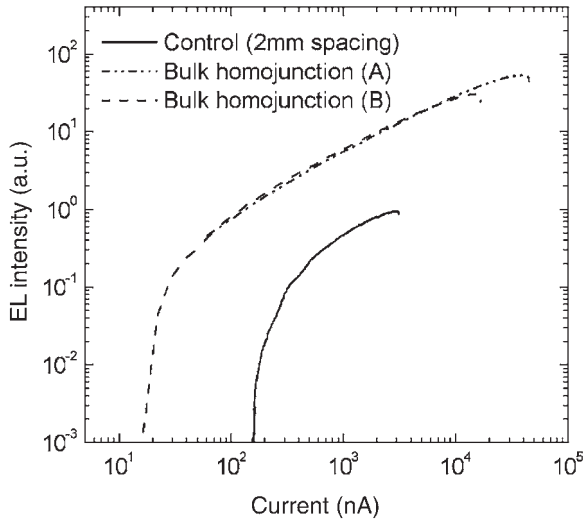


Figure 5.25 EL intensity vs. device current for two green-emitting 2-mm bulk homojunction LECs containing ITO particles and a single-junction 2-mm control device. The bulk homojunction devices were tested at 325 K and (A) 750 V, (B) 700 V. The control device was tested at 330 K, 700 V (reprinted with permission from reference 133. Copyright 2006 American Institute of Physics)

containing ITO particles and a control single-junction green-emitting LEC of the same interelectrode spacing. Since the EL intensity is plotted against device current (L vs. I), the plots also provide a direct comparison of the external quantum efficiency of the devices. The L - I curves of the bulk homojunction LECs nearly overlap, but they are both significantly higher than that of the control device across the entire current range. An efficiency difference approaching 1000-fold exists between the devices at very low current level (150 nA \sim 200 nA). At high current level ($>1 \mu\text{A}$), the bulk homojunction LECs remained approximately 10 times more efficient than the control device.

Furthermore, both peak current and peak EL intensity attainable were more than 10 times higher in bulk homojunction devices. Similar efficiency increase had also been observed in MEH-PPV based bulk homojunction LECs containing ITO particles. In addition, the initial turn-on of the bulk homojunction devices was significantly faster, because the doping needs only to travel a small distance between adjacent particles to form a light-emitting junction. For example, light emission was detected from the ITO particle doped device in Figure 5.24 in less than 30 s, while it took more than 10 min to turn on a regular 2-mm device made of the same material under the same conditions. The formation of bulk homojunction is a general phenomenon not unique to the luminescent polymer or metallic particle. Figure 5.26 shows red-, green- and blue-emitting bulk homojunction planar LECs made with different luminescent polymers. Bulk homojunction LECs have also been successfully demonstrated with particles of gold, silver and zinc.

While the above proof-of-concept devices are not practical due to the extremely high series resistance, the concept of the bulk homojunction may lead to highly unique and efficient polymer photonic devices by device scaling. For example, creating an open circuit voltage of more than 100 V is possible by simply forming more junctions that use narrower

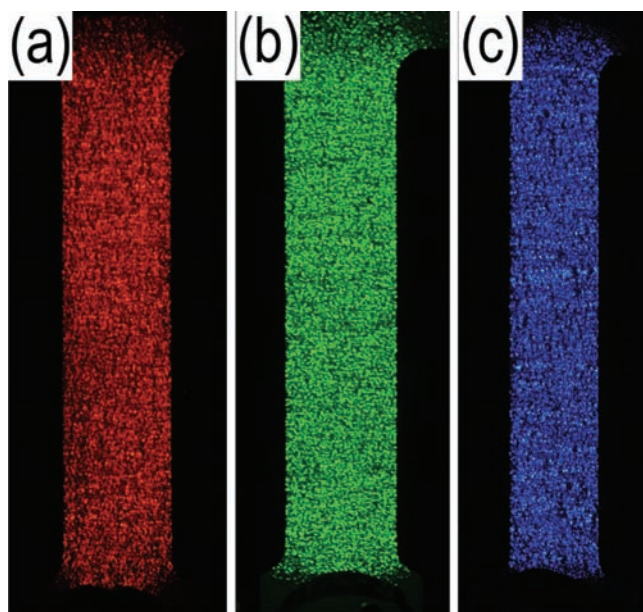


Figure 5.26 Red, green and blue bulk homojunction LECs incorporating ITO particles into the film: (a) 2-mm MEH-PPV-based device operated at 315 K and 600 V; (b) 2-mm ADS108GE-based device operated at 320 K and 500 V; (c) 1.5-mm blue-emitting device operated at 335 K and 700 V (reprinted with permission from [133]. Copyright 2006 American Institute of Physics)

metal strips or smaller metallic particles. The ITO particles used had a nominal size of less than $2\ \mu\text{m}$ in diameter. However, scanning electron microscopy (SEM) imaging of the polymer films shows both small particles less than $1\ \mu\text{m}$ in diameter as well as aggregates as large as $10\text{--}30\ \mu\text{m}$. The ITO aggregates were randomly distributed throughout the polymer film of about 100 nm in thickness. By using a thick (micrometer) sandwich device structure containing metallic nanoparticles, it is possible to achieve both a large device current and a large number of p-n junctions, which will result in more efficient light emission and photovoltaic conversion. For photovoltaic operation, the I_{SC} can be further increased by introducing acceptor species, such as fullerenes (C_{60}), to facilitate charge separation by photoinduced charge transfer.

5.6 CONCLUSIONS AND OUTLOOK

Modern battery-powered display and lighting applications have high demand for solid-state light-emitting devices with low operating voltage and high luminous efficiency. Organic and polymer LED technologies have succeeded via the use of ultra-thin films and dissimilar electrodes with a large work function difference. Polymer light-emitting electrochemical cells, on the other hand, utilize *in situ* electrochemical doping to simultaneously reduce the overall device resistance and achieve efficient and balanced charge injection. An operating

LEC is in effect a polymer light-emitting p-n junction possessing many desirable device characteristics similar to those of a conventional p-n junction LED.

The dynamic doping and dedoping processes in an LEC have been visualized by the time-lapse fluorescence imaging of planar LECs with an extremely large inter-electrode spacing of up to 11 mm. And the formation of a p-n junction has been shown to be essential in the operation of any true LEC. The demonstration of an operational 11-mm planar LEC is in itself a remarkable manifestation of LEC's unique operating mechanism among organic- and polymer-based devices. The unparalleled scalability affords LECs great flexibility in device design and characterization and has directly led to the demonstration of highly innovative polymer p-i-n junction LECs and polymer bulk homojunction LECs. In the foreseeable future, LECs will be continuously used as a powerful tool to study the fundamental science of luminescent conjugated polymers and polymer electrolytes, as well as a versatile building block for the demonstration of novel polymer based semiconductor device, such as solar cells, transistors or even diode lasers.

LECs are not yet practical, due mainly to their poor stability and slow response. Significant improvements have been made by experimenting with new, tailor-made luminescent materials and electrolytes for LECs. However, the ultimate solution to all of the LEC's drawbacks lies with the realization of frozen-junction LECs that can be operated at room temperature without doping relaxation. And this again requires the ingenuity of synthetic chemists to provide innovative LEC materials, especially luminescent polymers with better electrochemical stability and polymer electrolytes with negligible ion conductivity at RT (high T_g) but adequate ion-solvating power at high temperature.

REFERENCES

1. Pope, M., Kallmann, H.P. and Magnante, P. (1963) *J. Chem. Phys.* **38**: 2042–3.
2. Helfrich, W. and Schneider, W.G. (1965) *Phys. Rev. Lett.* **14**: 229–31.
3. Helfrich, W. and Schneider, W.G. (1966) *J. Chem. Phys.* **44**: 2902–9.
4. Pott, G.T. and Williams, D.F. (1969) *J. Chem. Phys.* **51**: 1901–6.
5. Schadt, M. and Williams, D.F. (1969) *J. Chem. Phys.* **50**: 4364–8.
6. Williams, D.F. and Schadt, M. (1970) *J. Chem. Phys.* **53**: 3480–7.
7. Mehl, W. and Funk, B. (1967) *Phys. Lett. A* **A25**: 364–5.
8. F. Lohmann, F. and Mehl, W. (1969) *J. Chem. Phys.* **50**, 500–6.
9. Kawabe, K. Masuda, and Namba, S. (1971) *Jap. J. App. Phys.* **10**: 527–9.
10. Wakayama, N.I., Wakayama, N. and Williams, D.F. (1973) *Bull. Chem. Soc. Jpn.* **46**: 3395–9.
11. Kampas, F.J. and Gouterman, M. (1977) *Chem. Phys. Lett.* **48**: 233–6.
12. Zschokke, I., Schwob, H.P. and Balding, E. (1967) *Solid State Comm.* **5**: 825–8.
13. Kalinowski, D. (1999) *J. Phys. D-App. Phys.* **32**: R179–249.
14. Sano, M., Pope, M. and Kallmann, H. (1965) *J. Chem. Phys.* **43**, 2920–1.
15. Gu, J., Kawabe, M., Masuda, K. and Namba, S. (1977) *J. App. Phys.* **48**: 2493–4.
16. Kalinowski, J. Godlewski, J. and Dreger, Z. (1985) *App. Phys. Mat. Sci. & Proc.* **37**: 179–86.
17. Hwang, W. and Kao, K.C. (1973) *J. Chem. Phys.* **58**: 3521–2.
18. Sinha, N.P., Misra, Y., Tripathi, L.N. and Misra, M. (1981) *Solid State Comm.* **39**: 89–91.
19. Wakayama, N.I., Wakayama, N. and Williams, D.F. (1974) *Mol. Cryst. & Liq. Cryst.* **26**: 275–80.
20. Tripathi, G.N.R. *et al.* (1977) *J. Phys. C – Sol. State Phys.* **10**: 2015–17.

21. Kalinowski, J. Godlewski, J. and Signerski, R. (1976) *Mol. Cryst. & Liq. Cryst.* **33**: 247–59.
22. Gonzalezbasurto, J. and Burshtein, Z. (1975) *Mol. Cryst. & Liq. Cryst.* **31**: 211–17.
23. Vincett, P.S., Barlow, W.A., Hann, R.A. and Roberts, G.G. (1982) *Thin Sol. Films* **94**: 171–83.
24. Tang, C.W. and Vanslyke, S.A. (1987) *App. Phys. Lett.* **51**: 913–5.
25. Adachi, C., Tokito, S., Tsutsui, T. and Saito, S. (1988) *Jap. J. App. Phys. Part 2-Lett.* **27**: L269–71.
26. Burroughes, J.H., Bradley, C.C. Brown, A.R. *et al.* (1990) *Nature* **347**: 539–41.
27. Braun, D. and Heeger, A.J. (1991) *App. Phys. Lett.* **58**: 1982–4.
28. Braun, D., Heeger, A.J. and Kroemer, H. (1991) *J. Elect. Mat.* **20**: 945–8.
29. Parker, I.D. (1990) *J. Appl. Phys.* **75**: 1656–66.
30. Blom, P.W.M., de Jong, M.J.M. and Vleggaar, J.J.M. (1996) *App. Phys. Lett.* **68**: 3308–10.
31. Becker, H., Lux, A., Holmes, A.B. and Friend, R.H. (1997) *Synth. Met.* **85**: 1289–90.
32. Yang, Y. and Heeger, A.J. (1994) *App. Phys. Lett.* **64**: 1245–7.
33. Karg, S., Scott, J.C., Salem, J.R. and Angelopoulos, M. (1996) *Synth. Met.* **80**: 111–7.
34. Carter, S.A., Angelopoulos, M., Karg, S., Brock, P.J. and Scott, J.C. (1997) *App. Phys. Lett.* **70**: 2067–9.
35. Romero, D.B., Schaer, M., Zuppiroli, L., Cesar, B. and Francois, B. (1995) *App. Phys. Lett.* **67**: 1659–61.
36. Huang, F., MacDiarmid, A.G. and Hsieh, B.R. (1997) *App. Phys. Lett.* **71**: 2415–17.
37. Itoh, E., Yamashita, T. and Miyairi, K. (2001) *Jpn. J. App. Phys. Part 1 Regular Papers Short Notes & Review Papers* **40**: 862–6.
38. Pei, Q.B., Yu, G., Zhang, C., Yang, Y. and Heeger, A.J. (1995) *Science* **269**: 1086–8.
39. Dini, D. (2005) *Chem. Mat.* **17**: 1933–45.
40. Armstrong, N.R., Wightman, R.M. and Gross, E.M. (2001) *Ann. Rev. Phys. Chem.* **52**: 391–422.
41. Smith, D.L. (1997) *J. App. Phys.* **81**: 2869–80.
42. Manzanares, J.A., Reiss, H. and Heeger, A.J. (1998) *J. Phys. Chem. B* **102**: 4327–36.
43. de Mello, J.C., Tessler, N., Graham, S.C. and Friend, R.H. (1998) *Phys. Rev. B* **57**: 12951–63.
44. Riess, I. and Cahen, D. (1997) *J. App. Phys.* **82**: 3147–51.
45. Pei, Q.B., Yang, Y., Yu, G., Zhang, C. and Heeger, A.J. (1996) *J. Am. Chem. Soc.* **118**: 3922–9.
46. Scrosati, B. (1995) *Solid State Electrochemistry* (Bruce, P.G. (ed.), Cambridge: Cambridge University Press.
47. Holt, A.L., Leger, J.M. and Carter, S.A. (2005) *J. Chem. Phys.* **123**: 044704.
48. Ouisse, T., Stephan, O., Armand, M. and Lepretre, J.C. (2002) *J. App. Phys.* **92**: 2795–802.
49. Yu, G., Cao, Y., Zhang, C., Li, Y.F., Gao, J. and Heeger, A.J. (1998) *App. Phys. Lett.* **73**: 111–13.
50. Holzer, L., Wenzl, F.P., Tasch, S. *et al.* (1999) *App. Phys. Lett.* **75**: 2014–16.
51. Johansson, T., Mammo, W., Andersson, M.R. and Inganäs, O. (1999) *Chem. Mat.* **11**: 3133–9.
52. Morgado, J., Friend, R.H., Cacialli, R., Chuah, B.S., Moratti, S.C. and Holmes, A.B. (1999) *J. App. Phys.* **86**: 6392–5.
53. Morgado, J., Friend, R.H. Cacialli, F., *et al.* (2001) *Synth. Met.* **122**: 111–13.
54. Morgado, J., Cacialli, F., Friend, R.H., Chuah, B.S., Rost, H. and Holmes, A.B. (2001) *Macromolecules* **34**: 3094–9.
55. Huang, C., Huang, W., Guo, J., Yang, C.Z. and Kang, E.T. (2001) *Polymer* **42**: 3929–38.
56. Wenzl, F.P., Pachler, P., Suess, C. *et al.* (2004) *Adv. Funct. Mat.* **14**: 441–50.
57. Sun, Q.J., Zhan, X.W., Zhang, B. *et al.* (2004) *Poly. Adv. Tech.* **15**: 70–4.
58. Gu, Z., Shen, Q.D., Zhang, J., Yang, C.Z. and Bao, Y.J. (2006) *J. App. Poly. Sci.* **100**: 2930–6.

59. Gu, Z., Bao, Y.J., Zhang, Y., Wang, M. and Shen, Q.D. (2006) *Macromolecules* **39**: 3125–31.
60. Wenzl, F.P., Suess, C., Pachler, P. *et al.* (2004) *Sol. St. Ion.* **169**: 161–6.
61. Edman, L., Moses, D. and Heeger, A.J. (2003) *Synth. Met.* **138**: 441–6.
62. Lemmer, U., Vacar, D., Moses, D., Heeger, A.J., Ohnishi, T. and Noguchi, T. (1996) *App. Phys. Lett.* **68**: 3007–9.
63. Yang, C.H., Sun, Q.J., Qiao, J. and Li, Y.F. (2003) *J. Phys. Chem. B* **107**: 12981–8.
64. Wang, H.L., Gopalan, A. and Wen, T.C. (2003) *Mat. Chem. Phys.* **82**: 793–800.
65. Gao, J. and Dane, J. (2003) *App. Phys. Lett.* **83**: 3027–9.
66. Yu, G., Yang, Y., Cao, Y., Pei, Q., Zhang, C. and Heeger, A.J. (1996) *Chem. Phys. Lett.* **259**: 465–8.
67. Sun, Q.J., Wang, H.Q., Yang, C.H., He, G.F. and Li, Y.F. (2002) *Synth. Met.* **128**: 161–5.
68. Stephan, O., Collomb, V., Vial, J.C. and Armand, M. (2000) *Synth. Met.* **113**: 257–62.
69. Cao, Y., Yu, G., Heeger, A.J. and Yang, C.Y. (1996) *App. Phys. Lett.* **68**: 3218–20.
70. Pei Q.B. and Yang, Y. (1996) *J. Am. Chem. Soc.* **118**: 7416–17.
71. Tasch, S., Gao, J., Wenzl, F.P. *et al.* (1999) *Electrochem. Sol. St. Lett.* **2**: 303–5.
72. Wang, J., Sun, R.G., Yu, G. and Heeger, A.J. (2002) *J. App. Phys.* **91**: 2417–22.
73. Cao, Y., Pei, Q.B., Andersson, M.R., Yu, G. and Heeger, A.J. (1997) *J. Electrochem. Soc.* **144**: L317–20.
74. Yang, Y., Pei, Q. and Heeger, A.J. (1996) *J. App. Phys.* **79**: 934–9.
75. Edman, L. (2005) *Electrochimica Acta* **50**: 3878–85.
76. Parker, I.D., Cao, Y. and Yang, C.Y. (1999) *J. App. Phys.* **85**: 2441–7
77. Friend, R.H., Gymer, R.W., Holmes, A.B. *et al.* (1999) *Nature* **397**: 121–8.
78. Habrard, F., Ouisse, T., Stephan, O. *et al.* (2004) *J. App. Phys.* **96**: 7219–24.
79. Heeger, A.J. (2001) *Rev. Mod. Phys.* **73**: 681–700.
80. *Handbook of Conducting Polymers*, (1998) 2nd edn, New York, Basel, Hong Kong: Marcel Dekker, Inc.
81. Yang Y. and Pei, Q.B. (1997) *J. App. Phys.* **81**: 3294–8.
82. Lee, J.I., Hwang, D.H., Park, H. *et al.* (2000) *Synth. Met.* **111**, 195–7.
83. Holzer, L., Winkler, B., Wenzl, F.P. *et al.* (1999) *Synth. Met.* **100**: 71–7.
84. Morgado, J., Cacialli, F., Friend, R.H., Chuah, B.S., Moratti, S.C and Holmes, A.B. (2000) *Synth. Met.* **111**: 449–52.
85. Kong, F., Wu, X.L., Zheng, Y. *et al.* (2006) *J. App. Phys.* **99**: 064505.
86. Carvalho, L.M., Santos, L.F., Guimaraes, F.E.G., Goncalves, D., Gomes, A.S. and Faria, R.M. (2001) *Synth. Met.* **119**: 361–2.
87. Ho, C.C., Yeh, K.M., and Chen, Y. (2004) *Synth. Met.* **45**: 8739–49.
88. Hwang, D.H., Chuah, B.S., Li, X.C. *et al.* (1998) *Macromol. Symp* **125**: 111–20.
89. Silva, R.A., Serein-Spirau, F., Bouachrine, M., Lere-Porte, J.P. and Moreau, J.J.E. (2004) *J. Mat. Chem.* **14**: 3043–50.
90. Sun, Q.J., Wang, H.Q., Yang, C.H. and Li, Y.F. (2003) *J. Mat. Chem.* **13**: 800–6.
91. Sun, Q.J., Wang, H.Q., Yang, C.H., Wang, X.G., Liu, D.S. and Li, Y.F. (2002) *Thin Sol. Films* **417**: 14–19.
92. Ko, H.C., Lim, D.K., Kim, S.H., Choi, W. and Lee, H. (2004) *Synth. Met.* **144**: 177–82.
93. Verbakel, F., Meskers, S.C.J. and Janssen, R.A.J. (2006) *Chem. Mat.* **18**: 2707–12.
94. Duan, L.A., Qiu, Y. and Wang, H.Q. (2003) *Synth. Met.* **137**: 1133–5.
95. Zou, Y.P., Tan, S.T., Yuan, Z.L. and Yu, Z.J. (2005) *J. Mat. Sci.* **40**: 3569–71.
96. Yang, Z., Sokolik, I. and Karasz, F.E. (1993) *Macromol.* **26**: 1188–90.
97. Gray, F.M. (1997) *Polymer Electrolytes*, New York, Weinheim (Germany), Cambridge (UK): The Royal Society of Chemistry
98. Gray, F.M. (1991) *Solid polymer electrolytes: fundamentals and technological applications*, New York, Weinheim (Germany), Cambridge (UK): VCH Publishers, Inc.
99. Edman, L., Pauchard, M., Moses, D. and Heeger, A.J. (2004) *J. App. Phys.* **95**: 4357–61.

100. Tasch, S., Holzer, L., Wenzl, F.P. *et al.* (1999) *Synth. Met.* **102**: 1046–9.
101. Ouisse, T., Armand, M., Kervella, Y. and Stephan, O. (2002) *App. Phys. Lett.* **81**: 3131–3.
102. Habrard, F., Ouisse, T. and Stephan, O. (2006) *J. Phys. Chem. B* **110**: 15049–51.
103. Shin, J.H., Xiao, S., Fransson, A. and Edman, L. (2005) *App. Phys. Lett.* **87**: 043506.
104. Yin, C., Zhao, Y.Z., Yang, C.Z. and Zhang, S.Y. (2000) *Chem. Mat.* **12**: 1853–6.
105. Kong, F., Zhang, S.Y., Zheng, Y., Ou, C.G., Yang, C.Z. and Yuan, R.K. (2006) *J. App. Poly. Sci.* **101**: 4253–5.
106. Cimrova, V., Schmidt, W., Rulkens, R., Schulze, M., Meyer, W. and Neher, D. (1996) *Adv. Mat.* **8**: 585.
107. Huang, F., Wu, H.B., Wang, D., Yang, W. and Cao, Y. (2004) *Chem. Mat.* **16**: 708–16.
108. Huang, F., Hou, L.T., Shen, H.L., Yang, R.Q., Hou, Q. and Cao, Y. (2006) *J. Poly. Sci. A.-Poly. Chem.* **44**: 2521–32.
109. Edman, L., Liu, B., Vehse, M., Swensen, J., Bazan, G.C. and Heeger, A.J. (2005) *J. App. Phys.* **98**: 044502.
110. Edman, L., Pauchard, M., Liu, B., Bazan, G., Moses, D. and Heeger, A.J. (2003) *App. Phys. Lett.* **82**: 3961–3.
111. Banerjee, S.K. *et al.* (2006) *Solid state electronic devices*, Upper Saddle Rivers, New Jersey: Pearson Prentice Hall.
112. Gao, J., Yu, G. and Heeger, A.J. (1997) *App. Phys. Lett.* **71**: 1293–5.
113. Gao, J., Li, Y.F., Yu, G. and Heeger, A.J. (1999) *J. App. Phys.* **86**: 4594–9.
114. Zhang, Y. and Gao, J. (2006) *J. App. Phys.* **100**: 084501.
115. Yu, G., Zhang, C. and Heeger, A.J. (1994) *App. Phys. Lett.* **64**: 1540–2.
116. Gao, J., Yu, G. and Heeger, A.J. (1998) *Adv. Mat.* **10**: 692–5.
117. Yu, G., Cao, T., Andersson, M., Gao, J. and Heeger, A.J. (1998) *Adv. Mat* **10**: 385–8.
118. Cao, Y., Parker, D., Yu, G., Zhang, C. and Heeger, A.J. (1999) *Nature* **397**: 414–7.
119. Yu, G., Pei, Q.B. and Heeger, A.J. (1997) *App. Phys. Lett.* **70**: 934–6.
120. Dick, D.J., Heeger, A.J., Yang, Y. and Pei, Q.B. (1996) *Adv. Mat.* **8**: 985–7.
121. Edman, L., Summers, M.A., Buratto, S.K. and Heeger, A.J. (2004) *Phys. Rev. B* **70**: 115212.
122. Gao, J. and Dane, J. (2004) *App. Phys. Lett.* **84**: 2778–80.
123. Dane, J., Tracy, C. and Gao, J. (2005) *App. Phys. Lett.* **86**: 153509.
124. Gao, J. and Dane, J. (2005) *J. App. Phys.* **98**: 063513.
125. Shin, J.H., Dzwilewski, A., Iwasiewicz, A. *et al* (2006) *App. Phys. Lett.* **89**: 013509.
126. Hu, Y., Tracy, C. and Gao, J. (2006) *App. Phys. Lett.* **88**: 123507.
127. Zhang, Y.G., Hu, Y.F. and Gao, J. (2006) *App. Phys. Lett.* **88**: 163507.
128. Yang Y. and Pei, Q.B. (1996) *App. Phys. Lett.* **68**: 2708–10.
129. Leger, J.M., Carter, S.A. and Ruhstaller, B. (2005) *J. App. Phys.* **98**: 124907.
130. Campbell, I.H., Smith, D.L., Neef, C.J. and Ferraris, J.P. (1998) *App. Phys. Lett.* **72**: 2565–7.
131. Li, Y.F., Gao, J., Yu, G., Cao, Y. and Heeger, A.J. (1998) *Chem. Phys. Lett.* **287**: 83–8.
132. Tracy, C. and Gao, J. (2005) *App. Phys. Lett.* **87**: 143502.
133. Tracy, C. and Gao, J. (2006) *J. App. Phys.* **100**: 104503.

6 LED Materials and Devices

Tsunemasa Taguchi

YAMAGUCHI UNIVERSITY, 2-16-1 Tokiwadai, Ube, Yamaguchi 755-8611, Japan

6.1 Introduction	207
6.2 LED Structures and efficiencies	208
6.3 Typical LED and features	211
6.4 Generation of white light	212
6.5 Devices and applications	218
6.6 Future prospects	220
6.7 Conclusions	222
References	222

6.1 INTRODUCTION

A light-emitting diode (LED) is an element that emits light by applying forward-bias current into the p-n junction of a semiconductor. LEDs on the market today are manufactured using III-V semiconductor materials (ternary and quaternary alloys using elements from the periodic groups III and V) such as GaAlAs, AlInGaP, InGaN and AlInGaN [1]. With recent technological advances, the function of LEDs has shifted from display to lighting, as they are increasingly being used as solid light sources and devices that have the same lighting properties as conventional incandescent bulbs and fluorescent lamps.

As LEDs are solid light sources, they offer high-level safety, as well as other advantages including low-voltage drive, are compact and lightweight, and have a long life. Red LEDs, which were commercialized in 1963, are already being used instead of incandescent bulbs on signboards [2]. Since 1993, however, high-intensity LEDs (which have 10-candela-class intensity) have been developed in the yellow-orange, green and blue short wavelengths. Since 1997, pseudo-white LEDs that use blue LEDs to excite fluorescent material have been commercialized, and applications have been developed for their use in light-guiding plates and LCD backlights [3].

With the higher intensity of blue LEDs, the luminous efficacy of white LEDs is now over 100 lm/W [4]. Near-ultraviolet (n-UV) and ultraviolet (UV) LEDs (360–410 nm) also have an external quantum efficiency of over 40%, and a new type of white LED lighting has been developed that offers high-level color rendering properties through the mixing of fluorescent materials in the three primary colors (RGB) [5, 6]. Research is also underway into 200–300 nm class deep ultraviolet LEDs using AlGaIn and AlN materials. Table 6.1

Table 6.1 Properties of various kinds of visible, n-UV, UV and white LEDs that are currently commercialized or developed

Color	Material	Emission wavelength (nm)	Brightness (cd)	External quantum efficiency (%)	Luminous efficacy (lm/W)
Red	GaAlAs	660	2	30	20
Yellow	AlInGaP	610–650	10	50	96
Orange	AlInGaP	595	2.6	>20	60
Green	InGaN	520	12	>20	40
Blue	InGaN	450–475	>2.5	>50	20
Near ultraviolet	InGaN	382–400		>43	
Ultraviolet	AlInGaN	360–371		>40	
Pseudo binary white	InGaN blue LED + yellow fluorescent material	465, 560	>10		>100
Pseudo 3-color white	InGaN blue LED + green, red fluorescent material	465, 520, 620			>30
3-wavelength white light	Near UV LED + RGB fluorescent material	465, 520, 612~640	>5		>40

shows some examples of the properties of various high-intensity, high-efficiency LEDs that are currently being commercialized (or developed for practical application).

There are five base technologies involved white LED lighting systems. These are:

1. epitaxial growth and property and device evaluation technology;
2. assembly and mounting technology;
3. illuminated light source and equipment production technology;
4. new system design technology; and
5. technology for improving LED light source safety and standardization [4].

6.2 LED STRUCTURES AND EFFICIENCIES

To develop efficient high-brightness LED light sources, we have focused on:

- fundamental studies of emission mechanisms in II-VI and III-V-based wide-band gap compound semiconductors;
- improvement of epitaxial growth methods of multiple quantum wells (MQWs) and external quantum efficiency LEDs;

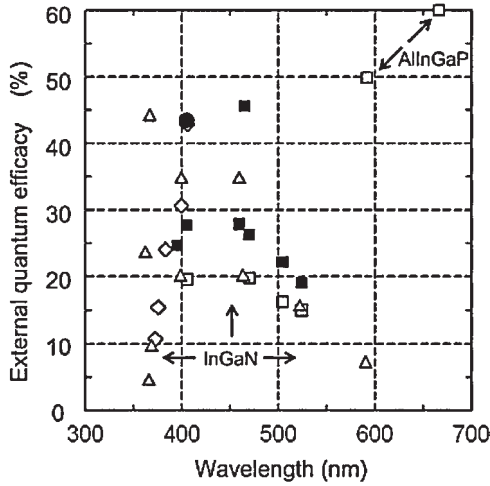


Figure 6.1 External quantum (η_e) in InGaN- and AlInGaP-based visible LEDs at a forward-bias current at 20 mA. (Δ : Nichia chemical Corp., \blacksquare : Cree, \square : Philips Lumileds, \bullet : Yamaguchi University, and \diamond : Mitsubishi Cable Ind.)

- production of large substrates for homoepitaxial growth;
- development of multicolor, UV-excited phosphors that generate white light; and
- illumination sources and fixtures using white LEDs.

There are several basic research issues concerning the reduction of defect densities and the identification of recombination centers for improvement of the external quantum efficiency and luminous efficacy [3, 5].

In general, the wallplug efficiency (η_{wp}) of a p-n heterojunction LED under a forward-bias condition is expressed by three physical parameters, being voltage efficiency η_v , internal quantum efficiency η_{int} and extraction efficiency η_{ext} :

$$\eta_{wp} = \eta_v \eta_{int} \eta_{ext} = \eta_v \eta_e$$

where η_v is controlled by resistance and voltage barrier, η_{int} is controlled by non-radiative recombination processes and η_{ext} is controlled by a loss of internal absorption. The product (η_e) of η_{int} and η_{ext} is so-called the external quantum efficiency.

Figure 6.1 shows the η_e measured at a forward-bias current of 20 mA in various kinds of LEDs reported by Nichia chemical Co., Cree, Mitsubishi Cable Ind., Philips Lumileds and Yamaguchi University [4].

Recently, the efficient InGaN-based blue and n-UV LEDs on patterned sapphire substrates using lateral epitaxy (LEPS) has been fabricated. The structure consists of four

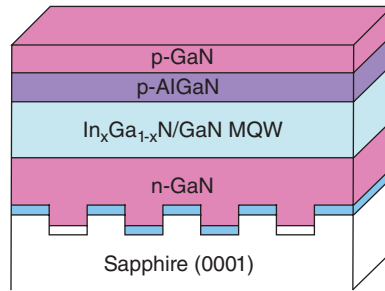


Figure 6.2 A structure of InGaN/GaN MQWs between n-AlGaN and p-AlGaN on a patterned sapphire substrate (LEPS)

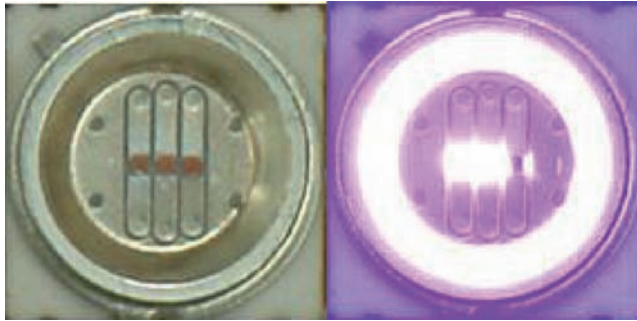


Figure 6.3 Flip-chip bonding onto AlN ceramic substrate (left-hand side) and an emission of about 405 nm at a forward-bias current of 20 mA (right-hand side)

periodic MQWs of InGaN/GaN, and the barrier layers are n- and p-type $\text{Al}_{0.2}\text{Ga}_{0.8}\text{N}$ (Figure 6.2). Cathodoluminescence measurements revealed that the dislocation densities involved in the active region of the devices are much reduced compared to those fabricated on unpatterned substrates. We can obtain high external quantum efficiency η_e over 43% by flip-chip bonding the device onto an AlN ceramic substrate without Si submount (Figure 6.3). In order to improve the extraction efficiency of the n-UV LEDs, we optimized the patterned structural configuration by means of photoluminescence measurements. When we operated the optimized LED at 20 mA, the device produced an estimated 26.1 mW of output power P_o at 405 nm, for a 43.4% efficiency (Figure 6.4). With increasing current, P_o increases linearly to an estimated about 115 mW at 100 mA in Figure 6.4.

For measuring the internal quantum efficiency (η_{im}), a method of selective excitation by Xe-Cl excimer or dye-laser for the MQW active layer has been proposed [7]. Figure 6.5 shows the schematic pictures for the excitation process to generate electrons and holes into the active layer in the LED structure.

Internal quantum efficiency is calculated by following method: the relative efficiency (= integrated photoluminescence (PL) intensity/excitation power density) is measured by the excitation power dependence at low temperature ($\sim 6\text{ K}$) and room temperature PL [7].

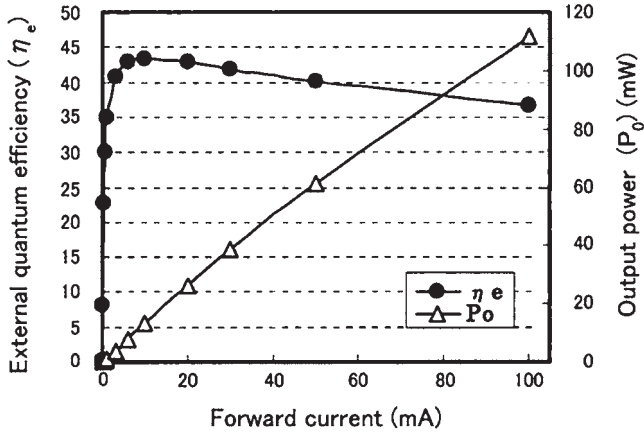


Figure 6.4 Room temperature performance plots for 43% efficient n-UV LED (Figure 6.3) show gradual decrease in external quantum efficiency and increase in optical output at drive currents above 20 mA

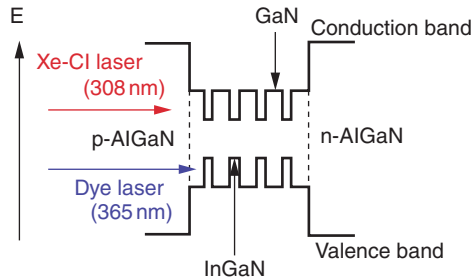


Figure 6.5 A schematic model for electron-hole injection into the MQW active layer under Xe-Cl excimer or dye laser excitation

Since nonradiative recombination will not be dominant at such low temperature, it is assumed that the maximum luminescence intensity is 100% at low temperatures due to all-dominant radiative recombination. Finally, the highest relative efficiency at RT-PL is the internal quantum efficiency of the measured sample. At present, the η_e in blue and n-UV LED is estimated to be approximately 85% and 70%, respectively.

6.3 TYPICAL LEDES AND FEATURES

Figure 6.6 shows the typical types of LED and their characteristics. With the emergence over time of higher output LEDs, mounting and packaging technology has also been upgraded in line with this. Lamp-type LEDs, for example, are suited for reflecting light with

Years	1963–1993	2000–2010 and beyond		2002–2010 and beyond
Type	Shell-type LED	Surface-mounted LED		Integrated LED
Configuration	 <p>Discrete parts</p>			 <p>Compact, multiple light source type <Hybrid></p>
Features	<ul style="list-style-type: none"> · Epoxy resin lens (3 mmϕ/5 mmϕ size) · At 20–30 mA, luminous flux of 1–2 lm 	<ul style="list-style-type: none"> · Optimal heat countermeasures · At 70 mA, luminous flux of around 4 lm or higher 	<ul style="list-style-type: none"> · Sufficient heat countermeasures · At 400 mA or higher, luminous flux of around 20 lm or higher. · Capable of output of several watts 	<ul style="list-style-type: none"> · Sufficient heat countermeasures · At 1 A or higher, luminous flux of 100 lm or higher, klm made possible by multiple light sources. · Optical system required. · Can replace chips with lamps. · Can be customized

Figure 6.6 Typical types of LEDs and their features

strong directional characteristics, whereas surface-mounted-device-type LEDs offer superior heat-loss countermeasures and enable higher outputs, and by applying high currents, can produce high-level luminous flux (tens of lm [lumen]). This has also enabled several dozen LED multi-chips to be mounted on a circuit board to produce a compact LED integrated light source, which makes possible an LED light source that has a high luminous flux of 1 Klum. Moreover, several hundred lm can be produced by LED single elements.

With regards to LED light environments and light control, it is unlikely that the shell-type optical wavelength LEDs sold commercially today have really been developed for light with the strong directional properties emitted by LEDs, as will be shown later.

6.4 GENERATION OF WHITE LIGHT

6.4.1 Two methods

There are currently two methods commonly used for LED-based white light generation:

- individual red-green-blue (RGB) LED combinations that mix to generate white light; and
- $\text{In}_x\text{Ga}_{1-x}\text{N}$ -based blue and near-UV (380 to 410 nm) LED systems incorporating fluorescent phosphors to down-convert some of the emission to generate a mix of white lights (Figures 6.7 (a), (b) and (c)).

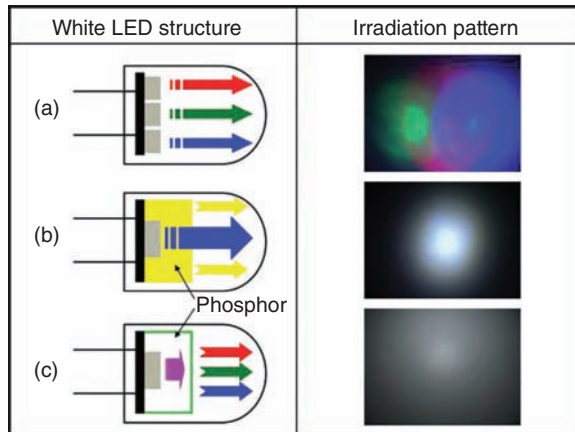


Figure 6.7 Three types of white LEDs and its irradiation pattern: (a) RGB individual LEDs; (b) blue LED and YAG:Ce yellow phosphor; and (c) n-UV LED and RGB white phosphor

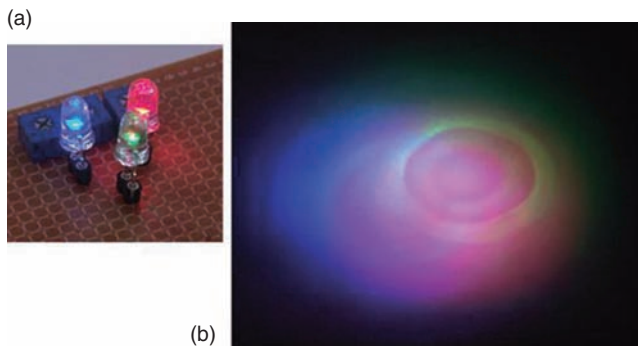


Figure 6.8 RGB shell-type individual LEDs at (a) 20 mA and (b) its no-mixing color at the irradiation plane

The RGB approach (Figure 6.7 (a)) requires at least three LEDs, and each device must be adjusted by individual supply circuits to balance the emission intensity of each color for proper white light generation (Figures 6.8 (a) and (b)). However, since each illuminance distribution is different, it is very difficult to produce a mixed homogeneous white light.

Several problems that currently exist with white-light devices composed of blue LEDs and Ce^{3+} -doped yttrium aluminum garnet (Ce: YAG) yellow phosphors (Figure 6.7(b)) that mix blue and yellow light to produce what appears to be white light. These include the halo effect of blue/yellow color separation, strong temperature and current dependence of chromaticity, and poor color rendering due to the lack of green and red components.

A light source requires high-quality light radiation because when we look at objects we see the reflected light. The spectrum of the illumination source affects the appearances of objects, producing the phenomenon we call color rendering. If the illumination source does not induce a spectrum close to that of incandescent bulbs or the Sun, then the color of

objects will be different from what we are accustomed to. If we can match the appropriate multicolor phosphor and encapsulation material to the n-UV region, then we can obtain white LEDs with both high color rendering and high luminous efficacy. In fact, we have developed a new type of silicone for encapsulation and high efficiencies of green and red phosphor materials for n-UV excitation [8].

6.4.2 Characteristics of n-UV white LEDs

The n-UV white LED approach (Figure 6.7 (c)) is analogous to three-color fluorescent lamp technology, which is based on the conversion of n-UV radiation to visible light via the photoluminescence process in phosphor materials. In the blue/YAG process, a sharp blue light from the blue LED source is an essential component of white light, and is strongly affected by temperature and drive current. UV light, on the other hand, is not included in the white light generation from n-UV-based devices. This technology can thus provide a higher quality of white light compared to the blue YAG method.

The three spectra in Figure 6.9 are produced by day (D), white (W) and incandescent lamp (L)-white LEDs, high-color-rendering-index (Ra) LEDs having different components of red, green and blue phosphor materials. The value of Ra >90 is close to that of a three-band emission fluorescent lamp. We estimated the luminous efficacy of radiation as about 30lm/W for the present high-Ra white LED. Both components of green and red emission are crucial to improve the color temperature and the color-rendering index. A typical photoluminescence spectrum of RGB phosphor materials excited at 382nm contains at least three main peaks locating at 447, 528 and 626nm, respectively (Figure 6.9). The 447nm blue emission, 528nm green emission and 626nm red emission bands originate from the fluorescent emission of Sr, Ca, Ba, Mg)₁₀(PO₄)₆Cl:Eu²⁺, ZnS:Cu,Al and La₂O₂S:Eu³⁺ phosphors, respectively. The blue phosphor indicates two absorption peaks at about 330 and

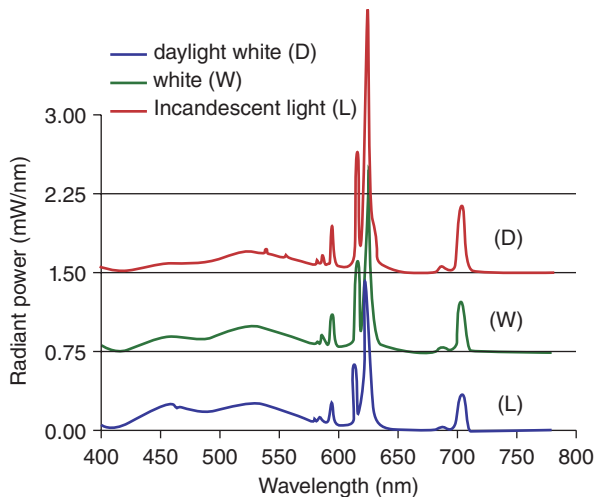


Figure 6.9 Typical emission spectra obtained from three white LEDs: day light white (D); white (W); and incandescent light (L), across the visible spectral region

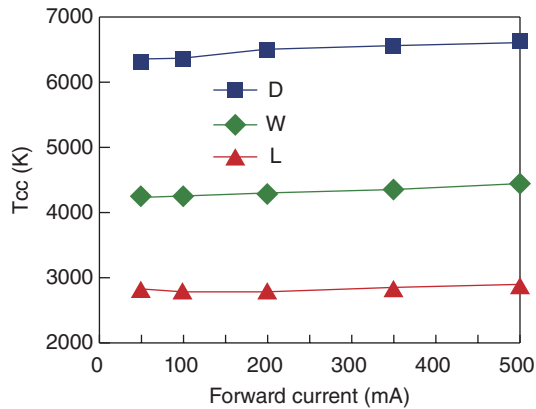


Figure 6.10 A change of correlated color temperature (T_{cc}) at three white LEDs: D, W and L (Figure 6.9) as a function of forward-bias current between 50 and 500 mA

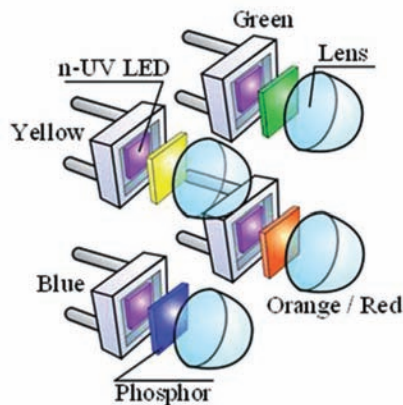


Figure 6.11 A novel type of visible LED consisting of n-UV LED, and red, green, blue and orange phosphor

380 nm and occurs at the $4f^7 \rightarrow 4fd^5d^1$ optical transition in Eu^{2+} ions. The green phosphor indicates an absorption peak at about 400 nm and occurs at a donor-acceptor pair transition. The red phosphor indicates an absorption peak at 350 nm and occurs both in the f-f transition in Eu^{3+} ions and in a charge transfer process. The illuminance distribution from the high-Ra type white LED indicates the full radiation as described by $\cos \theta$. We estimate the lifetime as more than 6000 hrs at a forward bias of 20 mA.

Figure 6.10 shows almost no change in the correlated color-temperature (T_{cc}) of the three white LEDs as a function of forward current between 20 and 500 mA. For lighting applications, it is essential to keep a constant T_{cc} with increasing current.

The realization of high-performance white-light LEDs requires new phosphor materials. We have developed an orange/red, yellow, green and blue (OYGB), white LED consisting of OYGB phosphor materials and an n-UV LED, as shown in Figure 6.11. The device generates three peaks located at 450, 520 and 580 nm, which are produced by fluorescent

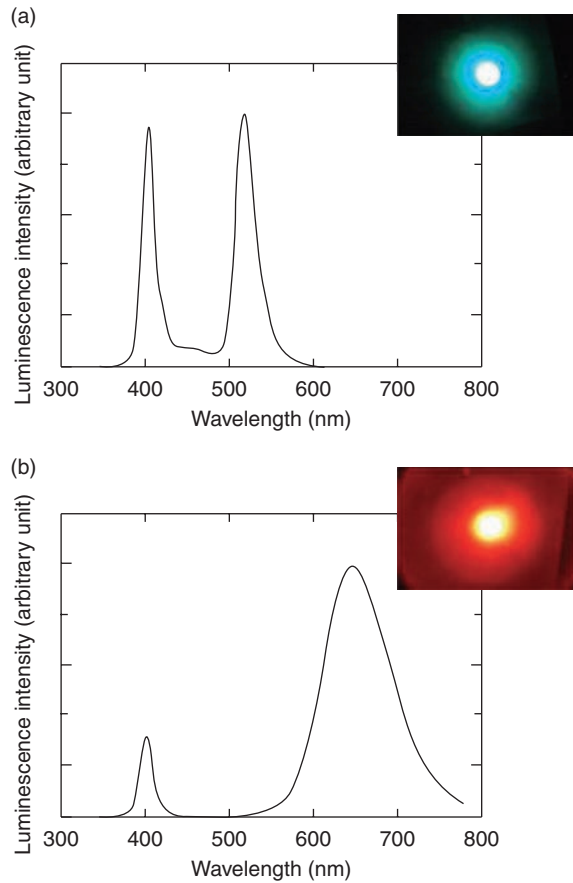


Figure 6.12 Photograph and emission spectrum obtained from (a) green phosphor under an excitation of n-UV LED at 405 nm; and (b) red phosphor under an excitation of n-UV LED at 405 nm

emissions of strontium- and ZnS-based long-wavelength phosphor materials, respectively. Interesting, the devices demonstrated white luminescence with $T_{cc} = 3700$ K, $R_a \geq 93$, $K = 40$ lm/W and a chromaticity $(x, y) = (0.39, 0.39)$. The OYGB device generates a luminescence spectrum broader than that of an RGB white LED, and a better color rendering index.

Using new phosphor material, such as SrBaSiO compound for green emission and CaAlSiN:Eu²⁺ for red emission, superior high-Ra warm white LED has been developed and its emission spectrum is shown in Figures 6.12 (a) and (b), respectively.

Figure 6.13 shows a typical emission spectrum of the high-Ra white LED operated at 20 mA, which is composed of n-UV LED and RGB white phosphor ($R_a = 96$). Table 6.2 shows the color-rendering index (R_a), R_9 and R_{15} that have been obtained in white LED. These values are compared with those obtained in blue-yellow ($R_a = 85$) and blue-orange ($R_a = 76$) commercialized white LEDs.

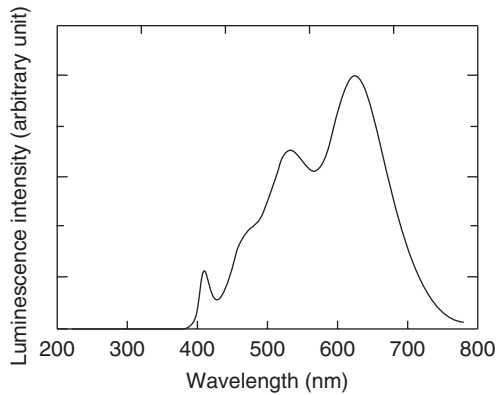


Figure 6.13 Emission spectrum obtained from high-Ra (>96) white LED

Table 6.2 A comparison in average color-rendering index (Ra), ($R_1 \sim R_8$) and special Ra ($R_9 \sim R_{15}$) among blue-yellow white, blue-orange and n-UV (RGB) white LEDs

	Ra	R1	R2	R3	R4	R5	R6	R7	R8	R9	R10	R11	R12	R13	R14	R15
BY	85	88	97	92	74	83	88	83	74	45	91	70	60	93	97	88
BO	76	72	87	96	67	70	81	81	53	-11	69	60	51	75	98	65
n-UV RGB	96	95	97	96	92	96	95	95	96	95	95	89	95	95	97	98

6.4.3 Design and system

We now need to promote product and lighting design that takes these properties into account. The characteristic features of LED lighting (in terms of light distribution and intensity, etc.) are strongly dependent on the light source design, and thus we need to design products that take into consideration both product design (tangible [hardware] considerations) and lighting design (intangible [software] considerations). So, using the keywords shown in Table 6.3, we need to examine production design and lighting design from a new perspective.

To obtain an LED lighting system therefore means converting LEDs from display technology into lighting technology. ('LED lighting system' here refers to hardware and software technology designed for lighting applications; in other words, all the technology involved, including the light source equipment, power source and control circuits.) It follows from this that the LED industry is likely to grow in size and eventually underpin world industry by 2020. The way we think about power distribution systems, telecommunication infrastructure and other electrical equipment is also expected to change dramatically. Using energy-saving LED lighting systems will enable the conversion of normal 100 V AC commercial power into DC, and open up the door for communication between LED lighting and mobile terminals.

As has already been discussed, optical light used for lighting needs to have design flexibility and needs to be safe. Therefore, essential to the development of a light source for

Table 6.3 Design concepts and keywords in product and lighting design using white LEDs

Design	Properties of white LED	Design concept (keywords)
Product design (tangible aspects)	Compact, thin, lightweight	Light, weightless, sharp, lightweight, portable, mobile, easy, ubiquitous
	Low-power, power-saving	Safety, energy-saving, resource-saving, reliable, high efficiency, economical, ecology
	Long-life, low pollution	Maintainability, natural environment, permanence, universality, recycling, economical clean
	Anti-shock, low-temperature resistant	Strength, reliability, accessibility, strong, adaptable, adjustable
Lighting design (intangible aspects)	High brightness, directional properties	Bright, shiny, glary, high-quality signals, messages, light presence
	Low heat output, optical wavelength range	Reliability, easiness, peace-of mind, healing, safety, easy on the eyes, contact with light
	Controllable, responsive	Rhythm, flow, dynamic, change, accuracy, entertainment, communication, interactive
	Light from white LED	Future, new, amazement, future, digital, fun, freedom, unknown, popularity

general lighting applications is a technology that uses white LED lighting. White light does not contain harmful substances as does light with acute directional properties, blue light (440–460 nm wavelengths) that can damage eyes and skin, ultraviolet light (360 nm and shorter wavelengths), mercury light, and so on.

6.5 DEVICES AND APPLICATIONS

As already shown in Figure 6.6, high-power and high-flux white LEDs have been developed.

Figure 6.14 shows the change in luminous efficacy of white LED light sources since 1998, as well as examples of practical commercial application, together with commercialization predictions for up to 2010. Also shown are predictions relating to falling costs per white LED unit. Based on the examples of practical applications provided to date, it is believed that a white LED illuminated light source will be produced in the future based on an all-new concept, and that practical applications will also be developed for white LEDs for general lighting.

Figure 6.15 shows the solar cells and white LED illuminated street lights set up at the Faculty of Engineering of Yamaguchi University, Japan. There are currently several hundred of these street lamps in operation around Japan. There are special applications of white LEDs to medical fields and ink painting. Figure 6.16 shows the white LED endoscope

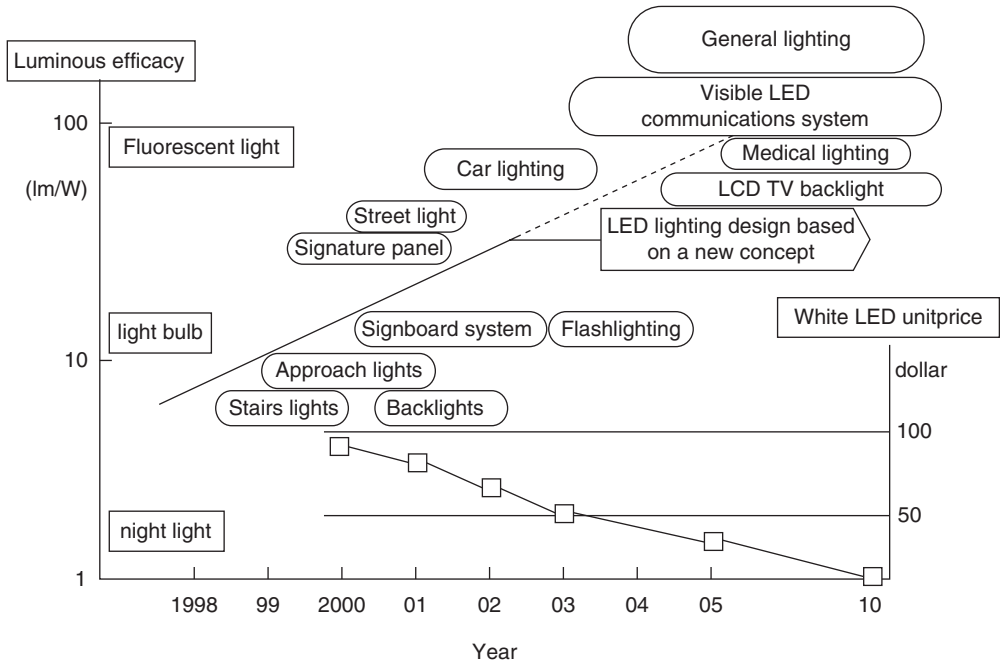


Figure 6.14 Changes in luminous efficacy of white LED light source, with examples of practical applications and commercialization predictions up to 2010. Also, prediction of costs per white LED unit



Figure 6.15 Solar cells and white LED lighting street lamp system at Faculty of Engineering, Yamaguchi University, Japan

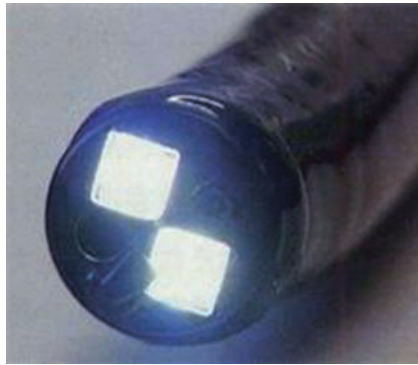


Figure 6.16 LED digestive endoscope with two white LEDs



Figure 6.17 Exhibition of white LED lighting for antique ink painting in Yamaguchi Museum of Art. The picture was delivered from a part of TV news (1 November 2007) (courtesy of Yamaguchi Asahi TV)

consisting of n-UV LED and RGB white phosphor with 30lm/W and $R_a = 96$ [9]. Figure 6.17 shows the high- R_a white LED lighting system for ink painting in an art museum.

6.6 FUTURE PROSPECTS

By improving quantum efficiency of fluorescent material, the luminous efficacy of fluorescent white LEDs is expected to go from the current 30lm/W to around 120lm/W by 2010, and to approach a theoretical value of about 300lm/W by 2020 in Japan (Figure 6.18). As a result, the adoption rate of white LED lighting is expected to be several percent by 2010, and over 30% from around 2020 onwards. Worldwide, the transition from fluorescent lighting is likely to progress rapidly, and is likely to dramatically boost awareness surrounding illuminated lighting environments and systems for ordinary households, buildings and shops. This is because, unlike conventional illuminated lighting, LED lighting enables the flexible control and adjustment of intensity and color temperature (color tinting). In other words, this will enable people to control the light settings in their living environments for

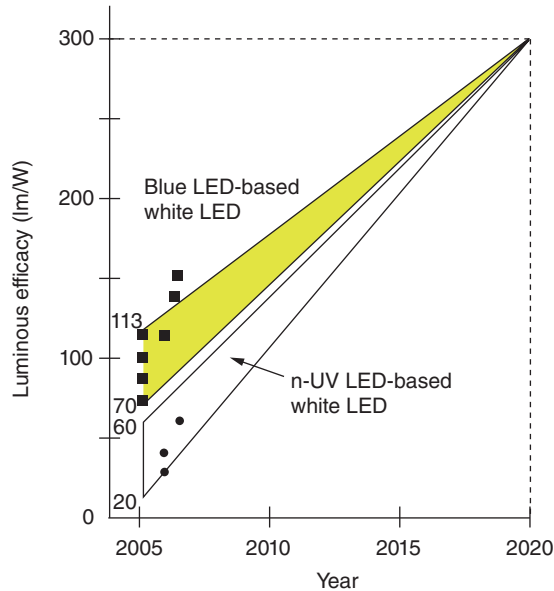


Figure 6.18 A roadmap of luminous efficacy of two types of white LEDs from 2005 to 2020 (■: Nichia Chemical Ind. and ●: Yamaguchi University)

the morning, middle of the day and evening, providing them with an indoor lighting environment that replicates natural light surroundings.

Visual images and lighting that are designed mainly to illuminate are culturally linked, and therefore different countries take different approaches to lighting. For example, in Japan, fluorescent lamps are used extensively for lighting, while in the United States and Europe, people prefer softer incandescent lighting and tend to steer clear of very pale or very bright lighting. On the other hand, in Asia, people prefer red, yellow and green-toned lighting that is closer to primary light colors, and so the preference in Asia is for bright and flashy lighting and visual images. There is global consensus, however, on the issues of energy conservation and environmental preservation. If from 2010, white LED lighting can replace conventional lighting technology, then this will surely have an even greater impact on society than the move from vacuum tubes to transistors.

Predictions suggest that from 2010 onwards, roughly 10% of all light bulbs and fluorescent lamps will be replaced with LED lighting, and by this time, the LED lighting market is expected to be worth some 500 billion yen (4.2 billion dollars). Under the Japanese government's energy conservation targets for 2010, crude oil use is to be reduced by 18.6 million kl in the civil sector, and if LED lighting expands as predicted, then LED lighting alone will be able to achieve roughly a 3.4% reduction towards meeting these energy conservation targets. In addition to these energy conservation benefits, LED lighting is also important in providing every citizen with the chance to be able to take steps to use less energy. In the future, just buying LED lighting will potentially enable all people to contribute to the prevention of global warming and the protection of the global environment.

6.7 CONCLUSIONS

We have focused research on the development of high-brightness blue and UV devices based on III-nitrides for the purpose of white-light LED sources. The idea of using near-UV LEDs and multicolor phosphor is similar to fluorescent lamps, to create an efficient white LED lighting system without either Hg or deep-UV radiation. This solid-state approach is connected with the development of new phosphor-converted white LEDs and could be improved by scientists and engineers involved in the compound semiconductor, phosphor and lighting communities.

Solid-state lighting will contribute to the reduction of greenhouse gases by reducing the amount of energy spent on artificial illumination. The high efficiency of white-light LEDs means that the active potential exists for enormous energy savings. Improved structures and new phosphors yield high-efficiency, UV-driven white-light LEDs.

REFERENCES

1. Nakamura, S. and Fasol, G. (1997) *The blue laser diode*, Berlin: Springer-Verlag.
2. Williams, E.W. and Hall, R. (1978) *Luminescence and light Emitting Diode*, Oxford: Pergamon Press.
3. Craford, J. (2005) 'LEDs for solid state lighting and other emerging applications: status, trends and challenges', *Proc. SPIE*, **5941**: 1–10.
4. Taguchi, T. (2006) 'Developing white LED lighting technologies and its roadmap in Japan', *J. Light and Vis. Env.* **30**: 65–70.
5. Taguchi, T. (2001) 'Japanese semiconductor lighting project based on ultraviolet LED and phosphor system', *Proc. SPIE* **4445**: 5–12.
6. Uchida, Y. and Taguchi, T. (2005) 'Lighting theory and luminous characteristics of white light-emitting diodes', *J. of Opt. Eng.* **44(12)**: 124003–9.
7. Watanabe, S., Yamada, N., Nagashima, M. *et al.* (2003) 'Internal quantum efficiency of highly-efficient $\text{In}_x\text{Ga}_{1-x}\text{N}$ based near ultraviolet light-emitting diodes', *Appl. Phys., Lett.* **83**: 4906–8.
8. Taguchi, T. (2002) 'Preparation and characterization of phosphor materials for semiconductor lighting application', *Proc. of Int. Conf. in EL*, Ghent, 245–50.
9. Taguchi, T., Uchida, Y. and Kobashi, K. (2004) 'Efficient white LED lighting and its application to medical fields', *Phys. Stat. Sol.*, **201(12)**: 2730–5.

7 Thin Film Electroluminescence

Adrian H. Kitai

McMASTER UNIVERSITY, Hamilton, Ontario, ON 68S-4L7, Canada

7.1 Introduction	223
7.2 Background of EL	223
7.3 Theory of operation	226
7.4 Electroluminescent phosphors	233
7.5 Device structures	235
7.6 EL phosphor thin film growth	242
7.7 Full color electroluminescence	245
7.8 Conclusions	247
References	248

7.1 INTRODUCTION

The solid state conversion of electrical energy to visible light has evolved into a diverse field. The requirements for various applications are diverse also. For example, high intensity **Light Emitting Diode (LED)** sources are well entrenched in LCD backlighting applications, and are entering the lighting market. **Powder Electroluminescence (Powder EL)** continues to serve in nightlights and keyboard illumination. **Organic Light Emitting Diode (OLED)** devices are entering the display market in portable displays. **Thin Film Electroluminescence (TFEL)** is being developed for color television applications.

7.2 BACKGROUND OF EL

This chapter focuses on TFEL materials and devices. There are distinct operating principles underlying these devices, which will be examined in detail. However, it is useful to start by examining features that distinguish both powder EL and TFEL materials and devices from diode-type devices.

The materials used in powder EL and TFEL devices are generally inorganic polycrystalline solids rather than the single crystal materials used in LEDs. This permits large area devices to be manufactured at a reasonable cost. Highly uniform light emission over large areas is available. This is difficult to achieve with LEDs that are small area, albeit intense, sources of light.

The polycrystalline nature of these EL powder and thin film materials is the key reason for the uniformity of the light emission. The light emitted from each grain of material is normally not seen as a distinct source by the observer, as the light per unit area emitted is the result of numerous grains or crystals. For this reason, a less perfect material than the single crystal LED materials is able to create highly reproducible lighting without requiring the binning associated with LED devices.

Another key distinction between LEDs and powder EL and TFEL materials lies in the light emission process. In LEDs, band-to-band recombination generally occurs. This means that traps and defects that lead to unwanted, non-emissive recombination events between electrons and holes must be minimized by using high purity, low defect density materials. This is fundamentally due to the delocalization of electrons and holes in energy bands. Since electron and hole conduction is a necessary condition for efficient diode type devices, conduction and valence band transport is necessary. This carrier delocalization is therefore a mixed blessing, as it allows for high current density carrier transport and the associated availability of electrons and holes to supply recombination. However, it also allows carriers relatively free access to any traps within a diffusion length of the carrier.

In powder EL and TFEL materials, luminescence is generally derived from non-mobile charges. They are trapped in donor/acceptor type traps (powder EL) or in recombination centers in the case of thin film EL. These are, not surprisingly, insulating materials. Charge transport now occurs by a mechanism other than band transport alone. Upon application of a high electric field, high field breakdown (avalanche breakdown) occurs and charges flow, even though the EL materials are insulators.

In this chapter, thin film EL will be reviewed and both the science and technology developments to date will be discussed.

In 1967, Russ and Kennedy [1] demonstrated a double insulating layer EL structure. Figure 7.1 shows the structure of a double-insulating layer TFEL device. It consists of a substrate, usually glass, on which a series of thin film layers is grown. There are two electrodes, two dielectric layers and a phosphor layer.

More recently, a number of variants on this structure have been developed in which thick films or even sheets are used in place of the thin film insulating layers. In all cases, we will classify these structures as TFEL devices because the phosphor layer, which emits the light, is always a thin film. Note that sometimes only one dielectric layer is shown. There is no requirement for two insulating layers, although historically TFEL devices were made this way. Two thin (e.g. 10 nm) interface layers at the two sides of the phosphor layer may be formed as part of the EL structures, even if there is only one thicker insulating layer.

More recently, a number of other important TFEL structures have been developed. These structures offer specific advantages for certain applications, and are now introduced. A more detailed discussion of each structure is presented in Section 7.5.

7.2.1 Thick film dielectric EL structure

Recently developed by iFire Inc, Thick Dielectric EL (TDEL) devices [2] offer high EL brightness and efficiency. Here, the thin film dielectric layers are replaced with a single thick film dielectric made from high dielectric constant (relative dielectric constant over 1000) ceramics such as barium titanates or lead zirconium titanates. The layer may be

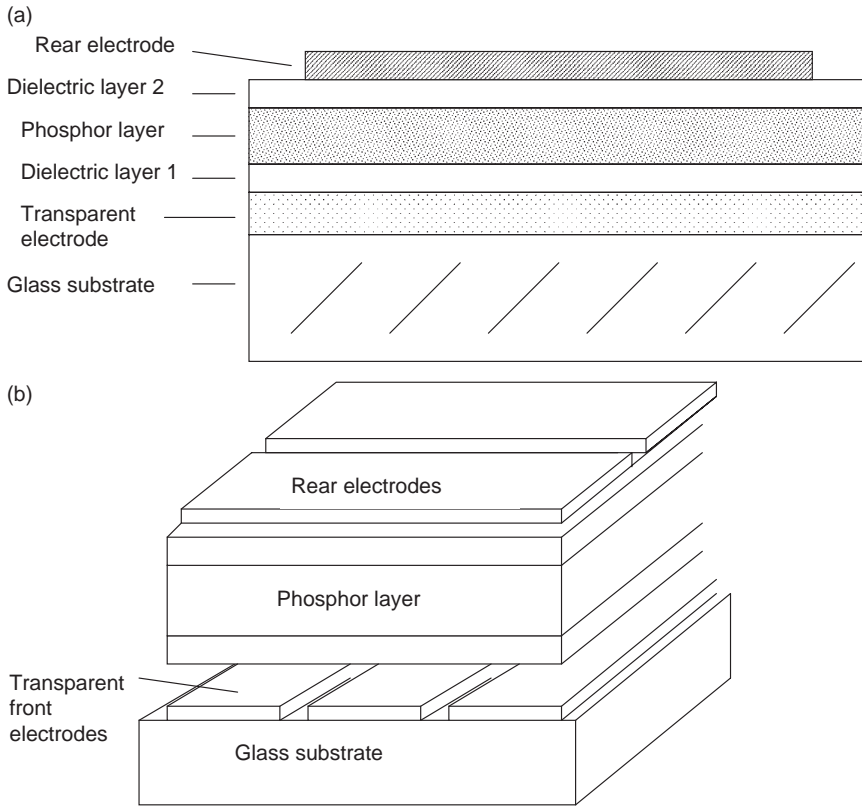


Figure 7.1 (a) Thin Film double-insulating-layer TFEL device structure showing sequence of layers deposited as thin films on a glass substrate. Typical materials used are:

- glass substrate: Corning 1737 glass;
- transparent electrode: Indium tin oxide (ITO), 150 nm;
- dielectric layers: Aluminium titanate, 200 nm each;
- phosphor layer: Manganese-doped zinc sulfide (ZnS:Mn), 500 nm;
- rear electrode: Aluminium, 100 nm.

(b) TFEL display with rows and columns. The sheet resistance of the transparent (ITO) electrodes is important for matrix addressing. ITO can be grown with under 10 ohms per square and over 80% transmission of light

deposited by screen printing. A subsequent planarization layer provides a sufficiently smooth dielectric surface to permit the deposition of good-quality phosphor thin films.

7.2.2 Ceramic sheet dielectric EL

The use of free-standing ceramic sheets for EL substrates has been employed to develop a number of new EL phosphors [3]. Typically a barium titanate ceramic is prepared by sintering barium titanate powder to form a dense ceramic and polishing at least one side of the

resulting ceramic sheet to prepare for the phosphor layer. The sheet is typically about 200 microns thick.

7.2.3 Thick top dielectric EL

Another interesting EL structure has been demonstrated [4], in which the light from the EL phosphor passes through a glass substrate, and the thick film dielectric layer is deposited on the back side of the phosphor layer. In principle, this structure can exhibit high brightness and efficiency similar to the TDEL structure, however, it has not been developed very extensively to date.

7.2.4 Sphere-supported thin film EL

The device structure [5] is effectively composed of numerous spherical, small-area TFEL devices embedded within a polymer (polypropylene) film. Each spherical TFEL device consists of a barium titanate sphere coated with a series of thin films, including the EL phosphor layer on the upper surface and an electrode on the lower surface.

7.3 THEORY OF OPERATION

The most important electronic processes occur within the phosphor layer as well as at the phosphor interfaces.

The phosphor layer must satisfy a large number of criteria to enable efficient light emission:

- It must be transparent to the wavelength of light being emitted.
- It must contain impurities having localized quantum states.
- It must be an electrical insulator.
- It must exhibit an avalanching-type breakdown process once a critical electric field is reached. The critical field is on the order of 10^8 V/m. A typical thickness of 1 micrometer means that this critical field is reached when about 100 V falls across it.
- The electrons that generate light must be able to fall into a localized ground state to cause light emission even in the presence of a high electric field in the phosphor layer.

The process by which light is emitted is shown in Figure 7.2 [6].

The light emission process begins upon application of a voltage across the electrodes of the TFEL device, causing the phosphor layer to sustain a high electric field. This electric field allows electrons trapped in interface states at the interface layer, on the left-hand side of Figure 7.2, to tunnel into the conduction band of the phosphor layer.

Once traveling in the conduction band, these electrons become 'hot', possessing a few electron volts of kinetic energy, and may impact-excite impurity centers causing the elec-

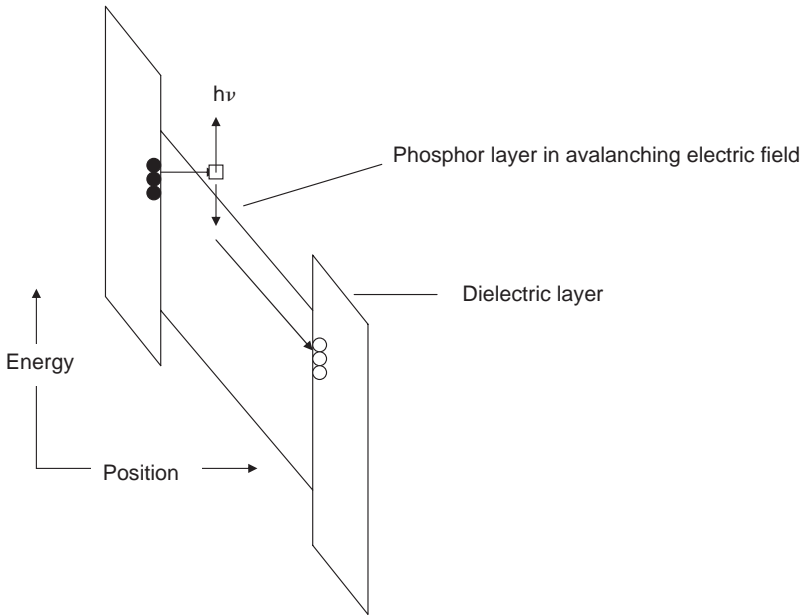


Figure 7.2 Energy band diagram of TFEL device showing electron trapping at phosphor/dielectric interfaces (solid circles are occupied traps, hollow circles are empty traps, tunneling, impact excitation of activator, and re-trapping)

trons in the ground state of the impurity center to become excited. When these excited electrons return to their ground state, light is emitted.

The conduction band electrons may also excite other valence band electrons into the conduction band by an avalanche process. These further electrons may also excite impurity centers.

Eventually, electrons in the conduction band reach the opposite interface layer on the right, and get trapped at interface states there. No further excitation occurs until the electric field is reversed in polarity, allowing these trapped electrons to return to the left interface layer. Light emission occurs again during this process. A certain proportion of the conduction band electrons will return to the valence band, allowing avalanche processes to repeat every time electrons cross the phosphor layer.

Light emission is pulsed, and an AC voltage is necessary for sustained operation of this light emission process. This voltage generally consists of a series of voltage pulses of peak voltage V_p , with alternating polarity. However, any AC voltage such as a sine wave will cause light emission, provided that the critical electric field is reached in the phosphor layer.

If a series of voltage pulses of the same voltage V_p is applied of only one polarity, then light emission will not occur.

The light emission from a typical device is shown in Figure 7.3 [7]. Here, the phosphor material is ZnS:Mn. ZnS is a well-known semiconductor having a valence band as well as a conduction band, with an energy gap of about 3.6 eV. Manganese is well known to possess a localized electronic ground state and an excited state.

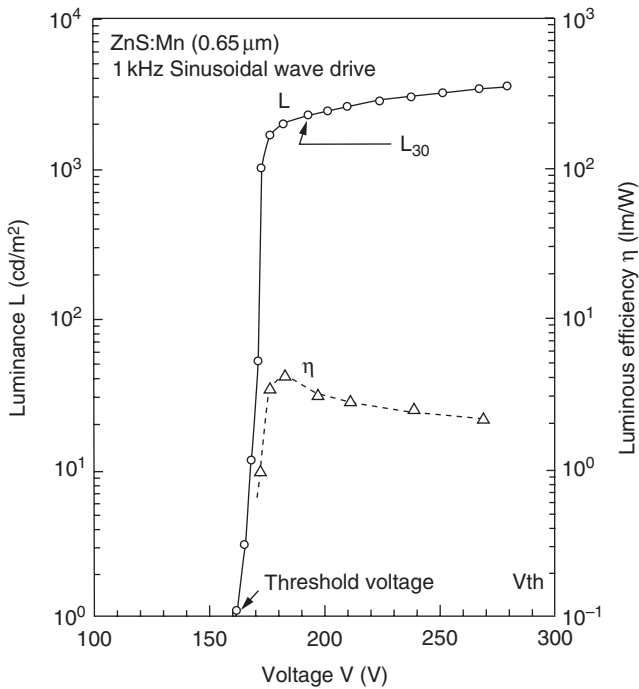


Figure 7.3 Brightness-voltage characteristic of ZnS:Mn EL phosphor measured in a thin film device similar to that shown in Figure 7.1. Note that the drive frequency is 1000 Hz. The device exhibits a sharp threshold voltage V_t characteristic near 160 V due to the critical electric field required for electron transport through the phosphor layer. The luminous efficiency is also shown (reprinted from Y. Ono, *Electroluminescent Displays, Series on Information Displays*, p. 10, copyright 1995, with permission from World Scientific Publishing Co. Pte Ltd)

Note the sudden onset of luminance at a specific threshold voltage V_t . This is inherent in an avalanche process, and is useful for display applications of TFEL. In a passive matrix flat panel TFEL display, partial voltages are present across ‘off’ pixels. If they lie below the threshold voltage, these partial voltages do not cause light emission, leading to high contrast flat panel displays. Details of multiplexing drive methods of a TFEL display are well described in the literature and will not be discussed further in this chapter [8].

It is now appropriate to describe the purpose of the dielectric insulator layer(s) in the EL device. For drive voltages below the threshold voltage, the phosphor layer is an insulator. However, for higher drive voltages, the phosphor layer is in an avalanche state, and therefore the voltage drop across this layer is clamped. Without the insulating layer, high currents could flow and damage the device. The dielectric layer limits the maximum current flow to the phosphor layer according to the general relationship

$$I = C dV/dt \quad (7.1)$$

where C is the effective dielectric layer capacitance per unit area and V is applied voltage (assumed to be larger than the threshold voltage).

An equivalent circuit of a TFEL device is shown in Figure 7.4. A capacitor C_i is connected in series with two back-to-back zener diodes. C_i represents the effective dielectric

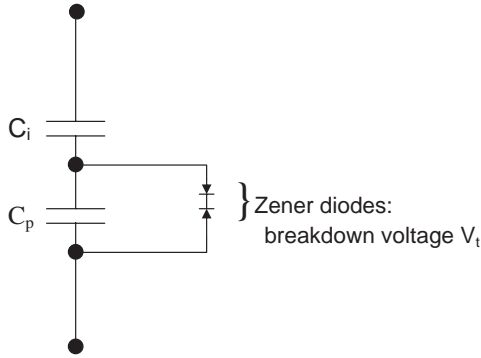


Figure 7.4 Equivalent circuit of TFEL device showing insulator capacitance C_i (note that this represents the series capacitance of both dielectric layers if two layers are present), C_p the phosphor layer capacitance, and phosphor breakdown voltage V_t represented as the zener diode turn-on voltage in reverse bias

capacitance per unit area of the TFEL device, and the back-to-back zener diodes represent the phosphor layer. The zener diode voltage represents the phosphor threshold voltage V_t (phosphor) and is determined by the critical electric field across the phosphor layer for avalanching to occur as well as the phosphor layer thickness.

It is experimentally determined that the brightness of an EL device is substantially proportional to the amount of charge per unit area that flows across the phosphor layer during each voltage pulse, as well as to the frequency of these pulses. The charge flowing through the phosphor layer flows only for applied voltages that exceed V_t and is determined from

$$Q = C_i(V - V_t) \tag{7.2}$$

where V_t is the threshold voltage and V is the applied voltage. Clearly, a high capacitance dielectric is desirable to maximize the transferred charge through the phosphor of the EL device and hence its brightness.

We know that

$$C_i = \epsilon_0 \epsilon_d / d \tag{7.3}$$

where d is the dielectric thickness and ϵ_d is the relative dielectric constant of the dielectric material. For this reason, high dielectric constant dielectric materials play an important role in high performance EL devices. In addition, the thickness of the dielectric layer needs to be minimized, but this thickness may be much higher for materials with high dielectric constants. For example, a 20 micron barium titanate-based layer having relative dielectric constant of 2000 will actually provide a value of C_i that is almost 4 times higher than a 0.4 micron alumina layer having a dielectric constant of 11. Now, $Q = C_i(V - V_t)$ will be higher, and the maximum EL brightness will increase.

Below the threshold voltage, the TFEL device, having capacitance C_{EL} per unit area, consists of two capacitors in series, represented by C_p (the phosphor capacitance per unit area) as well as by C_i (the insulator capacitance per unit area). As a result, the applied voltage V_a is divided as V_p across C_p and V_i across C_i according to the following equations:

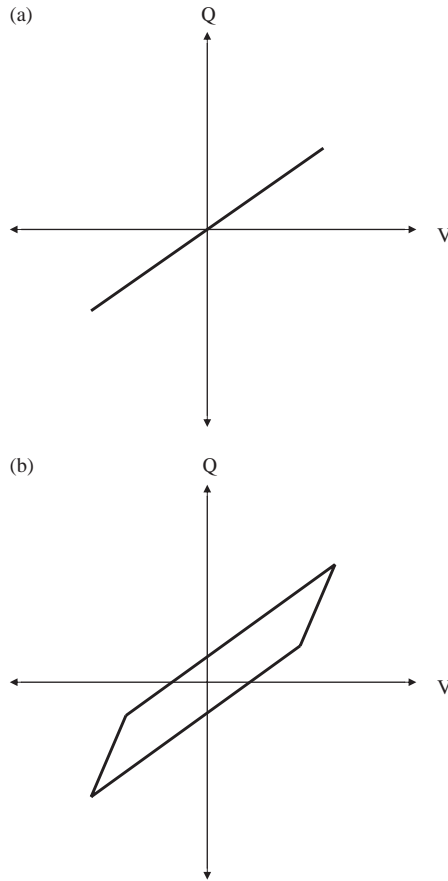


Figure 7.5 Q-V relation for EL devices operating (a) below and (b) above threshold voltage. Note the abrupt change in slope above the threshold voltage when avalanching in the phosphor layer occurs

$$V_p = V_a(C_i/(C_i + C_p)) \quad (7.4a)$$

$$V_i = V_a(C_p/(C_i + C_p)) \quad (7.4b)$$

with

$$C_{EL} = C_i C_p / (C_i + C_p) \quad (7.4c)$$

Once V_a reaches V_t , the EL device capacitance C_{EL} increases to C_i , and current flows through the phosphor layer. This results in power dissipation and transferred charge.

Figure 7.5 shows the relationship between transferred charge and applied voltage for an EL device operating below and above threshold voltage.

Note that below threshold voltage, the relationship follows the simple equation $Q = CV$ (Figure 7.5(a)). The Q-V plot is a straight line having slope C_{EL} , since C_{EL} represents the series combination of C_i and C_p , and there is no power consumption.

Above threshold, power consumption will occur as charge flows across the phosphor layer. This results in an area inside the Q-V plot (Figure 7.5(b)). This area precisely determines the electrical energy dissipated in the TFEL device per cycle. There are now two different slopes in the Q-V plot. The smaller slope is the same slope as observed in Figure 7.5(a). The larger slope is obtained when the electric field across the phosphor layer has reached the critical field, and therefore the voltage across the phosphor layer is clamped. Therefore, the larger slope is equal to C_i , the insulator capacitance.

As the voltage is increased further, the loop becomes larger as more charge is driven through the phosphor layer in each cycle. The additional applied voltage falls across the dielectric layer(s), and this dielectric must be capable of supporting the desired operating voltage.

The total charge that flows through the EL device may now be evaluated as the change in $Q = 2C_i(V_a - V_t)$, where V_a is the applied voltage, as the voltage goes from $-V_a$ to $+V_a$. Hence during one full cycle, the total charge that flows across the phosphor is

$$Q_{tot} = 4C_i(V_a - V_t).$$

The energy dissipated in one cycle is

$$[Q_{tot}] \times [E_{phos}] \times [d_{phos}]$$

where E_{phos} is the critical field in the phosphor layer and d_{phos} is the phosphor layer thickness. Hence the power dissipated is

$$P = 4C_i(V_a - V_t)[E_{phos}] \times [d_{phos}]f \tag{7.5}$$

where f is the frequency of the applied voltage.

A convenient way to measure these parameters is to use the Sawyer–Tower circuit method [9] to plot the charge-voltage curve. The charge is derived from a small voltage across a sense capacitor C_s inserted in series with the EL device such that the voltage drop across the sense capacitor V_s is always much smaller (about 100 times smaller) than the voltage drop across the EL device (Figure 7.6).

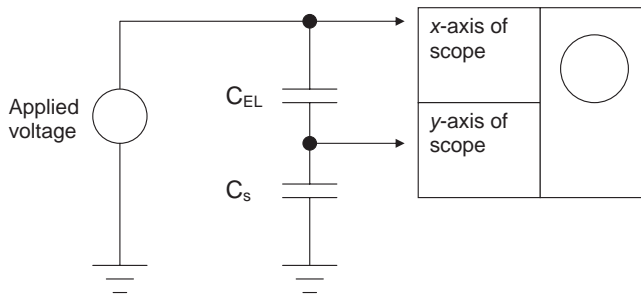


Figure 7.6 Sawyer–Tower Circuit showing the sense capacitor in series with the EL device. The sense capacitor is chosen to be approximately 100 times larger than the EL device capacitance

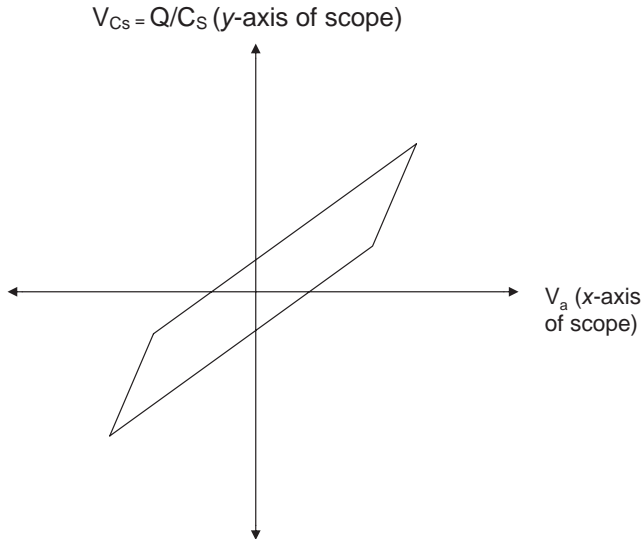


Figure 7.7 Sawyer-Tower output trace showing the charge vs. applied voltage relationship for an EL device. The charge is derived from the voltage across a sense capacitor according to $Q = C_s V_s$, and is plotted vs. applied voltage V_a

The x -axis of the oscilloscope is connected to the applied voltage, which is almost identical to the sample voltage, and the y -axis measures V_s . The oscilloscope is used in $x - y$ mode.

The shape of the oscillogram is therefore that of the QV loops (Figure 7.7). For a set of different applied voltages, the QV loops as well as the sample brightnesses in cd/m^2 are recorded.

The area A inside the loop on the oscillogram multiplied by the frequency f of the applied voltage is the electrical power dissipated. Therefore, from Equation 7.5:

$$P = 4C_i(V_a - V_t)[E_{\text{phos}}] \times [d_{\text{phos}}]f$$

The following information can now be obtained:

- capacitance of EL device below threshold;
- capacitance of EL device above threshold;
- degree of symmetry of turn-on characteristic for positive and negative-going voltages;
- threshold voltage;
- sharpness of threshold voltage;
- electrical power dissipation using loop area of QV loop;
- device efficiency in **lumens per watt** may be obtained by dividing the optical power emitted by the EL device (expressed in lumens) by the electrical power P dissipated (watts).

The efficiency plot in Figure 7.3 may be obtained using the Sawyer–Tower method. Therefore, this is a powerful tool in analysing and understanding EL device performance.

7.4 ELECTROLUMINESCENT PHOSPHORS

The first high performance phosphor material and still the material that has received the most study is ZnS:Mn. ZnS, a II-VI semiconductor with an energy gap of 3.6 eV. [10]. There are two structural variants, namely a cubic phase and a hexagonal phase. However, these two phases differ only in terms of second-nearest neighbors, and both phases are excellent EL phosphors. In either phase, each Zn^{2+} ion is coordinated by 4 S^{2-} ions in a tetrahedral configuration. ZnS is a relatively stable sulfide in that it may be stored in ambient atmospheric conditions without degradation. However, it does require moisture protection when it is subjected to high electric fields in an EL device. This may be due to the field-assisted dissociation of water to form OH-ions that hydrate the ZnS material.

The EL phosphor ZnS:Mn is more correctly described as $\text{Mn}_x\text{Zn}_{(1-x)}\text{S}$ with x in the range of 0.005 to 0.02. The dopant Mn provides the observed yellow luminescence, and Mn as a 2^+ ion substitutes effectively for Zn^{2+} ions. This is achieved since both Zn and Mn are 2^+ ions, have similar ionic radii. (radius of $\text{Zn}^{2+} = 0.74$ nm, radius of $\text{Mn}^{2+} = 0.8$ nm) and are able to bond in a tetrahedral configuration. Mn, being a transition metal, has an unfilled inner shell or 3d shell, which gives rise to a ground state as well as an excited state.

It is important to note that the electronic transition from excited state to ground state generates a photon, but it does not affect the charge on the Mn^{2+} ion, which remains at 2^+ throughout this transition. The luminescent process is therefore not a charge transfer process, whereas the luminescence in other well-known ZnS phosphors, such as CRT phosphors ZnS:Cu and ZnS:Ag, is a charge transfer processes. Here, an electron falls from a higher energy state elsewhere in the phosphor and is accepted by the Cu^{2+} or Ag^{2+} dopant. This results in a Cu^{1+} or Ag^{1+} state, and the luminescence results from the transfer of the electron to the metal ion, which is a trap-assisted electron-hole recombination process. However, the Mn^{2+} ion luminesces without charge transfer. This distinction is very important, as only luminescent centers that function without charge transfer generally exhibit good EL properties, including high efficiency and long life.

When a high electric field is applied to the EL phosphor, the avalanche process takes place, and the hot electrons generated impact-excite the Mn centers. This impact-excitation process is characterized by an impact excitation cross-section, which describes the success rate of hot electrons exciting the Mn^{2+} ion. Mn has a large impact excitation cross-section in ZnS, and the applied electric field does not modify the efficient recombination process that takes place within the Mn^{2+} ion.

Trap-assisted electron-hole luminescence processes are not useful for high field EL, since the electric fields established to cause avalanching, as well as the acceleration of electrons to become ‘hot’, sweep free carriers away and prevent their recombination. Therefore electrons that normally recombine and generate photons in CRT phosphors, such as ZnS:Cu and ZnS:Ag, are driven back and forth between the phosphor/dielectric interfaces under EL drive conditions, and eventually may find their way back to the valence band via non-radiative trapping. For this reason, ZnS:Cu and ZnS:Ag are not used as thin film EL phosphors.

Table 7.1 Important sulfide and oxide EL phosphors showing their composition color, CIE coordinates and reported luminous efficiency. Note that in many cases a range of efficiency values is given, since various values are known depending on the device structure and preparation conditions

Phosphor	Color	CIE coordinates	Efficiency, l/W	Reference
1) ZnS:Mn	yellow	0.5, 0.5	3–10	[14]
2) ZnS:Tb	green	0.32, 0.6	0.5–2	[14]
3) SrS:Ce	blue-green	0.19, 0.38	0.5–1.5	[14]
4) SrS:Ce, Eu	white	0.41, 0.39	0.4	[14]
5) BaAl ₂ S ₄ :Eu	blue	0.135, 0.1	0.5–1.5	[16]
6) SrGa ₂ S ₄ :Eu	green	0.226, 0.701	1–2	[12]
7) Zn ₂ SiO ₄ :Mn	green	0.2, 0.7	0.5–2	[17]
8) Zn ₂ Si _x Ge _{1-x} O ₄ :Mn	green	0.2, 0.7	1–3	[17]
9) ZnGa ₂ O ₄ :Mn	green	0.08, 0.68	1–2	[17]
10) Ga ₂ O ₃ :Eu	red	0.64, 0.36	0.5–1	[15]
11) Y ₂ O ₃ :Mn	yellow	0.51, 0.44	10	[18]
12) Y _x Ga _y O ₃ :Mn	yellow	0.54, 0.46	10	[18]
13) Y _x Ge _y O ₃ :Mn	yellow	0.43, 0.44	10	[18]

Mn²⁺ ions may also generate green luminescence in other EL phosphor hosts. An effective oxide phosphor Zn_{2-x}Mn_xSiO₄ [3] relies on the same inner-shell radiative transition as in ZnS:Mn. The color of the luminescence is green instead of yellow, due to a change in the crystal field surrounding the Mn²⁺ ion.

Other efficient EL luminescent centers exist. Both sulfide and oxide compounds exist. Nitride and fluoride host materials have also been identified, but EL performance has not been as successful to date. Eu²⁺ exhibits excellent blue luminescence in BaAl₂S₄ phosphors. Eu²⁺ has a 4f-4d transition. Ce³⁺ exhibits bright green-blue luminescence in SrS phosphors, and Ce³⁺ has a 4f-4d transition.

A large number of host materials are available from modifications of other hosts. For example, Mg_xZn_{1-x}S:Mn phosphors exhibit a blue-shift compared to ZnS:Mn material, which gives this phosphor a peak wavelength below 580 nm [11]. SrGa₂S₄:Eu is a green EL phosphor [12] not the same as, but related to, BaAl₂S₄:Eu. Zn₂Si_{1-x}Ge_xO₄:Mn represents a family of green oxide phosphors with higher brightness and efficiency and relatively low processing temperature requirements compared to other oxide phosphors, such as Zn₂SiO₄:Mn [13].

ZnS:Tb is also a bright green phosphor [14] that is unusual in that Tb is not readily soluble in the ZnS host due to the incompatible size and charge of the Tb³⁺ ion. A charge compensation co-activator, such as F or O, can play a role in improving the performance of these phosphors.

Eu³⁺ exhibits bright orange-red luminescence in Ga₂O₃ host material. Eu³⁺ has a 4f-4f transition. This phosphor is unusual in that it works in an amorphous phase, demonstrating that crystallization is not a requirement for all EL phosphors. Eu³⁺ is not size-compatible with the Ga cations in the host material [15].

A list of some important EL phosphors together with their properties is shown in Table 7.1.

7.5 DEVICE STRUCTURES

The range of reported TFEL structures includes:

- glass substrate thin film dielectric EL
- thick film dielectric EL
- ceramic sheet dielectric EL
- thick rear film top dielectric EL
- sphere-supported thin film EL

These structures will now be reviewed in detail.

7.5.1 Glass substrate thin film dielectric EL

This device structure is shown in Figure 7.1. The most successfully commercialized structure, it relies on thin film processing for all the layers, as well as the superior properties of glass substrates in terms of smoothness, thermal stability and transparency. Aluminosilicate glass used in Active Matrix LCD manufacturing is an excellent substrate material.

One key feature of this structure is the need for high-quality, thin film dielectrics. These may be grown by RF sputtering or by ion-assisted deposition. From Equations 7.2 and 7.3 it is clear that we wish to use dielectric materials with high dielectric constants, which also exhibit high breakdown voltages. Binary oxide dielectric materials include silica, alumina, silicon nitride and yttrium oxide. These may be grown by RF sputtering or by electron-beam evaporation (Table 7.2).

With the exception of SiO_2 , whose dielectric constant is too low, these materials are all suitable for EL dielectrics. Nevertheless, the desire for higher dielectric constant materials has motivated the development of more complex oxide and oxynitride dielectric materials (Table 7.3).

In the thin film double-insulating-layer TFEL device structure of Figure 7.1, the choice of dielectrics is limited. This comes about owing to the desire for self-healing behavior of the completed EL device. Micron- or submicron-sized weak spots in the dielectric or phosphor layers generally exist. These may occur due to imperfections in the layers such as pinholes, impurities, particulates or substrate non-uniformities. The result is that these weak

Table 7.2 Dielectric properties of binary oxide dielectrics [19]

Oxide	Dielectric constant	Breakdown field ($\times 10^8$ V/m)
SiO_2	4.0	6
Al_2O_3	8	5
Si_3N_4	8	6–8
Y_2O_3	12	3–5

Table 7.3 Complex oxide dielectrics [19]

	Dielectric constant	Breakdown field ($\times 10^8$ V/m)
SiAlON	6	7
BaTa ₂ O ₅	22	3.5
SrTiO ₃	140	1.5–2
BaTa ₂ O ₆	22	3.5
PbTiO ₃	150	0.5

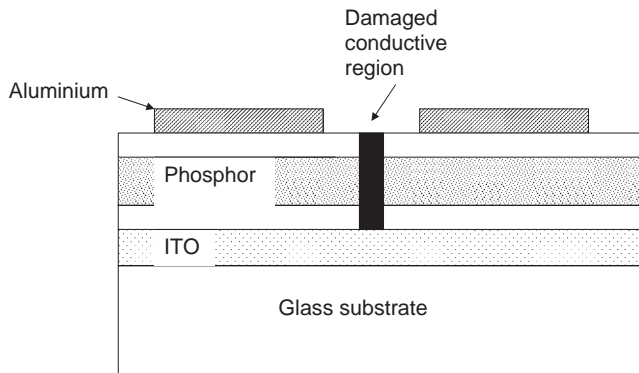


Figure 7.8 Self-healing mechanism in which a defect in the EL stack is isolated from the remaining EL device through melting of the electrode layer in thin film double-insulating-layer TFEL device. The front electrode is ITO, and the rear electrode is aluminium. The small thickness (100nm) and relatively low melting point of aluminium (660 °C) allow self-healing

spots are susceptible to catastrophic dielectric breakdown at voltages that are required for the normal operation of the device.

Self-healing behavior allows this highly localized breakdown to occur without causing the overall failure of the EL device. The key is to allow at least one of the electrodes to fail around the defect, thereby isolating it from the remainder of the device (Figure 7.8). Note that heat is created at the defect as leakage current flows, and the weakest electrode opens like a protective fuse around the defect. Since the size of this open region is in the micron scale, it is not visible to the naked eye in a working EL display.

Self-healing requires a suitable combination of dielectric layers and electrode materials in suitable thickness ranges. For example, if the dielectrics are damaged by heat before the electrode has a chance to open, then propagating breakdown will occur. Here, the heat causes a hot spot to travel along a random path within the EL device and the entire EL device will be destroyed. If the aluminium layer of Figure 7.8 were too thick, this could occur. If the aluminium were replaced by a high melting point metal such as tungsten, this might also occur. Note that the transparent ITO electrode in Figure 7.8 would not self-heal because ITO is a high melting point oxide material. In addition, the ITO is sandwiched between other materials that conduct heat away from it.

Almost all commercially successful EL devices to date have taken advantage of the self-healing properties of aluminium thin film rear electrodes.

In addition, the choice of dielectric also determines the ability of self-healing to function. Unfortunately, the high dielectric constant dielectric materials such as BaTiO_3 are chemically far less stable than simpler dielectrics such as Al_2O_3 , and catastrophic dielectric degradation may occur before the rear electrode is able to become an open circuit around the defect.

7.5.2 Thick film dielectric EL

This device structure was first demonstrated using thick film capacitor dielectric material made by the green sheet process [20, 21]. Here, a powder of high dielectric constant material, such as BaTiO_3 , may be mixed with additives and combined with an organic binder to form a slurry. This slurry is then doctor-bladed to form a green tape. This tape may then be metalized with a thick film metal layer, and stacked together with more dielectric layers for further support to form a green laminate. Sintering results in a dense and rigid metal/ceramic plate. If a phosphor layer and a transparent top contact are deposited on the thick film laminate, then an EL device may be formed (Figure 7.9).

A substantial development program was initiated in 1989, culminating in high performance Thick Dielectric EL (TDEL) technology [2] aimed at television applications. Several improvements were made to the process and structure (Figure 7.10). The supporting material is replaced with a glass sheet. Both the thick film metalization and the thick film dielectric layers are screen printed on the glass substrate. In order to create a smooth surface for the subsequently applied thin film layers, the thick film dielectric layer must be planarized to avoid phosphor defects. The phosphor layer and transparent contact may be grown by vacuum deposition processes, such as evaporation or sputtering.

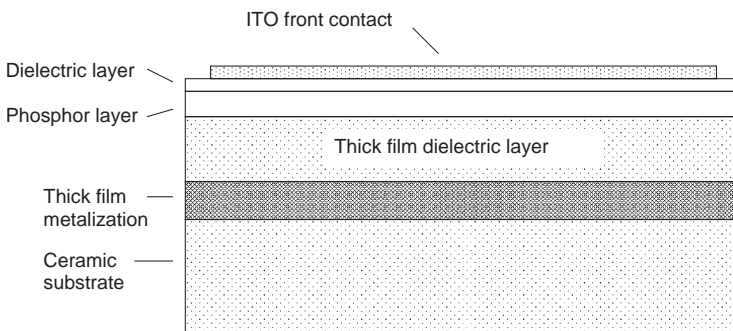


Figure 7.9 Thick film ceramic dielectric EL device. The thin film EL phosphor and front electrode are grown on a thick film laminate to form a robust EL device. This structure has the advantage of a thick dielectric layer that is far less sensitive to defects than thin film dielectric layers. As a result of the high dielectric constant of the dielectric layer, high charge injection levels may be reached that permit higher phosphor brightness. In addition, more efficient light out-coupling than for the structure of Figure 7.1 may be obtained

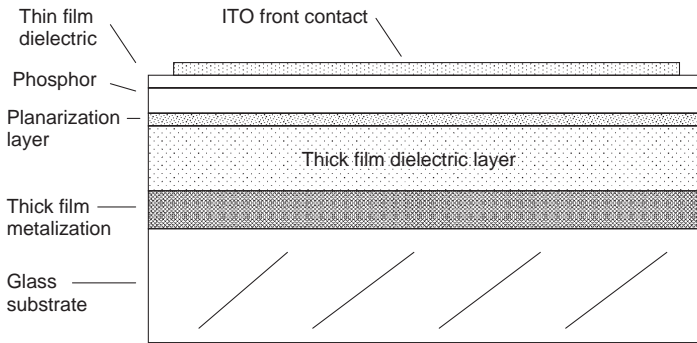


Figure 7.10 Thick dielectric layer EL device structure. A glass substrate supports a printed, thick film metallization, followed by a screen-printed thick film dielectric layer. In order to provide a smooth surface for the phosphor layer, a planarization layer is provided

The key advantage of this structure is the dielectric layer which is much more robust than thin film dielectrics. In the thickness range of about 10–20 microns, this layer is not prone to pinholes, and in all cases, self-healing is achieved should defects in any of the layers be present.

Also of significance is the superior brightness and efficiency of this structure compared to thin film dielectric EL. Brightness is increased since the relative dielectric constant of the dielectric layer may be 2000 or more, whereas the dielectric constants of self-healing thin film dielectrics are generally limited to under 20. From Equations 7.2 and 7.3, the transferred charge and hence the brightness of the EL device is proportional to ϵ_d/d . Although d is larger in TDEL devices than typical thin film dielectric thicknesses, which are in the submicron range, this is more than compensated for by the large increase in ϵ_d , from 10 to 20 in typical thin film dielectrics that offer self-healing behavior, to 2000 or more.

An additional factor in the improvement has to do with the onset of dielectric breakdown in thin film dielectric layers. For voltages above threshold, the electric field builds up rapidly in the dielectric layers. This is due to the field clamping behavior in the phosphor layer, which is in avalanche mode, thereby preventing additional voltage drop in the phosphor layer. At a critical applied voltage, one (or both) of the dielectric layers will reach its breakdown field. At this point, catastrophic failure of the EL device is likely. To prevent this condition in normal operation, applied voltages are kept well below this point, which establishes a limit to the display brightness. On the other hand, the use of a thick dielectric layer allows substantially higher charge transfer across the phosphor layer without dielectric breakdown. The electric field in the phosphor layer is low even during high brightness operation. For example, with a 15 micron BaTiO_3 thick film dielectric, the dielectric electric field at an operating voltage 60 V above threshold has increased from the threshold field by only $60/15 \times 10^{-6} = 4 \times 10^6$ V/m. In the case of a thin film dielectric, such as a 0.2 micron layer of Al_2O_3 , the field increase from threshold will be $60/0.2 \times 10^{-6} = 3 \times 10^8$ V/m. Note that this is close to the breakdown field of Al_2O_3 . The relative charge transfer for the thick BaTiO_3 dielectric having $\epsilon_d = 2000$ compared to the thin Al_2O_3 dielectric having $\epsilon_d = 11$ at this operating point will be:

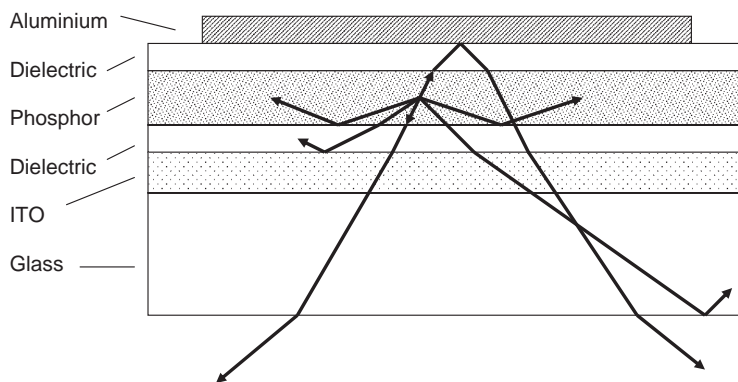


Figure 7.11 Optical wave-guiding in glass substrate EL device. Light rays that exceed the critical angle will be guided through the glass. The phosphor layer and insulating layers also suffer from total internal reflection as illustrated. Note that light from the phosphor can also reflect off the rear aluminium electrode and add to the device brightness

$$(2000/11) \times (0.2/15) = 2.42.$$

Therefore, the allowable charge transfer and hence the brightness are increased.

Another advantage to the thick film approach is optical out-coupling. Figure 7.11 [22] shows generated light rays within a glass substrate thin film EL device. The luminescent centers in the phosphor emit light with spherical symmetry. However, the light is both internally reflected and refracted by interfaces between layers as well as by the substrate. Note that the aluminium rear electrode reflects light forwards, which adds to the brightness. Light that exceeds a critical angle between the phosphor layer and the insulating layer will be internally reflected inside the phosphor layer, and light guiding will occur. Since grain boundaries and other defects in the phosphor layer generally exist, this light will tend to be scattered out or will be absorbed within the phosphor layer before it can travel more than several tens or hundreds of microns. Some light scattering also occurs for light within most dielectric layers.

On the other hand, light that exceeds a critical angle between the glass substrate and air will be internally reflected and can travel substantial distances as a guided wave in the glass until it emerges at the edges of the EL device. The critical angle can be obtained from Snell's Law:

$$\sin\theta_{\text{air}}/\sin\theta_{\text{glass}} = n_{\text{glass}}/n_{\text{air}}$$

At the critical angle, $\sin\theta_{\text{air}} = 1$. For $n_{\text{glass}} = 1.5$ and $n_{\text{air}} = 1$, $\theta_{\text{glass}} (\text{critical}) = 42^\circ$. The fraction of light that now emerges is given by 42° :

$$4\pi r^2 \int_0^{42^\circ} \sin\theta d\theta \left(\frac{1}{4\pi r^2} \right) = 26\%$$

This neglects absorption losses in the phosphor and dielectric layers, and assumes that light from the thin film layers does reach the glass.

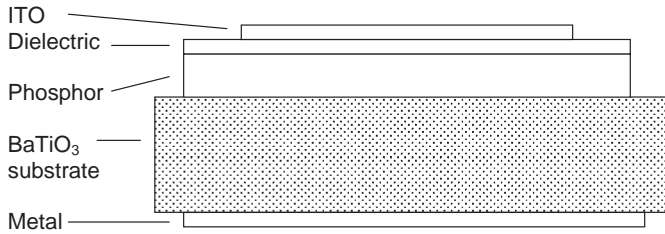


Figure 7.12 Ceramic Sheet Dielectric EL device showing self-supporting substrate design. Rear electrode may be a thin film metallization. Due to the brittle nature of the thin ceramic sheet, only small-area devices are practical. The barium titanate substrate is typically 200 microns in thickness

In a thick film dielectric EL device, there is no glass layer in the EL stack, and light scattering from the thick and thin films will directly cause light to be emitted. The result is that a more efficient out-coupling of light is enabled than in glass substrate EL devices. Modeling this is complicated by the lack of precise scattering parameters, which depend on the surface roughness and dielectric properties of the thick film dielectric layer. It is found that externally measured EL efficiency in glass-based devices has reached 7 lumens per watt. However, thick dielectric layer EL efficiencies of over 10 lumens per watt are possible.

There are other interesting aspects of thick film EL, which will be covered in the section on full-color EL architectures.

7.5.3 Ceramic sheet dielectric EL

Minami reported the use of a self-supporting ceramic sheet for an EL device [3]. This method takes advantage of the increased thickness allowable for high dielectric constant insulators such as BaTiO_3 (Figure 7.12).

The advantage of this structure is the high temperature capability. Phosphors grown on the barium titanate may be sintered at temperatures in excess of 1000°C , and both the front and rear electrodes are generally deposited after the high temperature processing step.

This architecture is useful for small light emitting areas, since thin BaTiO_3 ceramics are fragile. A feature of these devices is the ability to contact the device with exposed top and bottom connections. The ceramic sheet is cast and fired before the phosphor film is applied, and may be polished to allow for a smooth phosphor layer. If high purity BaTiO_3 material is used, the substrate material can permit high temperature processing ($\sim 1000^\circ\text{C}$) of phosphor thin films, which glass substrates cannot tolerate. This has led to the use of this architecture for the development and evaluation of a wide range of oxide EL phosphors, which often require high processing temperatures.

7.5.4 Thick rear dielectric EL devices

Another interesting EL device architecture involves the use of a thick film dielectric on top of the EL phosphor. In this architecture, a glass substrate is used, followed by a transparent electrode, an interface layer, the phosphor layer and then a rear, thick film dielectric layer

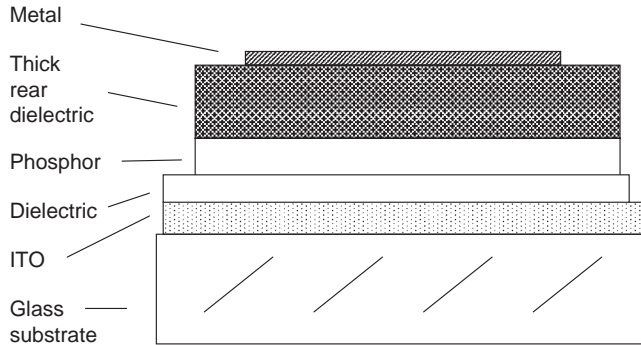


Figure 7.13 Rear Thick Dielectric EL Device. Note that the EL phosphor is grown on ITO-coated glass before the thick film dielectric is applied. The usual benefits of thick film dielectrics, including high charge transfer and excellent electrical ruggedness, may be realized by this structure

applied using a thick film process such as screen printing. The thick film must generally be fired to drive off the binders, and this must be accomplished without degrading the EL phosphor layer.

The device structure is shown in Figure 7.13. The noted merit of this approach [4] is to allow for high contrast: If the thick dielectric layer is dark in color, it will absorb ambient light that enters the EL device through the glass substrate and the thin film layers. This does decrease brightness since EL light is also absorbed, but contrast in bright ambient conditions may be much improved.

7.5.5 Sphere-supported thin film EL (SSTFEL)

This novel structure takes advantage of high dielectric constant ceramic spheres as a support for the thin film EL phosphor [5] (Figures 7.14 and 7.15). The use of spherical BaTiO_3 particles offers a low cost route to making a flexible EL device. The spheres may be manufactured by a spray drying process and after sintering, they are placed on a ceramic plate and phosphor is coated by sputtering. Following the phosphor annealing step, the spheres are embedded into a polymer sheet and electrodes are applied on either side of the plastic sheet. Note that a portion of each sphere protrudes from the plastic sheet on both sides, allowing intimate contact to the electrodes. The plastic therefore provides both mechanical support to hold the spheres together as well as flexibility. It also acts as an electrical insulator, preventing the upper and lower electrodes from shorting. The Al_2O_3 layers are sputtered sandwiching the phosphor layer in order to provide charge injection interfaces. Underneath the front ITO layer, a gold layer is deposited only on the polymer sheet in order to provide improved conductivity.

The barium titanate spheres used in the SSTFEL device comprise spray-dried BaTiO_3 spherical agglomerates with a diameter of approximately $60\mu\text{m}$. They are sintered before being phosphor coated (Figure 7.15).

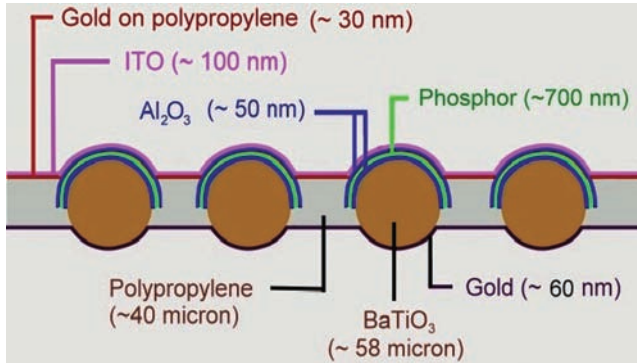


Figure 7.14 High dielectric constant BaTiO_3 spheres are sandwiched between upper and lower electrodes to form many individual TFEL devices that form a flexible sheet of light. BaTiO_3 spheres are coated with thin film interface layers and phosphor layer on the upper side and conductive electrode layers on both upper and lower sides

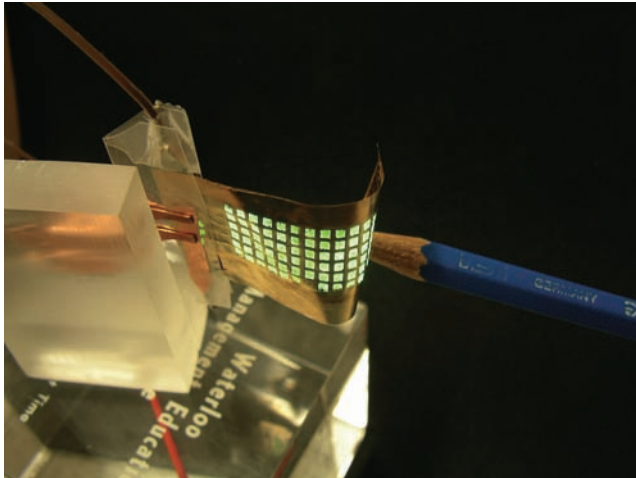


Figure 7.15 Working Flexible SSTFEL device. The green emission is obtained from oxide phosphor $\text{Zn}_2\text{Si}_{0.5}\text{Ge}_{0.5}\text{O}_4:\text{Mn}$. Note the high degree of flexibility obtained from this structure

7.6 EL PHOSPHOR THIN FILM GROWTH

A common feature of all these device types is the thin film phosphor layer, and a variety of growth techniques have been used to prepare high performance EL phosphors. These will be reviewed in the context of known EL phosphors.

7.6.1 Vacuum evaporation

Originally used to prepare $\text{ZnS}:\text{Mn}$ thin film phosphors, this technique involves heating solid $\text{ZnS}:\text{Mn}$ material in vacuum until it sublimates. This may be achieved using a tantalum

or tungsten boat in a vacuum chamber capable of 1×10^{-6} torr or lower base pressure. Alternatively, an electron beam source may be used. The substrate should be heated to approx. 200°C to decrease contamination during growth, and to yield a stoichiometric cation/anion ratio of 1:1 in the film. A high growth rate of 5 to 10 nm/s is appropriate.

7.6.1.1 Thick rear dielectric EL devices

Unfortunately, Mn will not evaporate congruently with ZnS. This means that the Mn concentration in the phosphor will vary as the deposition proceeds. The solution to this is to co-evaporate from two sources. For example, a ZnS source can be used in conjunction with a Mn metal source or a MnS source. Accurate rate control of these two sources is required.

7.6.1.2 Thick rear dielectric EL devices

Dual or multi-source evaporation is not always a desirable deposition approach for the following reasons:

- Source rate control is critical
- Source material must be replaced frequently
- Compositional uniformity over the substrate is not perfect and for large substrates, evaporation from point sources is not an economical way to grow uniform films.
- For these reasons, other deposition methods have been developed for EL phosphors.

7.6.2 Atomic layer deposition

This technique was originally developed by Suntola [23]. The deposition process was originally called atomic layer epitaxy (ALE), and was derived from molecular beam epitaxy (MBE). During the deposition of ZnS, for example, ALE takes advantage of the large difference between the weak bonding strengths of Zn–Zn or S–S bonds compared with the stronger Zn–S bond. The effusion cells containing S and Zn in the MBE machine are opened sequentially to allow either S or Zn atoms alone to be available to the substrate. At a suitable substrate temperature, only the Zn–S bonds are stable, and therefore only one monolayer of each atomic species is able to grow during each exposure to either Zn or S atoms. This is a self-limiting process, which can readily be shown. Varying the dose of the S or Zn atoms will not affect the growth rate, provided one monolayer can be formed.

MBE growth is not economically useful for production, and growth systems using the ALE principle have been developed for polycrystalline thin film growth. This technique is called Atomic Layer Deposition (ALD), which is often conveniently performed using compound starting materials. For ZnS growth, Dimethyl Zinc and H_2S molecules are convenient since they permit vapor streams of the precursor molecules to pass over the substrate surface in a low-cost deposition chamber. Due to the size of the starting molecules, as well as the

lack of single crystal growth, it may be difficult to achieve precisely one full monolayer of growth per exposure; however, high-quality films are nevertheless achievable.

The growth system now resembles a chemical vapor deposition (CVD) system. The CVD system is augmented by computer-controlled valves to allow the sequential growth process to occur, and it is also possible to place a large number of substrates into a CVD system: Since the growth rate of ALD material is self-limiting, a highly uniform film over a large number of substrates can be achieved, even if the flow rate of the precursor species varies significantly between substrates or as a function of position over a single substrate. On the other hand, the growth rate is typically slow (~ 0.1 nm/s), and production cost and throughput need to be carefully assessed.

High-quality, pinhole-free films are achievable due to the layer-by-layer growth process, and a large number of compounds, including ZnS, ITO, CdS, ZnO, MgO, SrS, BaS, CaS, GaAs, AlGaAs and Al_2O_3 , have been grown by ALD or ALE.

7.6.3 Sputter deposition

RF magnetron sputtering has become a standard way to deposit insulating compounds in optics electronics. It is ideal for production since it is scaleable and can cover generation 8 substrates for LCD production with excellent uniformity. It has therefore been applied to thin film phosphor deposition. Thin film EL phosphor sputtering targets are generally insulating and do require RF sputtering. However, in some cases, reactive sputtering may be used, in which case the target can be a metal alloy. The cations from the target then react with anions introduced as a gas in the plasma to form the phosphor.

One example of a sulfide EL phosphor will now be described, namely the $\text{BaAl}_2\text{S}_4:\text{Eu}$ blue-emitting phosphor.

This material was first prepared by Miura at Meiji University [24]. It is currently the most promising blue-emitting TFEL material. It was originally grown by a dual-source electron beam evaporation process, but sputtering has now been employed in industry to enable reproducible, large-area deposition. Sputter deposition was first attempted using a dual target method, in which BaS from one target was combined with Al from a second metal target [25].

Subsequently, this method was modified to permit sputter deposition from a single composite target [26]. This single target was made by combining both Al metal and BaS powder in a composite target, in which BaS powder was captured in pockets in a specially formed aluminium block. It was found that the precise ratio Al to Ba could be achieved by controlling the sulfur content of the gas introduced during sputtering. Eu may be incorporated in the BaS powder.

Most recently, a sputtering process developed at iFire uses a metal target, which contains an appropriate alloy of Al, Ba and Eu [27]. The formation of a sulfide thin film is achieved by reactive sputtering. Target stability and repeatability is now improved, since sputtering can no longer deplete any component in the target. In addition, target preparation is simplified since metal alloys are generally easier to fabricate and shape than sulfide compounds.

$\text{ZnS}:\text{Tb}$, $\text{Zn}_2\text{SiO}_4:\text{Mn}$, $\text{Zn}_2(\text{Si},\text{Ge})\text{O}_4:\text{Mn}$ and $\text{ZnGa}_2\text{O}_4:\text{Mn}$ green-emitting EL thin film phosphors, $\text{Ga}_2\text{O}_3:\text{Eu}$ red-emitting phosphors and a number of other sulfide and oxide phosphors have been prepared by sputter deposition (Table 7.1). Typical deposition condi-

tions are RF magnetron sputtering from a pressed ceramic target in an argon/oxygen gas mixture followed in most cases by a high temperature anneal step to recrystallize the phosphor.

7.7 FULL-COLOR ELECTROLUMINESCENCE

A major challenge in the development of thin film electroluminescence has been the achievement of full-color EL displays. A number of different approaches have been pursued, and will be reviewed.

7.7.1 Color by white

The simplest approach to the fabrication of a full-color EL displays is to take advantage of the approach used in color liquid crystal displays. Here, trichromatic, white light is filtered through plastic dye filters positioned at appropriate pixels to create red, green or blue light emission. This means that the EL pixels must be surface-emitting rather than emitting through a sheet of glass, and must be positioned adjacent to the filters. This may be achieved conveniently using thick dielectric EL structures, or any structure that places the supporting substrate behind, rather than in front of, the thin film phosphor layer. Color-by-white architecture is shown in Figure 7.16.

A bright, trichromatic EL white phosphor is required, since color filtering lowers the resulting EL brightness [28].

In a similar structure using thin film dielectrics, the white-emitting phosphor SrS:Ce, Eu was used by Mita *et al.* Ce provides green and blue emission in SrS, and Eu provides red emission. Alternatively, a multilayer phosphor stack can be used to obtain a white emission.

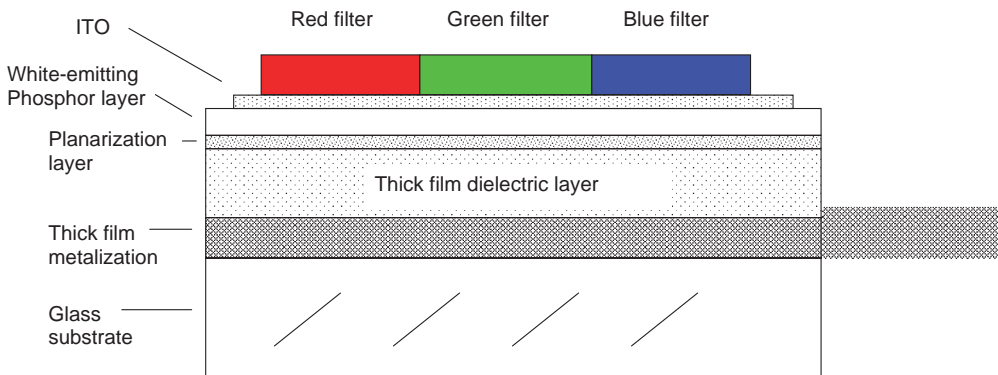


Figure 7.16 Color by white EL display structure showing application of color filters to a white-emitting EL phosphor. The thick film dielectric structure is illustrated. Note that the placement of the color filters directly against the thin film stack is essential to avoid parallax. For simplicity, thin film dielectric layers are omitted in the figure

These approaches have been tested [29]. Unfortunately they suffer from poor brightness, and screen brightnesses of under 20 cd/m^2 are typically achieved. Although white light filtering works well for LCD displays, the loss of light by filtering in EL is not practical. This is explained by the much higher white light brightness and efficiency in LCD backlights: A typical cold-cathode LCD backlight operates at 60l/W, whereas white EL phosphors achieve under 10l/W. Color by white does have the advantage of simplicity and good contrast. However, it has generally been abandoned in favor of more efficient schemes.

7.7.2 Patterned phosphors

The amount of filtering may be substantially reduced if phosphor patterning is used. For example, CaS:Eu and SrS:Ce phosphors may be spatially patterned. In this architecture, red light is emitted by CaS:Eu phosphors without the need for further filtering to produce red pixels. The green and blue pixels are achieved by filtering the phosphor SrS:Ce with green and blue filters, respectively. This increases overall efficiency due to the reduction of light sacrificed to filter absorption.

A disadvantage of this approach is the requirement for both patterned filters as well as patterned phosphors, which adds to the cost and complexity of the design. In principle, a full-color display could be fabricated without any filtering if suitable red, green and blue EL phosphors are used. Drawbacks to this approach include the patterning and processing of three separate EL phosphors.

7.7.3 Color by blue

A newer approach pioneered by iFire has been the use of fluorescent dye materials that may be efficiently stimulated with blue light. Here, blue EL emission from the BaAl_2S_4 :Eu EL phosphor is used to excite green and red light emission from dye-containing materials that are placed directly in front of the phosphor layer to create green and red sub-pixels. The blue pixels are derived from the blue phosphor directly, with or without a blue color filter [30] (Figure 5.17).

The color by blue approach has some desirable features as it lowers production cost since the EL phosphor layer does not require patterning. It provides highly uniform and predictable luminance levels from all pixels, since the electrical operating characteristics are the same for all the color pixels. Although these benefits also apply in the case of color by white, the efficiency and brightness are now much higher.

There are also some drawbacks to this approach. There is a certain loss of light by the conversion process. This occurs due to imperfect absorption and re-emission through the dye layers, and well as through the fundamental photon energy decrease as blue light is down-shifted in energy in the dye materials. In addition, exposure of the dye materials to ambient light must be controlled: The green and red dyes must not be exposed to blue ambient light, otherwise they will fluoresce and greatly degrade display contrast. This may be prevented using filters applied to the front of the EL display. Contrast will be controlled by the details of the dye characteristics as well as filter characteristics, and the fundamental advantage of the transparent EL phosphor layer in enabling high contrast EL displays is now highly dependent on the front layers of the device.

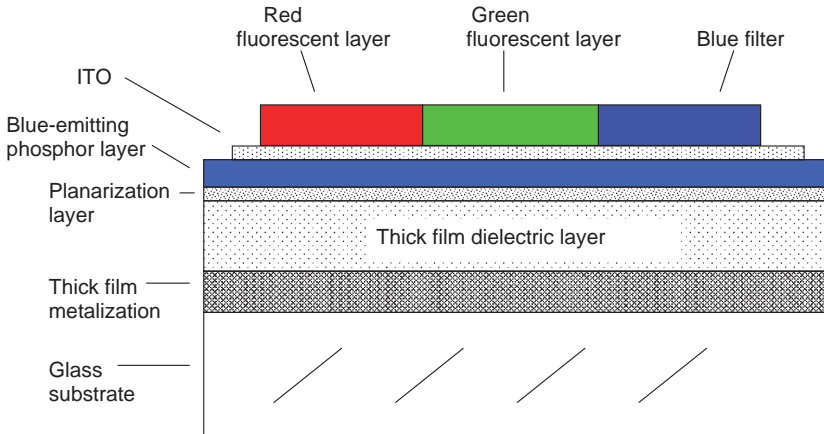


Figure 7.17 Color-by-blue approach to full-color electroluminescence. Only one blue-emitting phosphor layer is required. Blue light stimulates red and green light emission from dye-containing polymer coatings in front of the phosphor. For simplicity, thin film dielectric layers are omitted in the figure

Nevertheless, the color by blue approach has allowed the best full-color EL display performance to be achieved, a 760×1280 full-color EL display with excellent color gamut and brightness (iFire Inc).

7.8 CONCLUSIONS

From early monochrome EL displays in the 1980s to full-color EL displays of 2006, the field of thin film EL has been active. In particular, the achievement of a wide range of new EL phosphor compounds has been impressive, particularly in that new EL phosphor materials cannot be modeled and then fabricated due to our incomplete understanding of hot electron processes, as well our lack of models of electric field effects on luminescent centers. Phosphor compounds for thin film EL devices are almost always distinct from successful powder phosphors used in fluorescent lamps and CRTs.

The innovative range of device structures is also particularly noteworthy. Ceramic, glasses, thick films thin films, as well as a wide range of fabrication processes and methods, have been developed for thin film EL materials.

The commercial availability of LCD and Plasma display panels has currently reduced the large-scale development of thin film EL devices. However, the desire for a truly solid state flat panel is still there. Organic light-emitting diode (OLED) displays are another development that has taken attention away from thin film electroluminescence. However, OLED displays have not yet reached performance levels that allow them to compete in most flat panel display markets.

This film electroluminescence will continue to be a fascinating technology and further developments in fundamental physics, materials, fabrication techniques and architectures will continue.

REFERENCES

1. Russ M.J. and Kennedy, D.I. (1967) *J. Electrochem. Soc.* **114**: 1066.
2. Wu, X., Carkner, D., Hamada, H., Yoshida, I, Kutsukake, M. and Dantani, K. (2004) *SID Digest* **35**: 1146.
3. Minami, T., *et al.* (1991) *Jpn. J. App. Phys.* **30**: T. L117.
4. Heikenfeld, J., Jones, R.A. and Steckl, A.J. (2003) *SID Digest* **34**: 1110.
5. Xiang, Y., Kitai, A.H. and Cox, B. (2005) *J. Soc. Info. Display* **13**: 493.
6. Ono, Y.A. (1995) *Electroluminescent Displays*, Singapore: World Scientific Press, p. 9.
7. Ono, Y.A. (1995) *Electroluminescent Displays*, Singapore: World Scientific Press, p. 10.
8. Ono, Y.A. (1995) *Electroluminescent Displays*, Singapore: World Scientific Press, p. 98.
9. Ono, Y.A. (1995) *Electroluminescent Displays*, Singapore: World Scientific Press, p. 34.
10. Ono, Y.A. (1995) *Electroluminescent Displays*, Singapore: World Scientific Press, p. 44.
11. Mikami, A. (1997) *Proc SID Int. Symp Dig.* **28**: 851.
12. Yano, Y., Oike, T. and Nagano, K. (2002) *Proc. EL2002*, Gent, Belgium, p. 225.
13. Xiao, T., Kitai, A.H., Liu, G. and Nakua, A. (1997) *SID Digest* **28**: 415.
14. Ono, Y.A. (1995) *Electroluminescent Displays*, Singapore: World Scientific Press, p. 84.
15. Stodilka, D., Kitai, A.H., Huang, Z. and Cook, K. (2000) *SID Int'l. Symp. Dig.* **31(May)**: 11.
16. Xin, Y., Hunt, T. and Acchione, J. (2004) *SID Digest* **35**: 1138.
17. Minami, T. (1998) Ex. Abst., *4th Int'l Conf. Sci. and Tech. of Display Phosphors*, p. 195.
18. Minami, T. (2002) *Proc. EL2002*, Gent, Belgium, p. 219.
19. Ono, Y.A. (1995) *Electroluminescent Displays*, Singapore: World Scientific Press, p. 65.
20. Sano, Y., Nunomura, K., Koyama, N., Sakuma, H. and Itsumi, K. (1986) *Proc. SID* **27**: 169.
21. Dalacu, N. and Kitai, A.H. (1989) *J. Appl. Phys.* **66(6)**: 2734.
22. Ono, Y.A. (1995) *Electroluminescent Displays*, Singapore: World Scientific Press, p. 23.
23. Kitai, A.H. (ed) (1995) *Solid State Luminescence*, London: Chapman and Hall, p. 294.
24. Miura, N., Yokoyama, T., Matsumoto, H. and Nakano, R. (1997) Ext. Abst., *3rd Int Conf. Sci & Tech of Display Phosphors*, p. 121.
25. Kosyachko, A. (2003) *SID Digest* **34**: 1118.
26. Kosyachko, A. (2005) *SID Digest* **36**: 120.
27. Acchione, J. and Kosyachkov, A. (2005) *Proc Int'l Disp. Workshop/Asia Display 05*, 1623.
28. Ono, Y.A. (1995) *Electroluminescent Displays*, Singapore: World Scientific Press, p. 131.
29. Ono, Y.A. (1995) *Electroluminescent Displays*, Singapore: World Scientific Press, p. 122.
30. Yang, M., Nakua, A. and Cheong, D. (2003) *Proc. 10th Intl. Display Workshop IDW03*, p. 1097.

8 AC Powder Electroluminescence

Feng Chen and Yingwei Xiang

McMASTER UNIVERSITY, Hamilton, Ontario, L8S 4L7, Canada

8.1 Background	249
8.2 Structure and materials of AC powder EL devices	254
8.3 The mechanism of light emission for AC ZnS-powder-EL devices	257
8.4 EL characteristics of AC powder EL materials	261
8.5 Preparation of Powder EL devices	262
8.6 Limitations of AC Powder EL Devices	265
8.7 Applications of ACPEL	267
References	267

8.1 BACKGROUND

Inorganic powder phosphor electroluminescence is divided into AC powder EL (ACPEL) and DC powder EL (DCPEL) to distinguish the form of the driving voltage. This chapter introduces and describes ACPEL in detail. By way of introduction, both DC and AC powder EL will be reviewed.

8.1.1 Direct current powder electroluminescence (DCPEL)

DCPEL was first reported in an unbound powder phosphor system by Zalm in 1954 [1]. In 1955, Nicoll [2] and Bowtell [3] observed EL in DC-excited CRT phosphors. In 1959, Kazankin [4] reported DCPEL in ZnS:Mn, Cu powder phosphor suspended in castor oil. This early work had identified that DCPEL could only be observed in a phosphor with an electrically conductive coating. However, the development of a DCPEL display did not begin until 1966 when Vecht and co-workers started systematic and sustained study of DCPEL in ZnS:Mn, Cu phosphors [5, 6]. In 1984, their research effort eventually led to the production of DCPEL devices consisting of 640×256 individually addressable pixels that could display 2000 characters at a luminance of $85\text{--}103\text{ cd/m}^2$ [7]. Although DCPEL displays showed potential as segmented and graphic displays, little effort has been devoted to the development of new host lattices, especially for the preparation of multicolored phosphor systems. Only a few commercially useful devices were produced, such as car dashboards, dealer room applications and medical scanners.

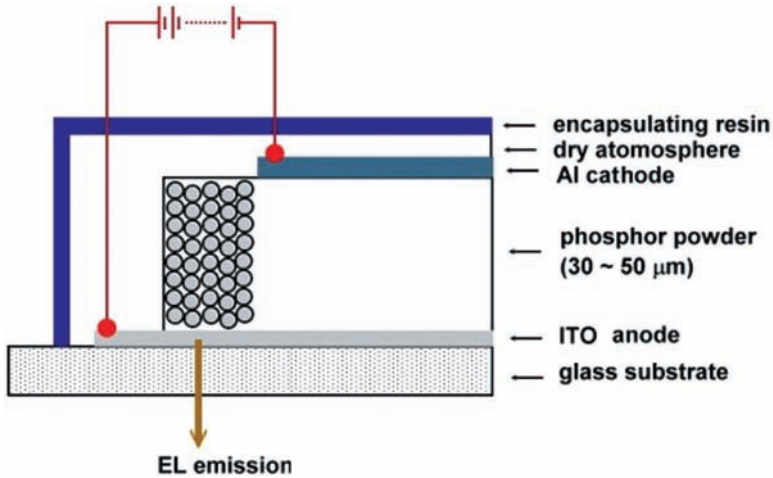


Figure 8.1 Typical DCPEL device structure

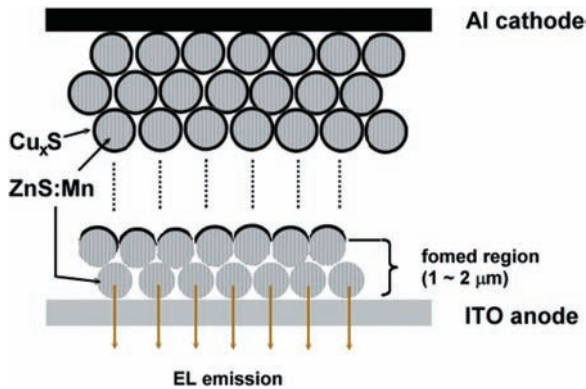


Figure 8.2 Schematic diagram of a formed ZnS:Mn, Cu power phosphor layer

A typical DCPEL device structure is shown in Figure 8.1. An EL active layer composed of ZnS:Mn, Cu powder phosphor mixed with a very little amount of binder is sandwiched between the front transparent ITO electrode and the Al back electrode. The typical thickness of the powder phosphor layer is 30–50 μm . Compared with a particle size of 5–20 μm in the AC powder electroluminescence (ACPEL), the particle size of DCPEL is much smaller, approximately 0.5–1 μm . Initially, the fine phosphor particles are highly insulating. By immersing the phosphor particles into a hot CuSO_4 solution, a conductive Cu_xS surface layer can be chemically formed, which is called a Cu-coating process. Since ZnS is moisture sensitive and there is no protection inside the device structure, the entire structure must be sealed hermetically.

The operating mode of the DCPEL device is essentially a resistive process. A fresh DCPEL device does not emit light until it undergoes a forming process (Figure 8.2). A suitably Cu-coated powder phosphor layer mixed with a minimum of binder typically has

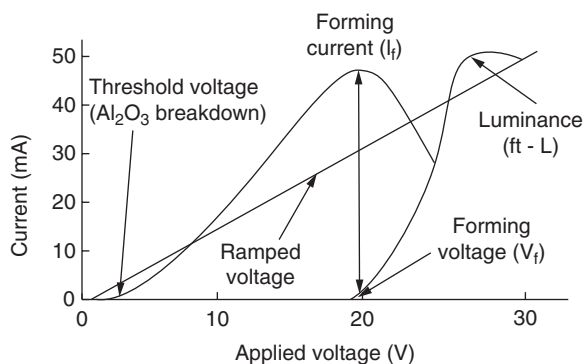


Figure 8.3 A typical forming trace for a DCPEL cell (0.2cm^2 area). *Solid State Luminescence*, A. H. Kitai, p. 189, Copyright (1993) Chapman & Hall. With kind permission of Springer Science and Business Media

a resistivity of 1–2 ohm-meters [8]. When a DC voltage with the Al electrode negatively biased is applied to the fresh device, a large current flows because of the conductive Cu_xS surface layer. At this point in time the Mn activator is not excited. With the increase of the applied voltage, the phosphor layer starts to heat up, allowing Cu^+ ions to migrate towards the negative electrode. As this process continues, a thin layer of Cu-free insulating ZnS is formed near the ITO anode. When this layer reaches a thickness of 1–2 μm , light is emitted from this insulating layer. With the onset of light emission, the current drops rapidly (Figure 8.3) [9].

Because of the continuous migration of Cu^+ ions, the region undergoing the formation process keeps growing, which gradually decreases the electric field of the region. The light-emitting process becomes self-limiting.

The thickness of the Cu-free formed region is 1–2 μm when light emission begins. Most of the applied voltage (on the order of 100 V) drops across this region, resulting in an electric field around 10^8 V/m .

Figure 8.4 shows the light emission mechanism of a DCPEL device. Under the high electric field, electrons are injected from the conduction band of the Cu_xS layer into the Cu-free ZnS:Mn region by a tunneling effect. Then the injected electrons are accelerated by the high electric field and excite the Mn^{2+} luminescent centers by impact excitation. Light emission occurs when the excited luminescent centers make radiative transitions to their ground states.

Note that the mechanism is similar to AC thin film electroluminescence, covered in Chapter 7.

The initial DCPEL device was confined to continuous current operation mode. Because of the self-limiting process of the light emission in the DCPEL device, the applied voltage must be increased continuously to maintain luminance until electrical breakdown destroys the film. In the 1970s, the pulse-wave operation mode was developed, which greatly improved the lifetime of the device and the discrimination ratio, since the device could be operated beyond the forming voltage without producing any further formation. For well encapsulated, moisture-resistant devices, a typical lifetime was about 1000 hours in dc drive mode and 5000 hours in pulse-wave drive mode [10]. If operated at low luminance, such as 85 cd/m^2 , the lifetime could be more than 10000 hours [11].

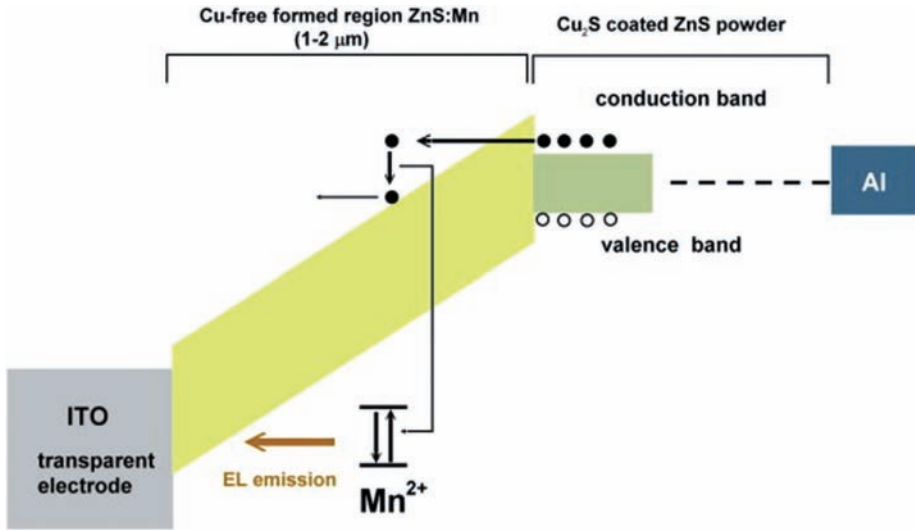


Figure 8.4 Energy band model of DCPEL device

In spite of these improvements, DCPEL is not an active field today, and no commercial devices are manufactured.

8.1.2 AC powder electroluminescence (ACPEL)

Historically, the phenomenon of electroluminescence was first observed in SiC by Round in 1907 [12]. He reported visible light emitted from the negative contact when an electrical current was passed through a rectifying contact on SiC. In the 1920s and 1930s, Lossev [13, 14, 15] of the Nijni-Novgorod Radio Laboratory in the Soviet Union, reported light emission after performing a series of experiments of rectifying contacts on SiC in more detail. This type of electroluminescence was known as the ‘Lossev effect’ and today is known as junction electroluminescence in a semiconductor [16]. The underlying light-emitting mechanism is the injection of minority carriers across a forward-biased p-n junction, followed by radiative recombination of electrons and holes.

In 1936, Destriau [17] discovered light emission in zinc sulfide powder activated with an excess of copper. This was the first record of electroluminescence in powder materials under applied voltage, and became known as ‘Destriau effect’. The device structure Destriau used was a large capacitor with a mercury electrode (Figure 8.5). This structure was soon modified to a demountable capacitor (Figure 8.6) [18]. The phosphor powder was mixed with castor oil and spread in a thin layer on a metal plate. A insulating transparent mica layer was placed on the top of the phosphor-castor oil layer. Over the mica layer is a layer of salt water used as top electrode. It should be remembered that no transparent conducting electrodes were available at that time. ZnS powder phosphor was placed in oil with high dielectric constant. The electroluminescence was extremely poor although it was excited at very high AC voltage (15kV). This effect received very little attention in the following decade. Even in 1950, Leverenz [19] questioned the mechanism of the light emission

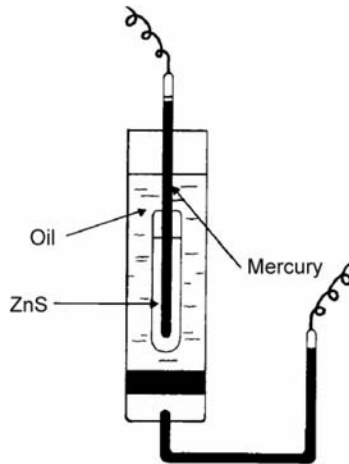


Figure 8.5 The original Destriau cell

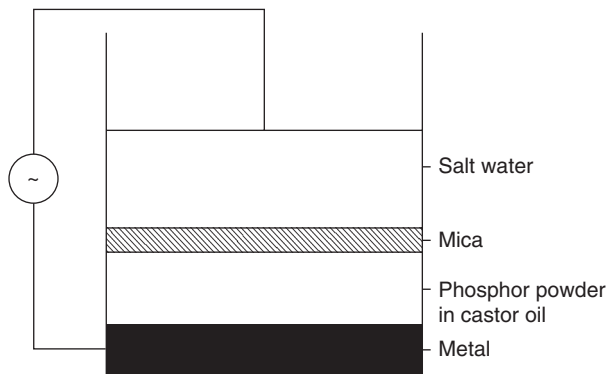


Figure 8.6 A schematic diagram of a modified Destriau cell [18]. *Solid State Luminescence*, A. H. Kitai, p. 189, Copyright (1993) Chapman & Hall, with kind permission of Springer Science and Business Media

reported by Destriau. He suggested that the powder phosphor may in fact be excited by the UV light emitted by the electrical breakdown of the gases in the fairly porous powder phosphors.

During the Second World War through to the late 1940s, development of high performance polymers and ceramics was initiated. More importantly, transparent conducting electrodes were achieved for the first time. These developments triggered great interest in AC powder electroluminescence (ACPEL). From the 1950s to the mid-1960s, large academic and industrial research efforts were devoted to ACPEL displays. Most of the work in that period was reviewed by Ivey [20] and Henisch [21].

ACPEL has a simple device structure and can be fabricated with low-cost manufacturing method. At a low luminance of 3.4 cd/m^2 , its lifetime (operating time for the luminance to drop to half of its original luminance) is nearly infinite. ACPEL lights have been known to operate continuously for over 10 years at 100 V rms at 60 Hz . However, ACPEL has several significant challenges for display application:

- Low discrimination ratio, which is defined as the ratio of luminance at V to the luminance at $V/2$;
- Low contrast ratio;
- Short lifetime at moderate to high luminance.

The low discrimination ratio is due to the fundamental physics of the light-emitting mechanism of the AC powder phosphor. This feature indicates that ACPEL is not suitable for high resolution multiplexed displays. One way to overcome this issue is to incorporate a Thin Film Transistor (TFT) drive circuit into the ACTFEL display, as suggested by Fisher in 1971 [22] and explored by Brody [23]. Unfortunately, experimental devices had a considerable number of blemishes resulting from the poor quality of the TFTs. At that time, TFTs were in their early stages and amorphous silicon technology did not exist. Hence this technology was soon abandoned.

The low contrast ratio in moderate to high ambient illumination is due to the high reflectivity of the powder phosphor itself. Filters can be used to increase the contrast ratio at the cost of decreased luminance. Therefore, higher voltages and frequencies were required to drive the display, which greatly decreased the lifetime of the ACPEL display.

The short lifetime at moderate to high luminance is due to the exponential decay feature of the AC powder EL phosphors. Fisher [22] explained that the decay in brightness is related to the blunting of microscopic tips of Cu_2S precipitates inside the ZnS phosphor particles. The blunting occurs by the migration of the copper ions when they are exposed to the high electric field. The degradation is accelerated by moisture, high operating temperature and frequency. At about 170 cd/m^2 , the typical lifetime of ACPEL lamps is 1000 hours.

In spite of the considerable technical effort from the 1950s to the mid-1960s, the inability to improve the lifetime of ACPEL displays led to its disfavor in the late 1960s. At the same time, other technologies, such as gas discharge, light-emitting diodes, vacuum fluorescence, liquid crystals and thin film electroluminescence, attracted increasing research interest. These newly emerging technologies greatly diminished interest in ACPEL. By 1974, when Sharp developed a double-insulator AC thin film electroluminescent display with high performance and reliability, almost all of the research and development teams at the various companies throughout the USA, who had been working on EL during the 1950s and 1960s, had been disbanded [24]. Since then, no fundamental work has been published, which has dramatically reduced the performance of ACPEL lamp or displays, although important progress has been made in packaging. A CVD method is used to encapsulate ZnS:Cu,Cl phosphor particles with a Ti-Si-O film, in order to improve the lifetime by preventing moisture penetration [25]. By maintaining constant current or constant power, the lifetime of an ACPEL device producing 200 cd/m^2 has been extended to more than 3000 hours [26].

8.2 STRUCTURE AND MATERIALS OF AC POWDER EL DEVICES

AC powder EL devices were first developed by Sylvania in the first era of EL devices. A typical structure of an AC powder ZnS EL device is shown in Figure 8.7. To date, the well-known excitation of powder phosphors by an alternating electric field is limited to a comparatively small group of phosphors, mainly of the ZnS type. As shown in Figure 8.7, the

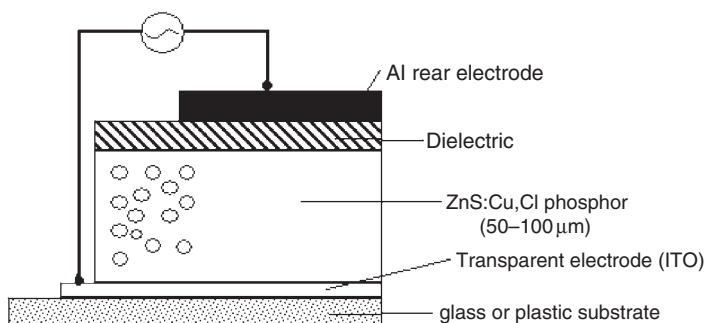


Figure 8.7 Typical structure of AC powder phosphor EL device

Table 8.1 Some of the powder phosphors known to exhibit EL under AC. *J. Electrochem. Soc.*, Vol. 104, No. 1, W. Lehmann, 'Cross section of the electro . . .', p. 46, Copyright (1957). Reproduced by permission of ECS—The Electrochemical Society

Phosphor	Colour	Reference
ZnS : Cu,Cl(Br, I)	Blue	[27, 28]
ZnS : Cu,Cl(Br, I)	Green	[27, 28]
ZnS : Mn, Cl	Yellow	[29]
ZnS : Mn, Cu, Cl	Yellow	[30]
ZnSe : Cu, Cl	Yellow	[30]
ZnSSe : Cu, Cl	Yellow	[30]
ZnCdS : Mn, Cl (Cu)	Yellow	[27]
ZnCdS : Ag,Cl (Au)	Blue	[27]
ZnS : Cu,Al	Blue	[31]

EL active phosphor layer consists of suitably doped ZnS powders with particle size of 5–20 μm suspended in a dielectric, which also acts as a binder. This phosphor layer is 50–100 μm thick and is sandwiched between two electrodes, one of which is transparent and is supported by a substrate, consisting of either glass or flexible plastic. The EL color of the film depends on the activator of the ZnS phosphors. The most common ZnS phosphor used is the green-emitting ZnS:Cu, Cl(or Al); in this material, the Cu activator acts as an acceptor and is responsible for the color of the emission, while Cl (or Al) works as a donor. The amount of the Cu added in the preparation process of these phosphors is 10^{-3} to 10^{-4} gram per gram of ZnS, and is one order of magnitude larger than that added to ZnS phosphors used in CRTs. As discussed below, the Cu plays an import role in high-field AC powder EL in addition to acting as the activator.

Table 8.1 shows some of the binary and ternary systems that have been investigated over the years used for AC powder EL.

The embedding dielectric in the device is an organic material with a large dielectric constant, such as cyanoethylcellulose, or low melting glass [32]. In order to increase the stability and protect the EL device against catastrophic dielectric breakdown, an insulating layer, consisting of BaTiO₃ powders dispersed in other dielectric materials, is often inserted between the EL active layer and the Al rear electrode.

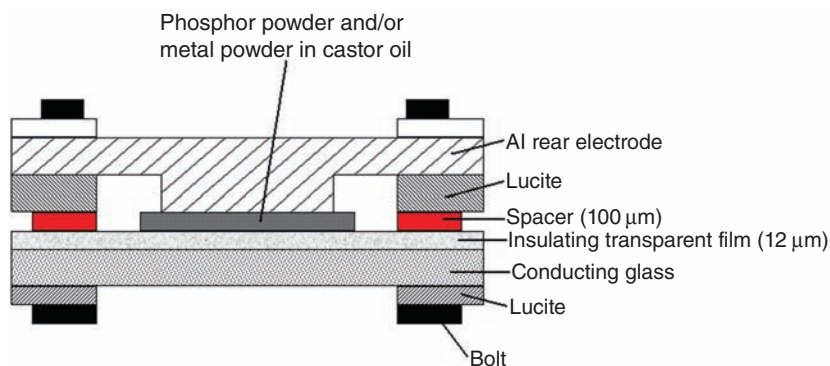


Figure 8.8 The arrangement of Lehmann's contact EL. *J. Electrochem. Soc.*, Vol. 104, No. 1, W. Lehmann, 'Cross section of the electro . . .', p. 46, Copyright (1957). Reproduced by permission of ECS—The Electrochemical Society

Lehmann [33] reported that many powdered crystal phosphors, which are normally non-electroluminescent, become electroluminescent if they are simply mixed with suitable powdered metals, or with some non-metals of good electrical conductivity. This phenomenon is termed as 'contact electroluminescence' or 'contact EL'.

The arrangement of the contact EL is shown in Figure 8.8. Powdered phosphors which are unable to electroluminesce under usual conditions in a strong alternating electric field have been mixed mechanically with metal powders. This mixture, with castor oil as the embedding dielectric, is placed in a normal plaque cell consisting of a front electrode of conducting glass overcoated with a thin, transparent, insulating film and a back electrode of Al. When an alternating voltage is applied to the cell, the mixture of phosphor and metal is electroluminescent.

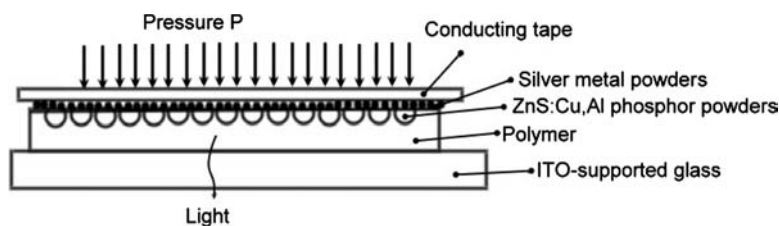
Many phosphors, which are able to PL but EL, can show this contact EL. A qualitative survey of some results obtained with mixtures of various phosphors with metal powder is given in Table 8.2 for an applied sinusoidal voltage of 600 V rms and a frequency of 10000 cps. The embedding dielectric material here was castor oil; however, similar results are obtained with other organic dielectric materials or even with air as the embedding material [33]. The emission color of some phosphors is different for photo- and electroluminescence, indicating that the phosphors have been excited by the electric field instead of UV radiation generated by a glow discharge in the cell. Although no direct relationship could be found between the nature of the phosphor and its ability to be excited by contact EL, the crystallinity, the activator concentration (if activators are necessary) and other properties may have an influence on contact EL in addition to the general type of material.

Recently, we performed an experiment similar to Lehmann's contact EL. In this case, a phosphor powder of ZnS:Cu,Al was embedded into a polymer, which was supported by a glass substrate coated with a thin layer of indium tin oxide (ITO). Spherical silver metal powders with diameter of 1–3 μm are pressed onto a conducting tape and put on top of the phosphor layer. When both the pressure and the alternating electric field are applied to the cell, green light can be generated from the phosphor layer. We call this phenomenon 'powder contact EL' (Figure 8.9).

Table 8.2 Photoluminescent and electroluminescent emission of various phosphors [33]

Phosphor	Photoluminescence		Electroluminescence	
	2537 Å	3650 Å	Pure Phosphor	Mixed with metal powder
ZnS-Cu (0.03%)	br green	br green	—	m blue
ZnS-Cu (0.1%)	br blue green	br blue green	m blue	br blue
ZnS-Cu (0.01%)	br green	br green	—	m green
ZnS-Ag (0.03%)	br blue	br blue	—	br blue
ZnS-Mn (1 %)	m yellow	br yellow	—	br yellow
(ZnCd)S-Cu	br yellow	br yellow	—	w green
(ZnCd)S-Ag	br yellow	br yellow	—	br yellow-green
CaS-Bi	m blue	m blue	—	w blue
(CaSr)S-Bi	m blue	m blue	—	w blue
Zn ₂ SiO ₄ -Mn	br green	vw green	—	br green
Zn ₃ GeO ₅ -Mn	br green	—	—	m green
CaWO ₄ -Pb	br white	—	—	vw blue
Cd ₂ B ₂ O ₅	br red	w red	—	vw red
Cd ₂ SiO ₄ -U-Sm	br pink	w red	—	w green
CaPO ₄ -Tl	br white	br white	—	m white
UO ₂ (NO ₃) ₂ ·6H ₂ O	br green	br green	—	w green
Anthracene	br blue	br blue	—	w blue

Intensities: br = bright, m = moderate, w = weak, vw = very weak

**Figure 8.9** Arrangement of powder contact EL device

8.3 THE MECHANISM OF LIGHT EMISSION FOR AC ZNS-POWDER-EL DEVICE

Many theories have been proposed to explain AC-excited EL of embedded ZnS-type powders, i.e.:

- *impact* ionization model
- zener emission model
- inverted impact ionization model.

However, until now the most popular and reasonable theory has been *the bipolar field-emission model*, proposed by Fisher. A careful study of the interior of ZnS:Cu,Cl particles using

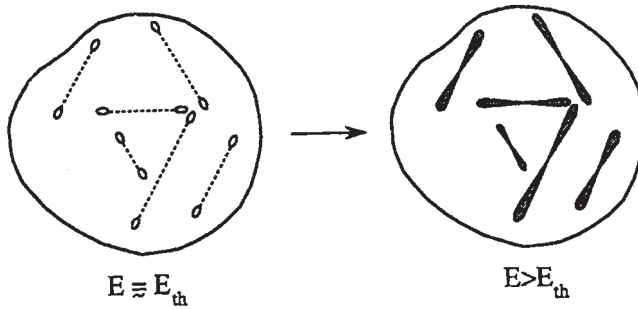


Figure 8.10 Typical microscopic view of EL from ZnS:Cu,Cl particles. Double lines at threshold voltage and above the threshold voltage are illustrated [34]. *J. Electrochem. Soc.*, 109, 11, A. G. Fisher, 'EL lines drawn from . . .', p. 1047, Copyright (1962). Reproduced by permission of ECS—The Electrochemical Society

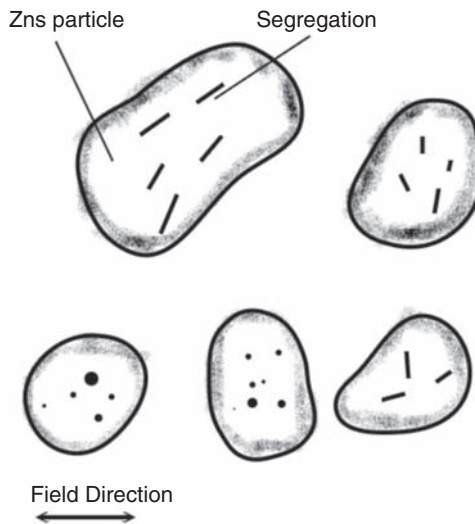


Figure 8.11 Phosphor particles containing dark segregations and emitting spots

an optical microscope was performed. It was observed that the shape of the lighting-emitting region with a single EL particle takes the form of double lines with shapes similar to twinkling tails of a comet (Figure 8.10).

On further observing the ZnS phosphor particles under the microscope, Fisher found that there were many dark segregations and precipitates inside the phosphor particles (Figure 8.11).

According to these observations, Fisher proposed the following model for the EL mechanism. ZnS EL powders are typically prepared by firing at high temperatures (1100–1200 °C), where the hexagonal wurtzite phase predominates. When the powders are cooled, there is a phase transition to the cubic zinc-blende structure. Copper preferentially precipitates on defects formed in the hexagonal-to-cubic transformation with the reduction of their solubility in ZnS. The Cu forms thin embedded Cu_{2-x}S needles in the crystal matrix (Figure 8.12(a)) [35]. Cu_{2-x}S is known to be a p-type semiconductor with high conductivity. Between these Cu_{2-x}S precipitates and ZnS powder hetero-junctions are formed (Figure 8.12(b)) [36].

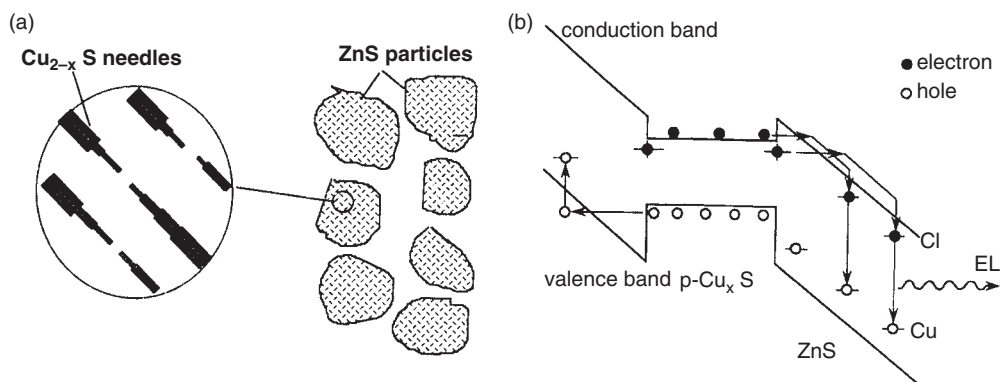


Figure 8.12 EL emission mechanism and schematic energy-band diagram of ac powder EL devices: (a) Cu_{2-x}S needles [35]. *Solid State Luminescence*, A. H. Kitai, p. 189, Copyright (1993) Chapman & Hall. With kind permission of Springer Science and Business Media; (b) energy-band diagram [36]. *J. Electrochem. Soc.* 110, A. G. Fisher, 'Biopolar Injection at . . .', pp. 733–748, Copyright (1963). Reproduced by permission of ECS—The Electrochemical Society

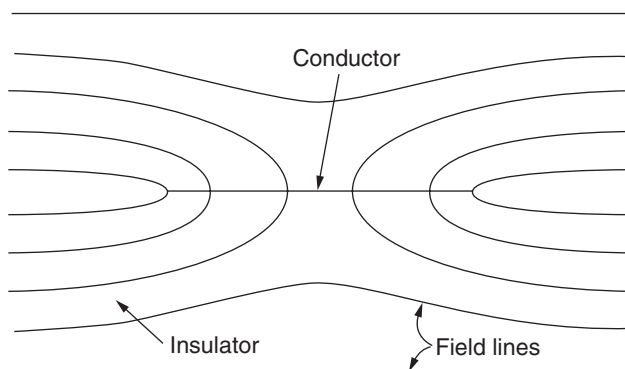


Figure 8.13 Conducting needle embedded in insulator. A uniform electric field is applied parallel to the needle. Geometrical field intensification occurs at the ends. *J. Electrochem. Soc.* 110, A. G. Fisher, 'Conducting needle . . .', pp. 733–748, Copyright (1963). Reproduced by permission of ECS—The Electrochemical Society

When an electric field is applied to the phosphor particles, relatively high electric fields will be concentrated on the tips of Cu_{2-x}S conducting needles (the effective tip radius is in the order of 100 nm) compared with that of other regions as (Figure 8.13) [36].

Therefore an applied field of 10⁶–10⁷ V/m can induce a local field of 10⁸ V/m or more. This electric field is strong enough to induce tunneling of holes from one end of the needle and electrons from the other to the ZnS:Cu,Cl lattice. The electrons are captured in shallow traps in Cl donor sites, while the holes are trapped by the Cu recombination centers (acceptor sites). When the field is reversed, the emitted electrons recombine with the trapped holes to produce EL. Figure 8.14 [36] shows the illustration of the basic principle of the bipolar field-emission model.

As a conclusion to the bipolar field emission model, EL emission from a ZnS-powder-EL device is caused by the radiative recombination of electron-hole pairs through donor accep-

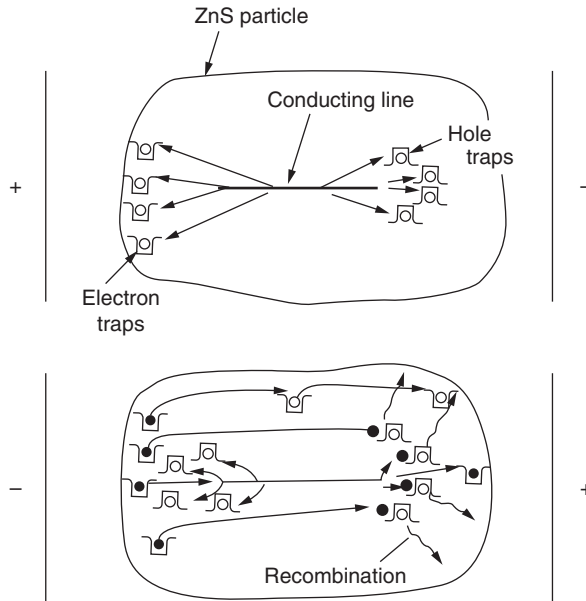


Figure 8.14 Illustration of the basic principle of field-emission model. Above, at field application, electrons and holes are ejected from the opposite ends of the conducting inclusion, where the field is intensified, into the ZnS lattice. Holes are trapped after a short path. Electrons can travel farther. Below, at field reversal, trapped electrons flow back to recombine with trapped holes (light emission). Other electrons are field-emitted into the trapped holes. New holes are field-emitted at the other end of the conducting line. [36]. J. Electrochem. Soc. 110, A. G. Fisher, 'Biopolar Injection at . . .', pp. 733–748, Copyright (1963). Reproduced by permission of ECS—The Electrochemical Society

tor pairs. The instantaneous field-emission current I through the Cu_xS -ZnS contact follows the Fowler – Nordheim equation:

$$I = A \frac{E^2}{W^{3/2}} \exp\left(-B \frac{W^{3/2}}{E}\right) \quad (8.1)$$

where A and B are constants, E is the field strength and W is the work function. In this case, W corresponds to the energy difference between the electron affinity of ZnS and that of Cu_xS .

Experimental evidence has been provided by Ono *et al.* [37] for the validity of Fisher's model, by carefully examining ZnS:Cu phosphor particles showing EL using a transmission electron microscope (TEM). Black specks in the shape of narrow needles with diameters of 20–40 nm along the boundaries of micro-twin crystals inside a ZnS particle were observed under TEM. The specks were believed to be the Cu_2S , further confirmed by measuring the wavelength of characteristic X-rays emitted from the precipitates. Cu_2S is well known to be a p-type semiconductor with high metallic conductivity. Therefore, these observations confirm Fisher's predictions.

As we know, one of the necessary requirements for contact EL is that the conducting powders must have relatively sharp edges. The explanation of powder contact EL can be found in the *bipolar field-emission model*. The electric field near sharp edges of the conducting powders, which contact with the phosphors is considerably higher than the average

electric field across the phosphor crystals. Therefore, the sharp-pointed powders perform the same role as the conducting Cu_xS imperfection lines embedded in ordinary EL ZnS powders. When an electric field is applied to the mixture, electrons will be ejected from the edges of the conducting powders into the ZnS lattice and recombine with the holes that are trapped by luminescent centers to produce EL.

8.4 EL CHARACTERISTICS OF AC POWDER EL MATERIALS

EL is observed when an AC voltage of about 100–200 V corresponding to an electric field of order of 10^4 Vcm^{-1} is applied across the electrodes of the device. Luminance-voltage characteristics of a typical EL device are shown in Figure 8.15 [38]. The observed dependence of the luminance (L) on the applied voltage (V) is expressed by

$$L = L_0 \exp\left(-\left(\frac{V_0}{V}\right)^{1/2}\right) \tag{8.2}$$

The parameters L_0 and V_0 depend on the particle size of the phosphor, the concentration of the powder in the dielectric, the dielectric constant of the embedding medium and the device thickness. It has been established empirically that one of the key parameters affecting EL characteristics is the particle size, and a critical trade-off between the EL efficiency and the operational lifetimes, defined by the time when the luminance becomes one half of the initial value, exists as follows. The efficiency increases in proportion to $\sim d^{-1/2}$, where d is the particle size; this leads to the nonlinearity of the luminance-voltage dependence. However, the operational lifetime, decreases in proportion to $\sim d$. In addition, the luminance increases with frequency in the frequency region of $\sim 100\text{--}10 \text{ kHz}$. Luminance of 100 cdm^{-2} has been achieved for devices driven at a frequency of 400 Hz and a voltage of 200 V [38].

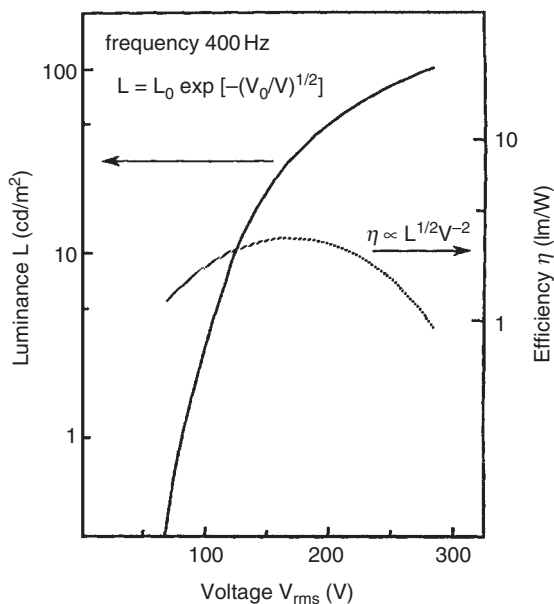


Figure 8.15 Typical luminance-voltage and efficiency-voltage characteristics of AC powder EL device

A typical voltage dependence of the EL efficiency, η , is also shown in Figure 8.15. Typical values of the efficiency are $1\text{--}10\text{lmW}^{-1}$. The efficiency increases initially with increased applied voltage up to a saturation value, but then decreases gradually with further increases in voltage. The EL efficiency dependence on the voltage V is expressed by $\gamma = L^{1/2}V^{-2}$. The maximum efficiency is obtained at a voltage well below the highest luminance level.

8.5 PREPARATION OF POWDER EL MATERIALS

Most powder EL research has been centered around the II-VI compounds and by far the most important EL lattice is zinc sulfide (ZnS). Zinc sulfide is a semiconductor material and exists in two main structural modifications. The low temperature form is cubic zinc-blende with band-gap energy of 3.7 eV, and the high temperature form is hexagonal wurtzite with band-gap energy of 3.8 eV. The two modifications are shown in Figure 8.16. Due to its excellent electrical properties such as the large band-gap energy, direct recombination and low leakage current, ZnS is ideal for being used as phosphor material by doping with transition metals or rare-earth metals [39, 40]. In addition, owing to the advantage of the simple manufacturing process, the convenience of being able to print large areas and the high power efficiency, ZnS phosphor powders are suitable for back lighting of liquid crystal panels or for flat panel displays [41]. Therefore, ZnS type phosphors, such as green-emitting ZnS:Cu,Al, are very important from a practical point of view. Luminescence centers in these phosphors are formed from deep donors or deep acceptors, or by their association at the nearest-neighbor sites.

The energy levels of ZnS:Cu,Al are shown in Figure 8.17 [42]. Before excitation, the Cu (acceptor) is monovalent (1^+), while the Al (donor) is trivalent (3^+), so that charge compensation is realized in the lattice. Absorption A of the figure located at about 400 nm gives the characteristic excitation band of the center. When excited, Cu and Al become divalent

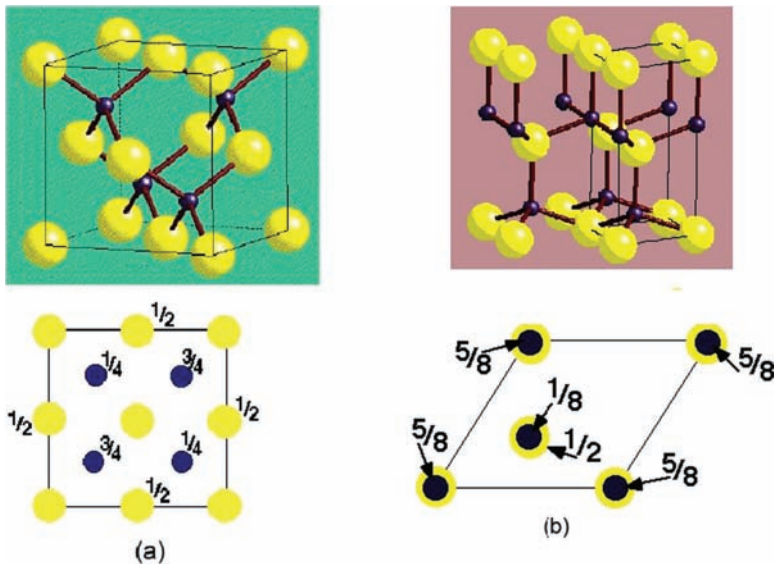


Figure 8.16 (a) Cubic zinc-blende, and (b) hexagonal wurtzite modifications of ZnS

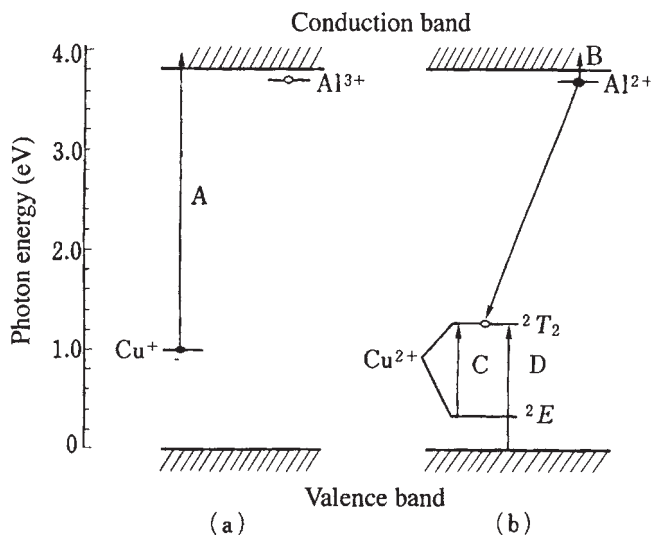


Figure 8.17 Energy levels and absorption transitions of ZnS:Cu, Al phosphor before excitation (a), and during excitation (b) (reprinted from A. Suzuki and S. Shionoya, *J. Phys. Soc. Japan* **31**, 1455, Copyright (1971) The Physical Society of Japan)

(2^+). The levels of Cu^{2+} ($3d^9$ configuration) are split by the crystal field into 2T_2 and 2E states, with 2T_2 lying higher in the zinc-blende structure. In the process of the relaxation due to the reverse of the electric field, the electron trapped by Al^{2+} would recombine with the hole trapped by Cu^{2+} and luminescence is generated. As a result, Al and Cu become monovalent and trivalent, respectively.

8.5.1 Preparation of pure II-VI compounds (starting materials)

The techniques used for preparation of the AC powder phosphors are described below. The recipes originally developed for the preparation of the CRT phosphors are modified for the manufacture of AC powder EL phosphors. Most luminescent and optoelectronic II-VI materials are prepared by the addition of controlled amounts of specific impurities (dopants), called ‘activators’ and ‘co-activators’, to high purity II-VI compounds.

In order to prepare high purity starting materials, three methods have been developed so far.

1. The first method is to use the direct reaction of the group II and VI elements, such as pure elemental S and Zn. However, this method is not practical since the reaction is difficult to control and is explosive, especially if the reagents are in the form of finely divided powders.
2. The second method is to thermally decompose suitable organometallic precursors, such as zinc or cadmium diethyldithiocarbates. The drawback of this method is the production of the toxic organic residues and traces of carbon due to the decomposition of the organometallic compounds. As a result, this method is also not recommended for the preparation

of the powder II–VI compounds, although this method has been used successfully for the deposition of thin films of ZnS [43].

3. The last developed method is to use the reaction of the aqueous group II salt solutions with gaseous hydrogen sulfide, selenide or telluride. The reaction between group II salt in aqueous medium with, for example, thiourea or thioacetamide that provides the sulfur also yields high purity ZnS. So far, this method is the most widely used for preparation of powder II–VI phosphors, compared with the other two methods mentioned above.

ZnS can be precipitated using a purified solution of a Zn salt and hydrogen or ammonium sulfide in alkaline or acidic conditions. The phosphor made using this technique contains only a few parts per million of heavy metal impurity. The firing of the dried precipitate in a nitrogen atmosphere reduces the non-metal impurity level to about 500 ppm. The firing also leads to an increase in the particle size and an improved crystallinity of the lattice. Methods for the preparation of the ZnS have been described in detail by Levernz [19].

8.5.2 Activators (dopants)

All phosphors consist of a host material and a light-emitting dopant called an activator or a luminescent center. Pure stoichiometric ZnS, for example, do not luminesce. Luminescence can be caused by the introduction of lattice defects, by deviation from the stoichiometric Zn-S ratio, and by the addition of certain atoms to the system. Often, when impurity atoms are introduced, defects and deviations from stoichiometry are simultaneously produced, either by the rearrangement of the crystal lattice or by the physical and chemical processing conditions under which the impurity is added. Typical examples of impurity atoms (activators) are Mn and Cu. Other impurities leading to the reduction of the EL phenomenon are termed ‘killers’ or ‘quenchers’. Co, Fe and Ni, for example, are well-known quenchers in CRT-type phosphors.

In normal AC powder EL phosphor preparation, the incorporation of the impurity atoms is carried out by adding the dopants either in a slurry form or by milling (dry or wet). If the addition is carried out by slurring or wet milling, the mixture has to be dried out completely before firing at elevated temperatures to assist the diffusion of the dopants into the host material lattices. Sometimes fluxes such as MgO, BaCl₂, and NaCl are also added in order to lower the activation temperature. Elements from group IB or VB (activators) are normally introduced with group IIIB or group VIIB impurities (co-activators). The primary reason for the addition of two or more types of impurities simultaneously is related to charge compensation in the II-VI phosphor lattice. In AC powder phosphors, Cu from group IB is the most important activator giving rise to both green and blue EL. Halide coactivators are normally employed, with Cl⁻ being preferred for the luminance [44].

8.5.3 EL emission spectra

The emission spectra of ACEL devices are shown in Figure 8.18 [26]. Emission colors depend on the different luminescent centers incorporated in the phosphors. When the ZnS lattice is activated with Cu (activators) and Cl, I and Al (co-activator), donor (co-activator)-

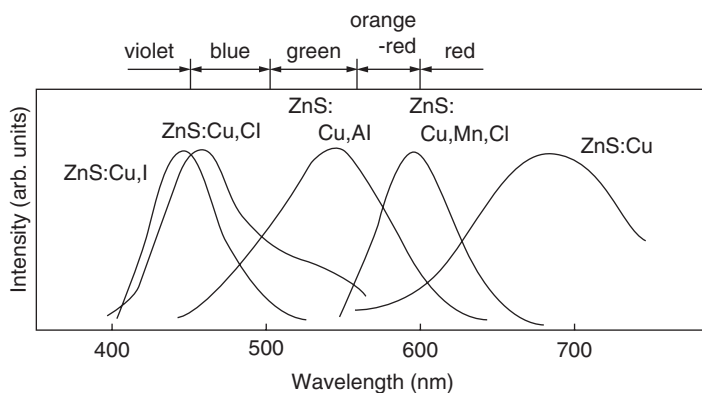


Figure 8.18 AC EL spectra of various kinds of ZnS powder phosphors

acceptor (activators) pairs are formed. As mentioned above, the EL is due to the radiative recombination of electron-hole pairs at donor-acceptor (D-A) pair sites. The combination of Cu and Al (ZnS:Cu,Al) produces green (~550 nm) emission color. The combination of Cu and Cl (ZnS:Cu, Cl) gives blue (~460 nm) and green emission bands, their relative intensity depending on the relative amount of Cu to Cl. ZnS:Cu,I shows a blue emission. It should be noted that ZnS:Cu, in which no co-activators are incorporated, shows a red emission. By further incorporating Mn^{2+} ions into ZnS:Cu,Cl phosphors, the resultant ZnS:Cu,Mn,Cl shows a yellow emission (~580 nm) due to Mn^{2+} .

8.6 LIMITATIONS OF AC POWDER EL DEVICES

In the 1950s and 1960s, research efforts were devoted to AC powder phosphor EL with the aim to fabricate efficient illumination panels. However, low luminance and significant luminance degradation in the course of operational times shorter than 500 hours have been serious problems for devices using powder phosphors. Fortunately, the research efforts were triggered again owing to the advance of AC thin film EL (ACTFEL) in 1974, with high luminance and lifetimes as long as 10000 hours [45].

8.6.1 Lifetime and luminance degradation

Lifetime and degradation is a key issue for the application of AC powder phosphor EL. Lifetime is defined as the operating time over which the luminance decreases to one half of the initial value. Figure 8.19 shows a typical example of EL light output vs. time. The degradation rate depends on driving conditions (such as frequency and luminance levels) and on environmental conditions, especially temperature and humidity. The luminance decay with time is usually expressed by $L/L_0 = (1 + \alpha t)^{-1}$, where α is a constant roughly proportional to the driving frequency [26]. Furthermore, it is difficult to have both long lifetime and high luminance simultaneously for powder EL devices because they are trade-off characteristics.

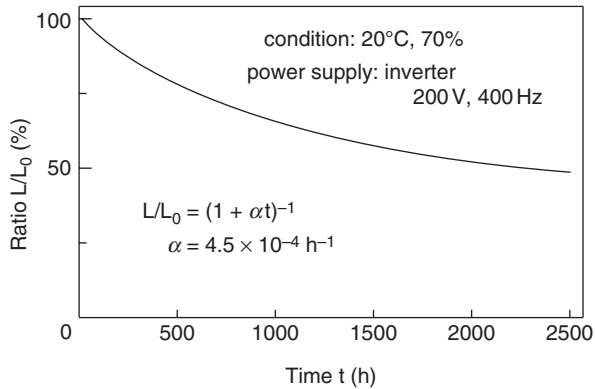


Figure 8.19 Typical luminance maintenance curve of AC powder EL device [46] (*Proc. Soc. Inform. Display*, **22**, 47, Copyright (1981) Reproduced by permission of the Society for Information Display)

According to Fisher's bipolar field-emission model, the degradation is related to the diffusion of copper in the ZnS lattice. As mentioned above, copper sulfide precipitate needles (dislocation lines) play an important role in EL emission. However, the tips of the copper-sulfide-decorated imperfection lines (not only the end tips but also the innumerable little rough areas) can be blunted by outward drift of copper ions, by attraction of ions from the adjacent host crystal or, most likely, by sideward-drift of copper ions in front of the tips during their back-and-forth oscillation under the influence of the high AC field in front of the tips [36]. As a result, the copper sulfide needles become increasingly shorter and end with isolated points with operational time.

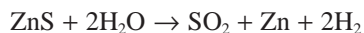
8.6.2 Luminance and relative high operating voltage

Typical values of luminance for AC ZnS-powder EL devices are from 3–10 cdm^{-2} and operating voltages are usually above 100 V. As mentioned above, luminance and lifetime are trade-off characteristics for power EL devices.

Recently the luminance has been improved steadily up to 100 cdm^{-2} , driven at a frequency of 400 Hz and a voltage of 200 V (Figure 8.19).

8.6.3 Moisture and operating environment

Another serious challenge for powder EL is that it is very sensitive to the moisture and operating environment. The reaction shown below occurs between ZnS and water to produce SiO_2 .



Through this reaction, sulfur escapes from the ZnS phosphor, generating sulfur and zinc vacancies in the phosphor. It has been reported that the luminance of the ZnS phosphor deteriorates when the number of sulfur vacancies increases [47]. For this reason, two

methods to prevent degradation have been developed. One method is using antihumidity film, such as the fluorocarbon film [48], to package the entire device. Another method is to coat the phosphor particles themselves by transparent thin films with antihumidity properties [49–52].

Generally speaking, as summarized by Peteryl and Fuller [53], EL lamps and information displays historically suffer from serious shortcomings, such as low luminance, short useful operating life, poor visibility in normal room light, and no visibility under high ambient light. In addition, the high voltage control circuit presented great obstacles, and operation at temperatures much above room temperature caused rapid deterioration of intensity of emitted light.

8.7 APPLICATIONS OF ACPEL

Due to the low brightness and short lifetime, the applications of ACPEL devices are mainly limited to backlighting and lamp applications that require low brightness. This includes low illumination environments, such as nightlights and backlighting for LCDs and keypads in portable electronics and home electronics. A unique feature of ACPEL is the plastic cell structure that provides great versatility in product design. Flexible ACPEL lamps can be folded, creased and pierced while maintaining complete functionality – allowing design concepts unachievable with other lamp types. This feature makes ACPEL the only truly thin and flexible light-emitting device in the current market. ACPEL continues to be the most commercially successful high-field EL device.

REFERENCES

1. Zalm, P. (1956) *Philips Res. Rep.* **11**: 353.
2. Nicoll, F.H. and Kazan, B. (1955) *Proc. IRE* **43**: 1012.
3. Bowtell, J.N. and Bate, H.C. (1956) *Proc. IRE* **44**: 697.
4. Kazankin, O.N., Pekerman, F.M. and Petoshina, L.M. (1959) *Opt. Spectrosc.* **7**: 458.
5. Vecht, A. and Ellis, R. (1966) *Nature* **210**: 1251.
6. Vecht, A.J. (1973) *Vac. Sci. Technol.* **10(5)**: 789.
7. Mayo, J., Hutchinson, P., Hayes, R. and Ellis, R. (1984) *SID Int. Symp. Digest*, p. 22.
8. Vecht, A. and Chadha, S.S. (1989) 'VLSI and Computer Peripherals. VLSI and Microelectronic Applications in Intelligent Peripherals and their Interconnection Networks', *CompEuro Proceedings*, pp. 2–24.
9. Kitai, A.H. (1993) *Solid State Luminescence*, London: Chapman & Hall, p. 189.
10. Ono, Y.A. (1995) *Electroluminescent Displays*, Singapore: World Scientific Publishing Co. Pte. Ltd, p. 14.
11. Shionoya, S. and Yen, W.M. (1998) *Phosphor Handbook*, New York: CRC Press LLC, p. 610.
12. Krasnov, A.N. (2003) *Displays*, **24**: 73.
13. Lossev, O.V. (1923) *Telegrafia Telefonica* **18**: 61.
14. Lossev, O.V. (1928) *Philos. Mag. Series* **6(7)**: 1024.
15. Lossev, O.V. (1933) *Phys. Z* **34**: 397.
16. Grimmeiss, H.G. and Allen, J.W. (2006) *J. Non-Cryst. Solids* **352**: 871.
17. Destriau, G.. (1936) *J. Chem. Phys.* **33**: 587.
18. Kitai, A.H. (1993) *Solid State Luminescence*, London: Chapman & Hall, p. 160.

19. Leverenz, H.W. (1950) *An introduction to Luminescence of Solids*, New York: Wiley, p. 61.
20. Ivey, H.F. (1966) 'Advances in Electronics and Electron Physics', Suppl. 1, *Electroluminescence and Related Effects*, New York: Academic Press.
21. Hensch, H.K. (1962) *Electroluminescence*, Oxford: Pergamon.
22. Fischer, A.G.. (1971) *J. Electrochem. Soc.* **118**: 139c.
23. Brody, T.P. and Yu, K.K. (1975) *IEEE Trans. Electron Devices*, **22**: 739.
24. Tannas, L.E., Jr. (1985) *Flat-Panel Displays and CRTs*, Van Nostrand Reinhold Company Inc., p. 244.
25. Sawada, M., Oobayashi, S., Yamaguchi, K. *et al.* (2002) *Jpn. J. Appl. Phys.* **41(1)(6A)**: 3885–9.
26. Shionoya, S. and Yen, W.M. (1998) *Phosphor handbook*, New York: CRC Press LLC, p. 606.
27. Destriau, G. J. (1937) *Chim. Phys.* **34**: 327.
28. Jaffe, P.M. (1961) *J. Electrochem. Soc.* **108**: 711.
29. Gobrecht, H. and Gumlich, H.E. (1956) *J. Phys. Radium* **17**: 754.
30. Thornton, W.A. (1958) *Bull. Am. Phys. Soc.* **3**: 233.
31. Gobrecht, H., Gumlich, H.E., Nelkowiak, H. and Langar, D.Z. (1957) *Z. Phys.* **149**: 504.
32. Ono, Y. (1995) *Electroluminescent Displays, Series on Information Display*, Singapore: World Scientific Publishing Co. Pte. Ltd, p. 11.
33. Lehmann, W. J. (1957) *Electrochem. Soc.* **104(1)**: 45–50.
34. Fisher, A.G. (1962) *J. Electrochem. Soc.* **109(11)**: 1043–9.
35. Kitai, A.H. (1993) *Solid State Luminescence*, London: Chapman & Hall, p. 209.
36. Fisher, A.G. J. (1963) *Electrochem. Soc.* **110(July)**: 733–48.
37. Ono., Y., Shiraga, N., Kadokura, H. and Yamada, K. (1990) *Electron. Inform. Commun. Eng., Tech. Rep.*, **89(378)**.
38. Shionoya, S. and Yen, W.M. (1998) *Phosphor handbook*, New York: CRC Press LLC, p. 603.
39. McClure, D.S. (1963) *J. Chem. Phys.* **39**: 2850.
40. Shrader, R.E., Larach, S. and Yocom, P.N. (1971) *J. Appl. Phys.* **42**: 4529.
41. Nien, Y.T., Chen, I.G., Hwang, C.S. and Chu, W.Y. (2006) *J. Electroceram*, **17**: 299–303.
42. Suzuki, A. and Shionoya, S. (1971) *J. Phys. Soc. Jpn.* **31**: 1455.
43. Vecht, A., Smith, D.W., Chadha, S.S., Morton, D.C. and Miller, M.R. (1990) *Electrochem. Soc. Extended Abstracts*, **Oct(525)**: 896–7.
44. Kitai, A.H. (1993) *Solid State Luminescence*, London: Chapman & Hall, p. 171.
45. Shionoya, S. and Yen, W.M. (1998) *Phosphor handbook*, New York: CRC Press LLC, p. 601.
46. Howard, W.E. (1981) *Proc. Soc. Display* **22**: 47.
47. Hirabayashi, K., Kozawaguchi, H. and Tsujiyama, B. (1983) *J. Electrochem. Soc.* **130**: 2259.
48. Hirabayashi, K., Kozawaguchi, H. and Tsujiyama, B. (1985) *Kenkyu Jitsuyoka, Hokoku*, **34**: 525 [in Japanese].
49. Sigai, A.G. (1991) US Pat. 5,051,277.
50. Yan, S., Maeda, H., Hayashi, J.-I., Kusakabe, K., Morooka, S. and Okubo, T. (1993) *J. Mater. Sci.* **28**: 1829.
51. Budd, K.D. (1995) US Pat. 5,418,062.
52. Budd, K.D. (1999) US Pat. 5,958,591.
53. Tannas, L.E. Jr. (1985) *Flat-Panel Displays and CRTs*, Van Nostrand Reinhold Company Inc. p. 241.

Index

Note: Figures and Tables are indicated by *italic page numbers*

- AC powder electroluminescence (ACPEL) 252–4
 - compared with DCPEL 250
 - light emission mechanism 257–61
- AC powder electroluminescent (ACPEL) devices
 - applications 253–4, 267
 - limitations 254, 265–7
 - high operating voltages 266
 - lifetime and luminance degradation 254, 265–6
 - low luminance 266
 - moisture sensitivity 266–7
 - materials 262–5
 - operational characteristics 253, 261–2
 - phosphors used 252, 255
 - structure 255
- accelerating point charge
 - electric field emanating from 2–3
 - magnetic field emanating from 3
- activators (for phosphors) 34, 43, 81, 103, 255, 263, 264
- active matrix OLED (AMOLED) displays 111–12, 124, 125, 126, 127–8, 136
 - manufacturing processes 149–55
- ADS108GE luminescent polymer 177
 - in planar LECs 190, 199, 201
- AlInAsP LEDs
 - color triangle (on CIE diagram) 77
 - properties compared with other light sources 144
- AlInGaP LEDs, properties 208
- alkaline earth metal oxo-nitride phosphors 102
- alkaline earth metal silicate phosphors 94–5
- alkaline earth metal silico-nitride phosphors 101
- alkaline earth metal sulfide phosphors 96–7, 234
- alkaline earth metal thiogallate phosphors 97–9
- alternating current . . . *see* AC . . .
- anthracene
 - electroluminescence of 162, 166, 257
 - in OLEDs 114, 118, 120, 121, 162
 - photoluminescence 257
- anti-Stokes shift 32
- artificial atoms (quantum dots) 23, 25
- atomic layer deposition (ALD) process
 - phosphor films in TFEL devices 243–4
 - thin-film encapsulation 154–5
- atomic layer epitaxy (ALE) 243
- Auger electrons 21, 35
- Auger recombination process 31, 35, 56
- avalanche breakdown, in TFEL devices 224, 226
- BaAl₂S₄:Eu phosphor 244, 246
- backlighting applications 228, 262
- band edge emission 31–2
 - improvement in CdS Qdots 51
- band gap 19, 20, 26–7
 - effect of quantum confinement (Qdots) 25, 26–30

- listed for various semiconductors 28, 43, 46, 50, 56, 59
 - see also* energy band diagram
- barium sulfide (BaS) 19
- Barix multilayers, thin-film encapsulation of
 - OLEDs by 154, 155
- BaY₂SiAl₄O₁₂:Ce phosphor 93
- BDOH-PF 179
- BDOH-PF-based LECs 174, 178, 180, 182
- binary oxide dielectrics, properties 235
- bipolar field-emission model 260
 - applied to ZnS:Cu phosphor in ACPEL 258–60
 - experimental evidence 260
- blackbody radiation 2, 12–15
 - Planckian locus in CIE diagram 84, 112, 113
 - spectrum 15
- blinking effect in quantum dots 35, 36
- block copolymers, in LECs 180
- blue LEDs 76, 208, 212
 - wavelength for maximum efficiency 78, 80
- Boltzmann statistics 12
- bulk homojunction LECs 196–201

- Ca₃Sc₂Si₃O₁₂:Ce phosphor 93
- CaAlSiN phosphor 216
- CaAlSiN₃:Eu²⁺ phosphor 101
- cadmium selenide (CdSe) 24, 26, 28
- cadmium selenide (CdSe) quantum dots 56–9
 - bioapplications 59
 - blinking effect 35, 36
 - doped CdSe Qdots 59
 - electroluminescence device using 58
 - optical properties 56–7
 - surface passivation of 57–8
- cadmium sulfide (CdS) 24, 28, 50
- cadmium sulfide (CdS) quantum dots 29, 50–5
 - as bio-imaging probes 53–5
 - doped CdS Qdots 51–2
 - electroluminescence devices using 52–3, 54
 - metal-coated 51
 - optical properties 50–1
- cadmium sulfoselenide (CdS_xSe_{1-x}) 24
- cadmium telluride (CdTe), properties 28, 59
- cadmium telluride (CdTe) quantum dots 59–62
 - bioapplications 61–2
 - in photonic devices 62
 - surface passivation of 59–60
 - type II 60–1
- cathodoluminescence (CL) 2, 20, 21, 22
- cathodoluminescent phosphors 83, 95, 97
- ceramic sheet dielectric electroluminescent devices 225–6, 240
- cerium-activated phosphors 81, 83–93, 94, 234, 234
- chemical vapor deposition (CVD) 42, 154, 244
- chemiluminescence 20
- CIE chromaticity diagram 112, 113
 - blackbody radiation locus 84, 112, 113
 - coordinates, various phosphors 84, 86, 98, 234
 - emitters for white OLED 121
 - LEDs 77
 - Planckian Locus 84, 112, 113
 - tandem white OLEDs + improved color filters 139, 140
 - thiogallate phosphors 98
 - YAG phosphors 84, 86
- color conversion phosphors 75–109
 - activators for 81
 - alkaline earth metal oxo-nitrides 102
 - disadvantages of using LEDs without 76–8
 - excitation wavelengths listed 103
 - metal nitrides 100–1
 - metal oxide based phosphors 83–95
 - metal sulfide based phosphors 95–100
 - problems outstanding 82–3
 - properties required 80
 - requirements 79–80
 - synthesis 83
 - white light generation using 76, 81–2
- color correlation temperature (CCT)
 - lighting applications 112, 146
 - phosphors 83
 - white LEDs 215
- color displays
 - RGBW 4-pixel patterning 127–8
 - tandem OLEDs 136–7
 - white emitter + RGB color filters 123, 124–6
- color rendering 79, 213–14
- color rendering index (CRI) 79
 - improvement using tandem white OLEDs 144–5
 - requirements for various situations 79
 - various OLEDs 144
- color-cathode LCDs 137, 246
- complex oxide dielectrics, properties 236
- computerized tomography (CT), contrast agents 53
- ‘conducting polymers’ 176
- conduction band 19, 20, 227
- conjugated polymers

- electroluminescence from 142, 163–5, 167, 176
 - LECs based on 176
 - OLEDs based on 142–3, 164–5
- contact electroluminescence 256
- copper(I) chloride (CuCl) 24
- Coulombic attraction 27
- Coulombic interaction energy 17, 28, 29–30
- crown ether–alkali metal complexes 182
- crown ethers
 - in backbone of luminescent polymers 179, 180
 - as electrolyte in LECs 182, 188
 - as side groups on luminescent polymers 178
- crystal field splitting 17–18

- DC powder electroluminescence (DCPEL) 249–52
 - compared with ACPEL 250
 - light emission mechanism 251, 252
- DC powder electroluminescent (DCPEL) devices
 - operating mechanism 250–1
 - pulse-wave mode 251
 - structure 250
- defect emission 32–3
- degenerate orbitals
 - doubly degenerate 18
 - five-fold degenerate 18
 - triply degenerate 18
- density of states (DOS) 22, 23
- Destriau cell 252, 253
- Destriau effect 161, 252–3
- dielectrics
 - in ACPEL devices 255
 - in TFEL devices 235, 236
- dipole–dipole energy transfer 15–16
- dipole radiator 5
- direct band gap semiconductor 20
- direct current . . . *see* DC . . .
- display applications
 - OLEDs 112, 122–30, 223
 - TFEL devices 245–7
- dopants (for phosphors) *see* activators
- dynamic bond percolation (DBP) theory 10

- effective mass approximation (EMA)
 - model 27–8
- Einstein coefficients 8–9
- electrical double layer, at LEC
 - electrode–polymer interface 171
- electrochemical doping, in LECs 170, 171
- electroluminescence, first reported 75
- electroluminescence (EL) 2, 20, 21, 21, 161
 - applications 2, 161
 - conjugated polymers 142–3, 163–5
 - first observed 21, 75, 252
 - luminous efficiency 2
 - small organic molecules 114, 162–3
 - see also* powder electroluminescence; thin-film electroluminescence
- electroluminescent (EL) devices
 - advantages in lighting applications 21
 - applications 2, 161, 223
 - compared with other devices 144, 224
 - materials used 223
 - quantum dots used 52–3, 54, 58
- electroluminescent (EL) phosphors 95, 97, 233–4, 257
- electroluminescent (EL) turn-n voltage, listed for various materials 166
- electromagnetic radiation
 - energy released as 3–4, 7
 - selection rules and 7
- electromagnetic spectrum
 - blackbody radiation 15
 - visible light 1
- electron beam lithography 39
- electron spin resonance (ESR) spectroscopy, Mn-doped ZnS Qdots 47
- energy band diagram
 - ACPEL device 259
 - DCPEL device 252
 - semiconductors 20
 - TFEL devices 227
 - see also* band gap
- energy level diagram, ZnS:Cu,Al phosphor 262–3
- etching processes, Qdots manufactured using 39
- europium-activated phosphors 81, 94–5, 96–100, 234, 234
- exciton binding energy 27
 - listed for various semiconductors 28
- exciton Bohr radius 27
- excitons, relaxation processes 30–5
- external quantum efficiency (EQE) 209
 - LECs 178, 188
 - LEDs 77, 209, 210
 - OLEDs 141
- extrinsic luminescence 34

- flash evaporation sources, OLED
 manufacture 152–3
- flexible ACPEL lamps 267
- flexible electroluminescent film 164, 241, 242
- flip–flop bonding of LEDs 210
- fluorescence 31
- fluorescent lighting
 compared with other light sources 144, 219
 requirements for OLEDs in competition 143
- focused ion beam (FIB) technique 39
- Förster resonance energy transfer (FRET) 59, 60
- Fowler–Nordheim equation 259–60
- frozen-junction LECs 171, 183–8
 current/voltage/light intensity characteristics 184
 drawback 187
 EL turn-on response 184–5
 operational stability 185
 photovoltaic response 186–7
 in planar configuration 185–6
 room temperature operation 187–8
- full-color displays
 FTEL 245–7
 LCD 128, 245
 OLED 127–8, 136–7, 156
- full-color electroluminescence
 color-by-blue approach 246–7
 color-by-white approach 245–6
 patterned phosphors used 246
- gadolinium-functionalized quantum dots 52, 54–5, 56
- gallium aluminoarsenide (GaAlAs) LEDs 208
- gallium arsenide (GaAs) 28, 62
- gallium arsenophosphide (GaAsP) LEDs 76
- gallium nitride (GaN) 28, 62
- gallium phosphide (GaP) 20, 28, 62
- germanium, properties 28
- glass substrate thin film dielectric
 electroluminescent devices 224, 225, 235–7
- green LEDs 76, 208
- harmonic perturbation 9–12
- highest occupied molecular orbital (HOMO) 20, 29
- hot-solution decomposition process, Qdots synthesized using 41
- hydrothermal synthesis, of quantum dots 41
- impact-excitation/ionization,
 electroluminescence caused by 161, 162, 233, 257
- incandescent lamps, compared with other light sources 144, 219
- indirect band gap semiconductor 20
- indium antimonide (InSb) 28
- indium arsenide (InAs) 28, 62
- indium gallonitride (InGaN) LEDs 76, 208
 color triangle (on CIE diagram) 77
 luminous efficiency compared with other light sources 77
 properties 208, 209
 with ‘green’ and ‘red’ phosphors 102, 208
- indium nitride (InN) 28, 62
- indium phosphide (InP) 28, 62
- ink paintings, illumination of 220
- inkjet printing, color patterning of OLEDs using 124–5, 142
- internal quantum efficiency (IQE)
 calculations 211
 fluorescent vs phosphorescent emitters in OLEDs 140
 LEDs 210–11
 plot vs emission wavelength 78
 quantum dots 48, 49, 52, 56, 57, 61
- Laporte selection rule 21, 34
- large-area coatings, OLEDs, manufacturing processes 149–55
- large-area displays, OLED-based 124–6
- laser thermal printing, color patterning of OLEDs using 125
- lateral epitaxy on patterned sapphire (LEPS) 209–10
- LCAO-MO model 29–30
- lead selenide (PbSe) quantum dots 63, 63, 64
- lead sulfide (PbS) 24, 28
- LECs *see* polymer light-emitting electrochemical cells
- LED lighting
 applications 219, 220
 characteristic features 217, 218, 220
 energy conservation benefits 221
 future prospects 220–1
- ‘light-emitting battery’, LEC as 174
- light-emitting diodes (LEDs)
 color conversion phosphors 79–83
 alkaline earth metal oxo-nitrides 102
 metal nitrides 100–1
 metal oxide based phosphors 83–95

- metal sulfide based phosphors 95–100
- disadvantages without color conversion phosphors 76–8
- green window problem 78
- history of development 75–6
- inorganic
 - applications 207
 - compared with other devices 143, 144, 183, 224
 - mode of operation 207
 - RGB LEDs approach to white light 76, 81, 208, 212, 213
 - types 211–12
 - see also* organic light-emitting diodes (OLEDs)
- lighting applications
 - comparison of various light sources 144
 - white OLEDs for 112, 143–8
 - performance and cost goals 143–4
- linear combination of atomic orbitals (LCAO) theory 29
 - see also* LCAO-MO model
- liquid crystal display (LCD) TV
 - applications 128, 247
 - color filters 137, 139, 245
- Lossev effect 252
- lowest unoccupied molecular orbital (LUMO) 20, 29
- LS* coupling 17
- luminance
 - ACPEL devices 261
 - LECs 171, 173, 178, 182, 188, 189
 - OLEDs 118, 134, 144
 - quantum dots 58
- luminance efficacy
 - OLEDs 117, 118
 - polymer OLEDs 143
 - tandem OLEDs 133, 134
- luminescence
 - principles 1–18
 - types 2, 20
 - see also* cathodoluminescence; electroluminescence; photoluminescence
- luminescent conjugated polyelectrolytes (LCPEs) 183
- luminescent polymers
 - block copolymers with ion-conductive side groups 180
 - conventional conjugated polymers 142, 176, 177
 - with ion-conductive side groups 176, 178–80
- in LECs 176–80
- in OLEDs 142, 164
- various phosphors (listed) 234
- luminous efficacy/efficiency
 - thiogallate phosphors 99, 100
 - white LEDs 214, 219, 220, 221
 - white OLEDs, compared with other light sources 144
- YAG:Ce phosphors 86–7
 - effect of praseodymium as co-activator 88–90
 - factors affecting 87–8, 92–3
 - (Y_xGd_{1-x})AG:Ce phosphors 91
- magnetic resonance imaging (MRI) properties, quantum dots 52, 54–5, 56
- manganese-activated phosphors 43, 46–7, 227–8, 233, 234
- mechanoluminescence 20
- medical applications, white LEDs 218, 220
- MEH-PPV based LECs
 - blend with PEO + OCA 181–2
 - bulk homojunction LECs 198, 200, 201
 - device characteristics 171, 172, 173
 - factors affecting stability 185–6
 - planar LECs 188, 189, 191, 194–5
- MEH-PPV based LEDs 142–3, 164, 166, 167
- MEH-PPV polymer 177
 - electroluminescence from 142–3, 164–5, 166
 - photoluminescence 191
- metal chalcogenide phosphors 96, 234
- metal nitride based phosphors 100–1, 234
- metal oxide based phosphors 83–95, 234
- metal sulfide based phosphors 95–9, 234
- micro-displays, OLED-based 124, 125
- microemulsion techniques, Qdots synthesized using 40, 49
- molecular beam epitaxy (MBE) 42, 243
- molecular orbital (MO) theory *see* LCAO-MO model
- moving point charge, magnetic field emanating from 1, 2
- multicolor optical coding technique, quantum dots used 56–7, 59
- Na₂Gd₂B₂O₇:Ce³⁺,Tb³⁺ phosphor 94
- nanomaterials 22–3
- nanoparticles, size 23
- nanostructure, categories 22
- nanostructured materials 22–3

- National Television System Committee (NTSC)
 color gamut ratio 135
 listed for white tandem OLEDs 134, 136,
 137
- near-infrared-emitting quantum dots 61
- near-ultraviolet LEDs 207
- phosphors for 95
- properties 208
- in white light generation
 four (OYGB) phosphor approach 215–16
 three (RGB) phosphor approach 208,
 214–15
- nitride phosphors 100–1
- non-radiative relaxation process 34–5
- octyl cyanoacetate (OCA), as additive to
 electrolyte in LECs 181–2
- office lighting requirements 144
- OLEDs *see* organic light-emitting diodes
- oligo(ethylene oxide)
 in backbone of luminescent polymers 179,
 180
 as side groups on luminescent polymers 178,
 179
- on–off bioswitches 59
- operational stability
 LECs 174
 OLEDs 117–19
- organic light-emitting diodes (OLEDs) 111–59
 compared with other light sources 143, 144
 display applications 112, 122–30, 163, 223
 driving voltage of various
 configurations 165, 166
 early developments 111, 163
 electron-transport layer (ETL) in 114, 163
 hole-transport layer (HTL) in 114, 163
 lighting applications 112, 143–8
 manufacturing processes 149–55, 156
 flash evaporation sources 152–3
 thin-film encapsulation 153–5
 vacuum-thermal evaporation using linear
 sources 150–1
 photon emission modes 145–6, 145
 two-layer 113–14, 163
see also white OLEDs
- Ostwald ripening 41
- particle-in-a-box model 27
- passive matrix (PM) displays 111, 228
- patterned phosphors, in full-color EL
 displays 246
- phase transitions
 effects on optical properties of Qdots 26
 factors affecting 26
- phosphor-converted LEDs (pcLEDs) 76, 81–2
- phosphorescence 31
- phosphorescent emitters, OLEDs using 140,
 141, 156
- phosphors
 in ACPEL 255
 activators for 34, 43, 81, 103, 255, 263, 264
 color conversion phosphors 75–109
 electroluminescent 233–4, 257
 thin-film growth 242–5
 meaning of term 19
 photoluminescent 79–83, 257
 quenchers 264
 synthesis 83, 96, 97, 99, 263–4
see also color conversion phosphors
- photoluminescence (PL) 2, 20, 21, 21
- photoluminescence quenching, in planar
 LECs 191
- photoluminescent phosphor(s) 79–83, 257
- photovoltaic systems 62
- physical vapor deposition (PVD) 42
- planar LECs 188–201
 benefit of planar configuration 189
 bulk homojunction LECs 196–201
 with millimeter inter-electrode
 spacing 190–5
 multiple 197–9
 with relaxed p-n junction 195–6
 temperature dependence of doping
 propagation speed 193–4
 time-lapse fluorescence imaging studies 192–
 3, 194–5
- plasma-enhanced chemical vapor deposition
 (PECVD) 154
- point charge *see* accelerating point charge;
 moving point charge; stationary point
 charge
- poly(ethylene oxide) (PEO), as electrolyte in
 LECs 180–2
- polyfluorene-based LECs, ‘turn-on’
 characteristics 173, 174
- polyfluorene-based OLEDs 143
- polymer light-emitting diodes (PLEDs) 142–3,
 156, 164–5, 166, 167
 compared with inorganic LEDs 167
 compared with LECs 168, 173, 186
- polymer light-emitting electrochemical cells
 (LECs) 161–205

- background to development 167–8
- compared with inorganic LEDs 183
- compared with polymer LEDs 168, 173
- current/voltage/light intensity
 - characteristics 171–2
- device characteristics 171–5
- doping relaxation in frozen-junction planar LECs 186, 195–6
- drawbacks 173–5, 183, 195
- dynamic-junction compared with frozen-junction LECs 175, 184–5
- early development 168
- EL turn-on voltage 172–3
- electrochemical doping in 170, 188, 192, 201
- electrode–polymer interface in 170–1
- frozen-junction LECs 171, 183–8
- future developments 202
- as ‘light-emitting battery’ 174
- materials
 - luminescent polymers 176–80
 - polymer electrolytes 168, 180–3
- nature of electric current in 171
- operating mechanism 168–71, 190, 192, 201–2
- phase morphology 174, 175, 178, 183
 - see also* frozen-junction LECs; planar LECs
- poly(*p*-phenylene vinylene) (PPV) 177
 - electroluminescence 142, 164, 166
 - see also* MEH-PPV polymer
- powder contact EL device 256, 257
- powder electroluminescence 249–68
 - light emission mechanisms 224, 251, 252, 257–61
 - preparation of phosphors 263–4
 - see also* AC powder electroluminescence; DC powder electroluminescence
- Poynting vector 4
- praseodymium-activated phosphors 88–90
- quantum confinement 25
 - effects on band gap 25, 26–30
- quantum deficit 79
- quantum dots (Qdots) 23–30
 - advantages over organic dyes in
 - bioapplications 23–4, 35, 56–7, 59
 - blinking effect in 35, 36
 - as color converters for LEDs 103–4
 - core/shell Qdots 38, 45, 48, 57–8
 - double-shell nanostructures 58
 - future research 64
 - history 24–5
 - inorganically capped 37–8
 - meaning of term 22
 - non-radiative relaxation process 34–5
 - optical properties and applications
 - 42–63
 - II–VI Qdots 42–62
 - III–V Qdots 62, 63
 - IV–VI Qdots 63, 64
 - organically capped 36–7
 - radiative relaxation processes 30–4
 - structure–properties relationship
 - 25–6
 - surface passivation of 35–8, 45, 47–8, 57–8, 59–60
 - surface-to-volume ratio 25
 - synthesis processes 38–42
 - bottom-up approaches 39–42
 - top-down approaches 38–9
 - use in colored glasses 24
- quantum efficiency *see* external quantum efficiency; internal quantum efficiency
- quantum electrodynamics 9
- quantum mechanics 5–6
- quantum numbers 16
- quantum well–quantum dot (QW–QD) nanostructures 58
- quenchers (of phosphors) 264
- radiation theory 1–4
- radiation-induced sublimation transfer (RIST) process 125–6
- radiative relaxation processes 30–4
 - activator emission 34
 - band edge emission 31–2
 - defect emission 32–3
- reactive ion etching (RIE) 39
- red LEDs 76, 207
- relaxation processes 30–5
 - non-radiative relaxation 34–5
 - radiative relaxation 30–4
- reverse micelle process 40
- reverse micelle technique (for synthesis of quantum dots) 40, 51
- RF magnetron sputtering, phosphor films in TFEL devices 244–5
- RGBW 4-pixel pattern format
 - development of 126–7
 - full-color displays based on 127–8
- roll-to-roll manufacturing, OLED devices 149, 153, 164
- Ryberg energy 28

- Sawyer–Tower method (of plotting charge–voltage relationship in EL devices) 231–2
output trace 232
- scattering layer, OLED efficiency enhanced by 145–6
- Schrödinger equation 16
- selection rules 7–8, 21, 34
- self-healing mechanisms, for thin-film electroluminescent devices 236–7
- ‘semi-conducting polymers’ 176
see also conjugated polymers
- semiconductors
II–VI compounds 28, 42, 263–4
III–V compounds 28, 62
IV–VI compounds 28, 63
properties listed 28
- shadow masking, color patterning using 122–3
- Sialon-type phosphors 102
- silicate garnet phosphors 93
- silicon, properties 28
- simple harmonic radiator 4–5
- Snell’s Law 239
- sol–gel techniques, nanoparticles synthesized using 40
- solar cells 46, 62, 186
- solid-state lighting (SSL)
applications 148, 219–20
energy conservation benefits 221
panels 147–8
manufacture of 149
white OLEDs 112, 143–8
performance and cost goals 143–4
- solvothermal synthesis, alkaline earth metal sulfide phosphors 97
- sphere-supported thin-film electroluminescent (SSTFEL) devices 226, 241, 242
- spherical harmonics 17
- spin–orbit coupling 8, 16
- spin selection rule 21, 34
- spontaneous emission 9, 12, 30
- sputter deposition, phosphor films in TFEL devices 244–5
- SrBa phosphor 216
- $\text{Sr}_x\text{Ca}_{1-x}\text{S}:\text{Eu}$ phosphor 96
- $\text{SrGa}_2\text{S}_4:\text{Eu}^{2+}$ phosphor 97, 234
- $\text{SrS}:\text{Ce},\text{Eu}$ phosphor 234, 245
properties 234
- stationary point charge, electric field emanating from 1, 2
- stimulated emission 9, 34
- Stokes shift 31–2, 79
- street lighting system 218, 219
- strong field scheme (in crystal field theory) 18
- ‘superyellow’ luminescent polymer 177
LEC based on 188
- surface passivation, quantum dots 35–8, 45, 47–8, 57–8, 59–60
- surface states on quantum dots
effects on optical properties 25
factors affecting 33
- tandem OLEDs *see* white OLEDs, tandem
- Tang cell 163
- terbium-activated phosphors 94, 234
- thermoluminescence 20
- thick dielectric electroluminescent (TDEL) devices 224–5, 237–40
in full-color displays 245
- thick top dielectric electroluminescent devices 226, 240–1
- thin film electroluminescence (TFEL) 21, 223–48
light emission mechanism 224
- thin film electroluminescent (TFEL) devices
charge–voltage relation 229–31
method of determining 231–2
equivalent circuit 228–9, 229
self-healing of damaged region 236
structure 224–6, 235–42
theory of operation 226–33
- thin film encapsulation, OLEDs 153–5
- thin film transistor (TFTs), in ACTFEL displays 254
- thiogallate phosphors 97–9
- total internal reflection 145, 146, 239
- triplets, white OLEDs based on 140–2
- tris-(8-hydroxyquinolino)aluminium (Alq), in OLEDs 114, 163
- ultrasound method for Qdot production 41
- ultraviolet irradiation, luminescence quantum efficiency of ZnS Qdots affected by 48
- ultraviolet LEDs 207
phosphors for 79, 82, 94
- ‘upconversion’ 32, 57
- vacuum-thermal evaporation
linear sources, in OLED manufacture 150–1
thin film EL devices prepared using 242–3
- valence band 19, 20, 227
- vanadate garnet phosphors 94

- wallplug efficiency, LEDs 209
- waveguide emission
 in glass substrate EL device 239
 in OLEDs 145, 146
- white LEDs 207–8
 applications 218–20
 costs 219
 design of lighting system 217–18
 luminous efficacy 214, 219, 220, 221
 properties 218
- white light
 generation strategies using LEDs 76, 81–2, 212–18
 blue LED + one (yellow-orange) phosphor 76, 82, 208, 213
 blue LED + two (green + red) phosphors 76, 81, 102, 208
 near-UV LED + four (OYGB) phosphors 215–16
 near-UV LED + three (RGB) phosphors 208, 212, 213, 214–15
 OLEDs 113–22
 three (RGB) LEDs 76, 81, 208, 212, 213
 UV LED + three (RGB) phosphors 82, 103
- white light-emitting LEDs *see* white LEDs
- white light-emitting OLEDs *see* white OLEDs
- white OLEDs
 display applications 112, 122–30
 color-patterning methods 122–3
 emitter selection method 121–2
 fluorescent and phosphorescent emitters in 141
 four-layer 128, 129
 spectrum 129
 large-area displays based on 124–6
 lighting applications 112, 143–8
 low-voltage 128–30
 polymer-based 142–3
 tandem OLEDs
 architecture 131
 fluorescent combined with phosphorescent emitters 141–2
 full-color displays using 136–7, 156
 improved color filters for wide color gamut 137–9
 optimization of tandem stacks 131–2
 performance 133–5
 scattering layer 146, 147
 spectra 132, 133, 136, 138, 145
 structures for improved color gamut 135–6
- three-layer 112–13, 128, 129
 spectrum 129
- triplet-based 140–2
- two-layer 113–14
 color stability 117, 118, 119
 color stability compared with other colored LEDs 120
 half-life data 117–18, 119
 mechanism of operational stability 120–1
 operational stability 117–19
 optimization of white color 114–17
 performance 117–19
 spectra 115, 118, 119
- wurtzite crystal structure 43, 262
 semiconductors 28
- $\text{YCa}_3\text{M}_3\text{B}_4\text{O}_{15}:\text{Eu}^{3+}$ phosphor 94
 $(\text{Y}_{2-x-y}\text{Eu}_x\text{Bi}_y)\text{O}_3$ phosphors 94
- yttrium aluminium garnet (YAG)
 Ce^{3+} -activated phosphor 83–5, 213
 theoretical limit of luminous efficacy 86–8
 $\text{Ce}^{3+}/\text{Pr}^{3+}$ -co-activated phosphor 85–90
- yttrium/gadolinium aluminium garnet, Ce^{3+} -activated phosphor 90–2
- zener diodes, in TFEL equivalent circuit 229
- zener emission effect 161, 257
- zero-dimension nanostructures *see* quantum dots
- zinc blende crystal structure 43, 262
 semiconductors 28
- zinc oxide (ZnO)
 manganese-doped 44
 properties 28, 43
- zinc oxide (ZnO) quantum dots 43–6
 applications in solar cells 46
 defect states in 33
 doped ZnO Qdots 44–5
 photoluminescence properties 43–4
 quantum efficiency 44
 surface passivation of 45
 synthesis of 40
- zinc selenide (ZnSe), properties 28, 48
- zinc selenide (ZnSe) quantum dots 48–50
 enhancement of luminescence in 49–50
 photoluminescence properties 48–9
- zinc sulfide (ZnS)
 AC EL spectra of various activated powder phosphors 264–5
 copper-activated 252, 257, 265
 Cu,Al doped 255, 265

- Cu,Cl doped 258–9, 265
- Cu,I doped 255, 265
- manganese-doped 43, 46–7, 227–8, 233, 234, 257
 - preparation of thin-film phosphors 242–3
- Mn,Cu doped 249–50, 255
- Mn,Cu,Cl doped 255, 265
- properties 28, 46, 262
 - structural modifications 262
 - terbium doped 234
- zinc sulfide (ZnS) quantum dots 46–8
 - doped ZnS Qdots 46–7
 - surface passivation of 47–8
 - UV irradiation effects 48
- zinc sulfoselenide ($\text{ZnS}_{1-x}\text{Se}_x$) 20
 - Cu,Cl doped 255
- zinc telluride (ZnTe) 28